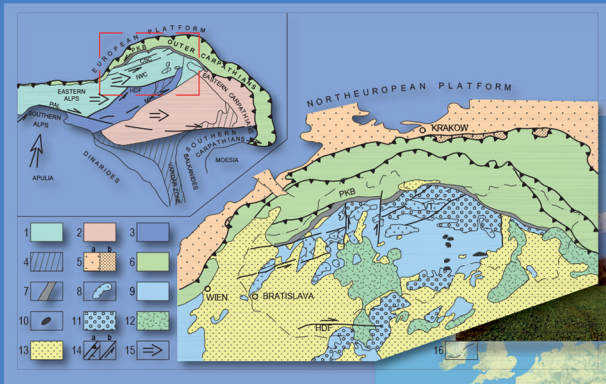


52/2/2020
 ISSN 1338-3523
 ISSN 0369-2086

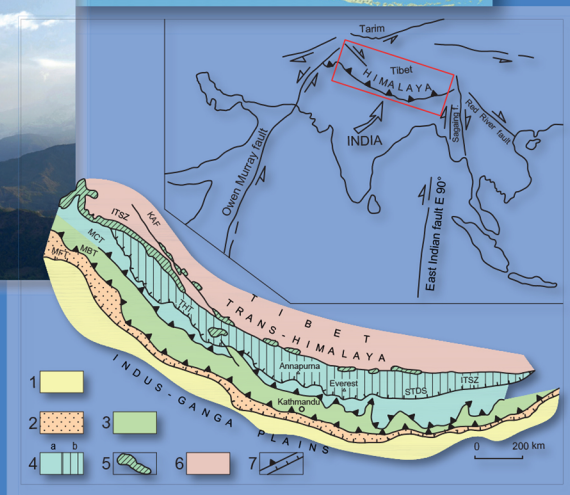
Mineralia Slovaca



W. CARPATHIANS



HIMALAYAS



Štátny geologický ústav Dionýza Štúra Bratislava



PRESEDA VYDAVATELSKEJ RADY – CHAIRMAN OF EDITORIAL BOARD

IGOR SLANINKA

Štátny geologický ústav Dionýza Štúra Bratislava

VEDECKÝ / VEDÚCI REDAKTOR – SCIENTIFIC AND MANAGING EDITOR

ZOLTÁN NÉMETH

Štátny geologický ústav Dionýza Štúra
Regionálne centrum Košice
Jesenského 8, 040 01 Košice
zoltan.nemeth@geology.sk

REDAKČNÁ RADA – EDITORIAL BOARD

KLEMENT FORDINÁL, Štátny geologický ústav D. Štúra Bratislava
ĽUBOMÍR HRAŠKO, Štátny geologický ústav D. Štúra Bratislava
VLASTA JÁNOVÁ, Ministerstvo životného prostredia SR Bratislava
JOZEF KORDÍK, Štátny geologický ústav D. Štúra Bratislava
PETER MALIK, Štátny geologický ústav D. Štúra Bratislava
JOZEF MICHALÍK, Ústav vied o Zemi SAV Bratislava

ĽUBOMÍR PETRO, Štátny geologický ústav D. Štúra Košice
DUŠAN PLAŠIENKA, Prírodovedecká fakulta UK Bratislava
MARIÁN PUTIŠ, Prírodovedecká fakulta UK Bratislava
JÁN SOTÁK, Ústav vied o Zemi Banská Bystrica
LADISLAV ŠIMON, Štátny geologický ústav D. Štúra Bratislava
PAVEL UHER, Prírodovedecká fakulta UK Bratislava

REDAKCIA – EDITORIAL STAFF

Vedúci oddelenia vydavateľstva ŠGÚDŠ a propagácie – Head of the Department of ŠGÚDŠ Publishers and Promotion

LADISLAV MARTINSKÝ

ladislav.martinsky@geology.sk

Jazykoví redaktori – Lingual editors

Janka Hrtusová – Zoltán Németh

janka.hrtusova@geology.sk

Grafická úprava a technické spracovanie – DTP processing

Slávka Žideková

slavka.zidekova@geology.sk

Mineralia Slovaca (Web ISSN 1338-3523, ISSN 0369-2086), EV 3534/09, vychádza dvakrát ročne. Vydavateľ a tlač: Štátny geologický ústav Dionýza Štúra, Mlynská dolina 1, 817 04 Bratislava, IČO 31 753 604. Dátum vydania čísla 52/2/2020: február 2021. Predplatné v roku 2020 vrátane DPH, poštovného a balného pre jednotlivcov 22,00 €, pre členov SGS a geologických asociácií 20,90 €, pre organizácie v SR 31,90 €, pre organizácie v ČR 55,00 €. Cena jednotlivého čísla pri osobnom nákupe v predajniach ŠGÚDŠ v Bratislave a v Košiciach je 6,05 € vrátane DPH. Časopis možno objednať v redakcii a v knižnici regionálneho centra v Košiciach. Adresa redakcie: Štátny geologický ústav D. Štúra – RC Košice (Mineralia Slovaca), Jesenského 8, 040 01 Košice. Telefón: 055/625 00 43; fax: 055/625 00 44, e-mail: mineralia.slovaca@geology.sk, e-mail knižnica: secretary.ke@geology.sk

Mineralia Slovaca (Web ISSN 1338-3523, ISSN 0369-2086) is published twice a year by the State Geological Institute of Dionýz Štúr Bratislava, Slovak Republic. The date of issuing of the number 52/2/2020: February 2021.

Subscription for the whole 2020 calendar year (two numbers of the journal): 66.00 € (Europe), 77.00 € (besides Europe), including VAT, postage and packing cost. Claims for nonreceipt of any issue will be filled gratis.

Order of the Editorial Office: Štátny geologický ústav D. Štúra – RC Košice (Library), Jesenského 8, SK-040 01 Košice, Slovak Republic. Phone: +421/55/625 00 43; fax: +421/55/625 00 44, e-mail: mineralia.slovaca@geology.sk, library: secretary.ke@geology.sk

© Štátny geologický ústav Dionýza Štúra Bratislava

PŮVODNÉ ČLÁNKY – ORIGINAL PAPERS

Marko, F., Sigdel, A., Bielik, M., Bezák, V., Mojzeš, A., Madarás, J., Papčo, J., Siman, P., Acharya, S. & Fekete, K.

A comparison of Cenozoic Neo-Alpine tectonic evolution of the Western Carpathian and Himalayan orogenic belts (Slovakia – Nepal)

Porovnanie kenozoickej neoalpínskej tektonickej evolúcie Západných Karpát a Himalájí (Slovensko – Nepál) 63

Potočný, T., Méres, Š. & Plašienka, D.

Geological structure and tectonometamorphic evolution of the Veporic–Gemic contact zone constrained by the monazite age data (Slavošovce–Štítňík area, Western Carpathians, Slovakia)

Geologická stavba a tektonometamorfný vývoj kontaktnej zóny veporika a gemerika dokumentovaný rádiometrickými vekmi monazitu (oblasť Slavošovce – Štítňík, stredné Slovensko) 83

Radvanec, M. & Gonda, S.

Successive formation of Fe and Mn skarns in the Čučma locality (Gemic unit, W. Carpathians): from metasomatic stage through the amphibolite facies overprint with Ti-rich tephroite to retrograde stilpnomelane-chlorite zone

Postupný vznik Fe a Mn skarnov na lokalite Čučma v gemeriku: od metasomatózy s následnou rekryštalizáciou v amfibolitovej fácií a vznikom Ti tefroitu až po retrográdnú metamorfózu v stilpnomelánovo-chloritovej zóne 103

Horváthová, H., Jurkovič, Ľ., Macek, J., Tóth, R. & Kravchenko, D.

Nanodegradation of chlorinated hydrocarbons from groundwater in the native geological environment (laboratory batch experiment)

Nanodegradácia chlórovaných uhľovodíkov z podzemnej vody v natívnom geologickom prostredí (laboratórny vsádzkový experiment) 133

OBÁLKA:

Porovnanie kenozoického geologického vývoja Západných Karpát a Himalájí ako dvoch vzdialených segmentov alpsko-himalájskeho orogénneho pásma (obrázok v strede) je v článku Marko et al. v tomto čísle na s. 63 – 82. Neoalpínska geodynamika, tektonické rozdelenie a morfológia Západných Karpát sú zobrazené na dvoch horných obrázkoch a v prípade Himalájí na dvoch spodných obrázkoch. Fotografie odd. geol. a paleont. Univ. Komenského a J. Madarás.

COVER:

Cenozoic geological evolution of Western Carpathians and Himalayas as two distant segments of Alpine-Himalayan orogenic belt (picture in the middle) is compared in the paper by Marko et al. in this issue on pp. 63–82. The Neo-Alpine geodynamics, tectonic division and morphology of the Western Carpathians are displayed in two upper pictures, and those of Himalayas in two pictures below. Photographs by the Dpt. of Geol. and Paleont., Comenius Univ., and J. Madarás.

A comparison of Cenozoic Neo-Alpine tectonic evolution of the Western Carpathian and Himalayan orogenic belts (Slovakia – Nepal)

FRANTIŠEK MARKO^{1*}, ASHOK SIGDEL^{2*}, MIROSLAV BIELIK^{1,3}, VLADIMÍR BEZÁK³,
ANDREJ MOJZEŠ¹, JÁN MADARÁS³, JURAJ PAPČO⁴, PAVOL SIMAN^{3,5}, SUBASH ACHARYA²
and KAMIL FEKETE⁶

¹ Comenius University in Bratislava, Faculty of Natural Sciences, Ilkovičova 6, SK-842 15 Bratislava, Slovakia;
frantisek.marko@uniba.sk

² Tribhuvan University, Department of Geology, Tri-Chandra Multiple Campus, Ghantaghar, Kathmandu, Nepal;
ashoksigdel80@gmail.com

³ Slovak Academy of Sciences, Earth Science Institute, Dúbravská cesta 9, SK-845 28 Bratislava, Slovakia

⁴ Slovak University of Technology, Faculty of Civil Engineering,
Radlinského 11, SK-810 05 Bratislava, Slovakia

⁵ Office of Slovak Academy of Sciences, Štefánikova 49, SK-814 38 Bratislava, Slovakia

⁶ State Geological Institute of Dionýz Štúr, Mlynská dolina 1, SK-817 04 Bratislava, Slovakia

* corresponding authors

Abstract: The Western Carpathians and Himalayas belong to the same global Alpidic orogenic system, which is the result of Euroasian plate collision with the continental fragments of Gondwana after closing of the Tethys ocean. Having the field experiences from both distant mountain ranges of the same orogenic system and applying the principles of comparative tectonics, they were evaluated and compared in the paper. Generally, they have the same collisional structural-tectonic style, but there are as well many peculiarities and differences resulting from the specific conditions of collision in the Western Carpathian and Himalayan areas. The Western Carpathians structure is a result of gradual alternation of Variscan (Hercynian; Paleozoic), Paleo-Alpine (Mesozoic) and Neo-Alpine (Cenozoic) convergent and divergent plate tectonic processes, while the Himalayas represents purely Neo-Alpine Cenozoic structure evolved during the continual long lasting and rapid plate convergence. Despite the geosutures from the earlier orogenic evolutions are known in the parallel north-located zone, too. As the most important factors, influencing character of collision, seems to be the geometry of converging plate margins and the rate of the ocean floor spreading/subduction, driving the orogenesis. Paper gives a brief overview of tectonic architecture and evolution of both mountain ranges and compares their common features and contrasts.

Key words: comparative tectonics, Tethyan Alpides, Western Carpathians, Himalayas

Graphical abstract



Highlights

- Paper compares tectonic architecture of two distant orogenic segments of Tethyan Alpides.
- The differences of W. Carpathians and Himalayas Cenozoic Neo-Alpine collisions result from the geometry of plate margins and rates of plates convergence during the Tethys ocean closure – W. Carpathians are characterized with oblique Cenozoic collision of strike-slip-orogen type, but Himalayas are a result of frontal collision, which in contrast with W. Carpathians still continues with high rates of recent movements, strong erosion and extreme seismicity.

1. Introduction

There are two prominent young and not yet denuded global orogenic systems of the world – a meridional pan-American Circum Pacific (South American Andes and North American Cordilleras) and equatorial Alpine-Himalayan (A-H) belts. They both evolved at active margins of converging lithospheric plates. The pan-American orogenic belt as a part of circum Pacific mobile zone is Andian and Cordillera type orogen, meanwhile A-H orogen is a collisional Alpine-type orogen (sensu Dewey & Bird, 1970). In terms of plate tectonics, the Alpine-Himalayan orogenic belt is a result of continent-continent collision, imprinting to collisional zone the tectonic style of extreme shortening and uplifting, produced predominantly by thrusting, with an important role of strike-slip tectonics

genetic belt as a part of circum Pacific mobile zone is Andian and Cordillera type orogen, meanwhile A-H orogen is a collisional Alpine-type orogen (sensu Dewey & Bird, 1970). In terms of plate tectonics, the Alpine-Himalayan orogenic belt is a result of continent-continent collision, imprinting to collisional zone the tectonic style of extreme shortening and uplifting, produced predominantly by thrusting, with an important role of strike-slip tectonics

as well. The Alpine-Himalayan global world collisional zone is composed of many mountain systems, listed from the west: North African Atlas, Betic cordillera, Pyrenees, Apennines, Western, Central and Eastern Alps, Western, Eastern and Southern Carpathians, Dinarides, Balkanides, Hellenides, Anatolides (Pontides and Taurides), Caucasus, Iranides (Zagros, Elburz and Kopet Dag), Hindukus, Pamir, Karakoram and Himalayas. The southern continuation of this mobile belt is indicated by subduction zones of Sunda-Java trenches and Alpine mobile belts of Barma, Malaysia, Sumatra, Borneo, Java, Fiji and New Zealand (**Fig. 1**). Although all these segments of A-H belt have a common nature, there are particularities and some structural-tectonic differences between individual segments of this extended belt due to the local conditions and geometry of plate margins, type of collision, type and physical properties of lithosphere, rate of convergence, geological evolution, etc. In the frame of the Slovak research project APVV-16-0146 and in cooperation with the Department of Geology, Tri-Chandra Multiple Campus, Tribhuvan University in Nepal we realized the reconnaissance field research trip in april 2019 (**Fig. 6**). It was focussed on transect from Pokhara to Muktinath localities along Kali Gandaki river valley, crossing the zones of Lesser and Higher Himalayas in Nepal (Mojzeš et al., 2020). The Kali Gandaki river valley represents the deepest antecedent valley in the Himalayas. It provides a natural geological cross-section through the tectonic contact of the main Himalayan units. The main objective of our joint collaborative field work and review

of relevant literature was to compare structural evolution and tectonic style of two distant segments of the global equatorial orogenic system – the Western Carpathians of Slovakia and the Nepal Himalayas.

Tectonic architecture and evolution of compared orogens

Western Carpathians

The Carpathians represent a part of the Mesozoic-Cenozoic Alpine-Himalayan fold and thrust belt – the result of collision of Gondwana plates with Euro-Asian plate (Laurasia) during the closure of Tethys ocean. They are divided into Western, Eastern and Southern Carpathians. The Western Carpathians, covering the whole territory of Slovakia (**Fig. 2, 4a**), represent eastern orographic continuation of Eastern Alps and further east they continue to Eastern and next to Southern Carpathians. Although the Alps and Carpathians belong to the same Alpidic system, there are differences in Neo-Alpine (Neogene–Quaternary) evolution of individual orogenic segments. The Alps represent a zone of shortening due to typical frontal continental collision with a very deep orogenic roots, while the Carpathians are the result of tectonic escape of microplates (Inner Western Carpathians (IWC), Pelsö, Tisia) from the Alpine domain (Doglioni et al., 1991; Ratschbacher et al., 1991a, b) to the area of subducting oceanic lithosphere of the Magura basin, creating the embayment in the Euroasian lithospheric plate (EP). It led to the oblique continent-continent (CC)



Fig. 1. Tethyan Alpides of the world.

collision of IWC microplate with EP in the western part of the Western Carpathians and tectonic arrangement of flysch sediments of the Magura basin into the pile of nappes forming the current Outer Carpathians accretionary wedge. The Carpathian loop was formed during two successive orogenic events. At the Paleo- and Meso-Alpine Jurassic–Late Cretaceous–Early Paleogene epoch (Plašienka, 1999, 2018a) the nappe architecture of pre-Tertiary units was formed far from their recent position. During the Neo-Alpine Cenozoic epoch (Kováč, 2000) units which were consolidated earlier during the Paleo-Alpine epoch removed to Carpathian space and were arranged in a new configuration – the nappe structure of Paleogene sedimentary complexes in front of the prograding Paleo-Alpine units was formed. Final neo-tectonic character was imprinted to orogen in the latest Pliocene-Quaternary stages of tectonic evolution.

The principal tectonic division of the Western Carpathians is derived from the youngest Neo-Alpine

and mostly Miocene tectonic processes, when the flysch prism of the Outer Western Carpathians and the Pieniny Klippen Belt structure were created during collision of the Inner Western Carpathians block with the foreland. So, the Western Carpathians sensu Biely (1989) and Bezák et al. (2004) are divided to Inner and Outer Carpathians. The Inner Western Carpathians (IWC) are composed of the Tatric, Veporic and Gemeric Paleo-Alpine crustal basement nappe units and the Fatric, Hronic, Meliatic, Turnaic and Silicic detached superficial Mesozoic nappe units. The crustal basement units are formed of crystalline basement with incorporated fragments of Variscan (Hercynian) tectonic units, and covered by autochthonous Upper Paleozoic and Mesozoic formations. The Meliatic unit encompasses remnants of ophiolite suite of closed Jurassic ocean (Kozur & Mock, 1973; Kozur et al., 1996). The rare occurrences of Meliatic unit follows Paleo-Alpine collisional suture created after this Tethys-related Meliata Ocean closure (Plašienka et al., 2019). Another younger-Neo-Alpine

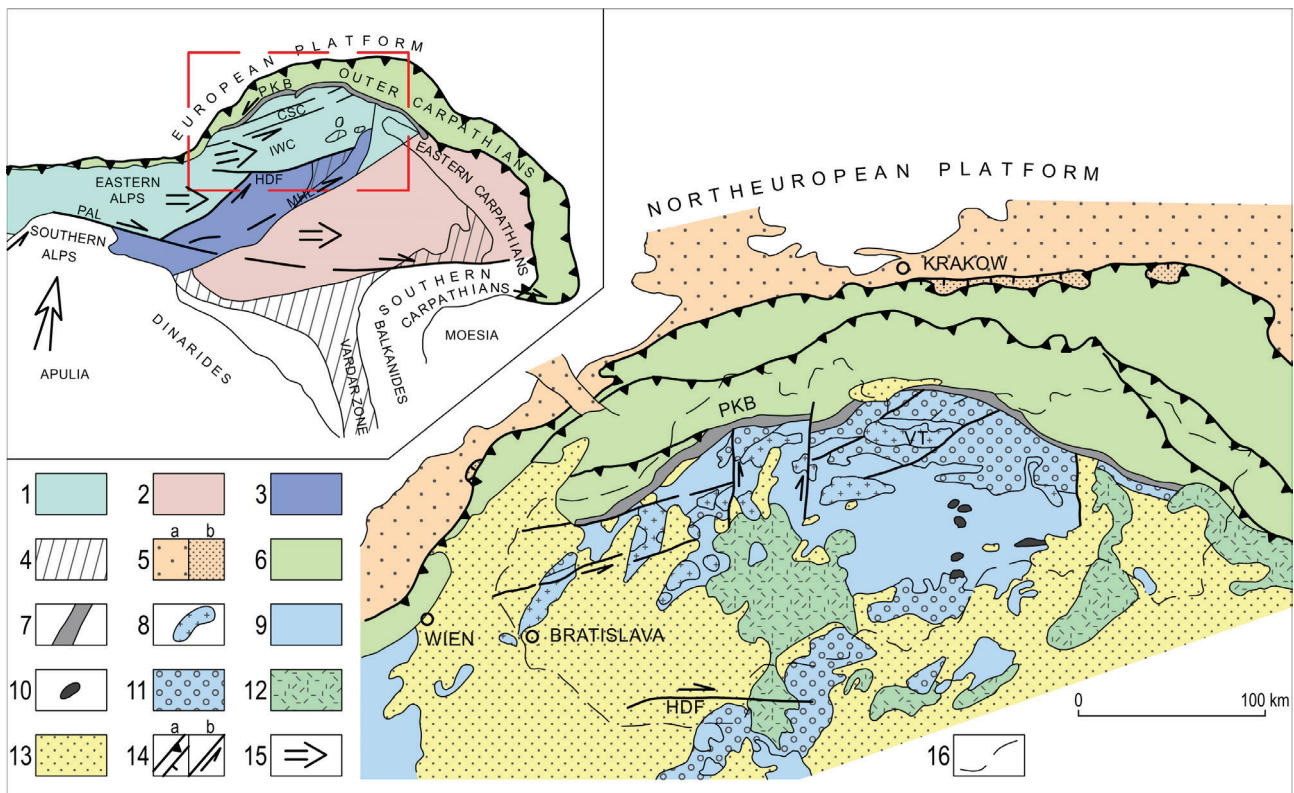


Fig. 2. Neo-Alpine architecture, dynamics and tectonic division of the Western Carpathians (compiled according to Kovács et al., 2000; Lexa et al., 2000; modified according Marko et al., 2017). Abbreviations: PKB – Pieniny Klippen Belt, VT – High Tatras = Vysoké Tatry Mts., IWC – Inner Western Carpathians, CSC – Carpathian Shear Corridor, HDF – Hurbanovo-Dijósjenő Fault, MHL – Mid-Hungarian Line, PAL – Peri-Adriatic Line. Explanations: 1 – ALCAPA micro-plate; 2 – Tisia micro-plate; 3 – Pelsö micro-plate; 4 – oceanic crust domains; OUTER (External) WESTERN CARPATHIANS: 5 – Miocene molasse sediments – a) autochthonous not deformed, b) mobilized, thrust and folded; 6 – Neo-Alpine orogenic accretionary prism of pre-dominantly Paleogene flysch sediments; INNER (Internal) WESTERN CARPATHIANS: 7 – Pieniny Klippen Belt – suture zone of extreme shortening and shearing; 8 – Paleozoic crystalline basement exhumed in core mountains; 9 – Paleozoic-Mesozoic complexes as a whole; 10 – Meliatic unit – ophiolites; 11 – Undeformed Inner Carpathian Paleogene sediments; 12 – Neogene syn- and post-collisional volcanites; 13 – Neogene back-arc and intra-arc sedimentary basins; 14 – a) Prominent thrust boundaries, b) Prominent strike-slip boundaries; 15 – Course of block extrusions; 16 – state border of Slovak Republic.

suture is represented by the Pieniny Klippen Belt (PKB) zone and cogenetic tectonic boundaries. PKB is described as a zone of extensive shortening and strike-slip shearing (e.g. Plašienka et al., 2020 and references therein). The sedimentary basins with the Upper Cretaceous, Paleogene and Neogene filling and neo-volcanic complexes represent the Neo-Alpine formations superimposed on Paleo-Alpine nappe system. The dynamic evolution of the Western Carpathians resulted in the Neogene sedimentary basins genetic variation. Depending on their geodynamic position within the orogenic belt, the fore-arc, inter-arc and back-arc basins are present (Kováč et al., 2016, 2017). There occur basins formed by lithospheric extension – thermal subsidence, flexure and strike-slip related basins (Vass, 1979, 1998; Kováč, 2000; Janočko et al., 2003a, b). The thin Penninic oceanic crust subducted during the oblique convergence, being melted in the upper mantle, thus providing a source for extensive subsequent volcanism, situated at the frontal edge as well as in the interior of the overriding crustal slab (e.g. Lexa & Konečný, 1998, Lexa et al., 2010).

The current morpho-structural character and shape of orogenic belt was to the Western Carpathians imprinted during the Neo-Alpine tectonic period. The shape of the Carpathian orogenic belt was constrained by the pre-collision shape of thin crust embayment of the flysch basin inside the stable North European Platform (NEP). The eastwardly prograding crustal segment of Internides (IWC) was broken into several different fragments, which underwent large translations, rotations, uplifts and subsidence, including tilting during the occupation of oceanic crust embayment in NEP (Marko et al., 2017; Bezák et al., 2020). This – with combination of astenolith arise and extension resulted in development of specific morpho-tectonic features, including alternating intra-montane sedimentary basins and core mountain horsts, structural bending, fan structures and robust Miocene volcanic activity; all peculiar particularly to the Western Carpathians.

The Western Carpathian part of the Alpine orogenic belt is recently generally inactive, because the driving force of collisional dynamics – the subduction and tectonic escape processes have already ceased in the Late Tertiary. This is the reason why the recent movements (max. first few mm/yr) and Neo-tectonic activity are very moderate, reflected in the weak intensity, character and distribution of earthquakes (Cipciar et al., 2016; Hók et al., 2016). The earthquakes are generated on the faults and fault zones, controlling relaxation post-collisional movements of individualized IWC blocks (Marko et al., 2017). Micro-earthquakes are prevailing, rare macro-seismic events reach an intensity of M 2.9. The clustering of more important macro-earthquakes, related to large faults, has been recorded only in a few areas (Dobrá Voda, Žilina,

Kolárovo, Komárno). The strongest recorded earthquake (1906) in the Dobrá Voda area had an intensity of M 5.7.

For the Western Carpathians, there is typical a distinctive polarity of the orogenic final overthrusts at the front of the Western Carpathians loop (Jiříček, 1979; Matenco & Bertoli, 2000). The active collisional front moved from the west to the east, and resulted in a complex, heterogeneous, polyphasic and diachronous structure of the Carpathian loop (Unrug, 1984). The same character has the Pieniny Klippen Belt structure (e.g. Andrusov, 1974; Birkenmajer, 1986; Plašienka, 2018b), on the border of IWC and OWC.

The crustal thickness (the Moho depth) of the Western Carpathians (Bielik et al., 2018 and references therein) ranges from 25 to 42 km. Its typical feature is that the thickness of the crust rises from south to north. While the southern parts of the Western Carpathians (IWC) are characterized by a thickness of only about 25 to 33 km, the northern parts (the Central and Outer Western Carpathians) by thicker crust (35–40 km). The thinnest crust of 25 km is observed beneath the Danube basin. On the contrary, the largest crustal thickness (Janík et al., 2011) in the Western Carpathians was measured northeast of the Vysoké Tatry Mts., which are the highest mountains of the Carpathians. In general, however, the Western Carpathian orogen is significant by crustal thickening also in comparison with Himalayan belt.

The crustal thickness of the Western Carpathians correlates very well with the thickness of the lithosphere-asthenosphere boundary (LAB). The thickening of the lithosphere in the south-north direction can also be observed. The IWC are accompanied by a thinner lithosphere of about 100–120 km. A slightly thicker lithosphere can be observed in the northern part of IWC and Outer Western Carpathians. An interesting pattern of the Carpathian lithosphere is its thickening also along strike of the Carpathian arc, when in the Eastern Carpathians the LAB reaches up to 240 km (Zeyen et al., 2002; Dérerová et al., 2006).

Himalayas

Geomorphologically and structurally the most spectacular segment of Tethyan Alpides is the Himalayan belt, one of the youngest gigantic mountain ranges of the world. This is an example of strongly polarized asymmetric, southvergent collisional orogen (**Fig. 3, 4b**). The high ranges of Himalayas were formed due to the Indian shield (a continental part of Indo-Australian plate) northward penetration into mega-embayment of the Tethys ocean in the Euroasian plate (e.g. Gansser, 1966; Golonka, 2000). The Alpine-Himalayan mobile belt is in various parts diachronous and heterogeneous, representing different final stages of Wilson cycle (*sensu* Dewey & Burke, 1974). Some parts are evolved between already collided

continental plates, some parts are situated in segments, where the oceanic crust was not completely consumed by subduction and the convergence still continues (Java, Fiji, etc.). The Himalayas represent the peculiar terminal stage of the Wilson cycle. The Himalayas have evolved due to the closure of Meso-Cenozoic ocean floor – the process, which did not terminated by continent-continent collision, but continental lithosphere of Indian plate after subduction of Tethyan ocean floor and initial collision (ca 50 Ma ago) also subducted ca 700 km under Euroasian plate (Dadlez & Jaroszewski, 1994; Lyon-Caen & Molnar, 1983). It is a very rare Ampferer's A-type subduction (sensu Bally, 1981), because continental lithosphere

usually does not undergo subduction, what is one from the basic paradigms of plate-tectonic concept. Nevertheless this continental plate subduction resulted in grandiose crustal thickening, which is responsible for the highest uplifts, creating the highest mountains and plateaus in the world. From this point of view the Himalayas represent a specific collisional orogen, which is characterized by the continental crust duplexing of the underthrusting Indian crust and the overthrusting Euroasian crust (Yeats, 2012). Similar style is typical for the Alps.

Based on tomographic inversion of regional earthquake data (Koulakov et al., 2015) and receive function image (Nábělek et al., 2009; Subedi et al., 2018) it was found

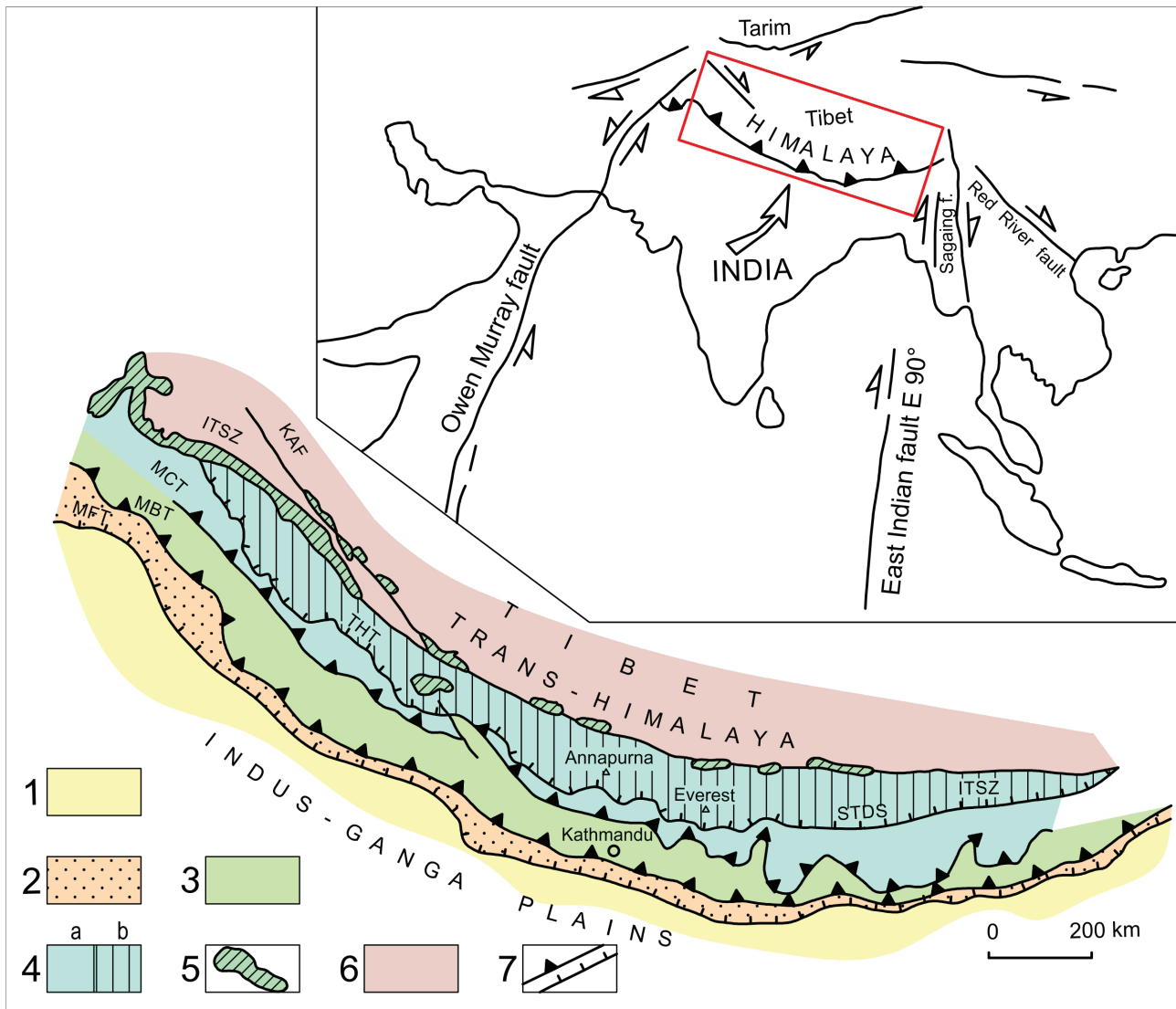


Fig. 3. Neo-Alpine architecture, dynamics and tectonic division of the Himalayas (after Valdiya, 1992, modified). Abbreviations: MFT – Main Frontal Thrust, MBT – Main Boundary Thrust, MCT – Main Central Thrust, THT – Trans-Himandry Thrust (in India), STDS (in Nepal), ITSZ – Indus-Tsang-Po Suture Zone, KAF – Karakoram Fault. Explanations: INDIAN PLATE: 1 – Indian plains of Quaternary alluvial deposits covering ancient not mobilized craton; 2–5 – Part of craton mobilized in orogenic accretionary prism: 2 – Sub-Himalaya – Miocene-Pleistocene molasse sediments of Siwalik Group; 3 – Lesser Himalaya; 4 – a) Higher Himalaya, b) Tibetan Tethys Zone; 5 – Ophiolites; ASIAN PLATE: 6 – Trans-Himalaya (Tibetan Himalaya); 7 – Prominent thrust boundaries, detachments.

out that the thickness of the crust beneath the Nepal Himalayas varies from ~40 to ~75 km. It increases across the Himalayas from the south to the north. Below the foothills (the Himalayan Main Frontal Thrust – MFT) and the Lesser Himalaya the crustal thickness is about 40 km, but beneath the Higher Himalayan range and Central Tibet Plateau (Lhasa and Qiangtang Blocks) it reaches already 65–75 km.

Despite the fact that the results related to the position of the LAB in the Himalayan region differ (e.g. Zhao et al., 2010; Xu et al., 2011; Deng et al., 2014) it can be generalized that the depth of the LAB increases in direction of the underthrusting of the Indian plate beneath the Eurasian plate. However, a change in lithosphere thickness can also be observed along the Himalayan orogen. According to S receive function results (Xu et al., 2011), the LAB under the MFT and the Lesser Himalaya ranges at depths of ~80–120 km, while under the Higher Himalayan range and the Central Tibet Plateau it reaches values up to ~180–240 km. Deng et al. (2014) suggest that the lithosphere can have a thickness of up to 300 km below the Central Tibet Plateau.

Approximately 1500 km northward drift of Indian plate and its invasion to Euroasian plate embayment was controlled by the first order N-S transcurrent dislocations Owen Murray and East Indian rift of 90° longitude. Owen Murray fault operated as a sinistral strike-slip and East Indian rift was reactivated as dextral strike-slip (Ollier & Clayton, 1984). These two block boundary faults – lateral ramp faults allowed invasion of Indian continental plate into the large Tethys ocean embayment within the Euroasian plate. Indian shield was separated from the Antarctica plate in the Early Cretaceous (ca 120 Ma) and thereafter drifted to the north; and Indian ocean floor subducted under the Euroasian plate (B-type subduction sensu Bally, 1981). Indian ocean floor subduction ceased beneath Indian–Euroasian collision zone during the peak of collision (40 Ma ago). Collision itself was diachronous (Searle, 1996), occurred earlier in the western part (Pakistan, 60 Ma), later in the eastern part (Southern Tibet). After initial collision of Indian shield with Euroasian plate margin (ca 50 Ma ago, Golonka et al., 2006) the Himalayan orogen nappe architecture formation has started and continental lithosphere of Indian shield subducted further under the Euroasian plate (A-type subduction sensu Bally, 1981). This process of nappes formation culminated in the Middle Miocene (Jaroš & Kalvoda, 1977) and it has operated continuously up till recent and the Himalayas are recently still in the active zone of plates convergence (recently ca 50 mm/yr by Minster & Jordan, 1978; 36–40 mm/yr by Sockuet et al., 2006 ex Yeats, 2012). This extreme dynamics is responsible for high seismicity related predominantly to southvergent thrusts (MFT, less MBT) separating the main Himalayan nappe megaunits, less to tear wrench

faults of these thrusts (Valdiya, 1992). The magnitudes of frequent and strong present-day and historical earthquakes reach average intensity M 7–9 (Valdiya, 1992; Yeats, 2012). As the strongest seismic events in the Central Himalayas are regarded historical superquakes 1505, 1835 and 1934 with estimated magnitudes M 8.2, 7.7 and 8.1 respectively (Pandey & Molnar, 1988; Yeats, 2012.). The last catastrophic earthquake with magnitude 7.8 affected Central Nepal Himalayas in 2015. The epicenters of earthquakes are generally clustered along the Himalayan front (MFT), Main Central Thrust and in Tibetan plateau along strike-slip faults controlling eastward escape of the Lhasa block. Currently the most seismically active is the Himalayan frontal area, where the plate boundary earthquakes are related to the Himalayan Main Frontal Thrust. For the earthquakes epicenters following MCT inside the Himalayan range is responsible the Main Detachment Fault (MDF) – the continuation of the Himalayan Frontal Thrust, which is situated deeper in the crust under MCT. MCT itself as well as MBT thrusts are recently inactive. Earthquakes are generated in depth due to frontal ramps on MDF, no seismogenic surface ruptures were described there. The Himalayas and Tibetan plateau are genetically tightly related. The long lasting northward movement of Indian plate into Euroasia lifted up the Himalayan range and affected Tibetan block, which one has been extruded eastwardly along the dextral Karakoram and sinistral Altyn Tagh strike-slip faults. These highly dynamic ruptures with the slip rate estimated to 30 mm/yr in average (Taylor & Yin, 2009) have been the source of strong earthquakes in Tibetan plateau.

The last gravitational nappes of Tethyan sedimentary sequences were thrust over the Great Himalaya crystalline basement in the Middle and Late Pleistocene. A very young Kathmandu nappe system – a Higher Himalayan crystalline slab was thrust over the Lesser Himalaya units. From the Holocene a vertical component of movements – uplifts has been prevailing (Kalvoda, 1978).

Generally, the tectonic activity during the Himalayan orogeny migrated southwards (Bogacz & Krokowski, 1983). The 50 Ma lasting collision and underthrusting of Indian continental plate result in grandiose southvergent nappe architecture of Himalayan orogen and extreme uplifts (l. c.). The crustal shortening due to collision has been mainly absorbed by the northern margin of the Indian plate (Bogacz & Krokowski, 1985). In process of collision of the Indian and Asian plates, the northern continental margin (current Himalayan range) of the Indian plate was split into nappes and blocks by intracrustal thrusts and strike-slips. Continual propagation of Indian plate to the north resulted in great shortening (estimated minimum 400–500 km by Kalvoda, 1976, 1978; 600–700 km by Le Fort, 1975; even 1500 km by Bouchez & Pecher, 1981) which was accommodated by thrusts and their tear faults. One of the largest movements were along MCT.

The Himalayas are divided to several longitudinal tectonic zones – superposed megaunits separated by boundary thrusts (Mísař, 1987; Valdiya, 1992) listed below from the south towards the north (**Fig. 3**).

i) Indo-Gangatic Plain (Foreland Basin)

This zone represents the northern border of the Indo-Gangetic alluvial plain (Indus–Ganga lowland) and forms the southernmost tectonic zone of Nepal (Upreti, 1999). It is delimited by the Main Frontal Thrust (MFT) to the north, which is exposed at many places. At many places along this thrust, the Churia rocks are exposed over the Terai sediments. Terai plain gradually rises from 60 m above the sea level in the south to more than 200 m in the north. It is covered by Quaternary to recent sediments which are about 1500 m thick. The recent alluvium is mainly derived from the Churia Hills (Siwaliks) and also from the Lesser Himalaya by the river systems.

ii) Sub-Himalaya (Siwalik)

The Sub-Himalaya is an autochthonous unit formed by Middle Miocene–Early Pliocene to Pleistocene molasse sediments (Yeats & Lillie, 1991; Upreti, 1999) filling the Himalaya foredeep basin. These are a few thousand meters (up to 6 km) thick fluvial sediments having the source area in uplifting Himalaya (Sigdel et al., 2011). Siwalik Group covers crystalline basement of Indian shield and itself is covered by hundred meters or even a few km thick fluvial Holocene sediments of Indus-Ganga lowland, and at the north it was in the Middle Miocene overthrust by the Lesser Himalaya nappe unit along the Main Boundary Thrust (MBT; Valdiya, 1992). MBT is recently reactivated as oblique dextral strike-slip (Yeats et al., 1992). Between the Sub-Himalaya's deformed Siwalik Group and stable Indian plate (Indian plains) is also a tectonic boundary represented by the Main Frontal Thrust (MFT; Yeats et al., 1992). MFT is near the surface steeply dipping zone of southvergent reverse faults and thrusts, respectively. According to Bogacz & Krokowski (1985), the MFT thrust was in the later stages of collision reactivated in the western part as a dextral strike-slip and in the eastern part as a sinistral strike-slip. It was caused by the arcuate shape of India–Tibet contact zone.

iii) Lesser Himalaya

This old mature, but recently rejuvenized terrain was thrust along MBT over the Outer Himalayan Siwalik Group in the Quaternary. Nappe mega-unit of Lesser Himalaya is composed of various metamorphic, as well non-metamorphic formations of wide stratigraphic range, from pre-Cambrian to Early Miocene. Lesser Himalaya is subdivided to three lithotectonic assemblages – superposed units:

- a) the parautochthonous Proterozoic sedimentary rocks in the lower part, overthrust by

- b) sheets of low-grade metamorphics associated with ca 2 Ga old granites, which are overthrust by
c) unit of medium-grade metamorphics intruded by ca 550 Ma old granitoid bodies.

The highest nappes represent isolated remnants – outliers of Higher Himalaya nappe unit, probably gravitationally slid from the Higher Himalayas realm due to uplifts.

The Lesser Himalaya is separated from the Higher Himalaya by the Main Central Thrust (MCT).

iv) Higher Himalaya (Great Himalaya)

This is the huge tectonic slab of pre-Cambrian highly metamorphosed and granitized crystalline basement (crystalline Tibetan slab, Himalayan gneiss zone) with its Tethyan Mesozoic cover sediments (Tibetan Tethys Zone) thrust along Main Central Thrust (MCT) over sedimentary units of the Lesser Himalaya. These Indian plate margin deposits, where limestones dominate, are intensely folded to overturned, even recumbent folds and thrust (Bogacz & Krokowski, 1983). Crystalline basement of Great Himalaya is composed of high-grade metamorphic rocks intruded by Mid-Tertiary granites, representing continental margin on which were deposited sediments of Tethyan sea. The basement crystalline complex is separated from the Tethyan Late Precambrian to Late Cretaceous sedimentary cover by detachment Trans-Himmandri Thrust (THT; Valdiya, 1992), South Tibetan Detachment System (STDS) respectively. The STDS is currently interpreted as a normal fault-shear zone. The Higher Himalaya with the southernmost part of Tibetan Tethys Zone is the best known and most attractive owing to occurrence of highest peaks of the world. Some of them are composed of Tethyan Late Paleozoic–Mesozoic–Eocene non-metamorphosed sedimentary rocks (Everest – Sagarmatha, Annapurna, Dhaulagiri). Although the main thrusting events were pre-Eocene and pre-Miocene, Pleistocene reactivation of thrusting was recorded and present activity is confirmed by repeating seismic events related mainly to tectonic contact of the Higher Himalaya nappe with Lesser Himalaya nappe.

v) Tibetan Tethys Zone

The northernmost tectonic zone of the Himalayas occupies a wide belt consisting of sedimentary rocks known as the Tibetan Tethys Zone (TTZ). The Tibetan Tethys Zone lies between the South Tibetan Detachment System – STDS [Trans-Himmandri Thrust – THT (sensu Valdiya, 1992) respectively] and the Indus–Tsang-Po Suture Zone (ITSZ). STDS is interpreted as a north dipping normal fault-shear zone. TTZ has undergone very little metamorphism, except at its base where it is close to the Higher Himalaya Zone. The rocks of TTZ consists of thick and nearly continuous Lower Paleozoic to Lower Tertiary marine, highly fossiliferous sedimentary

successions including slate, sandstone and limestone. The rocks are considered to have been deposited in a part of the Indian passive continental margin (Liu & Einsele, 1994). The Tibetan Tethys Zone formations are extensively folded (Fig. 4b) due to the extreme shortening in a proximity of the India–Asia contact zone (ITSZ). Folding in competent Tethyan sedimentary rocks accommodated a great deal of this shortening, while the rigid crystalline fundament of the upper crust was mainly thrust. This explains for the controversy in describing the Tibetan Tethys Zone southern boundary as a thrust (Trans-Himmanry Thrust; Valdiya, 1992), or a normal fault (South Tibetan Detachment System; Burchfiel et al., 1992; Hodges et al., 1992). Both structures represent the same block interface, the southern boundary of TTZ.

The Himalayan orogenic belt represents a piggy-back thrust sequence where the younger thrusts propagated towards the front of orogenic belt. At the first stages of India–Asia collision the Tethyan sediments of Indian plate margin were folded, detached from the basement and thrust, creating embryonal accretionary prism. At this period the southern tectonic boundary of TTZ operated as a thrust (Trans-Himmandri Thrust). Continual India–Asia convergence triggered development of younger thrusts (MCT, MBT, MFT). MCT accommodated crustal shortening by overriding of Higher Himalaya nappe, composed of crystalline basement, over the Lesser Himalaya formations. Long lasting plates convergence, producing crustal shortening of Indian plate, triggered gradual development of MBT and finally the MFT detachment zones, meanwhile the crustal slab of the Higher Himalaya was still pushed-up and extruded-up respectively. This dynamics of pushed-up Higher Himalaya terrane was controlled by the thrust kinematics of MCT and “normal” kinematics of THT, which is described currently as the South Tibetan Detachment System. So the southern tectonic boundary of TTZ operated as a thrust as well as a normal fault, in both cases in conditions of strong compression (Kellelt et al., 2018).

vi) Trans-Himalaya (Tibetan Himalaya)

This terrane of Asian plate is uplifted plateau composed of Tethyan formations. Stratigraphical diapason of units is pre-Cambrian–Middle Eocene (sedimentary sequence itself is Early Paleozoic–Eocene; Jaroš & Kalvoda, 1978). Tibetan plateau (highland) is separated from the Great Himalaya by the most pronounced first order crustal dislocation Indus–Tsang-Po Suture. The Indus–Tsang-Po Suture represents tectonic contact of Gondwana and Euroasia plates, being a result of Himalaya–Tibet collision. Within the steeply dipping tectonic zone of recently already inactive Indus–Tsang-Po Suture Zone (ITSZ) the members of ophiolite formation are localized, representing the obducted remnants of subducted Tethyan ocean floor.

The northern boundary of Tibetan plateau is represented by the Altyn Tagh strike-slip fault, controlling together with the Karakoram fault an eastward escape of Tibetan block and creating its contact with the Tarim basin.

Lateral extrusions, resp. tectonic escapes (Tapponier et al., 1986; Cobold & Davy, 1988) in collisional orogens result from the geometry of converging plate margins. This tectonic style, typical for Alpine type orogens, occurs in both peripheries of Himalayas (Pelzer & Tapponier, 1988). Collision and suturing of Indian plate to Asian plate triggered extensive strike-slip faulting in Asian plate (Knopp, 1997; Yeats, 2012). Due to movement of the Indian plate to the Euroasian plate, the Tibetan plateau extruded along the sinistral Altyn Tagh and dextral Karakoram boundary strike-slip faults from collisional zone towards the east and the Indo-China and South China micro-plates were along the Red river and Arakan-Yoma strike-slip faults extruded southeastward and southward (Golonka et al., 2006). Blocks of the Pamir Mts. and Hindukus Mts. foothills plateau were extruded towards the west along the Quetta-Chaman and Herat strike-slip boundary faults (e.g. Tapponier & Molnar, 1977; Cobbold & Davy, 1988).

Himalayan range is affected by systematic faulting, developed after folding and thrusting period, which finished in the Middle Miocene (Bogacz & Krokowski, 1983). Faulting is genetically associated with uplifting of the Himalayan range. There are longitudinal and transversal fault systems. Longitudinal faults represent orogen-parallel strike-slips generated due to indentation of Indian shield and its CCW rotation. Transversal faults display also strike-slip component of the movement, but dip-slip normal movements are prevailing (Bogacz & Krokowski, 1983, 1985). Transversal rivers cutting the Main Himalayan ridge follows these fault damage zones, and subsidence of intramontane Plio-Quaternary sedimentary basins is controlled by this youngest population of normal faults (e.g. Fort et al., 1982). This is the case of the Kali Gandaki river valley controlled by Thakkhola fault system interrupting the main Himalayan ridge in between the Dhaulagiri and Annapurna massifs.

A common features and contrasts of the Western Carpathian and Himalayan tectonic architecture

Both orogens are the result of the Tethys ocean closure followed by diachronous continent-continent collision, started in the Himalayas during the Paleocene/Eocene boundary and in the Western Carpathians in the Early Miocene. The Western Carpathians are north-vergent, while the Himalayas are south-vergent (**Fig. 4**). The Western Carpathians represents the northern branch of the bilateral symmetric Paleo-Alpine orogenic wedge – mega-flower structure and Dinarides are its southern south-vergent branch. Carpathians and Dinarides are separated by the Pannonian central block (Dadlez & Jaroszewski,

1994). The Himalayan collision was frontal, while the Western Carpathian one was oblique, typical for the strike-slip orogens (Badham & Halls, 1975). Different is also the rate of ocean floor subduction, which was much higher in the case of Himalayas. Ocean floor spreading driving the northward drift of Indian plate was estimated as much as 20 cm a year, while plate motion rates in the Carpathian realm were an order smaller. It is reflected in geomorphology and mountain altitudes – the Higher Himalaya relief is the most extreme one over the World (**Fig. 5**). High plate motion rates should be responsible as well for the tremendous crustal thickening by continental crust duplexing, which is the rare phenomena, specific for Himalayas and the Alps. Except of tectonic reasons as piling of nappes, the intense isostatic movements due to crustal thickening caused the extreme uplift.

Common features of both orogens is their Neo-Alpine nappe architecture, though involving different lithological units. The Western Carpathians comprise thrust Tertiary sedimentary sequences of orogenic accretionary wedge, while the Himalayan architecture involves also huge nappes of deep crystalline units creating the basement of the main Himalayan ridge and Mesozoic Tethyan units. We had an opportunity to observe these units and structures of both orogens in situ (**Fig. 6**). In the Western Carpathians, the basement nappes comprising crystalline basement are Paleo-Alpine (Cretaceous). Meanwhile tectonic evolution of Himalayas has been continual Tertiary-Quaternary process of plates collision, the Carpathians evolved during several tectonic stages divided by long lasting periods of extension and denudation. This is the reason of differences in structure, crustal thickness and morphology of both orogens.

The tectonic activity in both orogens displays a distinctive polarity of thrusting, which migrated from the internal to the external parts of the orogenic belt and from the west towards the east. In the Himalayas all thrusts are Neo-Alpine and active even in the Quaternary period till the present time. So the Himalayas are still active collisional zone/tectonic suture, which is evidenced by strong seismic activity and extensive recent vertical and horizontal movements. In the Western Carpathians the Inner block/terrane is formed by Paleo-Alpine (Late Cretaceous) nappes. The Neo-Alpine nappes, recently already inactive, create accretionary wedge of the Outer (External) Carpathians. The collision in the Western Carpathians has already ceased, recent moderate seismic activity is related to movements on relaxation faults. Recently active is the southern branch of European Alpine orogen – Dinarides, evidenced by strong seismic activity.

Shape of both orogenic arcs depends upon the pre-collisional geometry of foreland plate margins. It was produced by escape tectonics, controlled by strike-slip faults, which is a common feature of many segments of

Tethyan Alpides, Carpathians and Himalayas including (Yin & Taylor, 2011).

Tectonic sutures after ocean crust subduction are traced in both orogens by occurrences of ophiolites – the remnants of oceanic crust. Contrary to the huge Himalayan ophiolite belt following the Indus–Tsang–Po suture closed in Paleogene period, there are in the Western Carpathians the ophiolites preserved only rudimentarily (Meliata unit), but they are related to Paleo-Alpine subduction. Voluminously large occurrences of ophiolites comparable with Himalayan ones are situated in the Paleo-Alpine Vardar zone of the southern branch of the European Alpine belt.

The noticeable differences are in dimensions and recent movement rates and magnitudes – all are an order higher in the Himalayas, where collision has not finished yet.

Difference is also in magnitudes and origin of seismicity in both orogens, resulting from the character of collision and its maturity. While the Himalayan earthquakes are strong, focussed in great depths and related to the syn-collisional thrust faulting, the Western Carpathians earthquakes, resp. micro-earthquakes are much weaker and they are related mainly to post-collisional relaxation strike-slip, less dip-slip faults with moderate slips.

Almost all values of orogenic parameters are lower in the Western Carpathians than in the Himalayas, except the volume of subsequent Neo-Alpine volcanism, which is extensively developed in the Western Carpathians, while in the Himalayan orogenic accretionary prism not. On the other hand, the northern terrains of Himalayas are massively intruded by the Miocene granites exhumed due to extensive erosion and the extreme terrain morphology; and massive Tertiary volcanism is situated in the Lhasa block of Asian plate. This magmatism in both orogenic belts is related to melting of subducted crust.

For the internal part of the Western Carpathians is typical Neo-Alpine basin and range structure controlled by faulting and related block rotations and tilting. Neogene intramontane sedimentary basins of this type were not developed in the Himalayas due to extreme uplift, deep erosion and lack of extension. A mantle astenolith is not developed in part of the Himalayan orogenic accretionary prism. However, terrestrial Mio-Quaternary sediments were deposited in narrow fault controlled deep grabens (e.g. Mustang graben) crossing the main Himalayan structural direction (Adhikari & Wagneich, 2011).

Specific tectonic development of the Western Carpathians and Himalayas is also recorded in the gravity field (Bouguer anomalies) difference. On the one hand, both orogens create a regional negative Bouguer anomaly, which is a typical accompanying phenomenon of collisional orogens. However, the difference between the low gravity value of the Himalayas and the Western Carpathians is extraordinary. While the gravity low of the Himalayas reaches a maximum amplitude of almost

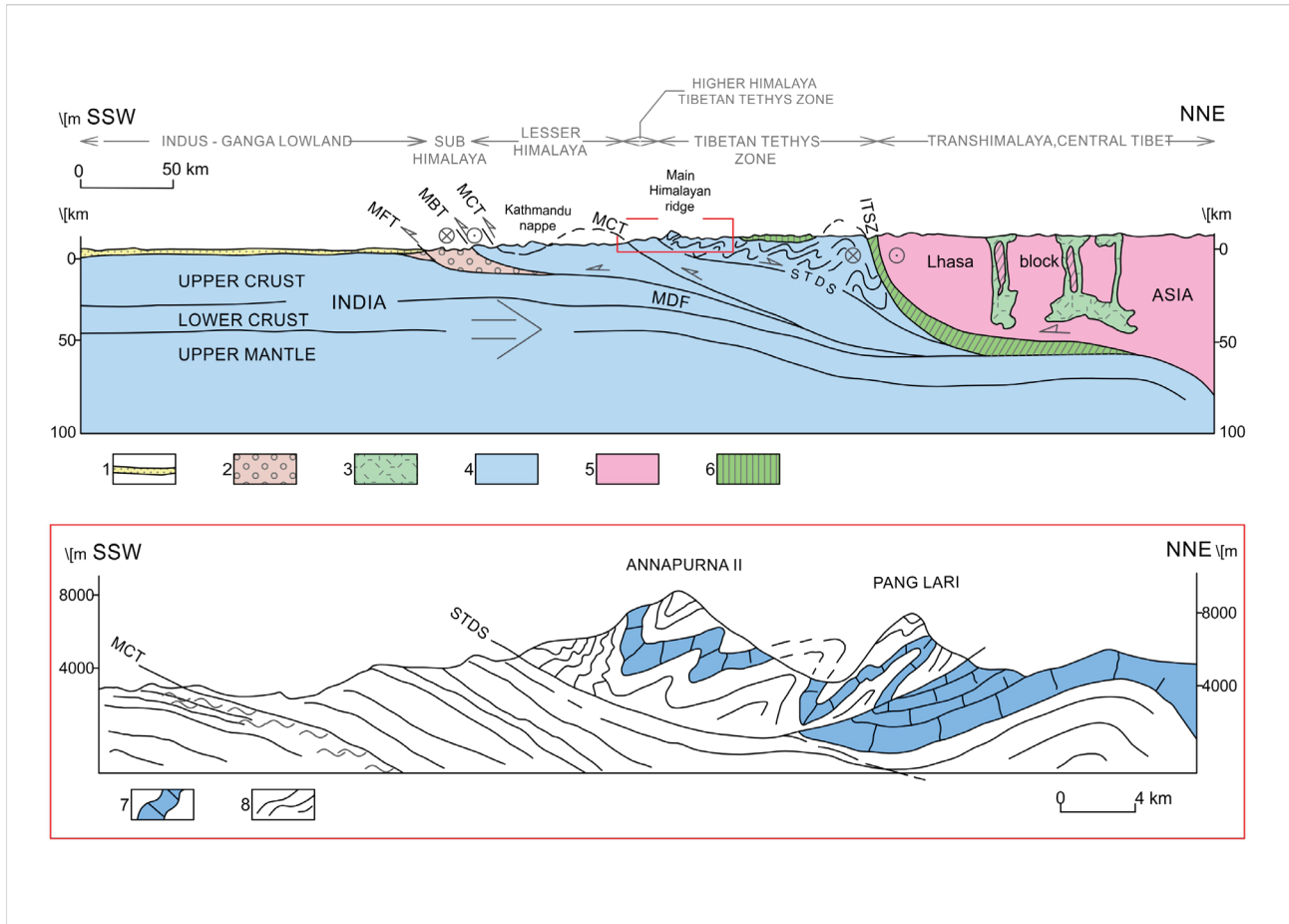
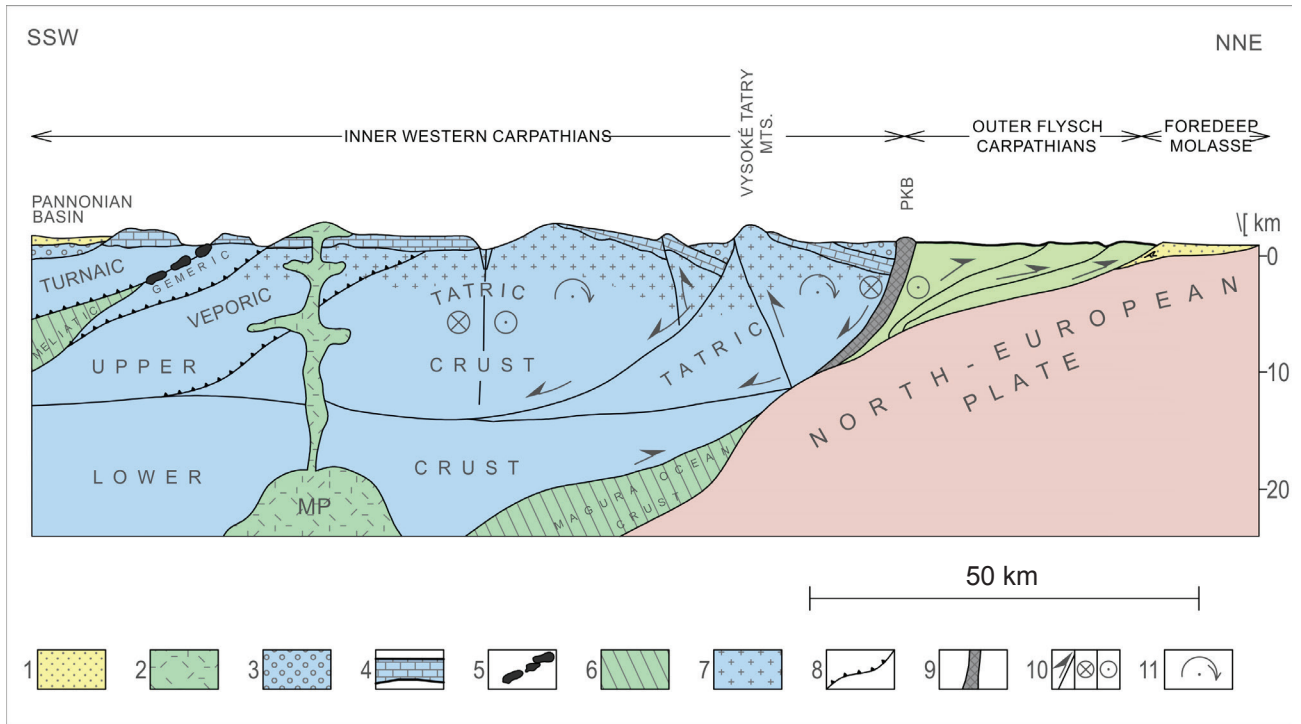




Fig. 4. A – Conceptual and generalized geological cross-section of the Western Carpathians. Scale is approximate and some structural phenomena are due to better readability exaggerated. Abbreviations: MP – Mantle plume (asthenolith), PKB – Pieniny Klippen Belt. Explanations: 1 – Neogene sediments; 2 – Neogene volcanites; 3 – Inner Carpathian Paleogene sediments; 4 – Late Paleozoic-Mesozoic cover units and Paleo-Alpine superficial nappe units of Mesozoic sequences; 5 – Ophiolites – remnants of subducted ocean crust of Meliatic unit; 6 – Ocean crust slabs; 7 – Variscan (Hercynian) Paleozoic crystalline basement units; 8 – Paleo-Alpine thrusts boundaries of basement nappes; 9 – Pieniny Klippen Belt – a Neo-Alpine suture zone; 10 – Neo-Alpine (Miocene) structures: a) thrusts, reverse and normal faults, b) strike-slip faults; 11 – block tilting. **B** – Generalized geological cross-section of the Central Himalaya (modified, compiled according to Gansser, 1980; Nábělek et al., 2009; Yeats, 2012; Yeats et al., 1992; Le Fort, 1975; Valdiya, 1992; Yeats & Thakur, 2008; Bagacz & Krokowski, 1983; Tapponier et al., 1982, detail of Annapurnas segment after Pecher, 1976; Le Fort, 1981). Some structural phenomena are due to better readability exaggerated. Abbreviations: HFT – Himalayan Frontal Thrust, MBT – Main Boundary Thrust, MCT – Main Central Thrust, THT – Trans-Himandry Thrust, STDS – South Tibetan Detachment System, ITSZ – Indus-Tsang-Po Suture Zone. Explanations: 1 – Holocene alluvial sediments of Indo Gangatic Plain; 2 – Miocene-Pleistocene molasse sediments of Siwalik Group; 3 – Cenozoic volcanites; 4 – Indian (Gondwana) Plate; 5 – Euro-Asian Plate; 6 – Ophiolite mélange – Tethys ocean crust incorporated to collisional suture (ITSZ), or obducted remnants; 7 – Tethyan Paleozoic limestones; 8 – Quartzites, schists and gneisses of Indian craton.

–600 mGal (Sandwell & Smith, 1997; Shin et al., 2007) whereas in the Western Carpathians it is only about –70 mGal (Bielik et al., 2006). Equally different are the values of the wavelengths of the gravity lows in both mountains. The Himalayan gravity low attains a value of about 500 km, while the Western Carpathian low gravity is characterized by 50–100 km. Lillie et al. (1994) calculated on the basis of a kinematic model of ocean basin closure and subsequent continental collision (Lillie, 1991) that the Western Carpathian narrow width of the gravity low suggests the continental convergence ceased soon after the ocean basin closure. So that only about 50 km of continental crustal shortening occurred in the Western Carpathians. The amplitude of the Western Carpathian gravity low further indicates small crustal root (on average 35 km with a maximum of 42 km). Taking into account the Lillie's model (Lillie, 1991) it can be suggested that the continental collision between the Indian and Eurasian plates was much stronger. The width of the Himalayan gravity low assumes that the Indian plate was after Tethys ocean closure underthrust beneath the Eurasian plate about 500 km. The amplitude of the gravity low indicates 70–80 km crustal root under the Himalayas. Which is in good agreement with seismic observations (e.g. Nábělek et al., 2009; Zhang et al., 2011; Koulakov et al., 2015; Subedi et al., 2018) and geophysical crustal models (e.g. Munt et al., 2008; Tenzer et al., 2015).

Discussion

Both compared distant orogenic belts of the same equatorial Alpidic orogenic system apparently belong to Intra-Pangea subduction-collisional zones (sensu Németh et al., 2016, 2017, 2018). Nevertheless, there are some peculiarities and differences in their tectonic architecture (see Tab. 1). The most prominent difference is in complexity of their tectonic evolution.

The Western Carpathians have evolved during the three Wilson cycles (Variscan, Paleo- and Neo-Alpine),

producing double collisional crustal thickening (Variscan and Paleo-Alpine), and related double unroofing during the post-collisional relaxations (Németh et al., 2016). So the WC structure is a result of multiple alternation of convergent and divergent geotectonic processes.

The Himalayas as a distinct mountain range is much simpler – they completely represent a Neo-Alpine structure, being the result of giant long lasting continual collision not interrupted by the relaxation extensional periods. The recent unroofing has taken place in Himalayas due to an extreme uplifting, related to the collision and isostatic forces, which have triggered the gravitatioanal nappes sliding during unroofing.

The distinct contrast between the Western Carpathians and the Himalayas during the Cenozoic Neo-Alpine evolution is the oposite vergency of subduction and following thrusting in orogenic collisional prism. While in the Western Carpathians the Neo-Alpine orogenic structure has evolved as forward thrusting nappes in the frontal rim and in the front of prograding overriding plate (IWC, ALCAPA respectively); in the Himalayas, the accretionary orogenic wedge evolved from backward thrusting (in relation to plate movement) tectonic slices detached from the subducting-underthrusting Indian plate.

Taking into account the wider regional relations – in the north-located zone of Tibetan Plateau, neighboring the Himalayas, there are known several parallel suture zones (cf. e.g. Chung et al., 2005; Zhu et al., 2013), whose geodynamic evolution could be parallelized with Variscan and Paleo-Alpine processes known in the western segment of Alpine-Carpathian-Himalayan orogenic belt, incl. Western Carpathians. This indicates a principle of pulsing (multiple repeated) divergent and convergent processes of tectonic evolution, valid in the whole orogenic belt of Intra-Pangea type (Németh, pers. com.).

Disregard the opposite vergency, concerning the Neo-Alpine processes, we can try to compare geometrically tectonic terranes of both orogens according to their

Tab. 1

A comparison of the Western Carpathian and the Himalayan geological features – a summary.

COMMON FEATURES		
PARAMETERS OF OROGEN	WESTERN CARPATHIANS	HIMALAYAN BELT
Affiliation to world orogenic system	Both orogenes belong to the same global Neo-Alpine equatorial Alpidic collisional orogenic system, which is the result of the Euroasian plate collision with the Gondwana continental fragments – microplates after closing the Tethys ocean.	
Regional Bouguer anomaly	Both orogens create a regional negative Bouguer anomaly, which is a typical accompanying phenomenon of collisional orogens.	
Symmetry of orogen	Structure of both orogenic belts is strongly asymmetric. In front of both orogens are well developed foredeep molasse basins fedded by clastic material coming from the growing orogen.	
General tectonic style	Convergent-collisional style, shortening is accommodated by thrusting and folding; as well as extrusions controlled by wrench faulting.	
Polarity of orogen	Continent-continent collision in Alpidic orogenic system was diachronous, both orogens display distinctive polarity of tectonic activity – thrusting, migrated from the internal to external parts of orogen and from the west eastward.	
Syn-orogenic magmatism	Crust subducted during the plate convergence was in both orogens melted in the upper mantle, thus providing a source for extensive subsequent Cenozoic magmatism and volcanism.	
Pre-collision constraints of orogen loop geometry	Shape of both orogenic arcs depends upon the pre-collisional geometry of foreland plate margins – an embayments of an ocean crust situated within the Euroasian plate.	

CONTRAST FEATURES		
PARAMETERS OF OROGEN	WESTERN CARPATHIANS	HIMALAYAS
Type of subduction	B-type subduction of the Magura basin thin lithosphere under progressing extruded Inner Western Carpathian micro-plates, followed by oblique continent-continent collision.	Benioff's B-type subduction of the Tethys ocean lithosphere was after collision followed by the Ampferer's A-type subduction – an underthrusting of the Indian plate continental lithosphere under the Asian plate resulting in the extreme lithosphere thickening due to the crustal duplexing.
Rate of plate motions driving Neo-Alpine orogenesis	Rate of the plates convergence in the Miocene is estimated up to 10 cm/yr.	Rate of the plates convergence in the Cenozoic is estimated up to 20 cm/yr.
Rate of recent plate motions	Recent plates convergence rate is almost zero.	Recent plates convergence rate is estimated ca 5 cm/yr.
Type of collision	Oblique continent-continent collision due to eastward extrusion of the Inner Western Carpathian crustal segments to embayment in NEP, typical for the strike-slip orogens.	Frontal continent-continent collision due to the India and Euroasia plate convergence, which resulted in the extreme shortening and crustal thickening accompanied by the strong isostatic movements – uplifts.
Duration and beginning of collision	Miocene (22–12 Ma). It started in the Early Miocene, because continent-continent collision was oblique, it was gradually prograding from the west eastward.	Paleogene – Recent (50 Ma – recent). It started in the Paleocene/Eocene boundary, collision – convergence of India and Asia is still in progress.
Age of collision related thrusting	Miocene, no Quaternary thrusting occurred.	Since the Paleogene to present day, extensive Quaternary thrusting is active.
Present day orogenic activity	Not active - the collisional orogenesis has already ceased.	Still active compressional orogenic belt, with active thrusting.
Orogen–thrusting vergency	North vergent	South vergent
Magnitude of crustal shortening	The narrow width of the gravity low suggests that the continental convergence ceased soon after the ocean basin closure. Estimated is only ca 50 km of overall crustal shortening.	The width of gravity low assumes extreme shortening ca 500–700 km, accommodated by the Indian plate underthrusting under the Asian plate as well as by thrusting and folding in frontal rim of the Indian plate.

Tab. 1
Continuation

CONTRAST FEATURES		
PARAMETERS OF OROGEN	WESTERN CARPATHIANS	HIMALAYAS
Structural style	For the internal part of the orogen (IWC) is typical Neo-Alpine basin and range structure controlled by faulting and related block rotations and tilting. Neo-Alpine nappe architecture is typical for the external part of orogen (OWC).	Whole mountain belt is composed of superposed Neo-Alpine compression and the rapid up-doming as well gravitational nappes.
Continuity of tectonic evolution	Process of orogenesis is not continual. Western Carpathians evolved during several Wilson cycles – orogeneses (Variscan, Paleo-Alpine and Neo-Alpine), interrupted by long-lasting periods of extension and denudation.	Tectonic evolution of the Himalayan belt represented a continual Tertiary–Quaternary process of 50 Ma lasting plates collision.
Seismic activity – origin and earthquake magnitudes	Micro-earthquakes, rarely macro-seismic events reaching average max. intensity M 3–5 are related mainly to post-collisional relaxation strike-slip, less dip-slip faults with moderate slips.	Earthquakes are strong, numerous, generated mainly in great depths and related to the syn-collisional thrust faulting. Strong present-day and historical earthquakes reach average intensity M 7–9.
Units incorporated to Neo-Alpine nappe architecture	The Neo-Alpine accretionary prism of the OWC has incorporated only Tertiary (Paleogene – Neogene) sedimentary sequences. Mesozoic Tethyan units and their Variscan crystalline fundament consolidated by Paleo-Alpine tectogenesis create IWC.	Except the Neogene-Quaternary Siwalik Formation there are in Neo-Alpine orogenic accretionary wedge involved huge nappes of deep crystalline units and Mesozoic Tethyan units.
Synorogenic sedimentary basins	There are genetically various Neogene basins. Depending on their geodynamic position within the orogenic belt there are fore-arc, inter-arc and back-arc basins. There occur marine basins formed by lithospheric extension – thermal subsidence, as well as basins formed by tectonically-fault controlled subsidence.	Except the Siwalik foredeep basin, being the largest in the world and situated in the Himalayan belt, there is a lack of synorogenic sedimentary basins in the terrane of accretionary orogenic wedge due to the extreme uplifting accommodated by the extreme erosion. Subsidence of several transversal intramontane terrestrial Plio-Quaternary sedimentary basins has been controlled by the population of normal faults genetically associated with uplifting Himalayan range.
Character of gravity field (Bouguer anomalies)	Gravity low reaches a maximum amplitude of only about –70 mGal.	Gravity low reaches a maximum amplitude of almost –600 mGal.
Crustal thickness	The amplitude of the gravity low indicates small crustal root (on average 35 km with a maximum of 42 km) under orogenic belt.	The amplitude of the gravity low indicates 70–80 km crustal root under orogenic belt.
Origin and tectonic position of synorogenic magmatic complexes	Volcanic complexes represent the Neo-Alpine formations superimposed on the Paleo-Alpine nappe system. Robust Miocene sub-volcanic and volcanic activity was except the subduction processes related as well to the asthenosphere upwelling – mantle diapirs.	Northern terrains of Himalayan belt are massively intruded by the Miocene granites exhumed due extreme uplift, accompanied by extensive erosion, but forming the extreme terrain morphology. Massive Tertiary volcanism is situated out of the orogenic belt in the Lhasa block of the Asian plate.
Ophiolite complexes – remnants of oceanic crust	The ophiolites related to the Jurassic subduction are preserved only rudimentary (Meliata unit), they are tracing the suture after the Paleo-Alpine ocean closure.	There is a huge ophiolite belt related to the Neo-Alpine collision following the Indus–Tsang-Po suture closed in the Paleogene period.
Fault network	Faults are numerous, fault network affecting IWC is regular. Important role had the wrench faulting accommodating the extrusion of internal Carpathian rigid blocks to the embayment of the subducting oceanic crust in the North European plate.	Brittle fault network is much more simple, less numerous, dominate faults striking perpendicularly to the Himalayan structure, which have operated as a tear faults of thrusts, as well as normal faults accommodating the extreme upwarping of the mountain belt. Orogen parallel strike-slips at the orogenic root zone accommodate processes of tectonic escape produced by the India plate push.
Dimensions of orogen	Width of orogenic belt is ca 200 km, length of WC orogen loop is ca 630 km, the highest mountain summit has an altitude of 2650 m a.s.l.	Width of orogenic belt is ca 330 km, length of orogenic loop is ca 2600 km, the highest mountain summit has an altitude of 8848 m a.s.l.

geotectonic position, structural style, kinematics and the age of tectonic activity (see cross-sections in **Fig. 4a, b**). From a geometric viewpoint we shall compare individual units of orogens listed from their frontal zones towards their root zones:

- In described Cenozoic Neo-Alpine evolution the North European Plate (a foreland of the Western Carpathians) should geometrically correspond to the Indian plate;
- Western Carpathians foredeep basin corresponds to Sub-Himalaya (Siwalik);
- Outer (External) Western Carpathians (Flysch nappes) correspond to Himalayan accretionary wedge (Lesser Himalaya, Higher Himalaya, Tibetan Tethys Zone?);
- Pieniny Klippen Belt corresponds to Indus–Tsang–Po suture zone. Curious is, that PKB comprises no ophiolites. Ophiolites are known from the Meliata suture situated in the root zone of the Western Carpathians, but this structure is not Neo-Alpine, but one Wilson cycle older – the Meliata ocean was closed in Paleo-Alpine (Mesozoic) Wilson cycle;

- Inner (Internal) Western Carpathians correspond to Trans Himalaya (Asian plate). Neo-Alpine tectonics of IWC is represented by faulting. An important role in Neo-Alpine period had strike-slips, similar as in Tibetan block of Trans Himalaya.

Conclusions

This study inspired by own field experience from two orogens is focussed to comparison of these distant mountain ranges based on classical principles of comparative tectonics defined by Hans Stille (Stille, 1924), applying the up-to date plate-tectonic approach.

The Himalayas and Carpathians belong to the same global Alpine orogenic system, having similar tectonic style of shortening by thrusting and extrusions. There are several fundamental common features, but a lot of peculiarities and differences in both orogens, too. Most noticeable difference is in the type of Gondwana microplates collision with the Euroasian plate. The Western Carpathians is a strike-slip orogen due to oblique collision, which already ceased after the full oceanic crust

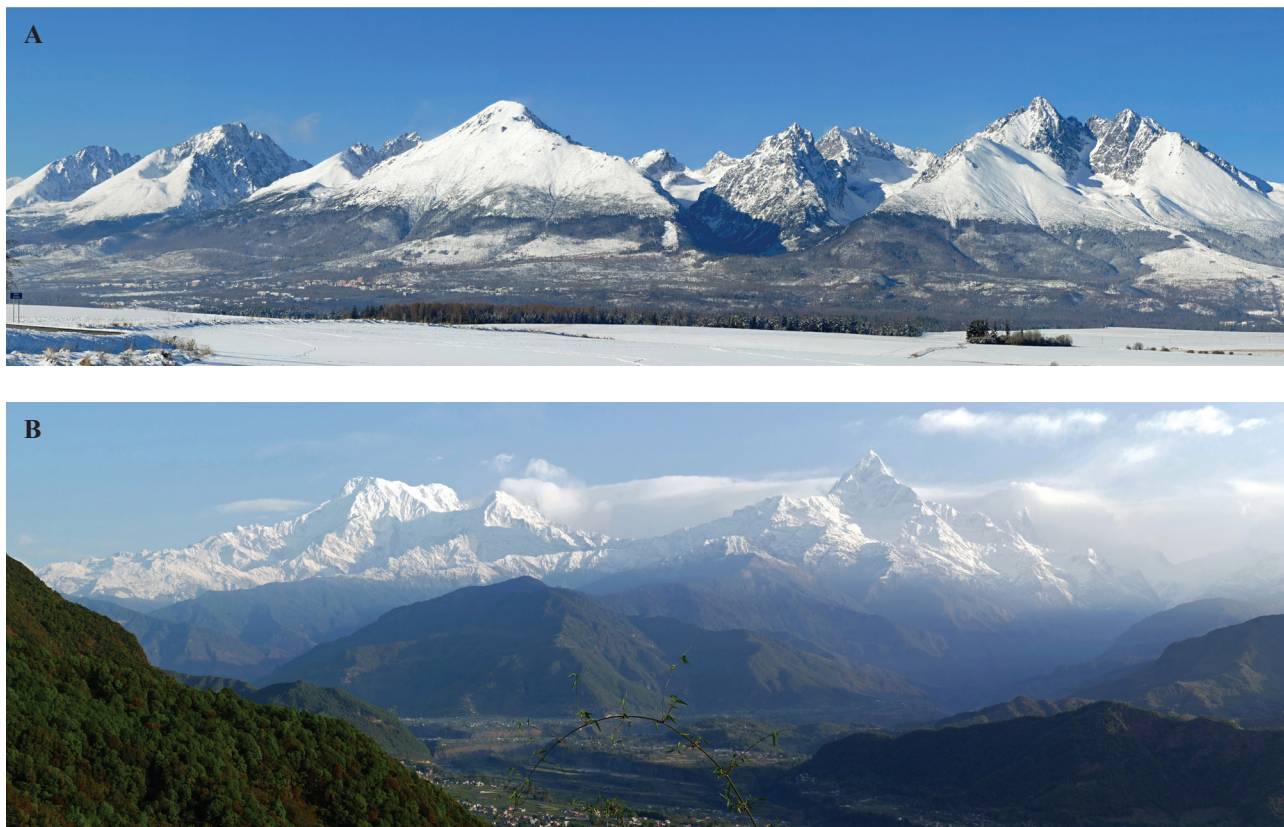


Fig. 5. A similar Alpine-type relief in the Western Carpathian and Himalayan mountain ranges. Difference is in dimensions and altitudes, the highest Gerlach peak in the High Tatras (Vysoké Tatry Mts.) in Western Carpathians reaches 2650 m a.s.l., while the highest peak of Himalayas Mount Everest has altitude 8848 m a.s.l. A panoramic view from the south northward of: **A** – the High Tatras – Vysoké Tatry Mts., Inner Western Carpathians, Tatric unit. **B** – Annapurnas group (left) and Machhapuchchhre (right) of the main ridge of Himalayas (Great Himalaya) seen from the view point near the Pokhara village (both photographs by J. Madarás).

subduction. Himalayas are a result of frontal collision, which after the oceanic crust consumption has continued further by underthrusting of Indian plate continental crust under the Asian one. It led to formation of the most extreme shortening and crustal thickening, accompanied with a largest uplift in the world and creation of the highest mountains. The Western Carpathians branch of the Alpine mobile belt is currently inactive. Nevertheless, the convergence of India and Asia plates continues at present day resulting in high seismic activity presumably related to frontal Himalayan thrusts.

The Himalayas are purely Cenozoic Neo-Alpine structure, while in the Western Carpathians there is preserved Variscan (Hercynian; Paleozoic) and Paleo-Alpine (Mesozoic) nappe architecture in the internal part of the orogen as well as the Neo-Alpine (Cenozoic) fold and thrust belt, creating the external part of the orogen. Complex brittle fault network is Neo-Alpine, affecting mostly the IWC block of the Western Carpathians. Dominant role had wrench faulting, accommodating the extrusion of internal Carpathian block to the embayment of subducting oceanic crust in the North European plate. Himalayan brittle fault network is much more simple, there dominate faults striking perpendicularly to Himalayan

structure, which have operated as a tear faults of thrusts, as well as normal faults accommodating the extreme upwarping of the mountain belt.

Acknowledgements

This paper is dedicated in memory of excellent geologist, charismatic university teacher and mountain climber Rudo Mock, a scientific participant of the Czechoslovak Himalayan expedition 1984 and Sagarmatha 1987. Authors of the paper express their thanks to the Slovak Research and Development Agency, which under the project contract No. APVV-16-0146 covered costs of the reconnaissance field works in Nepal part of the Himalaya Mts. conducted in April 2019. Participants of the field trip are grateful to Subin-Ghanesh Thakuri and his Utmost Adventure Trekking Pvt. Ltd. agency for perfect logistics, guiding and safety conditions arranged for our researchers during the trek in Nepal. This work was supported also by the Slovak Grant Agency VEGA, under grant 2/0006/19. Special thanks are expressed to Zoltán Németh for corrections and mainly for inspiring comments and recommendations which improved the manuscript.



Fig. 6. Participants of the field reconnaissance geological exploration trip along the Kali Gandaki river in front of the Department of Geology, Tri-Chandra Multiple Campus, Tribhuvan University in Kathmandu, listed from the left towards the right: Miroslav Bielik, Pavol Siman, Ján Madarás, Juraj Papčo, Ashok Sigdel, František Marko, Subash Acharya, Kamil Fekete and Andrej Mojzeš.

References

- ANDRUSOV, D., 1974: The Pieniny Klippen Belt. In: Mahel', M. (ed.): Tectonics of the Carpathian-Balkan regions. *Bratislava, Geol. Inst. D. Štúr*, 145–158.
- ADHIKARI, B. R. & WAGREICH, M., 2011: Provenance evolution of collapse graben fill in the Himalaya – The Miocene to Quaternary Thakkhola-Mustang Graben (Nepal). *Sed. Geol.*, 233, 1–14.
- BADHAM, J. P. & HALLS, C., 1975: Microplate tectonics, oblique collision and evolution of the Hercynian orogenic systems. *Geology*, 3, 373–376.
- BALLY, A. W., 1981: Thoughts on the tectonics of folded belts. *Geol. Soc. London, Spec. Publ.*, 9, 13–32.
- BARKA, A. A., 1992: The North Anatolian fault zone. *Ann. tectonic., Spec. Iss.*, VI, 164–195.
- BIELIK, M., KLOSKA, K., MEURERS, B., ŠVANCARA, J., WYBRANIEC, S., FANCSIK, T., GRAD, M., GRAND, T., GUTERCH, A., KATONA, M., KROLIKOWSKI, C., MIKUŠKA, J., PAŠTEKA, R., PETECKI, Z., POLECHONSKA, O., RUESS, D., SZALAIJOVA, V., ŠEFARA, J. & VOZÁR, J., 2006: Gravity anomaly map of the CELEBRATION, 2000 region. *Geol. Carpath.*, 57, 3, 145–156.
- BIELIK, M., MAKARENKO, I., CSICSAY, K., LEGOSTAEVA, O., STAROSTENKO, V., SAVCHENKO, A., ŠIMONOVÁ, B., DÉREROVÁ, J., FOJTÍKOVÁ, L., PAŠTEKA, R. & VOZÁR, J., 2018: The refined Moho depth map in the Carpathian-Pannonian region. *Contr. Geophys. Geod.*, 48, 2, 179–190. doi: 10.2478/congeo-2018-0007.
- BEZÁK, V., PEK, J., VOZÁR, J., MAJČIN, D., BIELIK, M. & TOMEK, Č., 2020: Geoelectrically distinct zones in the crust of the Western Carpathians: A consequence of Neogene strike-slip tectonics. *Geol. Carpath.*, 71, 14–23.
- BEZÁK, V., BROSKA, I., IVANIČKA, J., REICHWALDER, P., VOZÁR, J., POLÁK, M., HAVRILA, M., MELLO, J., BIELY, A., PLAŠIENKA, D., POTFAJ, M., KONEČNÝ, V., LEXA, J., KALIČIAK, M., ŽEC, B., VASS, D., ELEČKO, M., JANOČKO, J., PERESZLÉNYI, M., MARKO, F., MAGLAY, J. & PRISTAŠ, J., 2004: Tectonic map of Slovak Republic 1 : 500 000. Ed. V. Bezák. *Bratislava, St. Geol. Inst. D. Štúr*.
- BIRKENMAJER, K., 1986: Stages of structural evolution of the Pieniny Klippen Belt, Carpathians. *Stud. Geol. Pol.*, 88, 7–32.
- BOGACZ, W. & KROKOWSKI, J., 1983: Mesoscopic structural studies of post-metamorphic deformations and tectonic evolution of Central Nepal Himalayas. *Geologia*, 9, 4, 5–45.
- BOGACZ, W. & KROKOWSKI, J., 1985: The role of longitudinal shear (strike-slip) movements in orogenic belt evolution: An example from the Himalaya. *Bull. Pol. Acad. Sci., Earth Sci.*, 73, 3–4, 178–185.
- BOUCHEZ, J. & PECHER, A., 1981: The Himalayan Main Central Thrust pile and its quartz-rich tectonites in Central Nepal. *Tectonophysics*, 78, 23–50.
- BURCHFIEL, B. C., ZHILIANG, C., HODGES, K. V., YUPING, L., ROYDEN, L. H., CHANGRONG, D. & JIENE, X., 1992: The South Tibetan Detachment System, Himalayan orogen: Extension contemporaneous with and parallel to shortening in a collisional mountain belt. *Geol. Soc. Amer., Spec. Pap.*, 269.
- CHUNG, S. L., CHU, M. F., ZHANG, Y. Q., XIE, Y. W., LO, C. H., LEE, T. Y., LAN, C. Y., LI, X. H., ZHANG, Q. & WANG, Y. Z., 2005: Tibetan tectonic evolution inferred from spatial and temporal variations in post-collisional magmatism. *Earth Sci. Rev.*, 68, 3, 173–196.
- CIPCJAR, A., MARGOČOVÁ, Z., CSICSAY, K., KRISTEKOVÁ, M., FOJTÍKOVÁ, L., KYSEL, R., PAŽÁK, P., SRBECKÝ, M., BYSTRICKÝ, E., GÁLIS, M., KRISTEK, J. & MOCZO, P., 2016: Slovak Earthquakes Catalogue, Version 2016. *Earth Sci. Instit. Slov. Acad. Sci. doi:10.14470/FX099882*.
- COBBOLD, P. R. & DAVY, P., 1988: Indentation tectonics in nature and experiment. 2. Central Asia. *Bull. Geol. Inst. Univ. Uppsala (New Ser.)*, 14, 143–162.
- DADLEZ, R. & JAROSZEWSKI, W., 1994: Tektonika. *Warszawa, Wyd. Nauk. PWN*, 743 pp.
- DENG, Y., PANZA, G. F., ZHANG, Z., ROMANELLI, F., MA, T., DOGLIONI, C., WANG, P., ZHANG, X. & TENG, J., 2014: Transition from continental collision to tectonic escape? A geophysical perspective on lateral expansion of the northern Tibetan Plateau. *Earth, Planets Space*, 66, 1–10. <http://www.earth-planets-space.com/content/66/1/10>.
- DÉREROVÁ, J., ZEYEN, H., BIELIK, M. & SALMAN, K., 2006: Application of integrated geophysical modelling for determination of the continental lithospheric thermal structure in the eastern Carpathians. *Tectonics*, 25, 3, TC3009.
- DEWEY, J. F. & BIRD, J. M., 1970: Mountain belts and the new global tectonics. *J. Geophys. Res.*, 76, 2625–2647.
- DEWEY, J. F. & BURKE, K., 1974: Hotspots and continental break-up: implications for collisional orogeny. *Geology*, 2, 57–60.
- DOGLIONI, C., MORETTI, I. & ROURE, F., 1991: Basal lithospheric detachment, eastward mantle flow and mediterranean geodynamics: a discussion. *J. Geodyn.*, 13, 3, 47–65.
- FORT, M., FREYETET, P. & COLCHEN, M., 1982: Structural and sedimentological evolution of the Thakkhola Mustang Graben (Nepal Himalayas). *Z. Geomorph. N. F., Suppl. Berlin-Stuttgart*, 42, 75–98.
- GANSSER, A., 1966: The Indian Ocean and the Himalayas: a geological interpretation. *Eclogae Geol. Helv.*, 59, 2, 831–848.
- GANSSER, A., 1980: The Peri-Indian suture zone. In: Auboin, J. et al.: Geologie des chaines alpines issues de la Téthys. *Mém. B.R.G.M.*, 15, 140–148.
- GOLONKA, J., KROBICKI, M., PAJAK, J., VAN GIANG, N. & ZUCHIEWICZ, W., 2006: Global Plate Tectonics and paleogeography of Southeast Asia. *Kraków, Arkadia*, 128 pp.
- GOLONKA, J., 2000: Cambrian – Neogene plate tectonic maps. *Kraków, Wyd. Uniw. Jagelon.*, 126 pp.
- HODGES, K. V., PARRISH, R. R., HOUSH, T. B., LUX, D. R., BURCHFIEL, B. C., ROYDEN, L. H. & CHEN, Z., 1992: Simultaneous Miocene extension and shortening in the Himalayan orogen. *Science*, 258, 1466–1470.
- HÓK, J., KYSEL, R., KOVÁČ, M., MOCZO, P., KRISTEK, P., KRISTEKOVÁ, M. & ŠUJAN, M., 2016: A seismic source model for the seismic hazard assessment of Slovakia. *Geol. Carpath.*, 67, 3, 273–288.
- JANIK, T., GRAD, M., GUTERCH, A., VOZÁR, J., BIELIK, M., VOZÁROVÁ, A., HEGEDŰS, E., KOVÁCS, C. A., KOVÁCS, I. & CELEBRATION 2000 Working Group, 2011: Crustal structure of the Western Carpathians and Pannonian Basin

- System: seismic models from CELEBRATION 2000 data and geological implication. *J. Geodyn.*, 52, 2, 97–113.
- JANOČKO, J., ELEČKO, M., KAROLI, S., KONEČNÝ, V., KOVÁČ, M., NAGY, A., VASS, D., JACKO, S. JR. & KALIČIAK, M., 2003a: Sedimentary evolution of Western Carpathian Tertiary basins. *Miner. Slov.*, 3–4, 35, 181–254.
- JANOČKO, J., VASS, D., KOVÁČ, M., KONEČNÝ, V. & LEXA, J., 2003b: Tectono-sedimentary evolution of Western Carpathian Tertiary basins: An overview. *Miner. Slov.*, 3–4, 35, 161–168.
- JAROŠ, J. & KALVODA, J., 1978: Geological structure of the Himalayas, Mt. Everest-Makalu. *Rozpr. Čs. Akad. Věd, ř. mat. přír. v.*, 88, 1, 69 pp.
- JIMÉNEZ-MUNT, I., FERNÁNDEZ, M., VERGÉS, J. & PLATT, J. P., 2008: Lithosphere structure underneath the Tibetan Plateau inferred from elevation, gravity and geoid anomalies. *Earth Planet. Sci. Lett.*, 267, 276–289.
- JÍŘÍČEK, R., 1979: Tectogenetic development of the Carpathian arc in the Oligocene and Neogene. In: Mahel', M. (ed.): Tectonical profiles through the West Carpathians. *Bratislava, Geol. Inst. D. Štúr*, 205–214 (in Czech).
- KALVODA, J., 1976: The relief of Himalayas and its recent modelation. *Rozpr. Čs. Akad. Věd, ř. mat. přír. v.*, 86, 1, 52 pp.
- KALVODA, J., 1978: Genesis of the Mount Everest (Sagarmatha). *Rozpr. Čs. Akad. Věd, ř. mat. přír. v.*, 88, 2, 62 pp.
- KELLET, D. A., COTTLE, J. M. & LARSON, K. P., 2018: The South Tibetan Detachment System: history, advances, definition and future directions. In: Treloar, P. J. & Searle, M. P. (eds.): Himalayan Tectonics: A Modern Synthesis. *Geol. Soc. London, Spec. Publ.*, 483, <https://doi.org/10.1144/SP483.2>.
- KOPP, M. L., 1997: Lateral escape structures in the Alpine-Himalayan collisional belt (in Russian). *Struktury lateralnogo vyzhimania v Alpijsko-Gimalajskom kolizionnom pojase*. Moscow, Scientific World, Russian Academy of Sciences. *Transactions*, 506, 1–314.
- KOULAKOV, I., MAKSOVA, G., MUKHOPADHYAY, S., RAOOF, J., KAYAL, J. R., JAKOVLEV, A. & VASILEVSKY, A., 2015: Variations of the crustal thickness in Nepal Himalayas based on tomographic inversion of regional earthquake data. *Solid Earth*, 6, 207–216. doi:10.5194/se-6-207-2015.
- KOVÁCS, S., SZEDERKÉNYI, T., HAAS, J., BUDA, GY., CSÁSZÁR, G. & NAGYMAROSI, A., 2000: Tectonostratigraphic terranes in the pre-Neogene basement of the Hungarian part of the Pannonian area. *Acta Geol. Hung.*, 43, 225–328.
- KOVÁČ, M., 2000: Geodynamický, paleogeografický a štruktúrny vývoj karpatsko-panónskeho regiónu v miocéne: nový pohľad na neogénne panvy Slovenska. *Bratislava, Veda*, 203 pp.
- KOVÁČ, M., MÁRTON, E., OSZCZYPKO, N., VOJTKO, R., HÓK, J., KRÁLIKOVÁ, S., PLAŠIENKA, D., KLUČIAR, T., HUDÁČKOVÁ, N. & OSZCZYPKO-CLOWES, M., 2017: Neogene palaeogeography and basin evolution of the Western Carpathians, Northern Pannonian domain and adjoining areas. *Global Planet. Change*, 155, 133–154.
- KOVÁČ, M., PLAŠIENKA, D., SOTÁK, J., VOJTKO, R., OSZCZYPKO, N., LESS, GY., ČOSOVIC, V., FÜGENSCHUH, B. & KRÁLIKOVÁ, S., 2016: Paleogene palaeogeography and basin evolution of the Western Carpathians, Northern Pannonian domain and adjoining areas. *Global Planet. Change*, 140, 9–27.
- KOZUR, H. & MOCK, R., 1973: Zum alter und zur tektonischen Stellung der Meliata-serie. *Geol. Zbor.*, 24, 2, 364–374.
- KOZUR, H., MOCK, R. & OŽVOLDOVÁ, L., 1996: New biostratigraphic results in the Meliaticum in its type area around Meliata village (Slovakia) and their tectonic and paleogeographic significance. *Geol. paläont. Mitt. (Innsbruck)*, 21, 89–121.
- LE FORT, P., 1975: Himalaya: the collided range. Present knowledge of the continental arc. *Amer. J. Sci.*, 275A, 1–41.
- LE FORT, P., 1981: Manaslu Leucogranite; collision signature of the Himalaya; a model for its genesis and emplacement. *J. Geophys. Res.*, 86, B 11, 10 545–10 568.
- LEXA, J. & BEZÁK, V. et al., 2000: Geological map of Western Carpathians and adjacent. *Bratislava, Min. Enviorn. Slovak Rep. – St. Geol. Inst. D. Štúr*.
- LEXA, J. & KONEČNÝ, V., 1998: Geodynamic aspect of the Neogene to Quaternary volcanism. In: Rakús, M. (ed.): Geodynamic development of the Western Carpathians. *Bratislava, Geol. Surv. Slovak. Republ., Dionýz Štúr Publ.*, 219–240.
- LEXA, J., SEGHEDI, I., NÉMETH, K., SZAKÁCS, A., KONEČNÝ, V., PÉCSKAY, Z., FÜLÖP, A. & KOVACS, M., 2010: Neogene-Quaternary volcanic forms in the Carpathian-Pannonian region: a review. *Centr. Europ. J. Geosci.*, 2, 3, 207–270.
- LILLIE, R. J., 1991: Evolution of gravity anomalies across collisional mountain belts: Clues to the amount of continental convergence and underthrusting. *Tectonics*, 10, 672–687.
- LILLIE, R. J., BIELIK, M., BABUŠKA, L. & PLOMEROVÁ, J., 1994: Gravity modelling of the lithosphere in the eastern Alpine-Western Carpathian-Pannonian Basin region. *Tectonophysics*, 231, 215–235.
- LIU, G. & EINSELE, G., 1994: Sedimentary history of the Tethyan basin in the Tibetan Himalaya. *Geol. Rsch.*, 83: 32–61. *Bibcode:1994GeoRu..83...32L*. doi:10.1007/BF0021189.
- LYON-CAEN, H. & MOLNAR, P., 1983: Constraints on the structure of the Himalaya from the analysis of gravity anomalies and flexural model of the lithosphere. *J. Geophys. Res.*, 88, 8171–8191.
- MARKO, F., ANDRIESEN P. A. M., TOMEK, Č., BEZÁK, V., FOJTIKOVÁ, L., BOŠANSKÝ, M., PIOVARČI, M. & REICHWALDER, P., 2017: Carpathian Shear Corridor – A strike-slip boundary of an extruded crustal segment. *Tectonophysics*, 703–704, 119–134.
- MATENCO, L. & BERTOTTI, G., 2000: Tertiary tectonic evolution of the external East Carpathians (Romania). *Tectonophysics*, 316, 255–286.
- MINSTER, J. B. & JORDAN, T. M., 1978: Present-day plate motions. *J. Geophys. Res.*, 83, 5331–5354.
- MOJZEŠ, A., BIELIK, M., MARKO, F., MADARÁS, J., FEKETE, K., SIMAN, P., PAPČO, J., SIGDEL, A. & ACHARYA, S., 2020: Ambient radioactivity on a reconnaissance study tour of Bratislava – Dubai – Kathmandu – Nepal Himalaya. *Contr. Geophys. Geod.*, 50, 2, 201–221.
- MOLNAR, P. & DENG, Q., 1984: Faulting associated with large earthquakes and the average rate of deformation in central and eastern Asia. *J. Geophys. Res.*, 89, 6203–6227.
- NÁBĚLEK, J., HETÉNYI, G., VERGNE, J., SAPKOTA, S., KAFLE, B., JIANG, M., SU, H., CHEN, J., HUANG, B. S. & Hi-CLIMB Team, 2009: Underplating in the Himalaya-Tibet collision zone revealed by the Hi-CLIMB experiment. *Science*, 325, 1371–1374.

- NÉMETH, Z., 2018: Geodynamic background of the origin of Variscan and Paleo-Alpine metamorphic core complexes in the Western Carpathians and their metallogenetic importance. *XXI Int. Congress of the CBGA, Salzburg, Austria, September 10–13, 2018, Abstracts*, p. 211.
- NÉMETH, Z., PUTIŠ, M. & HRAŠKO, L., 2016: The relation of metallogeny to geodynamic processes – the natural prerequisite for the origin of mineral deposits of public importance (MDoPI): The case study in the Western Carpathians, Slovakia. *Miner. Slov.*, 48, 119–135.
- NÉMETH, Z., PUTIŠ, M. & HRAŠKO, L., 2017: Important periods with the genesis of vein and stratabound mineralization in the Western Carpathians as a consequence of polystadial orogenic evolution. *Proc. Open Geol. Congress, Vysoké Tatry 2017*, p. 46.
- OLLIER, C. & CLAYTON, K. M., 1984: Tectonics and landforms. *London – New York, Longman*.
- PANDEY, M. R. & MOLNAR, P., 1988: The distribution of intensity of the Bihar-Nepal earthquake of 15 January 1934 and bounds on the extent of the rupture zone. *J. Geol. Soc. Nepal*, 5, 4–22.
- PECHER, A., 1976: Geology of the Nepal Himalaya; deformation and petrography in the Main Central Thrust zone. *Coll. Intern. C.N.R.S.*, 268, *Ecol. Geol. Himal., Sevres, Ed., C.N.R.S., Paris, Sci. Terre*, 301–318.
- PELZER, G. & TAPPONIER, P., 1988: Formation of strike-slip faults, rifts and basins during the India-Asia collision: an experimental approach. *J. Geophys. Res.*, 93, 15 085–15 117.
- PLAŠIENKA, D., 1999: Tectochronology and paleotectonic model of the Jurassic-Cretaceous evolution of the Central Western Carpathians. *Bratislava, Veda*, 127 pp.
- PLAŠIENKA, D., 2018a: Continuity and episodicity in the early Alpine tectonic evolution of the Western Carpathians: How large-scale processes are expressed by the orogenic architecture and rock record data. *Tectonics*, 37, 7, 2029–2079.
- PLAŠIENKA, D., 2018b: The Carpathian Klippen Belt and types of its klippen – an attempt at a genetic classification. *Miner. Slov.*, 50, 1, 1–24.
- PLAŠIENKA, D., BUČOVÁ, J. & ŠIMONOVÁ, V., 2020: Variable structural styles and tectonic evolution of an ancient backstop boundary – the Pieniny Klippen Belt of the Western Carpathians. *Int. J. Earth Sci.*, 109, 4, 1355–1376.
- PLAŠIENKA, D., MÉRES, Š., IVAN, P., SÝKORA, M., SOTÁK, J., LAČNÝ, A., AUBRECHT, R., BELLOVÁ, S. & POTOČNÝ, T., 2019: Meliatic blueschists and their detritus in Cretaceous sediments: New data constraining tectonic evolution of the West Carpathians. *Swiss J. Geosci.*, 112, 1, 55–81.
- RATSCHBACHER, L., MERLE, O., DAVY, P. & COBBOLD, P., 1991a: Lateral extrusion in the Eastern Alps. Part I: Boundary conditions and experiments scaled for gravity. *Tectonics*, 10, 2, 245–256.
- RATSCHBACHER, L., FRISCH, W., LINZER, H. G. & MERLE, O., 1991b: Lateral extrusion in the Eastern Alps. Part II: Structural analysis. *Tectonics*, 10, 2, 257–271.
- SANDWELL, D. T. & SMITH, W. H. F., 1997: Marine gravity from Geosat and ERS 1 satellite altimetry. *J. Geophys. Res.*, 102, 10 039–10 054.
- SEARLE, M. P., 1996: Cooling history, exhumation and kinematics of the Himalaya-Karakorum-Tibet orogenic belt. In: Yin, A. & Harrison, T. M. (eds.): *The tectonics of Asia*. *New York, Cambridge Univ. Press*, 110–137.
- SHIN, Y. H., XU, H., BRINTENBERG, C., FANG, J. & WANG, Y., 2007: Moho undulations beneath Tibet from GRACE-integrated gravity data. *Geophys. J. Int.*, 170, 971–985.
- SIGDEL, A., SAKAI, T., ULAK, P. D., GAJUREL, A. P. & UPRETI, B. N., 2011: Lithostratigraphy of the Siwalik Group, Karnali River section, far-west Nepal Himalaya. *J. Nepal Geol. Soc.*, 43, 83–101.
- STILLE, H., 1924: Gruntfragen der vergleichenden Tektonik. *Verl. Gebrüder Borntraeger*.
- SUBEDI, S., HETÉNYI, G., VERGNE, J., BOLLINGER, L., LYON-CAEN, H., FARRA, V., ADHIKARI, L. B. & GUPTA, R. M., 2018: Imaging the Moho and the Main Himalayan Thrust in Western Nepal with receiver functions. *Geophys. Res. Lett.*, 45, 13 222–13 230. <https://doi.org/10.1029/2018GL080911>.
- TAPPONNIER, P. & MOLNAR, P., 1977: Active faulting and tectonics in China. *J. Geophys. Res.*, 82, 2905–2930.
- TAPPONNIER, P., PELZER, G. & ARAMIJO, R., 1986: On the mechanism of collision between India and Asia. In: Coward, M. P. & Ries, A. C. (eds.): *Collision tectonics*. *Spec. Publ. Geol. Soc. London*, 19, 115–157.
- TAPPONNIER, P., PELTZER, G., LE DAIN, A. Y., ARMIJO, R. & COBBOLD, P., 1982: Propagating extrusion tectonics in Asia: new insights from simple experiments with plasticine. *Geology*, 10, 611–616.
- TAYLOR, M. H. & YIN, A., 2009: Active structures of the Himalayan-Tibetan orogen and their relationships to earthquake distribution contemporary strain field, and Cenozoic volcanism. *Geosphere*, 5, 3, 199–214.
- TENZER, R., BAGHERBANDI, M., SJÖBERG, L. E. & NOVÁK, P., 2015: Isostatic crustal thickness under the Tibetan Plateau and Himalayas from satellite gravity gradiometry data. *Earth Sci. Res. J.*, 19, 2, 97–106. doi: <http://dx.doi.org/10.15446/esrj.v19n2.44574T>.
- UPRETI, B., 1999: An overview of the stratigraphy and tectonics of the Nepal Himalaya. *J. Asian Earth Sci.*, 17, 577–606.
- VALDIYA, K. S., 1992: The Main Boundary Thrust Zone of the Himalaya, India. In: Bucknam, C. & Hancock, P. (eds.): *Major active faults of the world, results of IGCP project 206*, *Ann. Tecton., Suppl.*, VI, 54–84.
- VASS, D., 1979: Genesis of inner-molasse basins in West Carpathians in light of leading function of mantle in Earth's crust development. *Czechosl. Geology and global tectonics*. *Bratislava, Veda*, 183–197.
- VASS, D., 1998: Neogene geodynamic development of the Carpathian arc and associated basins. In: Rakús, M. (ed.): *Geodynamic development of the Western Carpathians*. *Bratislava, GS SR, Dionýz Štúr Publ.*, 155–158.
- XU, Q., ZHAO, J., PE, S. & LIU, H., 2011: The lithosphere–asthenosphere boundary revealed by S-receiver functions from the Hi-CLIMB experiment. *Geophys. J. Int.*, 187, 414–420. doi: [10.1111/j.1365-246X.2011.05154.x](https://doi.org/10.1111/j.1365-246X.2011.05154.x).
- YIN, A. & TAYLOR, M. H., 2011: Mechanics of V-shaped conjugate strike-slip faults and the corresponding continuum mode of continental deformation. *Geol. Soc. Amer. Bull.*, 123, 9, 10, 1798–1821.

- YEATS, R. S., 2012: Active Faults of the World. *Cambridge Univ. press*, 621 pp.
- YEATS, R. S. & LILLIE, R. J., 1991: Contemporary tectonics of the Himalayan Frontal Fault System: folds, blind thrusts and the 1905 Kangra earthquake. *J. Struct. Geol.*, 13, 215–225.
- YEATS, R. S., NAKATA, T., FARAH, A., FORT, M., MIRZA, M. A., PANDEY, M. R. & STEIN, R. S., 1992: The Himalayan Frontal Fault System. In: Bucknam, C. & Hancock, P. (eds.): Major active faults of the world, results of IGCP project 206. *Ann. Tecton., Suppl.*, VI, 85–98.
- YEATS, R. S. & THAKUR, V. C., 2008: Active faulting south of the Himalayan front: establishing a new plate boundary. *Tectonophysics*, 453, 63–73.
- ZEYEN, H., DÉREROVÁ, J. & BIELIK, M., 2002: Determination of the continental lithosphere thermal structure in the western Carpathians: Integrated modeling of surface heat flow, gravity anomalies and topography. *Phys. Earth Planet. Inter.*, 134, 89–104.
- ZHANG, Z., DENG, Y., TENG, J., WANG, C., GAO, R., CHEN, Y. & FAN, W., 2011: An overview of the crustal structure of the Tibetan plateau after 35 years of deep seismic soundings. *J. Asian Earth Sci.*, 40, 4, 977–989.
- ZHAO, J., YUAN, X., LIU, H., KUMAR, P., PEI, S., KIND, R., ZHANG, Z., TENG, J., DING, J., GAO, X., XU, Q. & WANG, W., 2010: The boundary between the Indian and Asian tectonic plates below Tibet. *PNAS*, 107, 25, 11 229–11 233.
- ZHU, D.-CH., ZHAO, Z. D., NIU, Y., DILEK, Y., HOU, Z.-Q. & MO, X.-X., 2013: The origin and pre-Cenozoic evolution of the Tibetan Plateau. *Gondwana Res.*, 23, 4, 1429–1454.

Porovnanie kenozoickej neoalpínskej tektonickej evolúcie Západných Karpát a Himalájí (Slovensko – Nepál)

Na jar v roku 2019 kolektív autorov tohto príspevku absolvoval v rámci vedeckého projektu APVV-16-0146 krátku, ale programovo bohatú výskumnú terénnu cestu do nepálskej časti Centrálnych Himalájí. Jej cieľom bolo oboznámenie sa so stavbou tohto grandiózneho orogénneho pásma. Získaná terénna skúsenosť z najvyššieho pohoria sveta a rokmi nadobudnuté poznatky zo západokarpatských alpíd nás inšpirovali k zostaveniu porovnávacej štúdie tektonických štýlov oboch pohorí. Základy modernej komparatívnej tektoniky, z ktorej princípov sme vychádzali, položil už Stille (1924). Pri porovnávaní štruktúrno-tektonických črt oboch pohorí a tvorbe vlastného pohľadu na problematiku sme aplikovali princípy platňovej tektoniky a mohli sme sa oprieť aj o mnohé klasické práce zamerané na stavbu Himalájí a Západných Karpát.

Západné Karpaty aj Himaláje (obr. 2 a 3) sú súčasťou globálneho orogénneho systému tetýdnych alpíd (obr. 1). Generálne majú obe pohoria podobný tektonický štýl kolíznych orogénnych procesov, ale nachádzame aj niektoré odlišnosti a špeciality. Tie sú výsledkom špecifických podmienok pri kolízii fragmentov Gondwany s eurázijskou platňou v európskej a ázijskej časti orogénnej zóny, ktoré sa dnes nachádzajú v rôznych štádiách kolíznej fázy v rámci Wilsonovho orogénneho cyklu.

Najdôležitejším faktorom ovplyvňujúcim charakter a tvar orogénnej zóny je tvar konvergujúcich platní. Výsledkom šikmej kolízie je strižný (z anglického termínu *strike-slip*) typ západokarpatského orogénu (sensu Dadlez a Jaroszewski, 1994). Sformoval sa v neoalpínskej

epoche extrudovaním rigidných mikroplatní do zálivu v severoeurópskej platni tvoreného tenkou oceánskou kôrou, ktorá subdukovala pod prenikajúce mikroplatne karpatských jednotiek. Naproti tomu, himalájska orogénna kolízia je typickým príkladom čelnej kolízie. V Západných Karpatoch kolízia po konzumácii oceánskej kôry subdukciou vyvrcholila už v miocéne. V Himalájach tento proces pokračuje dodnes so všetkými sprievodnými znakmi, akými sú intenzívny výzdvih, erózia a extrémna seizmicita, generovaná najmä na rozhraniach nasúvajúcich sa príkrovov fundamentu. V Himalájach sa uplatňuje raritný typ platňovej konvergencie – kolízia typu A (Bally, 1981), pri ktorej sa po konzumácii tetýdnej oceánskej kôry indická kontinentálna platňa ďalej podsúva pod ázijskú kontinentálnu platňu, čím dochádza k extrémnemu zhrubnutiu litosféry. Na rozdiel od Západných Karpát, v Himalájach sú magnitúda a rýchlosť presunov príkrovov akrečnej prizmy orogénu aj dimenzie pohoria rádovo vyššie. Západokarpatský orogén sa sformoval superponovaním variských, paleo-, mezo- a neoalpínskych tektonických procesov oddelených etapami pokoja a denudácie. Variské, paleo- a mezoalpínske štruktúry sú zachované vo vnútrokarpatskom bloku južne od neoalpínskej orogénnej prizmy. Himalájsky orogén je výlučne neoalpínsky. Je výsledkom kontinuálnej, asi 50 mil. r. trvajúcej kolízie indickej platne s eurázijskou, počas ktorej bola a stále je generovaná orogénna akrečná prizma formujúca sa z jednotiek indickej platne. Špecifikom Západných Karpát je morfotektonický štýl striedania neogénnych

sedimentárnych bazénov a hrastí kontrolovaný zlomami, vyvinutý vo vnútrokarpatskom bloku orogénu, porušenom hustou sieťou zlomov viacerých genetických systémov. Rozsiahle zaoblúkové neogénne sedimentárne bazény, generované dominantne termálnou subsidenciou správanou mohutným subsekventným vulkanizmom, sú vyvinuté v tyle západokarpatského orogénu. V Himalájach mladé neogénne molasové sedimenty, geneticky korešpondujúce so sedimentmi karpatskej čelnej predhlbne, sú vo veľkom rozsahu situované vo frontálnej časti orogénu (Siwalik). Vnútri himalájskej orogénnej prizmy sú len sporadické úzke priečne grabeny kontrolované poklesovými zlomami (napr. graben Mustang), vyplnené miocénnymi a kvartérnymi fluvialno-glaciálnymi sedimentmi. Významné smernoposunové zlomy subparalelné s himalájskym orogénnym frontom

sú situované v tyle pohoria – v Transhimalájach, ktoré sú už súčasťou ázijskej platne. Tieto hlboké kôrové rozhrania prvého rádu sprostredkujú tektonický únik čiastkových blokov vyvolaný tlakom indickej platne. Je to proces, ktorým sa relaxuje časť energie konvergujúcich platní, indickej a ázijskej. Oba orogény sú výrazne asymetrické, no Západné Karpaty sú generálne severovergentné a Himaláje juhovergentné (obr. 4a, b). Oba orogény vykazujú polaritu kolízneho frontu postupujúceho zo západu na východ a z tyľa orogénu smerom do čela, teda ide o nesené (*piggy back*) násunové sekvencie.

Doručené / Received: 14. 10. 2020

Prijaté na publikovanie / Accepted: 18. 2. 2021

Geological structure and tectonometamorphic evolution of the Veporic–Gemic contact zone constrained by the monazite age data (Slavošovce–Štítnik area, Western Carpathians, Slovakia)

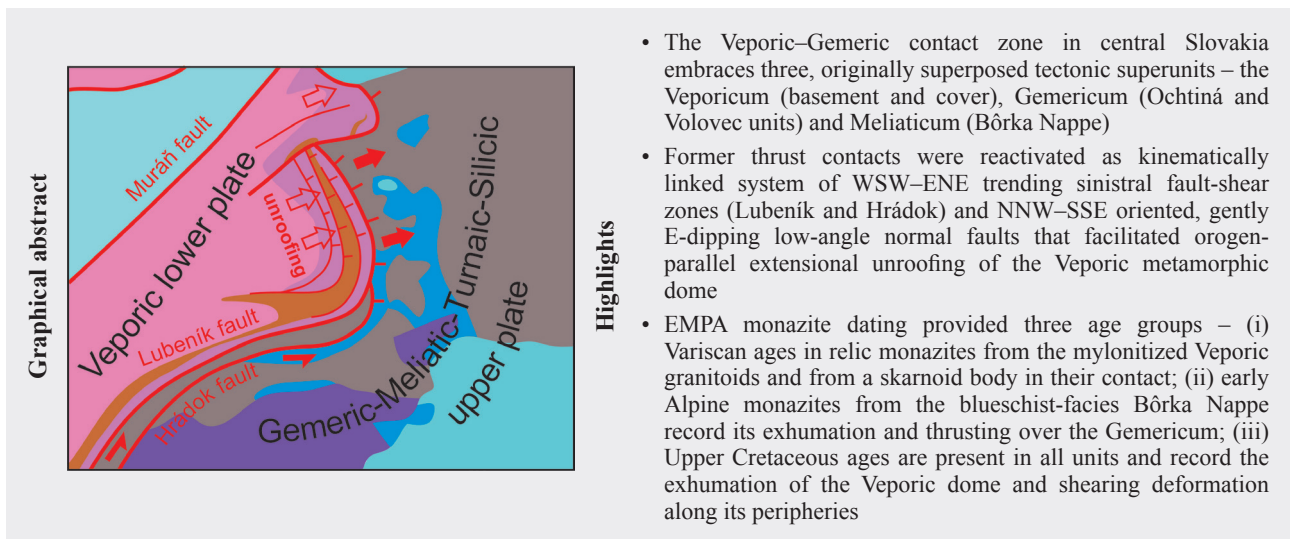
TOMÁŠ POTOČNÝ¹, ŠTEFAN MÉRÉS² and DUŠAN PLAŠIENKA¹

¹ Comenius University, Faculty of Natural Sciences, Department of Geology and Paleontology, Mlynská dolina, Ilkovičova 6, SK-842 15 Bratislava, Slovakia; potocny9@uniba.sk; dusan.plasienska@uniba.sk

² Comenius University, Faculty of Natural Sciences, Department of Geochemistry, Mlynská dolina, Ilkovičova 6, SK-842 15 Bratislava, Slovakia; stefan.meres@uniba.sk

Abstract: The investigated area represents a segment of the contiguous Veporic–Gemic zone characterized by the presence of several major superposed and/or juxtaposed tectonic units, exhibiting contrasting structural and metamorphic histories. Based on the structural, petrological and geochronological (EMPA dating of monazites) investigations, the principal Alpine tectono-metamorphic evolutionary stages were distinguished. Besides Variscan ages from the Veporic granitoids and skarnoids, the monazite dating provided evidence for the latest Jurassic–earliest Cretaceous event (150–140 Ma) in the Meliatic Bôrka Nappe, which was related to its exhumation and thrusting over the Gemic units. Younger Cretaceous ages (110–85 Ma) were detected in all units involved and were connected with the ongoing shortening and onset of the orogen-parallel extensional exhumation of the Veporic metamorphic dome. Exhumation was governed by the kinematically linked sinistral shearing along the WSW–ENE trending Veporic–Gemic contact zone (Lubeník and Hrádok fault zones) and by NNW–SSE oriented and east-dipping system of low-angle detachment normal faults that facilitated unroofing of the Veporic dome. Both segments reactivated in different ways the original overthrust contact between the Veporic lower plate and the Gemic–Meliatic–Turnaic–Silicic upper plate.

Key words: Veporic, Gemic, Meliatic, structural analysis, metamorphism, monazite dating



Introduction

In general, convergent orogens are characterized by stacking of thick- and thin-skinned thrust sheets composed of rock complexes derived from different paleogeographic and paleotectonic settings. During continuing shortening within the prograding orogenic wedge, the original thrust

contacts of major tectonic units are often affected by superimposed deformational and metamorphic processes like transpression, extension, or retrogression. As a result, these contact zones exhibit a complicated inner structure and sometimes patchy record of overprinting tectonic and metamorphic events within the units involved. Consequently, deciphering of structural and metamorphic

evolution of the tectonic interface zones is of primary importance for interpretations of the orogen-scale tectonic processes.

In the Western Carpathians, there are at least four such contact or transitional zones that follow boundaries of the principal crustal-scale thrust systems (e.g. Plašienka, 2018 and references therein): (1) the boundary between the Internal and Central Western Carpathians (IWC and CWC, respectively); (2) the contact zone of the Veporic and Gemeric basement-involved thrust sheets of the CWC; (3) the boundary between the Tatric and overriding Veporic thick-skinned thrust sheets of the CWC (known as the Čertovica fault zone or line); (4) the Central to External (EWC) contiguous zone followed by the Pieniny Klippen belt (PKB) – see Fig. 1. The IWC vs. CWC border zone is considered as an ophiolite- and blueschists-bearing suture after closure of the Meliata Ocean by some authors (e.g. Plašienka et al., 1997, 2019; Lexa et al., 2003; Faryad et al., 2005; Dallmeyer et al., 2008; named as the Rožňava–Šugov Suture Zone by Kozur & Mock, 1997). The Čertovica fault zone has been considered as a kind of an intra-continental suture, from which units of the Fatric cover nappe system were derived (e.g. Biely & Fusán, 1967; Andrusov, 1968; Plašienka, 2003; Prokešová et al., 2012). The narrow but lengthy PKB is a surface expression of the crust-scale boundary between the foreland North European Platform

overridden by the EWC accretionary wedge (Flysch Belt) and the Cretaceous thrust stack of the CWC units. At the same time, this boundary represents the suture zone after two branches of the Pennine oceanic realms – the southern Piemont–Váh and northern Valais–Magura oceans (e.g. Plašienka et al., 2020 and references therein).

In this contribution, we are dealing with the Veporic–Gemic contact zone (abbreviated as VGCZ hereafter), which is another “intracontinental suture” of the CWC in central Slovakia. It surrounds the Lubeník fault that is the eastern branch of the Lubeník–Margecany “Line” representing a fault interface between the Veporic and Gemeric basement-involved superunits. VGCZ is characterized by extensive shortening and complicated internal structure that records the original thrust plane of the Gemeric over Veporic, later affected by important transpressional and extensional reactivation. The deformation processes in this structurally complicated area resulted in a superposition and/or juxtaposition of several units that exhibit complex tectonic and metamorphic relationships. In the following, we present the structural, metamorphic and geochronological data providing some constraints on the VGCZ development. The tectonometamorphic evolution of the investigated area is partitioned into several distinctive stages.

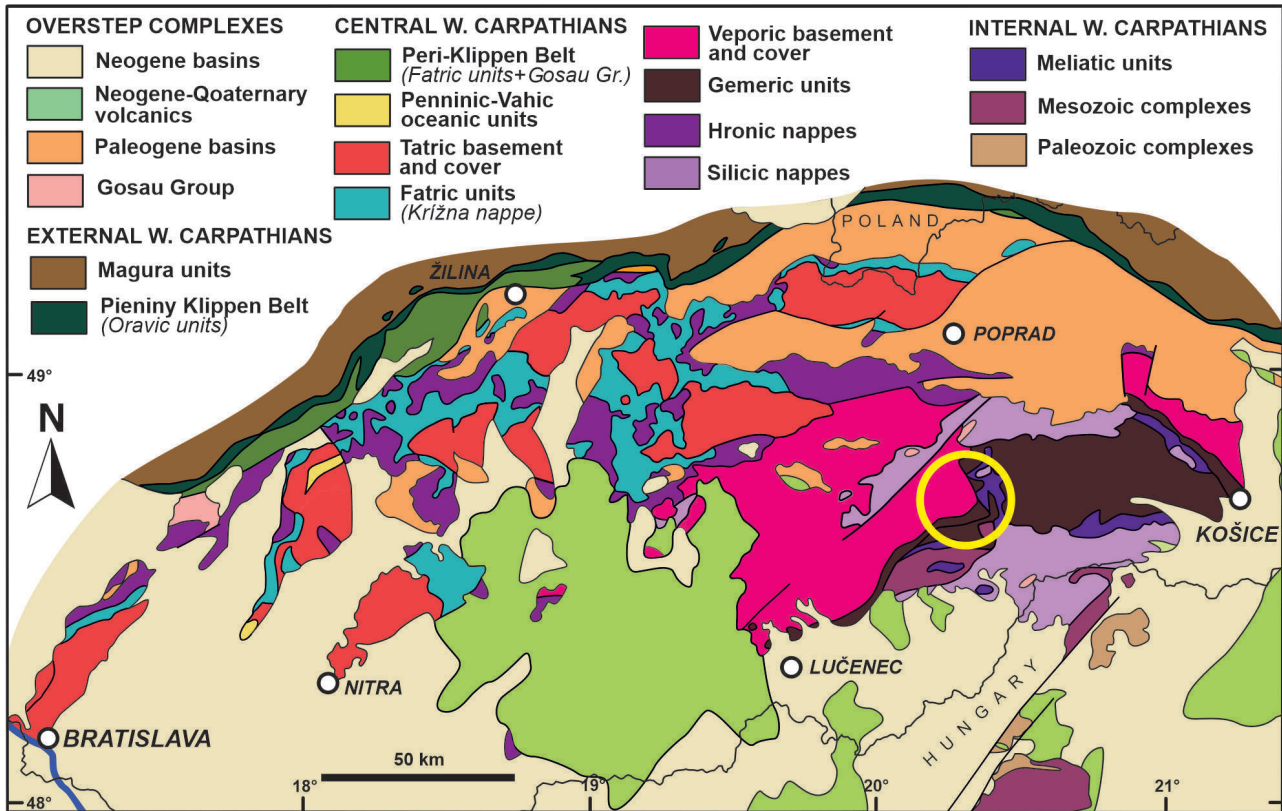


Fig. 1. Tectonic sketch map of the Western Carpathians (modified after Plašienka et al., 2019). The circle indicates the investigated area (Fig. 2).

Geological setting

We investigated about 15 km long and 10 km wide segment of the VGCZ in the NW–SE trending zone that crosses the regional structural trends and follows the valley of Štítik Brook between Čierna Lehota, Markuška, Honce and Chyžné villages in the eastern part of the Revúcka vrchovina Highland (Fig. 2). This comparatively small region is built up by six juxtaposed or superposed major Western Carpathian tectonic units. The lowermost structural position is occupied by the Veporic basement and cover complexes overridden by the Ochtiná and Volovec units assigned to the Gemic Superunit, and by tectonic outliers of the Meliatic Bôrka Nappe, as well as the Turňa Unit and Silica Nappe in the southeasternmost part of the region (Fig. 2).

The Veporic Superunit includes the pre-Alpine crystalline basement and the post-Variscan Upper Paleozoic–Triassic sedimentary cover (Revúcka Group and Foederata Unit). The Veporic basement is composed of polymetamorphic (Variscan and Alpine) metasediments and scarce metavolcanics (Hladomorná dolina Complex; HDC) intruded by Variscan granitoids of the Vepor pluton (Kráľova hoľa Complex; KHC – cf. Vrána, 1964; Klinec, 1966, 1971). In addition to the polyphase regional metamorphism, the HDC bears also two generations of contact metamorphic assemblages overprinting the

regional metamorphic associations. The older medium pressure – high temperature assemblage (Vozárová & Krištín, 1985) is concentrated to exocontacts of the Variscan granitic intrusions with the HDC, typically between Chyžné and Slavošovce villages (Fig. 2). The low pressure-high temperature contact aureole SW of Rochovce village is related to the hidden Upper Cretaceous granitic intrusion (Rochovce granite; Korikovsky et al., 1986; Vozárová, 1990; Poller et al., 2001; Kohút et al., 2013), which was encountered by drilling below the HDC rocks (e.g. Klinec, 1980). Along its southern margin and at the contact with overlying Gemic units, the HDC is discordantly overlain by clastic deposits of the Permian Rimava Formation forming a part of the South Veporic sedimentary cover (Revúcka Group, Vozárová & Vozár, 1988; Vozárová, 1996).

In the area south of the Štítik Valley, particularly north of Chyžné village (Fig. 2), the KHC granitoids show an intrusion contact into the HDC in the form of sill-like dykes concordant to the metamorphic foliation of the HDC. However, from Slavošovce northwards, the HDC is underlain by the Upper Carboniferous oligomict conglomerates (Háj Hill west of Slavošovce), sandstones and black shales of the Slatviná Formation (Vozárová & Vozár, 1982, 1988; Vozárová, 1996), which are in turn underlain by Permian clastics of the Rimava Formation directly overlying KHC north of Slavošovce (Fig. 2).

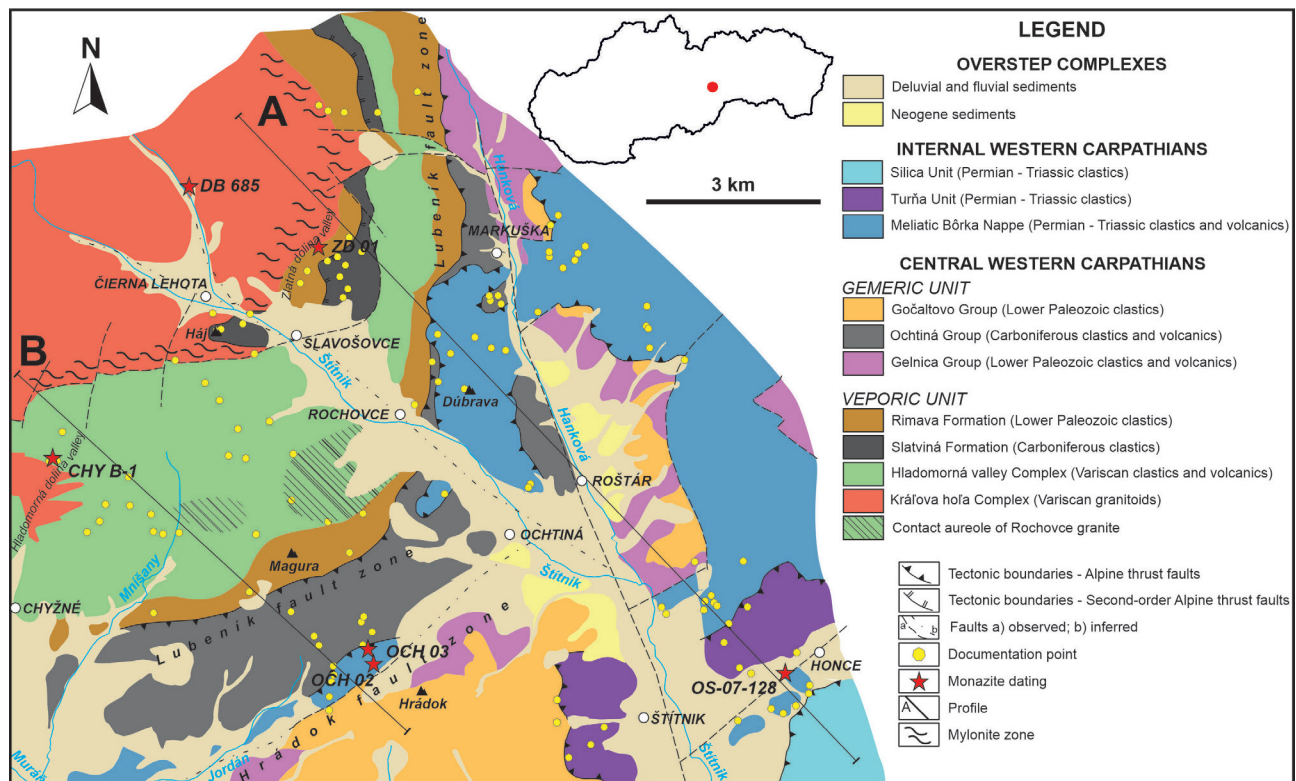


Fig. 2. Tectonic map of the investigated area (compiled from maps of Klinec, 1976; Bajanič et al., 1984; Grecula et al., 2009 and from our own observations).

Rocks at the contact of KHC with the Upper Paleozoic cover formations are strongly sheared and accompanied by a mylonitic zone hundreds of metres wide.

In the area north of the Štítňik Valley, the WSW–ENE striking Lubeník fault zone and the parallel regional structural trends are turned to the N–S to NNW–SSE direction. Bedding and metamorphic and mylonitic foliations are gently to moderately east-dipping, while the pervasive stretching lineation remains constantly plunging to the NE to E (Plašienka, 1993; Janák et al., 2001). This structure was known as the “Gemer ramp”, i.e. the regional axial plunge of the Veporic below Gemic units. As a result, the KHC is overlain by a gently east-dipping stack of various units – directly by the Permian cover (Rimava Fm.), next by the Pennsylvanian Slatviná Fm., afterwards by the HDC with the Permian (Rimava Fm.) and further north also Lower Triassic (Lúžna Fm.) cover rocks, and finally by the Gemic units overlain by

the Bôrka Nappe outliers (Fig. 2; 3A). This complicated structure was described as the NW-verging Markuška anticlinal recumbent fold (Zoubek & Snopko, 1954; Zoubek, 1957) with the HDC in its core, or as the Markuška Nappe by Plašienka (1980, 1984). Thanks to the eastward regional axial plunge, structures are obliquely cut by the topography, and interpretation of the cross-sectional morphology of the Markuška fold is enabled in the map view (e.g. Plašienka, 1984).

Along the SW–NE to WSW–ENE trending Lubeník fault zone, rocks of Veporic Rimava Fm. are juxtaposed to the Paleozoic complexes of the Gemic Superunit. In the direct contact with the Veporic units, the Gemicum is represented by the Ochtiná Unit, which is composed of the Mississippian Ochtiná Group overlain by Pennsylvanian clastics of the Hámor Fm. (e.g. Vozárová, 1996). The Ochtiná Group consists of the Viséan Hrádok Formation of flysch-type metasediments interlayered by basic

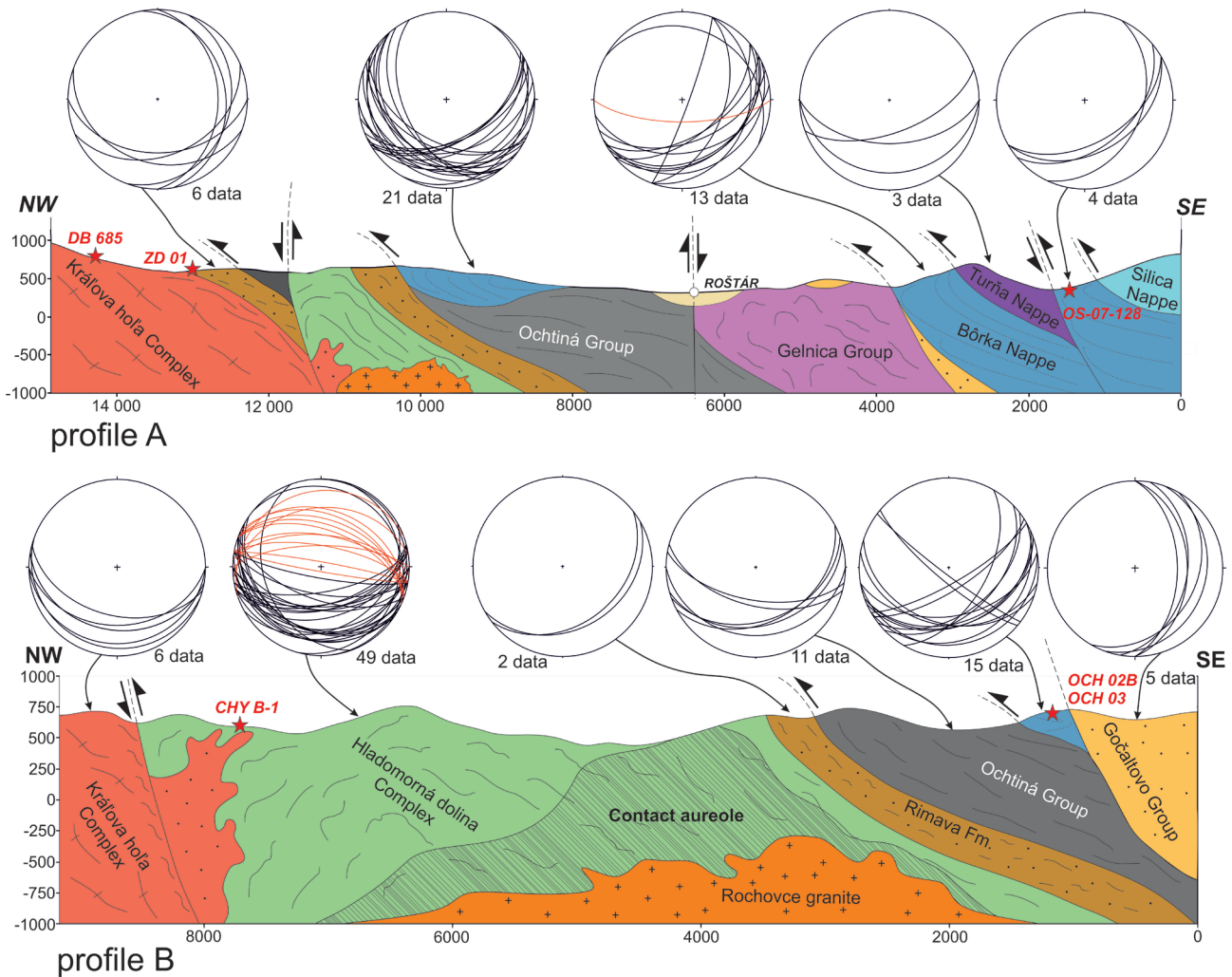


Fig. 3. Cross-sections A and B through the investigated area. For their position and legend see Fig. 2. Stereographic plots show orientation of planar structures in different rock complexes (equal area projection, lower hemisphere). Black – the main foliation (sedimentary, metamorphic, mylonitic), red – secondary cleavage.

MORB-type metavolcanics and bodies of ultramafics. The overlying upper Viséan–Serpukhovian Lubeník Formation includes black shales, bedded limestones and dolomites and large bodies of metasomatic magnesite (Kozur et al., 1976; Vozárová, 1996).

The Ochtiná Unit is overthrust by the Volovec Unit of the main Gemic basement-cover thrust sheet represented by the Lower Paleozoic polymetamorphic greenschist-facies volcanosedimentary formations (Gelnica Group) and by the very low-grade Permian clastic metasediments of the Gočaltovo Group (Fig. 2). In several segments of the VGCZ, the Ochtiná Unit is strongly sheared and includes slices from both the footwall Veporic cover and hangingwall Gemic metabasalts. This was described as a kind of thrust *mélange* developed along a decoupling zone between the two crustal-scale superunits (Novotná et al., 2015). The boundary of the Ochtiná and Volovec units is formed by the Hrádok fault zone that parallels the Lubeník fault zone in the southern part of the region (Figs 2, 3B). However, continuation of the Ochtiná Unit farther north, after turning of the Lubeník Line to the N–S direction is controversial. In the majority of published maps, various Carboniferous formations between Roštár and Markuška villages (Fig. 2) are assigned to the Zlatník and/or Hámor formations of the North Gemic Dobšiná Group (e.g. Bajaník et al., 1984). On the other hand, Grecula et al. (2009) classified these rocks as the Hrádok Formation of the Ochtiná Group. We share the latter view in Fig. 2.

The Gemic Volovec Unit is overridden by the Meliatic Superunit formed by the Bôrka Nappe (Leško & Varga, 1980; Mello et al., 1998) in the investigated area. According to the lithostratigraphic classification of Mello et al. (1998), the Bôrka Nappe includes the lower complex composed of Permian to Lower Triassic continental clastic metasediments with acid metavolcanics that are lithologically correlative with the underlying Gemic cover formations. The upper complex, which is in part structurally independent, involves the Middle Triassic metacarbonates with intercalations of metabasalts and metavolcaniclastics (Dúbrava Formation) followed by a thick complex of dark-grey phyllites with metasandstone beds and olistostrome bodies of probably Upper Triassic to Lower–Middle Jurassic? age (Hačava Formation).

In the investigated area, rock formations affiliated with the upper complex of the Bôrka Nappe occur as narrow slices within the Hrádok fault zone between the Ochtiná and Volovec units. The Bôrka Nappe covers a comparatively large area on the wide ridge north of Honce village (Fig. 2). This occurrence includes both the lower and upper complexes of the Bôrka Nappe within a N–S trending complex synform known as the Nižná Slaná depression (e.g. Németh, 1994). However, the presence of the Bôrka Nappe on Dúbrava Hill north of Ochtiná (Fig. 2) is disputable. Classified originally as

the Upper Carboniferous Dúbrava beds of the Ochtiná Group (e.g. Abonyi, 1971), and assigned to the Gemic Carboniferous strata also later (Gazdačko, 1995), this occurrence was reinterpreted as the type locality of the Middle Triassic Dúbrava Fm. of the Bôrka Nappe by Mello et al. (1998) afterwards. This interpretation is maintained in the majority of published geological and tectonic maps, except that of Grecula et al. (2009). We have not paid a special attention to this problem yet, but we take on the generally accepted affiliation of the Dúbrava Fm. with the Bôrka Nappe in Fig. 2.

The majority of the Bôrka Nappe rocks underwent the Late Jurassic blueschist-facies metamorphism which was often subsequently affected by the Cretaceous greenschist-facies retrogression (e.g. Faryad & Henjes-Kunst, 1997; Faryad & Hoinkes, 1999; Dallmeyer et al., 2008; Plašienka et al., 2019; Putiš et al., 2019; Nemeč et al., 2020). Farther south, the Meliaticum includes also a very low-grade Jurassic syn-orogenic flysch succession with huge olistostrome bodies (Meliata Unit s.s.; Mock et al., 1998; Árkai et al., 2003). Meliatic complexes are always tightly imbricated and form a combined accretionary complex with the overlying Turňa Unit represented by a system of partial nappes and duplexes consisting of low-grade Carboniferous to Triassic metasediments (Lačný et al., 2016). The Silica Nappe is the structurally highest unit of the region, which overlies the Meliatic–Turnaic accretionary complex with a pronounced structural and metamorphic discordance (Reichwalder, 1982). It is composed of the Lower Triassic clastic formations and the thick Middle–Upper Triassic carbonate platform complex.

Methods

Several methodological procedures were applied during the field research of the investigated area and the subsequent laboratory processing of the obtained data and samples. Field works were focused on structural mapping and sampling. In the laboratory, investigations continued with orientation analysis of measured data and petrographic microanalyses of samples in thin-sections. Several potential samples were selected for microprobe determination of minerals and EMPA dating of monazites.

During the field works, altogether 116 outcrops were documented (Fig. 2), 277 samples (25 oriented) were collected and petrographically described. Structural observations included gathering of oriented data of mesoscopic elements like metamorphic foliation, cleavage, shear zones, joints and folds. The Stereonet software (Cardozo & Allmendinger, 2013) was used for the evaluation of structural data, which are stored in a database for further analyses. Herein, some of the oriented structural data are plotted in the stereographic equal area projection on the lower hemisphere.

Thin-sections from all rock types were subjected to petrological study under the polarized microscope (295 thin sections) and electronic microanalyzer (152 thin sections) to obtain data about the lithology, metamorphism and microstructures. Localities of representative samples referred to in the text and figures are given in Table 1.

Several samples that contain metamorphic monazites were dated by the EMPA method providing crystallization ages using the CAMECA SX-100 electronic microanalyzer at the Laboratory of electron microanalysis of the State Geological Institute of Dionýz Štúr, which specializes in non-destructive microanalysis of solids and image analysis of samples. The chosen method is based on the accurate determination of the content of Th, U and Pb (CHIME – chemical Th-U-total Pb isochron method) in monazites and other proper minerals like xenotime and zircon. Owing to several factors, monazite is the most suitable candidate for this method (e.g. Sulovský et al., 2004). Statistical approach of Montel et al. (1996) was applied for determination of the resulting age and the DAMON

program was used for the age recalculations, histograms and isochron plots (Konečný et al., 2004).

Results

Structural observations and metamorphic petrography

The structural relationships of the Veporic–Gemic–Meliatic–Turnaic thrust stack are described along two subparallel, NW–SE trending profile lines in the studied area (Fig. 3A, B). The first profile A is located NE of the Štítnik Valley, where it crosses units of the Veporicum (KHC, HDC, Rimava Fm.), Gemicum (Ochtiná, Gelnica and Gočaltovo groups), Meliaticum (Bôrka Nappe), Turnaicum and Silicicum. The second profile (B in Fig. 3) follows the mountain ridge between the Štítnik and Muráň river valleys and includes from NW to SE the Veporic (KHC, HDC, Rimava Formation), Gemic (Ochtiná and Gočaltovo groups) and Meliatic units (Bôrka Nappe). The cross-sections A and B are supplemented by structural diagrams showing orientation of the macroscopically

Tab. 1

Locations of samples cited in the text and figures.

NAME	UNIT	GPS
HR 01	Bôrka Nappe	48.6597914N 20.2853714E
HR 09	Bôrka Nappe	48.6646808N 20.2861653E
OCH 02	Bôrka Nappe	48.6653611N 20.2932892E
OCH 03	Bôrka Nappe	48.6673878N 20.2928386E
OS-07-128	Bôrka Nappe	48.6631361N 20.3943119E
HR 06	Gemic – Ochtiná Gr.	48.6732967N 20.2760158E
HR 08	Gemic – Ochtiná Gr.	48.6675578N 20.2832472E
OCH 05	Gemic – Ochtiná Gr.	48.6701086N 20.2952206E
CHY B-1	Veporic – HDC	48.6963358N 20.2192642E
HÁJ 02	Veporic – HDC	48.7138764N 20.2675186E
SLV 01	Veporic – HDC	48.7032283N 20.2703081E
SLV 02	Veporic – HDC	48.7019114N 20.2634417E
SLV 03	Veporic – HDC	48.6985972N 20.2622186E
SLV 04	Veporic – HDC	48.6972236N 20.2647936E
SLV 05	Veporic – HDC	48.6903825N 20.2762519E
HÁJ 01	Veporic – mylonite	48.7186758N 20.2633344E
HÁJ 04	Veporic – mylonite	48.7202897N 20.2654586E
HAN 01	Veporic – mylonite	48.7526267N 20.2824747E
ZD 01	Veporic – mylonite	48.7311464N 20.2821528E
OCH 01	Veporic – Rimava Fm.	48.6828886N 20.2904139E
SLV 08	Veporic – Rimava Fm.	48.6881728N 20.2923667E
DB 685	Veporic – skarnoid	48.7399772N 20.2513825E

observed foliation planes. These are genetically different, however, since they include both the primary planar structures like bedding in sediments, which is commonly parallel to the superimposed metamorphic schistosity, and secondary deformation-related cleavages and mylonitic foliations. Nevertheless, attitudes of all foliation planes are generally subparallel (with the exception of HDC) and together with boundaries of major tectonic units they define the regional structural pattern and principal trends of the Alpine tectonic edifice of the area.

Structural data gathered from the HDC were collected at numerous surface exposures (Fig. 2). In most cases, the Variscan metamorphic foliation is only weakly affected by Alpine reworking, which is concentrated in narrow mylonite or phyllonite zones. Measured planar structures can be separated into two groups with different attitudes. The primary metamorphic foliation is gently SSW-dipping, while the superimposed cleavage is moderately NNE-dipping (cross-section B in Fig. 3). Nevertheless, both foliations appear to be pre-Alpine.

In general, majority of the measured metamorphic foliation planes outside HDC show moderate dips to the SE, which is correlated with the main Alpine tectonic stages. Alpine metamorphic foliation planes in the Rimava Fm. are parallel to moderately SE-dipping bedding planes (Fig. 3). Structural data from the Ochtiná Group, taken from the ridge between Hrádok and Magura hills (Fig.

3B), show a similar orientation. The same applies to the Bôrka Nappe.

The dip direction data of metamorphic foliations from HDC are clearly oblique to the Alpine foliations measured in the adjacent post-Variscan units, as they show the overall dip direction to the SW to S. This different orientation is considered to be inherited from the pre-Alpine period, as it is indicated also by their exploitation by the Variscan granitoid sills near Chyžné village (Fig. 2).

The HDC includes different types of metasediments (phyllites and gneisses) and basic metavolcanic rocks in the study area. Characteristic feature of metasediments is a very fine-grained matrix composed of garnet, chlorite, biotite, muscovite, quartz, plagioclase ± tourmaline, opaque minerals, monazite and zircon (Fig. 4). Contact metamorphism related to the underlying Rochovce granite intrusion produced porphyroblasts of garnet, biotite, cordierite and andalusite superimposed on the older regional metamorphic paragenesis.

Metabasites of the HDC are massive, medium-grained, grey-green rocks consisting of amphibole, epidote, chlorite and plagioclase, ± apatite, titanite and opaque minerals (Fig. 4C). Contact metamorphosed metabasites are affected by widespread biotitization, older amphibole is often replaced by younger actinolite.

Microstructural observations in thin-sections were performed along with their relationships to the newly-

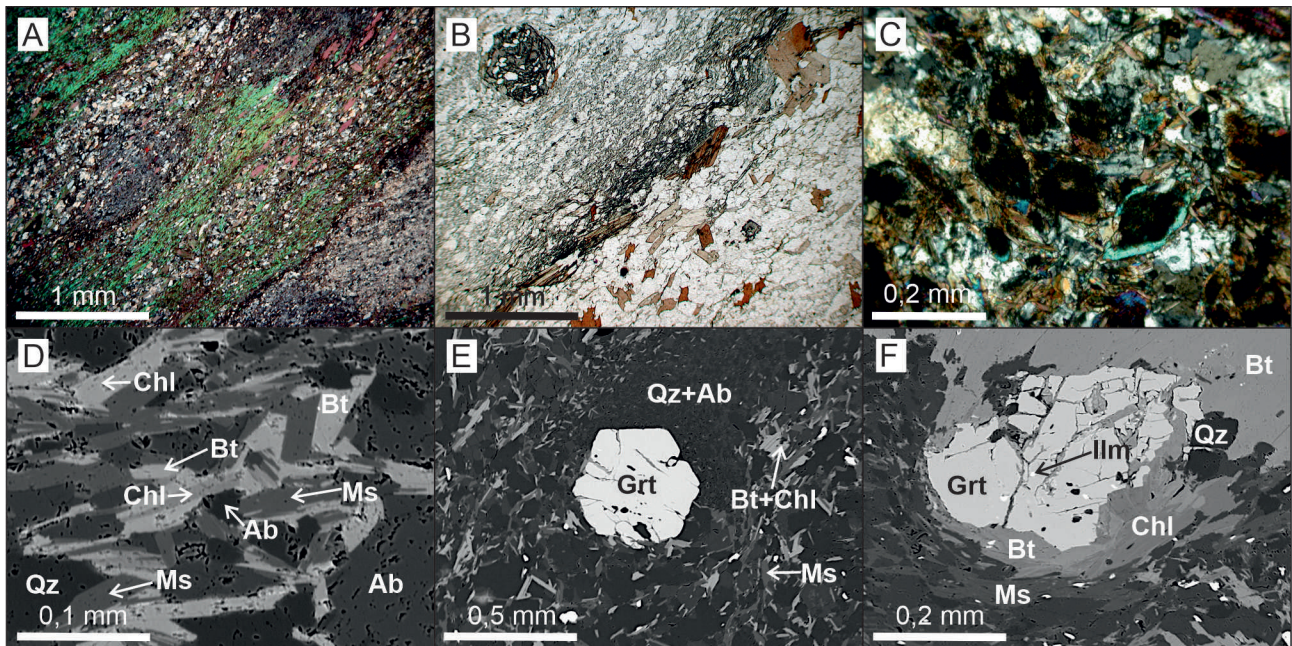


Fig. 4. Veporic basement – Hladomorná dolina Complex: A – photomicrograph of contact metamorphosed cordierite-biotitic gneiss (sample SLV 05) in polarized light; B – photomicrograph of muscovite-biotitic gneiss with garnet and well-preserved variable grain-size of the protolith (HAJ 02); C – photomicrograph of metabasite – epidote amphibolite (SLV 03) in polarized light; D – electron backscattered (BSE) images of fine-grained matrix of garnet-biotitic gneiss (SLV 01); E – BSE image of garnet porphyroblast in a fine-grained matrix (SLV 04); F – BSE image of garnet porphyroblast replaced by biotite and chlorite (SLV 02).

formed metamorphic minerals. In phyllites and gneisses of the HDC, the foliation is defined by alignment of fine-grained aggregate of phyllosilicates in the groundmass, occasionally also by abrupt grain-size changes that might indicate lithological variations of the protolith (Fig. 4B). Growth of porphyroblasts was either syn- or post-kinematic. The first case is documented by Fig. 5B. The garnet porphyroblast contains inclusion trails depicting helicitic microfolds (Fig. 4B). Similar microfolds are present at the contact of the fine- and coarse-grained domains in the thin-section. Since the garnet blastesis is interpreted as generated by intrusion of the Variscan granitoids into HDC, these relationships indicate that this intrusion was syn-kinematic. The different example is shown in Fig. 4A. Large porphyroblasts of cordierite overgrow the gneissic foliation shaped by alignment of fine-grained micas, which also form numerous inclusions in porphyroblasts with the same orientation. Hence the cordierite porphyroblasts grew post-kinematically. Their relationship to the contact aureole of the hidden Rochovce granite, independently from its known Cretaceous age, reveals its post-tectonic intrusion related to the final phases of Alpine tectonic evolution of the area under consideration.

The greenschist-facies Rimava Formation consists of light coloured, medium- to fine-grained siliciclastic metasediments, as well as acidic metavolcanites and metavolcaniclastics (Fig. 5). They are composed of fine-grained, strongly sheared matrix (sericite, quartz, albite, biotite, zircon, tourmaline, xenotime \pm opaque minerals) and recrystallized quartz clasts. Fe-oxides are often concentrated along the foliation planes.

Clastic metasediments and metavolcaniclastics of the Permian Rimava Fm. are characterized by distinct foliation formed by thin anastomosing seams and orientation of fine-grained mica-quartz aggregate (Fig. 5). The seams are composed of a dark aphanitic matter that most likely represents an insoluble residue after pressure solution processes. Quartz porphyroclasts show undulose extinction and incipient dynamic recrystallization by low-T grain

boundary migration (bulging). Post-kinematic tourmaline overgrows the matrix foliation. These features point to deformation at the low-grade metamorphic conditions during the Alpine orogenesis.

The Ochtiná Group is represented by metaconglomerates, different types of phyllites and metabasalts (Fig. 6). Phyllites are grey to dark grey, fine-grained rocks. They are composed of variable quantities of chlorite, sericite, albite, quartz, garnet and organic matter indicating the greenschist-facies metamorphic conditions. Parallel texture (alternation of layers with different grains size) is common. Grey and grey-green metabasites are characterized by massive and parallel texture. Their greenschist-facies mineral composition includes amphibole, chlorite and epidote. Two generations of amphiboles were detected – older in the cores of porphyroblasts and younger in the rims. Additional minerals are represented by titanite, albite, quartz and opaques. Metaconglomerates have a coarse-grained texture with lithoclasts of quartz and various schists.

Phyllitic black schists of the Ochtiná Group exhibit a pervasive foliation shaped by the uniform orientation of very fine-grained sericite and chlorite. Foliation is enhanced by pressure solution seams enriched in black insoluble material including carbonaceous matter, which separate microlithons augmented by fine-grained quartz (Fig. 6A).

In the investigated area, composition of Triassic–Jurassic rocks of the Bôrka Nappe includes alternating slices of metacarbonates, metabasites and chlorite-sericite phyllites (Dúbrava and Hačava formations; Fig. 7). Metacarbonates – calcite marbles are usually massive, coarse-grained and equigranular and only locally they exhibit compositional layering (Fig. 7A). Indistinct darker thin layers are enriched in quartz, albite, sericite and chlorite (Fig. 7F).

Chlorite, amphibole and epidote dominate in the greenschist-facies metabasites. Metabasites, mostly metavolcaniclastics, also show compositional layering with alternation of microlayers dominated either by epidote and amphibole or by chlorite (Fig. 7B). Ružička

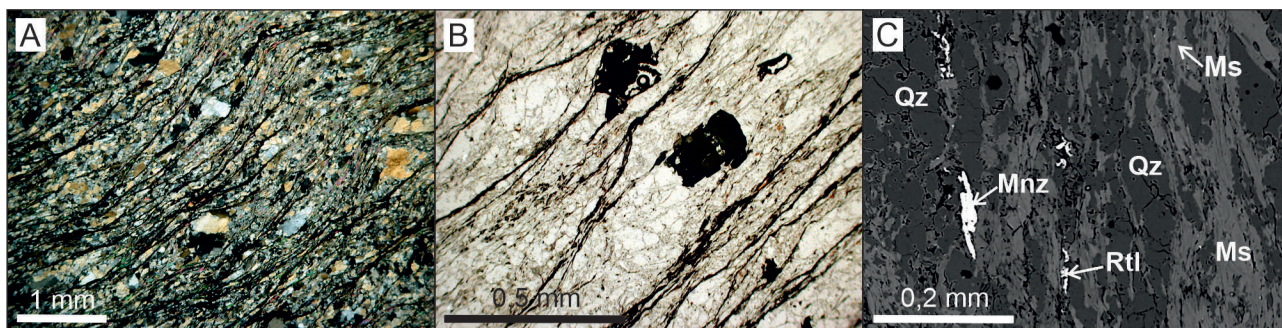


Fig. 5. Rimava Formation of the Permian Veporic cover: A – photomicrograph of acid metavolcaniclastics (SLV 08A) in polarized light; B – photomicrograph of acid metavolcaniclastics (SLV 08C); C – electron backscattered (BSE) images of acid metavolcaniclastics (OCH 01-1).

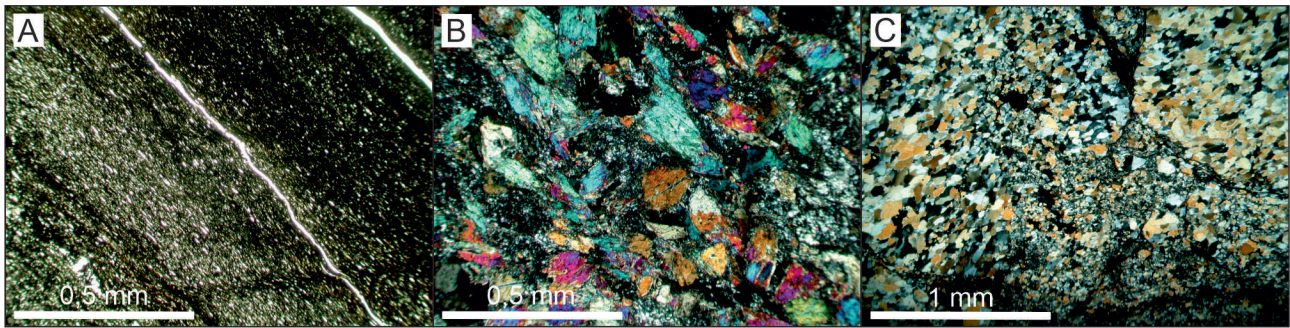


Fig. 6. Photomicrographs of rocks of the Gemic Ochtiná Group: A – graphite-sericite phyllite with very fine-grained matrix (OCH 05-1); B – metabasite with massive texture – metadolerite (HR 08-1) in polarized light; C – metaconglomerate (HR 06-1) in polarized light.

et al. (2019) reported presence of Mg-rich actinolite to tremolite, epidote, titanite, albite and Fe-apatite in metabasites and Mg-rich talc associated with clinocllore in marbles.

Phyllitic schists of the Bôrka Nappe are composed mainly of sericite, paragonite, chlorite, chloritoid, albite and quartz (Fig. 7C–E). Chlorite pseudomorphs after glaucophane are present at the Honce locality. Microstructural investigation of thin-sections from the Hrádok locality revealed that the macroscopically penetrative schistosity is in fact transposition cleavage produced by layer-parallel shortening of pre-existing metamorphic planar structure (Fig. 7E, F). Isoclinal, often rootless intrafolial microfolds partly preserve the original

structure and composition (quartz, albite, muscovite, chlorite) in the hinge zones of microfolds, while the fold limbs are strongly compressed with a reduced recrystallized grain size and alignment of phyllosilicates parallel to the new cleavage domains.

In addition, we have studied the mylonitic shear zone that follows approximately the contact of the Veporic basement and cover complexes, especially in the area where SW–NE contact zone turns to the N–S direction near Slavošovce village. The pre-Alpine granitoids (KHC), various Variscan and Alpine polymetamorphic rocks and clastic cover sediments, which were the parental rocks, exhibit a different degree of mylonitization from protomylonites (low degree) to ultramylonites (highest

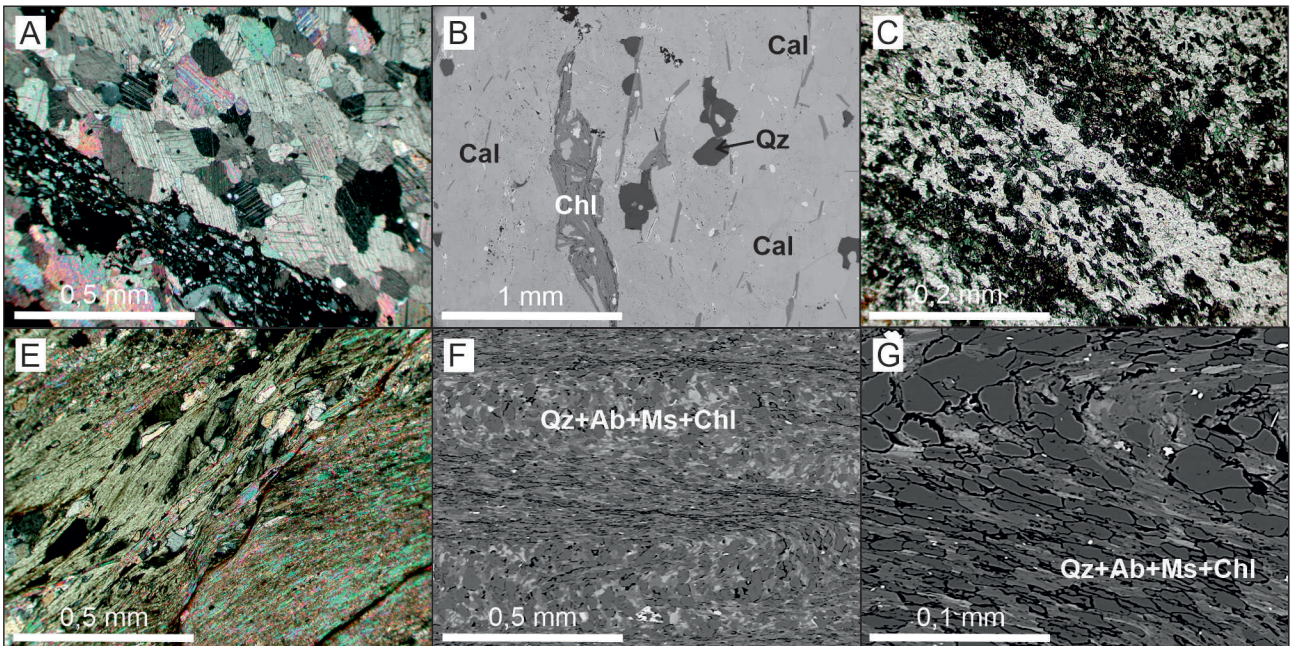


Fig. 7. Bôrka Nappe: A – photomicrograph of alternation of fine-grained chloritic phyllites and coarser-grained metacarbonates (HR 09-1) in polarized light; B – BSE image of marble with mineral impurities of quartz and chlorite (HR 09-1). C – photomicrograph of alternation of bands with predominance of quartz, albite and carbonate (lighter) and chlorite, epidote and actinolite (darker) (HR 01-1); D – photomicrograph of fine-grained sericite-chloritic phyllite (OCH 02B); E – electron backscattered (BSE) image of very fine-grained sericitic phyllite (OCH 03-5); F – detail of E.

degree). Partially preserved primary mineral composition of parental rocks can be observed in protomylonites (Fig. 8A), specifically in part sericitized and albitized K-feldspars (100–200 μm), muscovites and ilmenites (100 μm). Matrix of protomylonites forms 10–50 % of rock composition and includes mainly quartz, sericite, chlorite, biotite and albite. Zircon, ilmenite, rutile, apatite, allanite, xenotime, monazite and Fe-oxides are the less represented phases.

Mesomylonites (Fig. 8B, C) represent a medium degree of mylonitization and contain 50–90 % of matrix. In the mesomylonites, we observed significantly deformed relicts of K-feldspar, ilmenite, rutile and two generations of monazite.

Ultramylonites (Fig. 8E, D) represent the highest degree of mylonitization and show a penetrative foliation with typical dark-grey or black colour and more than 90 % of matrix. Mineral composition of the matrix includes very fine-grained chlorite, biotite, quartz, albite, sericite, paragonite, apatite, rutile, ilmenite and Fe-oxides with less amount of zircon, xenotime and monazite. The dark colour of the ultramylonites is caused by sub-microscopic chlorite, quartz and ore minerals ($< 5 \mu\text{m}$).

Monazite dating

The first set of monazite age data come from rock complexes occurring along the A profile line (Fig. 2). We investigated composition of a skarnoid body occurring

within the Variscan granitoids of KHC near Čierna Lehota village (Figs 2, 3A). The mineral composition is dominated by garnet, biotite and ore minerals, other common minerals include amphibole (grunerite-cummingtonite series), ilmenite, apatite, chlorite, muscovite, albite, K-feldspar, quartz and accessories like allanite, rutile and two generations of monazite (Fig. 9).

The older monazites Mnz1 show a rounded habitus, dimensions from 10 μm to 30 μm and always form inclusions in garnets. EMPA dating of Mnz1 revealed the Devonian–Carboniferous boundary ages ($359 \pm 4.2 \text{ Ma}$). The younger monazite generation (Mnz2) occurs permanently out of the garnets, most commonly in biotite or quartz. Mnz2 have a dendritic, strongly irregular habitus and are present in layers 30 μm to 100 μm thick along with older allanite. Mnz2 has the early Late Cretaceous age of $92 \pm 7.2 \text{ Ma}$ (Fig. 9).

Two generations of monazites were identified also in the protomylonitic granite of the KHC from the Zlatná dolina Valley NE of Slavošovce (Figs 2, 10). Older monazites Mnz1 are located in domains preserving the primary granitic fabric and have dimensions from 100 μm to 50 μm (Fig. 10A, B). Their crystallization age is approximately 355 Ma. The younger, smaller ($\pm 10 \mu\text{m}$; Fig. 10C, D) monazites are restricted to the Alpine mylonitic foliation planes and provided ages around 110 Ma.

We obtained other two distinct monazite age groups from the mylonitic granite and garnet-biotite gneiss located at the contact of KHC and HDC NE of Chyžné

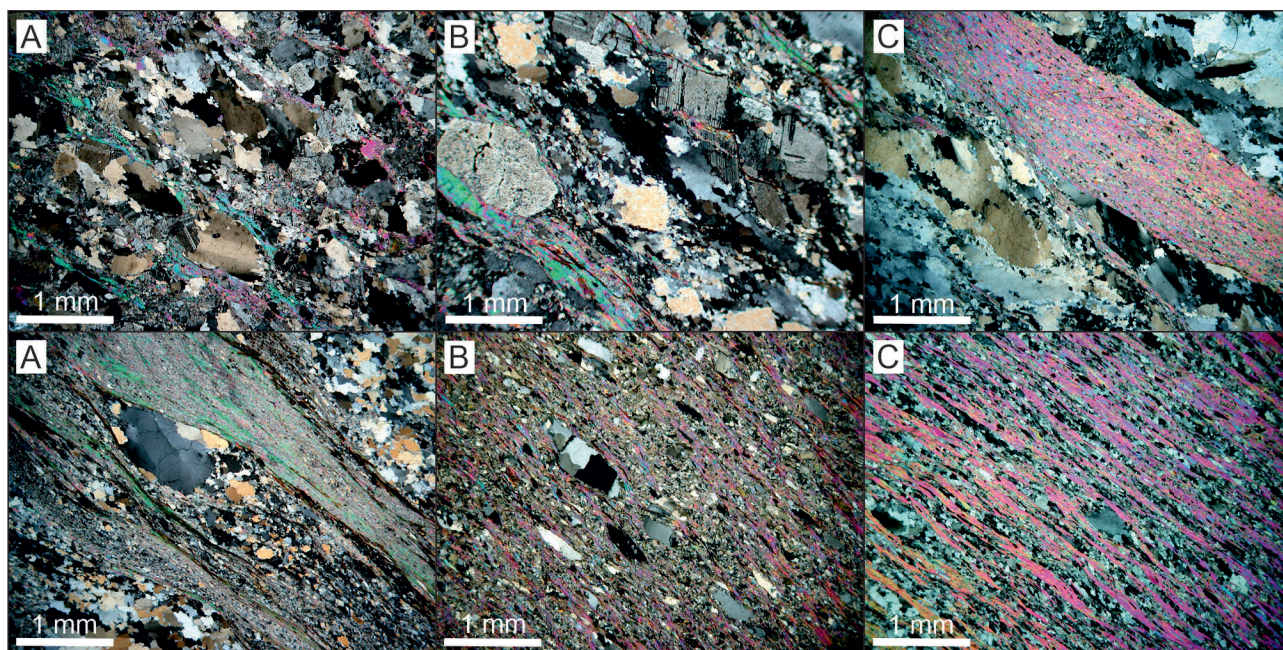


Fig. 8. Photomicrographs documenting development of mylonitization in granitoids: A – protomylonite (sample ZD 01); B – protomylonite (HAJ 04); C – mesomylonite (HAJ 01E); D – mesomylonite (HAJ 04); E – ultramylonite (HAJ 01A); F – ultramylonite (HAN 01C). Mylonitic foliation is defined by relic mica porphyroclasts and fine-grained sericite formed by breakdown of feldspars. Crossed polars in all images.

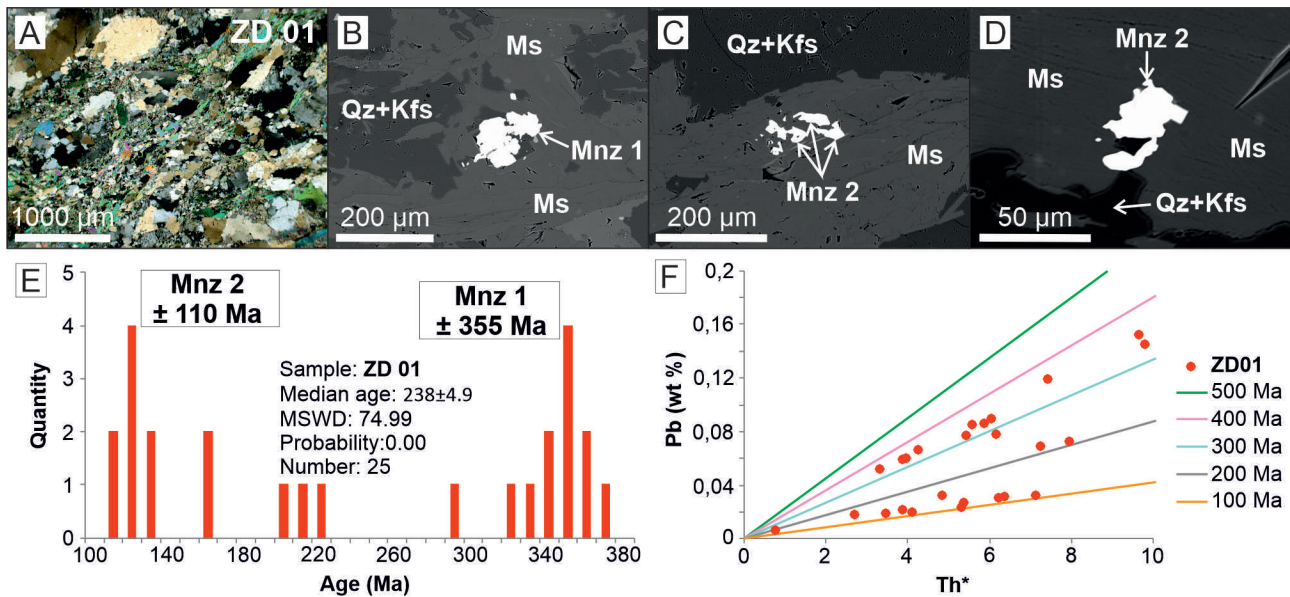


Fig. 9. Results of chemical (EMPA) U-Th-Pb dating of monazites from skarnoid body of the Veporic basement – Čierna Lehota locality (DB 685): A – photomicrograph of garnetiferous skarnoid; B – BSE image of older monazite Mnz1 occurring as inclusion in garnet; C – BSE image of younger monazite Mnz2 associated with biotite and muscovite; D – BSE image of younger dendritic monazites Mnz2; E – histogram with resultant 2 monazites ages groups; F – Pb vs. Th* (wt %) age monazite isochron diagram ($Th^* = Th + 3.15 \text{ wt } \%$).

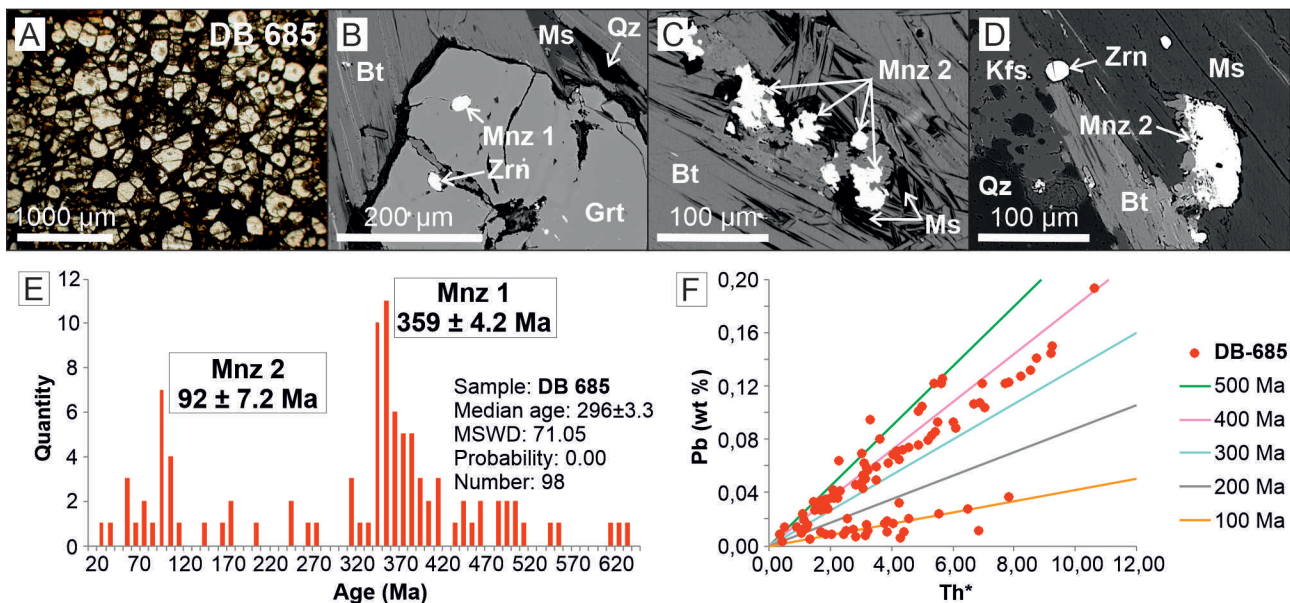


Fig. 10. Results of chemical (EMPA) U-Th-Pb dating of monazites from granite mylonite of the Veporic basement at Slavošovce – Zlatná dolina (sample ZD 01): A – photomicrograph of characteristic protomylonitic texture; B – BSE images of older monazites Mnz1 in relics of former granite; C and D – BSE image of younger monazite Mnz2 in deformed domains; E – histogram with resultant 2 monazites ages groups; F – Pb vs. Th* (wt %) monazite isochron age diagram ($Th^* = Th + 3.15 \text{ wt } \%$).

village (cross-section B in Fig. 2). Older monazite ages (around 355) Ma were obtained from the mylonitic granite, while younger monazite with ages around 88 Ma were identified in the garnet-biotite gneiss (Fig. 11). An analogous monazite age 88 Ma was obtained from the

metamorphosed cordierite-biotite gneiss (HDC) near the contact with the Permian Rimava Fm. NE of Magura Hill.

Two other, but different monazite age groups were acquired also from sericite-chlorite phyllites of the Bôrka Nappe (locality Hrádok, 5 km south of Slavošovce; Figs

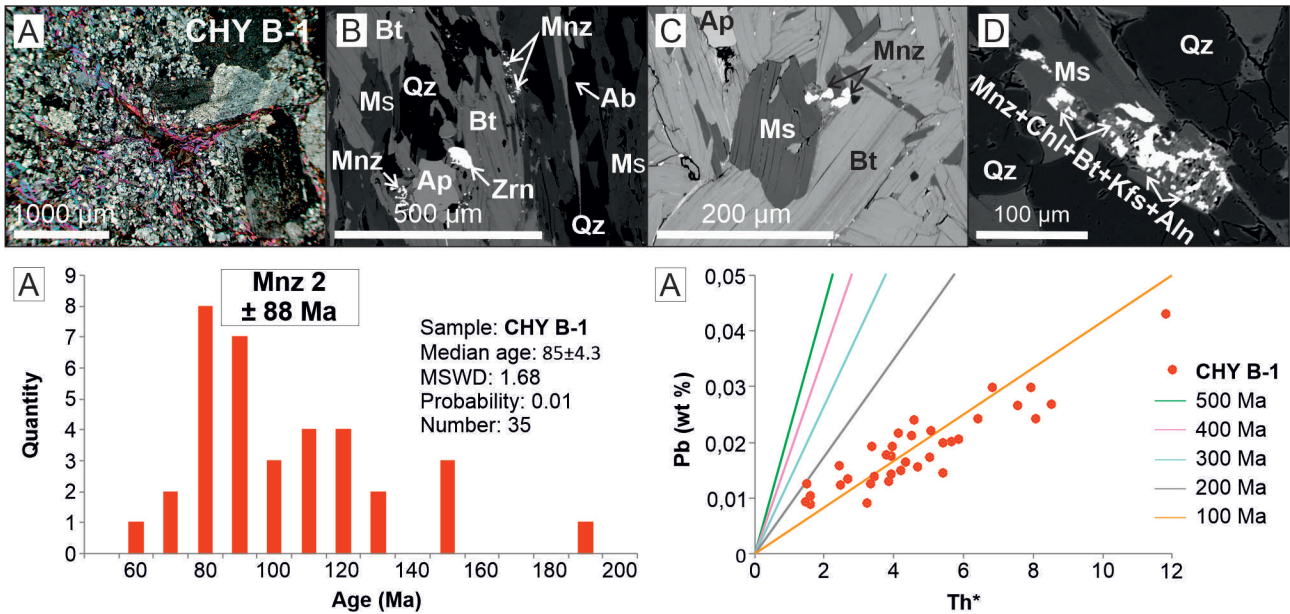


Fig. 11. Results of chemical (EMPA) U-Th-Pb dating of monazites from muscovite-biotite gneiss with garnet at Chyžné – Hladomorná dolina (sample CHY B-1): A – photomicrograph of gneissic structure, crossed polars; B – D BSE images of monazite appearance; E – histogram of measured ages; F – Pb vs. Th* (wt %) monazite isochron plot (Th* = Th + 3.15 wt %).

2 and 12). These monazites are very fine-grained (below 30 µm, frequently below 15 µm). EMPA dating of the sample OCH 02B provided two different age groups: 139 ± 13 Ma and 97 ± 5 Ma; the other sample OCH 03 gave 151 ± 5 Ma and 103 ± 4 Ma. Older monazites Mnz1 occur in the coarser-grained microlithons (Fig. 12B) and younger monazites Mnz2 are always present as elongated grains aligned within the very fine-grained cleavage domains transposing older metamorphic layering (Fig. 12C and D).

Further on, numerous post-kinematic idiomorphic porphyroblasts of monazites (30–500 µm in size) were observed in the sericite-chlorite phyllites of the Bôrka Nappe (locality Honce, 10 km SE of Slavošovce; Fig. 13). Monazites show a typical oscillation zonation which is reflected in their chemical composition. The EMPA dating of these monazites provided two, but rather indistinct age groups again: (1) 147 ± 17 Ma and (2) 89 ± 18 Ma.

Discussion Monazite age data

In general, three age groups were encountered by the EMPA-CHIME dating of monazites. The first Group 1 is restricted to the Variscan granitoids of the Veporic basement (KHC) and products of its contact metamorphic-metasomatic transformation of neighbouring rocks. The Group 1 is represented by the Mnz1 from the skarnoid body 359 ± 4.2 Ma and Mnz1 from mylonitized granitoids at the contact with the post-Variscan cover sediments that yielded the age of approximately 355 Ma. These data are

interpreted as the intrusion age of the KHC granitoids in the Slavošovce area.

The second Group 2 of ages was detected only in rocks of the Meliatic Bôrka Nappe. Mnz1 generation from the Hrádok locality provided ages 139 ± 13 Ma and 151 ± 5 Ma, Mnz1 from Honce yielded 147 ± 17 Ma. These ca 150–140 Ma ages (Tithonian–Berriasian) are slightly younger than those of the peak blueschist-facies metamorphic assemblages between 170 and 150 Ma (Oxfordian–Kimmeridgian) reported from the Bôrka Nappe by Maluski et al. (1993), Faryad and Henjes-Kunst (1997) and Dallmeyer et al. (2005, 2008). The latest Jurassic – earliest Cretaceous ages were interpreted as having been related to the post-subduction collisional exhumation of the Bôrka Nappe and its thrusting over the Gemic units (Plašienka et al., 2019).

The third Group 3 of monazite ages was detected in all analysed rock complexes. They are revealed by Mnz2 data from the Veporic skarnoid and mylonitized granitoids (92 ± 7.2 and about 110 Ma, respectively), monazites from the HDC gneisses (ca 88 Ma) and by Mnz2 from localities of the Bôrka Nappe (97 ± 5, 103 ± 4 and 89 ± 18 Ma). Generally, the early Upper Cretaceous ages roughly between 110 and 85 Ma (Albian–Santonian) correspond to the thrust stacking stage and maximum burial of the Veporic metamorphic complex, which was followed by its exhumation related to the shortening along the outer Veporic margin and underthrusting of the Veporic thrust wedge by the Tatric-Fatric crustal sheet (Janák et al., 2001; Dallmeyer et al., 2005; Jeřábek et al., 2012; Plašienka, 2018).

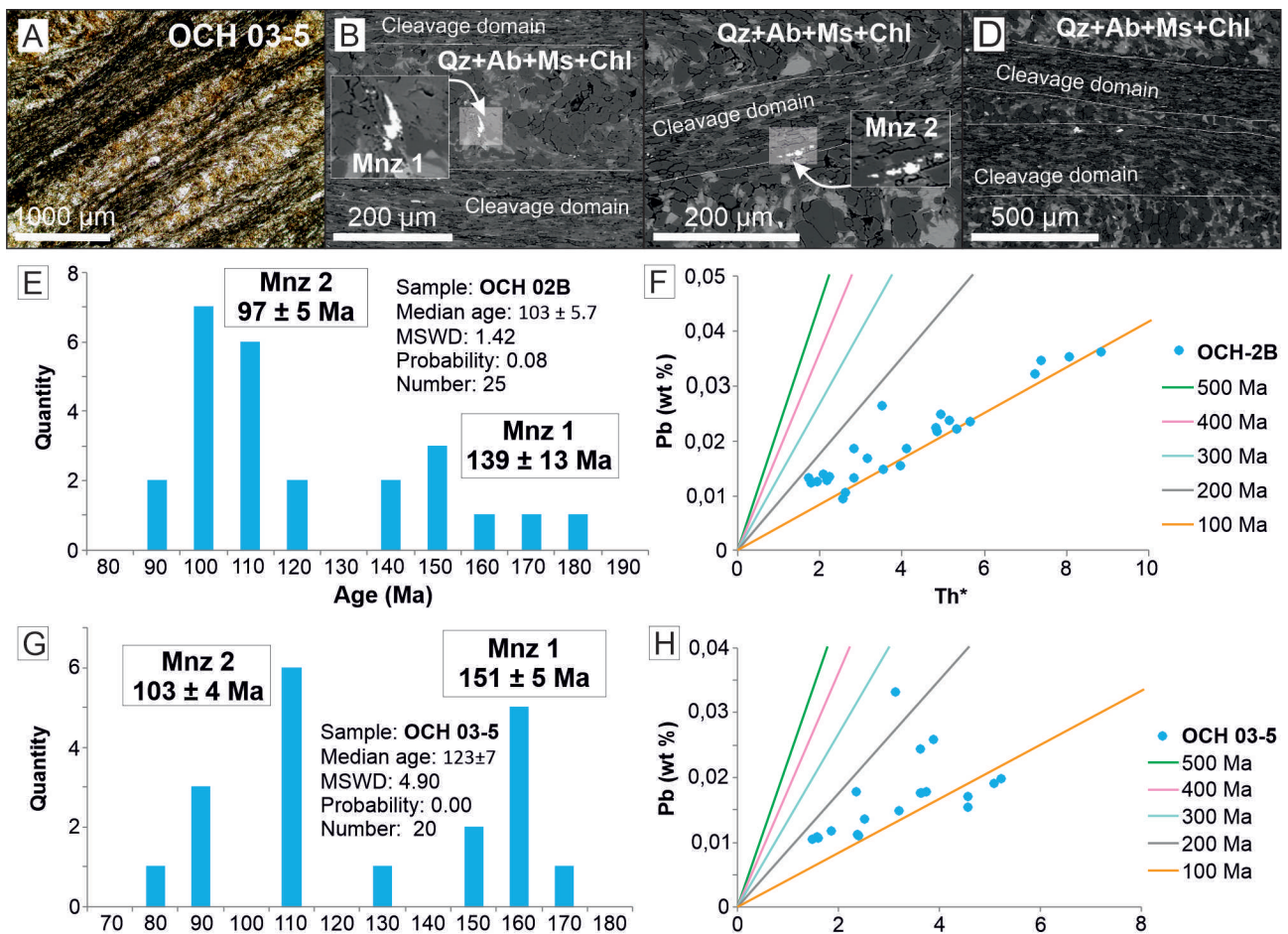


Fig. 12. Results of chemical (EMPA) U-Th-Pb dating of monazites from sericite-chlorite phyllite of the Bôrka Nappe – Hrádok locality (samples OCH 02B and OCH 03): A – photomicrograph of compositional layering of phyllite; B – BSE image of older monazite Mnz1; C and D – BSE images of elongated monazite grains Mnz2 occurring within the cleavage domain; E – histogram with resultant 2 monazites ages groups from the OCH 02B sample (adapted from Plašienka et al., 2019); F – Pb vs. Th* (wt %) monazite age isochron diagram of the OCH 02B sample ($Th^* = Th + 3.15$ wt %). G – histogram with resultant 2 monazites ages groups from the OCH 03 sample; H – Pb vs. Th* (wt %) monazite age isochron diagram of the OCH 03 sample ($Th^* = Th + 3.15$ wt %).

Due to a low content of radiogenic elements in monazites from the Bôrka Nappe, the gathered age data display a comparatively large scatter. Nevertheless, the textural relationships of the monazite growth to microstructures the host phyllites suggest some significant conclusions. Two monazite generations from the Hrádok samples clearly show their different relations to the microstructures – older Mnz1 is preserved in the equigranular and coarser-grained microlithons with indistinct foliation forming cores of isoclinal microfolds, where it grew together with other peak metamorphic minerals. On the other hand, younger Mnz2 are restricted to the fine-grained, pervasively foliated lithons that formed by strong compression and reduction of microfold limbs (Fig. 12). Therefore, the obtained age data are interpreted as directly dating distinct tectonic events – the Group 2 monazite ages 150–140 Ma likely indicate the first phases of exhumation of the Bôrka

rocks from the subduction channel and their subsequent thrusting over the Gemic units. The Group 3 monazites Mnz2 that yielded ages around 100–90 Ma provide dating of a compressional event connected with commencement of the sinistral transpressional activity within VGCZ along the Lubeník and Hrádok fault zones (e.g. Lexa et al., 2003; Novotná et al., 2015).

Monazites from the Honce locality show a very different depiction. Allocation into two age groups is less pronounced, almost indistinct. Monazites form large, oscillatory zoned idiomorphic crystals overgrowing the pre-existing planar fabric with numerous inclusions of older mineral phases. These features would indicate a long-termed monazite growth, possibly over tens of Myr, in the “post-tectonic”, kinematically stable conditions. However, decreasing Th content in zoned crystals and some retrograde recrystallization (pseudomorphs of

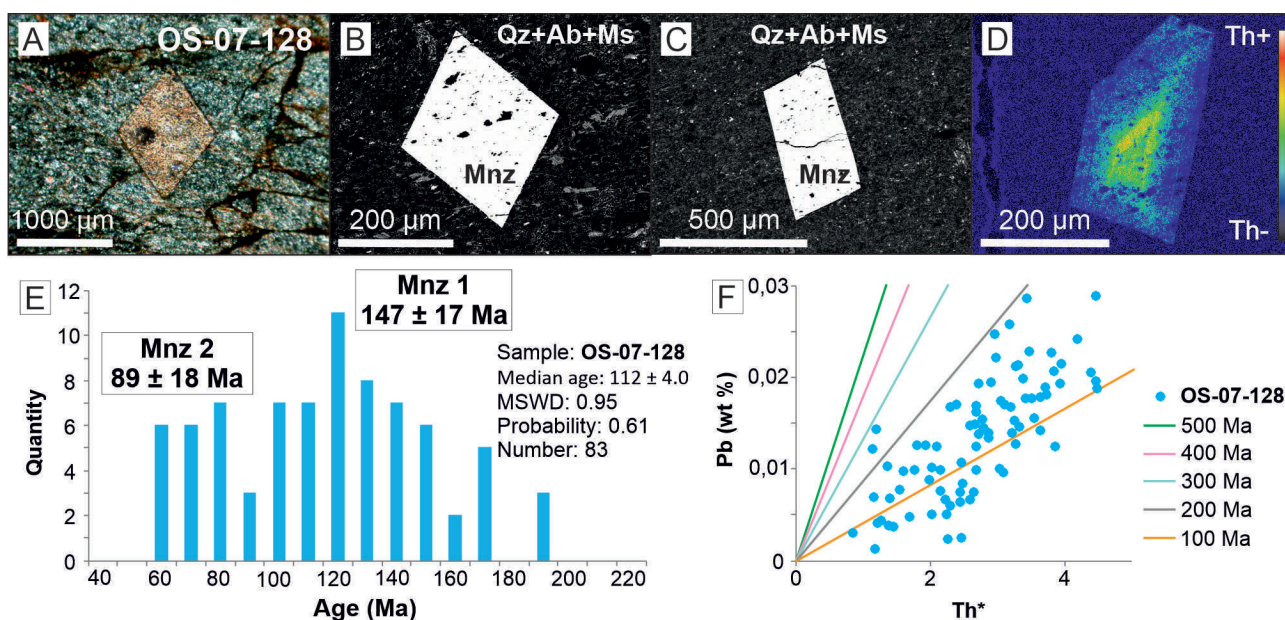


Fig. 13. Results of chemical (EMPA) U-Th-Pb dating of monazites from sericite-chlorite phyllite of the Bôrka Nappe – Honce locality (OS-17-128): A – photomicrograph of a big monazite porphyroblast; B and C – electron backscattered (BSE) images of idiomorphic monazites in very fine-grained matrix; D – X-ray compositional map of thorium content in monazite; E – histogram with resultant 2 monazites ages groups (adapted from Plašienka et al., 2019); F – Pb vs. Th* (wt %) age monazite isochron diagram ($Th^* = Th + 3.15 \text{ wt } \%$).

chlorite after glaucophane, see Fig. 8B in Plašienka et al., 2018) might indicate decreasing P-T metamorphic conditions from the blueschist to the greenschist facies.

Structure and tectonic evolution of the area

The age constraints for the Alpine tectonic evolution of broader surroundings of the VGCZ were reviewed by Plašienka (2018 and references therein). Our new results help to refine the tectonic scenario proposed there as follows:

The oldest tectonic event that resulted from the closure of the Meliata Ocean was the exhumation of the blueschist-facies Meliatic complexes (Bôrka Nappe) that postdated the peak high-pressure metamorphism (160–150 Ma) and occurred during the latest Jurassic, most probably in the 150–145 Ma time span. Subsequently, the Bôrka rocks were welded with the anchimetamorphic Meliatic ophiolitic mélanges and wildflysch sediments, as well as with the overriding Turnaic units derived from the southern Meliata margin. This united accretionary complex was then thrust over the Gemic – former northern passive margin of the Meliata Ocean at around 145–140 Ma (Fig. 14).

Progressing contraction of the collisional zone brought about shortening of the Gemic and overlying units with development of the Gemic cleavage fan (140–135 Ma), and their ensuing thrusting over the Veporic basement-cover substratum (135–125 Ma). This latter event is partly registered also by the oldest exhumation-related low-

temperature thermochronological data from the Bôrka Nappe (130–120 Ma; Putiš et al., 2014).

The time interval 125–100 Ma is poorly constrained, but data from the deeply buried Veporic basement complexes indicate attainment of the peak metamorphic conditions in the lower amphibolite facies associated with development of the main metamorphic schistosity in the Veporic rocks.

After 100 Ma, heterogeneous exhumation of the Veporic metamorphic dome commenced, as revealed by large-scale upright folding and some cooling-related geochronological data. It was initiated by positive inversion of the northern Veporic margin of the Fatric Zliechov basin and start of underthrusting of the Fatric basement substratum below the Veporic thrust wedge.

During the stage 90–70 Ma, the map-scale pattern of the principal fault-shear zones in the investigated area originated (Fig. 14). It was also the main phase of exhumation of the southern Veporic metamorphic dome. Cooling below ca 300 °C has been documented by various low-temperature geochronological methods – Rb/Sr and $^{40}\text{Ar}/^{39}\text{Ar}$ on muscovite and biotite, zircon fission-tracks (see reviews by Putiš et al., 2009; Vojtko et al., 2016; Plašienka, 2018). As revealed by structural data, exhumation was achieved by orogen-parallel extensional unroofing (Plašienka, 1993; Hók et al., 1993; Madarás et al., 1996; Janák et al., 2001; Jeřábek et al., 2007, 2012; Németh et al., 2012; Bukovská et al., 2013). The kinematic pattern of map-scale fault and fold structures was controlled by

the general N–S compression. Former Lower Cretaceous thrust faults like the Lubeník and Hrádok faults were reactivated as SW–NE to WSW–ENE trending, transpressional oblique-slip sinistral shear zones affecting several kilometres wide VGCZ that continues eastward into the so-called Trans-Gemic shear zone (TGSZ; e.g. Lexa et al., 2003; Németh et al., 2012; Fig. 14). The VGCZ–TGSZ was kinematically linked with the N–S to NNW–SSE striking segment of the former Lubeník thrust fault, which was reactivated as an east-dipping, low-angle normal fault system (lanf in Fig. 14). These extensional detachment faults are accompanied by wide mylonitic zones, especially along the Veporic basement/cover contact (see above), and were the principal structures that facilitated exhumation of the Veporic metamorphic dome by an eastward unroofing of the Gemic and overlying units. The NNW–SSE trending Nižná Slaná depression with preserved erosional remnants of the Meliatic and Silicic nappe outliers represents a kind

of a roll-over synform developed at the trailing edge of listric E-dipping detachment fault system (ros in Fig. 14). Low-angle normal faulting led also to a large omission of the hanging-wall units just at the Veporic–Gemic boundary, like for instance at Dúbrava Hill between Rochovce and Markuška villages (Fig. 2). In the central parts of the Veporic dome, slices of Gemic rocks (Ochtiná Group) overlying Veporic Foederata cover thus represent typical extensional allochthons (Plašienka & Soták, 2001). The Rochovce granite intrusion, dated to 80–75 Ma (Hraško et al., 1999; Poller et al., 2001; Kohút et al., 2013; ri in Fig. 14) occurs just at the turning point of the VGCZ from the WSW–ENE to the NNW–SSE strike. It is inferred that it was the place where tensile stresses were concentrated and facilitated the granite intrusion into comparatively shallow depths.

The succeeding latest Cretaceous–Paleogene tectonic development of the area was connected with the final

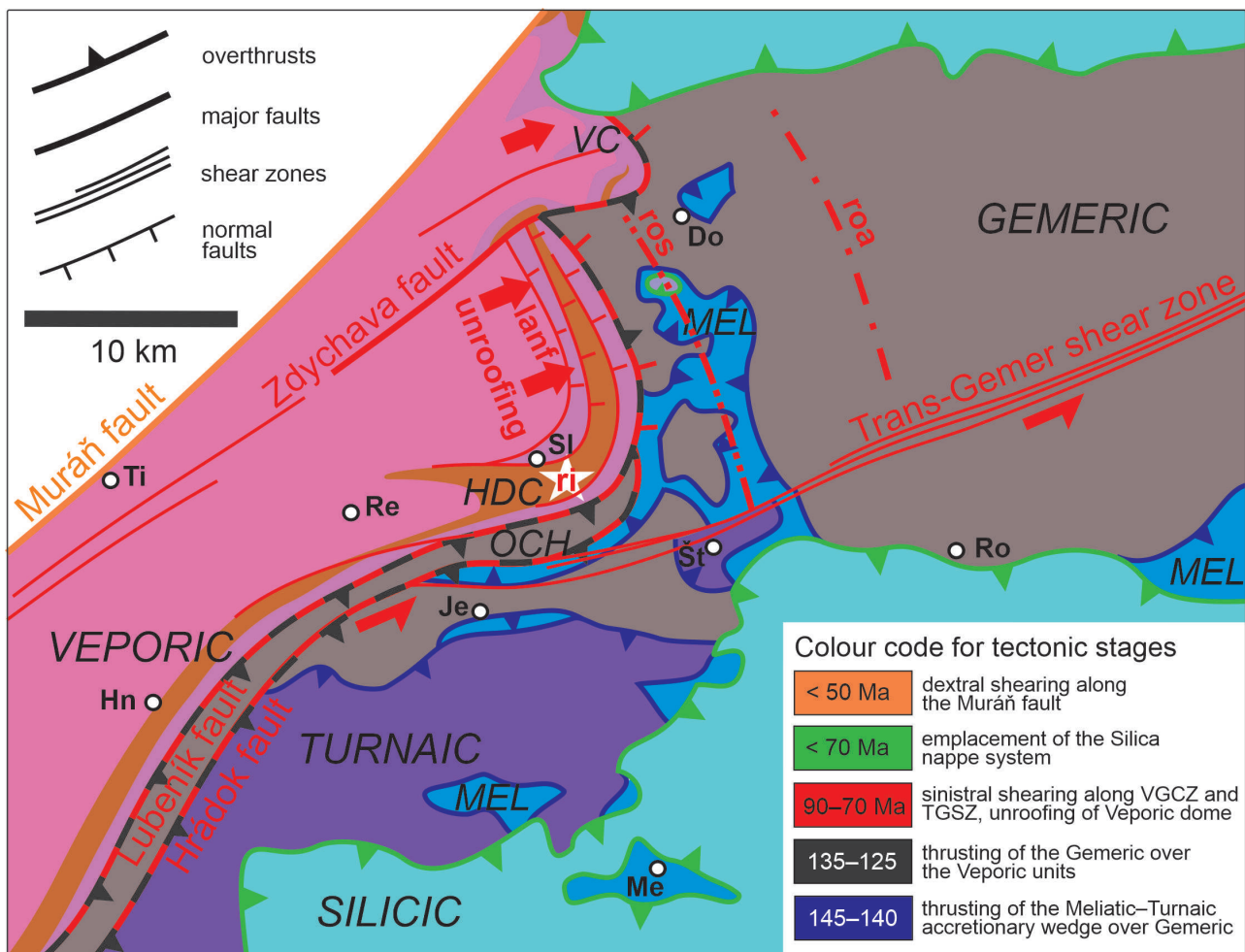


Fig. 14. Kinematic framework of the Veporic–Gemic thrust system. See text for explanations. Abbreviations: HDC – Hladomorná dolina Complex; VC – Veporic cover complexes (Revúca Group and Foederata Unit, including Markuška Nappe); OCH – Ochtiná Unit; lanf – low-angle normal faults; ros – roll-over synform; roa – roll-over anticline; ri – Rochovce granite intrusion. Towns/villages: Ti – Tisovec; Hn – Hnúšťa; Re – Revúca; Je – Jelšava; Sl – Slavošovce; Št – Štítnik; Do – Dobšiná; Ro – Rožňava; Me – Meliata.

exhumation and overall cooling recorded by very low-grade thermochronological data, like the apatite fission-track and (U-Th)/He dating methods (Putiš et al., 2014; Vojtko et al., 2016). However, this seemingly quiet period was interrupted by emplacement of the Silicic cover nappe system that overlapped the underlying structures with a pronounced metamorphic and structural discordance. Still younger are some important brittle strike-slip faults like the Muráň fault (e.g. Marko, 1993; Pelech & Kronome, 2019; Fig. 14).

Although our EMPA monazite age data seldom show narrow age ranges, they at least partly fit the scenario outlined above. The Variscan monazite age data around 360–355 Ma from granitoids and their contacts generally correspond to the known monazite ages from the Veporic granitoids (e.g. Finger et al., 2003; Hraško, 2005). The Alpine monazites from mylonitic granitoids (ca 110 Ma) are by some 20 Ma older than the suggested age of the corresponding mylonitic zones. We presume that these monazites might have formed during the peak Alpine metamorphic conditions (stage 3 of the scenario) and occur as relics in the mylonitic matrix, together with the Variscan monazites.

Older monazites (Group 2, 150–140 Ma) from the Bôrka Nappe suit with the scenario stages 1 to 2. However, interpretation of younger monazites makes some problems. In samples from the Hrádok locality, Mnz2 generation is clearly confined to the superimposed cleavage domains. Their age range 100–90 Ma would fit with the stage 4, i.e. with a compressional event producing tight upright folds with penetrative axial-plane crenulation cleavage (e.g. Jeřábek et al., 2012). Deformation concentrated in comparatively weak rocks, like mica schists within the Zdychava shear zone, black shales of the Ochtiná Group, and Bôrka phyllites. Afterwards (stage 5), these weak zones were transformed to the sinistral transpressional belts, typically along the VGCZ and TGSZ. However, another Bôrka locality at Honce village occurs out of VGCZ–TGSZ shear zone and is characterized by large zoned porphyroblasts that overgrow the matrix foliation. Hence, they likely grew in a low-strain domain during longer time in a kinematically little disturbed setting and reflect slow exhumation from the blueschist to the greenschist conditions. However, it is a preliminary conclusion and this issue would need further detailed investigations.

Conclusions

The investigated area represents a typical polymetamorphic and polydeformed region that embraces several superposed and/or juxtaposed major tectonic units. We have attempted at deciphering the structural-metamorphic history of rock complexes included by the field-based structural analysis and mapping, and petrographic-minera-

logical analyses of a number of samples collected from all units present in the area.

Three principal tectono-metamorphic events can be discerned based on our petrologic and structural investigations and monazite age data: (1) the oldest monazite ages (Group 1, ca 360–355 Ma) from the skarnoid body and from the mylonitized granites indicate the Variscan contact metamorphism resulting from intrusion of granitoids into the Lower Paleozoic metasedimentary protolith; (2) the monazites age Group 2 around 150–140 Ma from sericite-chlorite phyllites of the Bôrka Nappe likely indicates exhumation related to thrusting of the Meliatic accretionary wedge over the lower-plate Veporic and Gemeric units, following subduction of the Meliata Ocean; (3) the youngest monazite age Group 3 between 110 and 85 Ma detected in all analysed rock complexes records the Alpine overprint of the Veporic basement simultaneously with recrystallization of the Meliatic complexes during the main phase of the Western Carpathian nappe stacking and commencement of the extension-related exhumation of the Veporic metamorphic dome associated with transpressional shearing along the Veporic–Gemic contact zone.

In spite of a significant scatter, the gathered monazite EMPA age data together with petrological and microstructural observations generally correspond to various phases of tectonic evolution of the Veporic–Gemic contiguous zone, the investigated region of which represents one of the key areas.

Acknowledgements

Financial support from the Grant Agency for Science, Slovakia (project VEGA 1/0085/17) and from the Slovak Research and Development Agency (project APVV-17-0170) is gratefully appreciated. Authors wish to express their gratitude to reviewers Ľubomír Gazdačko (Košice) and Ján Madarás (Bratislava) for their constructive comments.

References

- ABONYI, A., 1971: The stratigraphical-tectonical evolution of the Gemeric Carboniferous. *Geol. Práce, Spr.*, 57, 339–348 (in Slovak with English summary).
- ANDRUSOV, D., 1968: Grundriss der Tektonik der nördlichen Karpaten. *Bratislava, Ver. Slov. Akad. Wiss.*, 188 p.
- ÁRKAI, P., FARYAD, S.W., VIDAL, O. & BALOGH, K., 2003: Very low-grade metamorphism of sedimentary rocks of the Meliata unit, Western Carpathians, Slovakia: implications of phyllosilicate characteristics. *Int. J. Earth Sci.*, 92, 68–85.
- BAJANÍK, Š. (ED.), IVANIČKA, J., MELLO, J., REICHWALDER, P., PRISTAŠ, J., SNOPKO, L., VOZÁR, J. & VOZÁROVÁ, A., 1984: Geological map of the Slovenské rudohorie Mountains – eastern part 1 : 50,000. *Bratislava, D. Štúr. Inst. Geol.*

- BIELY, A. & FUSÁN, O., 1967: Zum Problem der Wurzelzonen der subtatrischen Decken. *Geol. Práce, Zpr.*, 42, 51–64.
- BUKOVSKÁ, Z., JEŘÁBEK, P., LEXA, O., KONOPÁSEK, J., JANÁK, M. & KOŠLER, J., 2013: Kinematically unrelated C-S fabrics: an example of extensional shear band cleavage from the Veporic Unit (Western Carpathians). *Geol. Carpath.*, 64, 103–116.
- CARDOZO, N. & ALLMENDINGER, R.W., 2013: Spherical projections with OSXStereonet. *Comp. Geosci.*, 51, 193–205.
- DALLMEYER, R.D., NÉMETH, Z. & PUTIŠ, M., 2005: Regional tectonothermal events in Gemericum and adjacent units (Western Carpathians, Slovakia): Contribution by the $^{40}\text{Ar}/^{39}\text{Ar}$ dating. *Slovak Geol. Mag.*, 11, 2–3, 155–163.
- DALLMEYER, R.D., NEUBAUER, F. & FRITZ, H., 2008: The Meliata suture in the Carpathians: regional significance and implications for the evolution of high-pressure wedges within collisional orogens. In: Siegesmund, S., Fügenschuh, B. & Froitzheim, N. (eds): Tectonic aspects of the Alpine–Dinaride–Carpathian system. *Geol. Soc., London, Spec. Publ.*, 298, 101–115.
- FARYAD, S.W. & HENJES-KUNST, F., 1997: Petrological and K-Ar and ^{40}Ar - ^{39}Ar age constraints for the tectonothermal evolution of the high-pressure Meliata unit, Western Carpathians (Slovakia). *Tectonophysics*, 280, 141–156.
- FARYAD, S.W. & HOINKES, G., 1999: Two contrasting mineral assemblages in the Meliata blueschists, Western Carpathians, Slovakia. *Min. Mag.*, 63, 489–501.
- FARYAD, S.W., SPIŠIAK, P., HORVÁTH, P., HOVORKA, D., DIANIŠKA, I. & JÓZSA, S., 2005: Petrological and geochemical features of the Meliata mafic rocks from the sutured Triassic oceanic basin, Western Carpathians. *Ofoliti*, 30, 1, 27–35.
- FINGER, F., BROSKA, I., HAUNSCHMID, B., HRAŠKO, E., KOHÚT, M., KRENN, E., PETRÍK, I., RIEGEL, G. & UHER, P., 2003: Electron-microprobe dating of monazites from Western Carpathian basement granitoids: plutonic evidence for an important Permian rifting event subsequent to Variscan crustal anatexis. *Int. J. Earth Sci.*, 92, 86–98.
- GAZDAČKO, E., 1995: Lithological content and relation of the Bôrka nappe to ultrabasics in the surrounding of Markuška and Kobeliarovo villages. *Miner. Slov.*, 37, 214–216 (in Slovak with English abstract).
- GRECULA, P. (ed.), KOBULSKÝ, J., GAZDAČKO, E., NÉMETH, Z., HRAŠKO, E., NOVOTNÝ, L. & MAGLAY, J., 2009: Geological map of the Spiš-Gemer Ore Mts. 1 : 50,000. *Bratislava, St. Geol. Inst. D. Štúr*.
- HÓK, J., KOVÁČ, P. & MADARÁS, J., 1993: Extensional tectonic of the western part of the contact area between Veporicum and Gemericum, Western Carpathians. *Miner. Slov.*, 25, 172–176 (in Slovak with English summary).
- HRAŠKO, E., 2005: Geological, age and lithological characteristics of the Lower Carboniferous granitoids in the Kohút zone of the Veporic. *Miner. Slov.*, 37, 217–219 (in Slovak with English summary).
- HRAŠKO, E., HATÁR, J., HUHMA, H., MÄNTÄRI, I., MICHALCO, J. & VAASJOKI, M., 1999: U/Pb zircon dating of the Upper Cretaceous granite (Rochovce type) in the Western Carpathians. *Krystalinikum*, 25, 163–171.
- JANÁK, M., PLAŠIENKA, D., FREY, M., COSCA, M., SCHMIDT, S.Th., LUPTÁK, B. & MÉRES, Š., 2001: Cretaceous evolution of a metamorphic core complex, the Veporic unit, Western Carpathians (Slovakia): P-T conditions and in situ $^{40}\text{Ar}/^{39}\text{Ar}$ UV laser probe dating of metapelites. *J. Metamorphic Geol.*, 19, 197–216.
- JEŘÁBEK, P., STÜNITZ, H., HEILBRONNER, R., LEXA, O. & SCHULMANN, K., 2007: Microstructural-deformation record of an orogen-parallel extension in the Vepor Unit, West Carpathians. *J. Struct. Geol.*, 29, 1722–1743.
- JEŘÁBEK, P., LEXA, O., SCHULMANN, K. & PLAŠIENKA, D., 2012: Inverse ductile thinning via lower crustal flow and fold-induced doming in the West Carpathian Eo-Alpine collisional wedge. *Tectonics*, 31, TC5002.
- KLINEC, A., 1966: Zum Bau und Bildung des Veporiden-Kristallin. *Sbor. geol. Vied. Západ. Karpaty*, 6, 7–28 (in Slovak with German summary).
- KLINEC, A., 1971: The main tectonic elements in the eastern Veporides. *Geol. Práce, Spr.*, 57, 105–109 (in Slovak with English summary).
- KLINEC, A., 1976: Geological map of the Slovenské rudohorie and the Nízke Tatry Mts. 1 : 50,000. *Bratislava, D. Štúr Inst. Geol.*
- KLINEC, A., 1980: Contiguous zone of Gemerides and Veporides enlightened by well near Rochovce. *Geol. zbor. Geol. Carpath.*, 31, 537–540.
- KOHÚT, M., STEIN, H., UHER, P., ZIMMERMAN, A. & HRAŠKO, E., 2013: Re-Os and U-Th-Pb dating of the Rochovce granite and its mineralization (Western Carpathians, Slovakia). *Geol. Carpath.*, 64, 71–79.
- KONEČNÝ, P., SIMAN, P., HOLICKÝ, I., JANÁK, M., & KOLLÁROVÁ V., 2004: Methodics of monazite dating using an electron microprobe. *Miner. Slov.*, 36, 225–235 (in Slovak with English summary).
- KORIKOVSKY, S.P., JANÁK, M. & BORONICHIN, V.A., 1986: Geothermometry and mineral equilibria during recrystallization of garnet mica schists and cordierite-bearing hornfelses in the Rochovce granite aureole (Slovak Ore Mts., Rochovce-Chyžné district). *Geol. Zbor. Geol. Carpath.*, 37, 607–633 (in Russian with English abstract).
- KOZUR, H. & MOCK, R., 1997: New paleogeographic and tectonic interpretations in the Slovakian Carpathians and their implications for correlations with the Eastern Alps and other parts of the Western Tethys. Part II: Inner Western Carpathians. *Miner. Slov.*, 29, 164–209.
- KOZUR, H., MOCK, R. & MOSTLER, H., 1976: Stratigraphische Neueinstufung der Karbonatgesteine der unteren Schichtenfolge von Ochtiná (Slowakei) in das oberste Visé und Serpukhovian (Namur A). *Geol. Paläont. Mitt.*, 6, 1–29.
- LAČNÝ, A., PLAŠIENKA, D. & VOJTKO, R., 2016: Structural evolution of the Turňa Unit constrained by fold and cleavage analyses and its consequences for the regional tectonic models of the Western Carpathians. *Geol. Carpath.*, 67, 177–193.
- LEŠKO, B. & VARGA, I., 1980: Alpine elements in the West Carpathian structure and their significance. *Miner. Slov.*, 12, 97–130.
- LEXA, O., SCHULMANN, K. & JEŽEK, J., 2003: Cretaceous collision and indentation in the West Carpathians: View based on structural analysis and numerical modeling. *Tectonics*, 22, 6, 1066.

- MADARÁS, J., HÓK, J., SIMAN, P., BEZÁK, V., LEDRU, P. & LEXA, O., 1996: Extension tectonics and exhumation of crystalline basement of the Veporicum unit (Central Western Carpathians). *Slovak Geol. Mag.*, 3–4/96, 179–183.
- MALUSKI, H., RAJLICH, P. & MATTE, P., 1993: ^{40}Ar - ^{39}Ar dating of the Inner Carpathian Variscan Basement and Alpine mylonitic overprinting. *Tectonophysics*, 223, 313–337.
- MARKO, F., 1993: Kinematics of Muráň fault between Hrabušice and Tuhár village. In: Rakús, M. & Vozár, J. (eds): Geodynamic model and deep structure of the Western Carpathians. *Conf., Symp., Sem., Bratislava, D. Štúr Inst. Geol.*, 253–261.
- MELLO, J., REICHWALDER, P. & VOZÁROVÁ, A., 1998: Bôrka nappe: high-pressure relic from the subduction-accretion prism of the Meliata ocean (Inner Western Carpathians, Slovakia). *Slovak Geol. Mag.*, 4, 261–273.
- MOCK, R., SÝKORA, M., AUBRECHT, R., OŽVOLDOVÁ, L., KRONOME, B., REICHWALDER, P. & JABLONSKÝ, J., 1998: Petrology and stratigraphy of the Meliaticum near the Meliata and Jaklovce Villages, Slovakia. *Slovak Geol. Mag.*, 4, 223–260.
- MONTEL, J.M., FORET, S., VESCHAMBRE, M., NICOLLET, C. & PROVOST, A., 1996: Electron microprobe dating of monazite. *Chem. Geol.*, 131, 37–53.
- NEMEC, O., PUTIŠ, M., BAČÍK, P., RUŽIČKA, P. & NÉMETH, Z., 2020: Metamorphic conditions of Neotethyan Meliatic accretionary wedge estimated by thermodynamic modelling and geothermobarometry (Inner Western Carpathians, Slovakia). *Minerals*, 10, 1094.
- NÉMETH, Z., 1994: Alpine tectonics in the Nižná Slaná Depression (contact zone between Gemericum and Veporicum, Western Carpathians). *Miner. Slov.*, 26, 399–410 (in Slovak with English summary).
- NÉMETH, Z., RADVANEC, M., GAZDAČKO, Ľ. & KOBULSKÝ, J., 2012: Variscan tectonic setting vs. Alpine overprint in Gemericum (Inner Western Carpathians): Their role in the recent distribution of tectonic units in the eastern part of the territory as expressed in significant localities. *Miner. Slov., Geovest.*, 44, 1, 8–15.
- NOVOTNÁ, N., JEŘÁBEK, P., PITRA, P., LEXA, O. & RACEK, M., 2015: Repeated slip along a major decoupling horizon between crustal-scale nappes of the Central Western Carpathians documented in the Ochtiná tectonic mélange. *Tectonophysics*, 646, 50–64.
- PELECH, O. & KRONOME, B., 2019: Structural analysis in the wider zone of Muráň fault between Šumiac and Tisovec. *Geol. Práce, Spr.*, 134, 33–48 (in Slovak with English summary).
- PLAŠIENKA, D., 1980: Nappe position of the Hladomorná dolina group on the Foederata group in the Dobšiná half-window. *Geol. Zbor. Geol. Carpath.*, 31, 609–617.
- PLAŠIENKA, D., 1984: Represents the Markuška nappe an interconnecting element between the Veporic and Gemeric units? *Miner. Slov.*, 16, 187–193 (in Slovak with English summary).
- PLAŠIENKA, D., 1993: Structural pattern and partitioning of deformation in the Veporic Foederata cover unit (Central Western Carpathians). In: Rakús, M. & Vozár, J. (eds): Geodynamic model and deep structure of the Western Carpathians. *Conf., Symp., Sem. Bratislava, D. Štúr Inst. Geol.*, 269–277.
- PLAŠIENKA, D., 2003: Development of basement-involved fold and thrust structures exemplified by the Tatric-Fatric-Veporic nappe system of the Western Carpathians. *Geodinam. Acta*, 16, 21–38.
- PLAŠIENKA, D., 2018: Continuity and Episodicity in the Early Alpine Tectonic Evolution of the Western Carpathians: How Large-Scale Processes Are Expressed by the Orogenic Architecture and Rock Record Data. *Tectonics*, 37, 3, 2029–3079.
- PLAŠIENKA, D. & SOTÁK, J., 2001: Stratigraphic and tectonic position of Carboniferous sediments in the Furmanec Valley (Muráň Plateau, Central Western Carpathians). *Miner. Slov.*, 33, 29–44 (in Slovak with English summary).
- PLAŠIENKA, D., GRECUŁA, P., PUTIŠ, M., KOVÁČ, M. & HOVORKA, D., 1997: Evolution and structure of the Western Carpathians: an overview. In: Grecula, P., Hovorka, D. & Putiš, M. (eds): Geological evolution of the Western Carpathians. *Miner. Slov., Monogr.*, 1–24i.
- PLAŠIENKA, D., MÉRES, Š., IVAN, P., SÝKORA, M., SOTÁK, J., LAČNÝ, A., AUBRECHT, R., BELLOVÁ, S. & POTOČNÝ, T., 2019: Meliatic blueschists and their detritus in Cretaceous sediments: New data constraining tectonic evolution of the West Carpathians. *Swiss J. Geosci.*, 112, 55–81.
- PLAŠIENKA, D., BUČOVÁ, J. & ŠIMONOVÁ, V., 2020: Variable structural styles and tectonic evolution of an ancient backstop boundary – the Pieniny Klippen Belt of the Western Carpathians. *Int. J. Earth Sci.*, 109, 4, 1355–1376.
- PROKEŠOVÁ, R., PLAŠIENKA, D. & MILOVSKÝ, R., 2012: Structural pattern and emplacement mechanisms of the Krížna cover nappe (Western Carpathians, Slovakia). *Geol. Carpath.*, 63, 13–32.
- POLLER, U., UHER, P., JANÁK, M., PLAŠIENKA, D. & KOHÚT, M., 2001: Late Cretaceous age of the Rochovce granite, Western Carpathians, constrained by U-Pb single-zircon dating in combination with cathodoluminescence imaging. *Geol. Carpath.*, 52, 41–47.
- PUTIŠ, M., FRANK, W., PLAŠIENKA, D., SIMAN, P., SULÁK, M. & BIRÓN, A., 2009: Progradation of the Alpidic Central Western Carpathians orogenic wedge related to two subductions: constrained by $^{40}\text{Ar}/^{39}\text{Ar}$ ages of white micas. *Geodinam. Acta*, 22, 1–3, 31–56.
- PUTIŠ, M., DANIŠÍK, M., RUŽIČKA, P. & SCHMIEDT, I., 2014: Constraining exhumation pathway in accretionary wedge by (U-Th)/He thermochronology – Case study on Meliatic nappes in the Western Carpathians. *J. Geodynam.*, 81, 80–90.
- PUTIŠ, M., SOTÁK, J., QIU-LI, L., ONDREJKA, M., XIAN-HUA, L., ZHAOCHU, H., XIAOXIAO, L., NEMEC, O., NÉMETH, Z. & RUŽIČKA, P., 2019: Origin and age determination of the Neotethys Meliata basin ophiolite fragments in the Late Jurassic – Early Cretaceous accretionary wedge mélange (Inner Western Carpathians, Slovakia). *Minerals*, 9, 652.
- REICHWALDER, P., 1982: Structural characteristic of root zones of some nappes in innermost parts of West Carpathians. In: Maheľ, M. (ed.): Alpine structural elements: Carpathian-Balkan-Caucasus-Pamir orogene zone. *Bratislava, Veda*, 43–56.
- RUŽIČKA, P., BAČÍK, P. & KURYLO, S., 2019: Mineralogical characteristics of marbles associated with basalt metapyroclastics and chlorite schists from the locality Markuška (Slovak

- Republic). *Bull. Mineral. Petrol.*, 27, 2, 247–258 (in Slovak with English abstract).
- SULOVSÝ, P., ČOPIJKOVÁ, R. & ŠKODA, R., 2004: Possibility and constraints of CHIME dating method. *Zpr. geol. Výzk. v r. 2003 (Geosci. Res. Reports in 2003, Czech Geol. Survey)*, 37, 122–125 (in Czech with English abstract).
- VOJTKO, R., KRÁLIKOVÁ, S., JEŘÁBEK, P., SCHUSTER, R., DANIŠÍK, M., FÜGENSCHUH, B., MINÁR, J. & MADARÁS, J., 2016: Geochronological evidence for the Alpine tectono-thermal evolution of the Veporic Unit (Western Carpathians, Slovakia). *Tectonophysics*, 666, 48–65.
- VOZÁROVÁ, A., 1990: Development of metamorphism in the Gemer/Veporic contact zone (Western Carpathians). *Geol. Zbor. Geol. Carpath.*, 41, 475–502.
- VOZÁROVÁ, A., 1996: Tectono-sedimentary evolution of late Paleozoic basins based on interpretation of lithostratigraphic data (Western Carpathians, Slovakia). *Slovak Geol. Mag.*, 3–4/96, 251–271.
- VOZÁROVÁ, A. & KRISTÍN, J., 1985: Changes in chemical composition of garnets and biotites from contact aureole of Alpine granitoides in southern part of Veporicum. *Západ. Karpaty, Sér. Mineral. Petrogr. Geochém. Metalogen.*, 10, 199–221 (in Slovak with English summary).
- VOZÁROVÁ, A. & VOZÁR, J., 1982: New lithostratigraphical division of the basal part of the cover of Southern Veporicum. *Slovak Geol. Mag.*, 3–4/96, 251–271 (in Slovak with English summary).
- VOZÁROVÁ, A. & VOZÁR, J., 1988: Late Paleozoic in West Carpathians. *Bratislava, Geol. Inst. D. Štúr*, 314 p.
- VRÁNA, S., 1964: Petrogenese des Veporiden Kristallin in der Umgebung von Slavošovce. *Geol. Práce, Zpr.*, 33, 5–29 (in Czech with German summary).
- ZOUBEK, V., 1957: Grenze zwischen den Gemeriden und Veporiden. *Geol. Práce, Zoš.*, 46, 38–50 (in Czech with German summary).
- ZOUBEK, V. & SNOPKO, L., 1954: Zpráva o mapování styku veporid a gemerid mezi Slavošovci a Rejdovou (in Czech; Mapping report about the contact of the Veporides and Gemerides between Slavošovce and Rejdová villages). *Zpr. geol. Výzk. v r. 1954*, 211–213.

Geologická stavba a tektonometamorfny vývoj kontaktnej zóny veporika a gemerika dokumentovaný rádiometrickými vekmi monazitu (oblasť Slavošovce – Štítik, stredné Slovensko)

Skúmané územie sa nachádza pozdĺž stykovej zóny stredoslovenského veporika a priľahlého gemerika v miestach, kde sa lubenícko-hrádocká zlomová zóna prudko stáča zo smeru ZJZ – VSV do smeru SSZ – JJV (obr. 1). Tento systém zlomov, pôvodne spojený s násunom gemerika na veporikum, bol neskôr modifikovaný transpresnou a extenznou reaktiváciou. Výsledkom deformačných procesov v štruktúrne komplikovanej oblasti bola superpozícia niekoľkých jednotiek, ktoré vykazujú zložité tektonické a metamorfne vzťahy. Na relatívne malom území tu v tesnom kontakte vystupujú viaceré základné tektonické jednotky stavby Západných Karpát: v najnižšej štruktúrnej pozícii je veporický fundament a jeho mladopaleozoicko-triasový sedimentárny pokryv (revúcka skupina a föderatská jednotka), na veporikum je pozdĺž lubeníckej línie nasunutý gemerikum (ochtinská a volovská jednotka) a v jeho nadloží meliatikum (príkrov Bôrky), turnaikum a silicikum (obr. 2, 3).

Fundament veporika je pozdĺž stykovej zóny reprezentovaný súborom polymetamorfovaných sedimentov s ojedinelým výskytom bazických metavulkanitov (komplex Hladomornej doliny), do ktorých intrudovali variské granitoidy veporského plutónu (kráľovohorský komplex). Kontakt granitoidov a ich metamorfneho plášťa je sprevádzaný prejavmi kontaktnej metamorfózy v priľahlom komplexe Hladomornej doliny a metasomatózy (teleso skarnoidov pri Čiernej Lehote). Tento kontakt bol ale výrazne postihnutý aj naloženou alpínskou mylonitizáciou.

Sedimentárny obal veporického fundamentu reprezentujú klastické metasedimenty revúckej skupiny. Vrchnokarbonské slatvinské súvrstvie je zložené z oligomiktných konglomerátov, pieskocov a tmavých bridlic. Nadložné permské rimavské súvrstvie predstavuje súbor siliciklastických metasedimentov a acidných metavulkanoklastik. Pozdĺž lubeníckej línie je v priamom tektonickom kontakte s rimavským súvrstvom spodnokarbonska ochtinská jednotka gemerika. Reprezentuje ju súbor konglomerátov a pieskocov a rôzne typy fylitov v asociácii s bazickými horninami (hrádočeké súvrstvie) a karbonátmi s tmavými bridlicami (lubenícke súvrstvie). Nadložie ochtinskej skupiny tvorí volovská jednotka gemerika, ktorú zastupuje gelnická a gočaltovská skupina. Staropaleozoickú gelnickú skupinu predstavuje varisky nízko metamorfovaný vulkanosedimentárny komplex. Jej sedimentárny obal reprezentujú permské klastiká gočaltovskej skupiny. V oblasti kontaktu ochtinskej skupiny a volovskej jednotky sa pozdĺž hrádočekej zlomovej zóny vyskytujú tektonicky obmedzené šupiny meliatskeho príkrovu Bôrky (obr. 2, 3). Príkrov Bôrky zastupuje dúbavské súvrstvie. Je to komplex metamorfovaných karbonátov v asociácii s bazickými metavulkanoklastikami a jemnozrnnými metasedimentmi.

Územie má zložitú stavbu a ešte zložitejší tektonometamorfny vývoj, ktorý sme sa pokúsili interpretovať na základe podrobného štruktúrneho, petrologického a geochronologického výskumu. Mikroštruktúrne pozorovania a petrografické údaje z analyzovaných horninových

komplexov opísané v texte sú ilustrované na obr. 4 až 8. Vyplyva z nich polymetamorfný a polydeformačný charakter skúmaných jednotiek, ktorý je kombináciou viacerých fáz predalpínskeho (v prípade variského fundamentu) a alpínskeho tektonometamorfného vývoja.

Z vybraných vzoriek sa chemickou mikrosondovou datovacou metódou (EMPA) analyzovali monazity viacerých generácií. Získané vekové údaje možno rozdeliť na tri skupiny (obr. 9 až 13): 1. mylonitizované veporické granitoidy a skarnoidy poskytli okrem mladších alpínskych aj variské veky reliktných monazitov okolo 360 – 355 mil. r.; 2. len vo fylitoch príkrovu Bôrky boli identifikované veky medzi 150 a 140 mil. r. a interpretované ako etapa exhumácie a nasunutia meliatsko-turnaického akrečného komplexu na podložné gemerikum; 3. mladšie kriedové veky zhruba medzi 110 a 85 mil. r. sa zistili vo všetkých jednotkách, interpretujeme ich ako záznam počiatkov exhumácie veporického metamorfného dómu a strižných deformácií po jeho okrajoch.

Vývojový tektonický model (obr. 14) predpokladá, že exhumácia prebiehala na kinematicky spojenom systéme širokej sinistrálnej strižnej zóny pozdĺž lubenícko-hrádockej zlomovej zóny smeru ZJZ – VSV a nízkouhlových, na východ sklonených zlomov smeru SSZ – JJV na východnom okraji veporika pozdĺž tzv. gemerskej rampy. Nízkouhlové zlomy, sprevádzané širokými mylonitovými zónami hlav-

ne v granitoidoch veporického fundamentu bezprostredne pod sedimentárnym obalom, boli hlavnými štruktúrami, na ktorých prebehlo exhumačné odstrešenie vrchnokriedového veporického metamorfného dómu. Takzvaná vrása (resp. príkrov) Markušky predstavuje systém násunových šupín vrchných častí juhoveporického fundamentu (komplex Haldomornej doliny) a metasedimentov revúckej skupiny, šikmo narezaných eróziou v dôsledku osového ponoru veporika pod gemerikum. Nižnoslanská depresia s troskami príkrovu Bôrky a silického príkrovu (Radzim) je interpretovaná ako synforma v apikálnej časti nízkouhlového zlomového systému so značnou extenznou redukciou komplexov podložného gemerického fundamentu. Predpokladáme, že vrchnokriedová intrúzia rochovského granitu využila oslabenú zónu s koncentráciou tenzných napätí na ohybe lubenícko-hrádockých zlomov na prienik do relatívne plytkých úrovní stavby stykovej zóny. Veporické komplexy tak počas vrchnokriedového vývoja reprezentovali spodnú platňu a komplexy gemerika a nadložných jednotiek vrchnú platňu extenzného tektonického systému.

Doručené / Received: 4. 11. 2020

Prijaté na publikovanie / Accepted: 18. 2. 2021

Successive formation of Fe and Mn skarns in the Čučma locality (Gemic unit, W. Carpathians): from metasomatic stage through the amphibolite facies overprint with Ti-rich tephroite to retrograde stilpnomelane-chlorite zone

MARTIN RADVANEC and STANISLAV GONDA

State Geological Institute of Dionýz Štúr, Mlynská dolina 1, SK-817 04 Bratislava, Slovakia

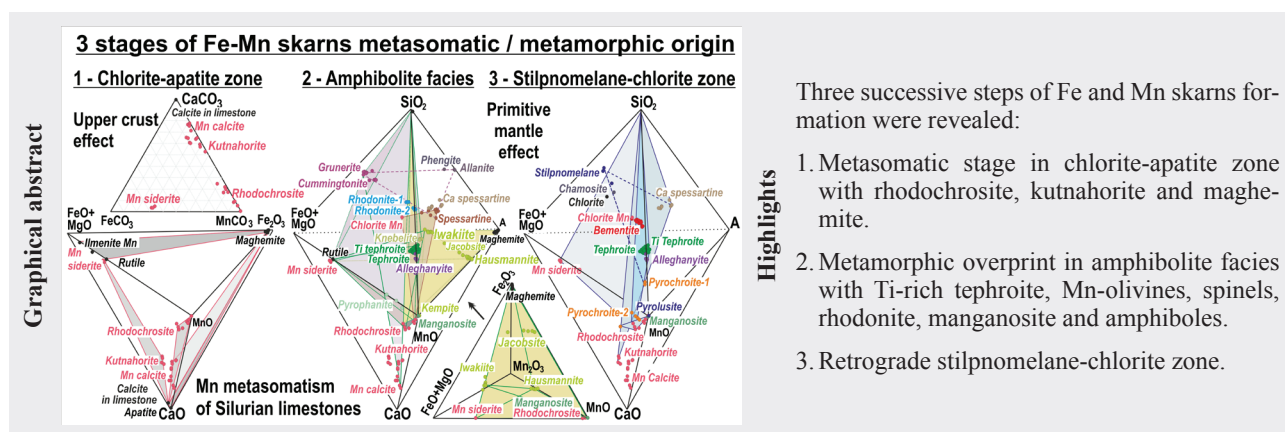
Abstract: Two lenticular ore bodies of Mn bearing skarn, closing a segment of Fe skarn, are located at the northern side of the Čučma village, about 6 km north-east of Rožňava town in the Gemic unit of the Internal (Inner) Western Carpathians. The Fe and Mn skarns formed during three metamorphic stages. The first stage gradually replaced the former Silurian limestones lenses into of Mn-rich calcite, kutnahorite (kutnohorite – IMA), rhodochrosite, Mn-rich siderite, fluorapatite, tourmaline, phengitic muscovite, Mn-rich chlorite. Rare pyrite, molybdenite, galena, chalcopyrite, pyrite, sphalerite and Ag-rich tetrahedrite occur there as well. Near the contact of former limestone with metapelite, the maghemite dominates over assemblage of Mn-rich carbonates to form Fe skarn. The replacement of limestones as well as the Fe skarn metasomatic origin took place in the chlorite-apatite zone at a temperature range 520–540 °C, where the maghemite and Mn-rich carbonates were generated by the fluid phase, released during anatectic melting of the upper crust during the older Permian metamorphic-magmatic-hydrothermal cycle (MMH of 281–273 Ma).

In the second prograde metamorphic stage, the first-stage minerals were continuously overheated in amphibolite facies (600–650 °C; ~ 4 Kbar), forming following minerals: spessartine, alleghanyite, pyrophanite, manganosite, kempite, jacobite, hausmannite, tephroite, Ti-rich tephroite, knebelite, rhodonite-1, rhodonite-2, cummingtonite, grunerite and allanite. This study brings an important finding of a new $Ti^{4+} = Si^{4+}$ substitution in the olivine group, where in the Ti-rich tephroite the Si content was replaced by Ti up to 0.159 apfu. Grains formation of Ti tephroite are controlled by the sector zoning, having different content of Ti in each sector.

In the final stage of skarns formation, the unstable minerals of previous two stages were replaced by the Si, Ba, H₂S and H₂O bearing fluid phase to form Ca-rich spessartine, bementite, pyrochroite, quartz, pyrolusite, baryte, chlorite and stilpnomelane during the retrograde stilpnomelane-chlorite zone metamorphism at 300–370 °C. This mineral assemblage was gradually formed in retrograde metamorphic path with decreasing temperature from the amphibolite facies to the stilpnomelane-chlorite zone. The prograde and retrograde metamorphic stages produced a group of Mn bearing garnets, humites, oxides, halides, spinels, olivines, pyroxenoides, amphiboles and they on the former Fe skarn formed a younger and fine to medium-grained Mn bearing part of the skarn. This metamorphic part of Mn skarn has the positive Eu anomaly and was formed by the fluid phase influenced by the primitive mantle in younger MMH cycle of the Permian, dated to 269–251 Ma.

In the paper, altogether 39 empiric reactions describe the successive formation of skarns. The source of Fe, Mn and Ba, necessary to skarns formation, was released to fluid phase by anatectic melting of the Silurian rhyolite and Devonian stratabound sulfidic mineralization in the Permian amphibolite facies metamorphism.

Key words: Fe skarn, Mn skarn, maghemite, rhodochrosite, manganosite, kempite, rhodonite, Mn-rich spinels, Ti-rich tephroite, Permian MMH cycle, Gemic unit



Introduction

Two lenticular ore bodies of Mn bearing skarn closing a segment of Fe skarn, known as the Black Mine (Feketebánya) or the Roszty Mine, are located at the northern side of the Čučma village on the western slope of the Stredná hill, about 6 km north-east of Rožňava town in the Gemeric unit (Fig. 1). The Gemeric unit is a part of the Internal (Inner) Western Carpathians. The Mn skarn was mined from the second half of the 19th century until the beginning of the 20th century. The subject of mining was mainly its part bearing pyrolusite (Bartalský et al., 1973; Grecula et al., 1995). The length of skarns bodies is 50 to 100 m, thickness 1–4 m, direction VSV and dip 50–60° to the south, having tectonic contact with the surrounding sericite-graphite phyllites (Bartalský et al., 1973; Grecula et al., 1995). The formation of Fe-Mn skarns is genetically dependent on occurrence of host limestones, being a host rock of Fe-Mn mineralization (Kantor, 1953; Grecula et al., 1995). In the Čučma area, altogether eight crystalline limestone lenses occur in sericite-graphite phyllites, graphite phyllites and lydite beds of Betliar Fm of Silurian age. The limestone lenses of EW direction and length up to 300 m are white, consisting of metamorphosed calcite. Their thickness is less than 5 m and dip 50–60° to the south (Fig. 1; Kantor, 1953; Grecula et al., 2009). In crystalline limestones the diopside and grossular with an andradite molecule content of up to 21 mol% were locally found (Ružička et al., 2020). Elsewhere the Mn rich garnet,

muscovite, chlorite, pyrite, quartz and amphibole occur in lenses respectively. The amphibole there has a prismatic shape and, according to its optical properties Kantor (1953) considered it as a tremolite. Near the transition zone to Mn mineralization in limestone lenses the short veins of Mn-rich calcite and pyrrhotite were found, though the amphibole has also been found in rocks around the limestone lenses (Kantor, 1953).

The body of Mn skarn in the former limestone reaches a thickness of 1.3 to 4 m and its length is 50–100 m. According to the mining maps from 1940 the Mn skarn does not exceed a depth of 15–20 m. The available field data provide an information on two separate skarn lenses in host limestones and information about their genesis indicates that conversion of limestone to skarn was at the beginning selectively metasomatic and later metamorphic, related to Variscan metamorphism (Kantor, 1953; Rojkovič, 1999, 2001).

In previous studies various authors focused on the description of the main Mn bearing mineralization, although the occurrence of Fe-rich oxides in the skarn was not negligible. These mineralogical studies confirmed that the main Mn-bearing mineralization of the skarn consists of rhodonite, rhodochrosite, kutnahorite (kutnohorite – IMA), pyroxmangite, spessartine, tephroite, calcite, Mn-rich calcite, quartz, hematite and Mn-rich magnetite. Rarely there occurred baryte, bementite, caryopilite, fluorapatite, hübnerite, pyrophanite, hausmannite, mangano-

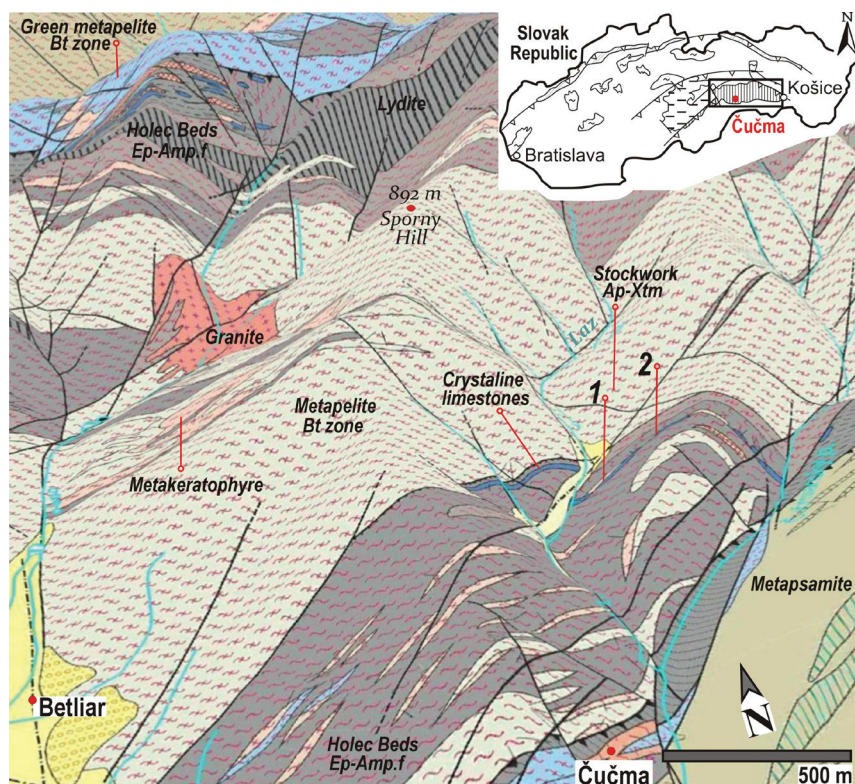


Fig. 1. Geological map and metamorphic zonation of Čučma area in the 3D model according to Grecula et al. (2009). **1** – Mn bearing skarn and **2** – Fe and Mn bearing skarn positions in crystalline limestone. The Holec Beds – a part the Silurian Betliar Fm are built of crystalline limestone, sericite-graphite phyllites, graphite phyllites and lydite. The position of apatite-xenotime stockwork is explained in more details in Radvanec & Gonda (2019).

site, jacobsonite, pyrosmalite-(Mn), rutile, stilpnomelane, muscovite, biotite, chlorite, albite, allanite-(Ce), quartz and prismatic amphiboles regarded as anthophyllite and tremolite. Disseminated sulfides such as alabandite, arsenopyrite, bismuthinite, galena, gersdorffite, glaucodote, chalcopyrite, cobaltite, pentlandite, pyrite, pyrrhotite, sphalerite and ullmannite were also locally found. The goethite, limonite, cryptomelane, manganite, melanterite, pyrolusite, sulfur, chamosite and todorokite occur in the supergenic mineralization zone (Kantor, 1953, 1954; Bartalský et al., 1973; Faryad, 1994; Grecula et al., 1995; Rojkovič, 2001; Peterec & Ďuďa, 2003; Peterec & Ďuďa, 2009; Števko et al., 2015). However, in published analyses of pyroxenoides (rhodonite, pyroxmangite) the content of CaSiO_3 ranges from 7.8 to 8.8 mol.% and according to the Momi (1964) classification, the CaSiO_3 content clearly shows generations of Fe-rich and pure rhodonite, so the published analyses of pyroxenoides by Rojkovič (2001) stated that pyroxmangite is the rhodonite as well.

The aim of present mineralogical and petrological study is to supplement by new data to previous findings about the development of skarns in the Čučma area (Fig. 1). In addition to the abovementioned minerals, we have identified following minerals: Ti-rich tephroite, knebelite, maghemite, spinels from the iwakiite-jacobsonite to hausmannite series, kempite, alleghanyite, pyrochroite, rhodonite, cummingtonite, grunerite, tourmaline, molybdenite and Ag-rich tetrahedrite. An important finding of this study is showing a new substitution in the olivine group, where the Si content is replaced by Ti up to 0.159 apfu in the Ti-rich tephroite. All new findings helped to identify the empirical reactions explaining the successive formation of the skarn from the stage when Mn carbonates and the Fe bearing part entered to the final stage of the Mn bearing skarn formation, depending on change of metasomatic and metamorphic conditions. The results on the formation of Mn mineralization complement the genetic model of Permian hydrothermal mineralization in the Gemic unit, which was presented by Radvanec & Gonda (2019).

Geological setting

Skarn represents mostly fine to medium-grained dark rock with a reddish-brown tint. Sometimes it is black or it has a pink colour respectively. Texture of skarn is most often fibro-granoblastic, less often granoblastic massively smoky or frequently banded (Figs. 2, 3, 4, 6, 7 and 9). Two bodies of skarn are tectonically separated and they are a part of the Holec Beds of Betliar Fm encompassing the Early Paleozoic – Silurian evolution of Gemic unit (Grecula et al., 2009). The Holec Beds consist of sericite-graphite phyllites, lenses of lydite and crystalline limestones bearing skarn in the Čučma area (Fig. 1). This occurrence of Holec Beds was metamorphosed in epidote-

amphibolite facies and a part of former limestone lenses was replaced by minerals of skarn (Kantor, 1953; Grecula et al., 2009; see Fig. 1 in Radvanec & Gonda, 2019). In the same position, on the lenses of former Silurian limestones, the Fe bearing skarn was formed in localities of Dlhá dolina area, Lipový and Hekerová hills (Radvanec & Gonda, 2019; Kantor, 1954). The Fe bearing skarn from Dlhá dolina was formed in the stilpnomelane-chlorite zone of Permian metamorphic-magmatic-hydrothermal cycle (MMH cycle). This skarn was found in the direct contact with the limestone lens as well as the direct contact with the magnesite body (Radvanec & Gonda, 2019). Position of skarn from Dlhá dolina area, Lipový and Hekerová hills is comparable with that of the Čučma skarn, however the development of the skarn in Čučma locality was gradual. Firstly a part of Fe skarn was formed and later there dominated Mn-type skarn (Figs. 3 and 4).

Methodology

Mineralogical, geochemical and petrological research was applied on two skarn bodies in known localities of Čučma area (Fig. 1).

The skarn mineralization was studied in samples from two dumps (dump-1; 48° 42' 31.05" N, 20° 32' 55.53" E; dump-2 (48° 42' 37.34" N, 20° 33' 14.95" E), applying polished thin sections and EMPA analyses. All above listed type rocks and mineralizations were analysed by quantitative analyses (Tab. 5). Chemical analyses were done in SGIDŠ GAL Laboratories in Spišská Nová Ves, Slovakia. The EMPA mineral analyses and their crystallization succession were obtained in the SGIDŠ Department of microanalysis, Bratislava. The Cameca SX-100 electron microscope was equipped by three spectrometers and Kevex delta IV EDS system. The natural and synthetic standards were used for calibration. Measuring conditions: acceleration voltages 15 KV and 25 KV, current 10 nA at analyses of carbonates or 20 nA at silicate analyses. The diameter of the electron beam was changed according to the type and size of minerals. Stilpnomelane and Mn-rich micas were measured by widened beam 7–10 μm , carbonates 10–15 μm and other minerals by 2–5 μm beam. The measurement time from 10 to 35 s was chosen with regard to achieve the required measurement accuracy of given element. Detection limit for individual elements is smaller than 0.05 wt.% with an error 1-sigma.

New mineralogical data in above listed places were classified in the same way. After study by optical microscope the EMPA results for all revealed minerals were projected in triangles and tetrahedrons, regarding three successive stages of skarn formations. These projections were done for carbonates, spinels, oxides, silicates and others minerals. Carbonates were projected in triangle diagrams of FeCO_3 – MnCO_3 – CaCO_3 resp. with end-members siderite, rhodochrosite and calcite

(Fig. 5). The projection of all analyses after re-calculation to chemical formula were shown in tetrahedron projections: FeO+MgO – CaO – Fe₂O₃ – MnO, FeO+MgO – MnO – A – SiO₂ and FeO+MgO – MnO – Fe₂O₃ – Mn₂O₃. In stages 2 and 3 of skarn formation, mineral position was visualized in individual tetrahedron projections, but their final processing were joined into one entity (Fig. 10). These projections intended their exact view in successive crystallization system of skarn, which is the result of 39 reactions. In projections the indexed minerals are shown, classifying individual mineralizations to zones from the chlorite-apatite zone through amphibolite facies to final stilpnomelane-chlorite zone.

The chemical analyses of Early Paleozoic metarhyolite from the outcrop on Stromiš hill (48° 48' 23.89" N, 20° 27' 0.82" E) and of S-type Permian granites from localities of medium- to fine-grained muscovite bearing granite from Dlhá dolina-Elisabeth mine (48° 46' 18.72" N, 20° 32' 36.38" E), the medium grained muscovite-biotite granite from the Súľová locality (48° 48' 57.31" N, 20° 28' 29.59" E) and three samples of skarn from Čučma area are shown in Table 5. The sample of Early Paleozoic metarhyolite supplemented previously published data on Early Paleozoic stratabound sulfidic mineralization of Smolník type and lydites as a source of elements in hydrothermal mineralization, which was formed in Permian after melting of these rocks in amphibolite facies. This anatectic melting, producing S-type granites in Permian, also released elements from Early Paleozoic rocks into the

fluid phase. Various mineral associations crystallized from this fluid phase depending on temperature and pressure decrease from the anatectic zone toward the surface (Radvanec & Gonda, 2019). The collection of S-type granite analyses was supplemented by two samples from localities of Dlhá dolina and Súľová (Tab. 5). All these granites formed in hotlines above subduction zone during the Permian development of Paleo-Gemericum during the metamorphic-magmatic-hydrothermal (MMH) cycle of Radvanec et al. (2009) and Radvanec & Gonda (2019).

Three bulk chemical analyses of skarn, Lower Paleozoic metarhyolite and S-type granites (Dlhá dolina and Súľová occurrences) were normalized according to REE standards (Sun and McDonough, 1989). Two distinguished groups of investigated samples suit to genetic model of Permian hydrothermal mineralization in Gemeric unit (Radvanec & Gonda, 2019): Older group suits to upper crust normalization and the second, younger group of samples suits to primitive mantle normalization (Fig. 11). Applying this REE normalization, the skarn samples were divided into "upper crust" and "primitive mantle" groups. Both groups are fully in line with their geotectonic background and formation of two age-different groups of anatectic S-type granite. Because S-type granites represent product of anatexis in amphibolite facies, in subsequent processing the group of analyses of the "upper crust" was normalized on porphyric granite, representing the source non-differentiated anatectic melt. This anatectic melt generated fluid phase, from

Tab. 1
Representative analyses of carbonates in Čučma skarns.

Mineral	Mn calcite	Kutnahorite	Kutnahorite	Kutnahorite	Mn siderite	Rhodochrosite	Rhodochrosite	Rhodochrosite	Rhodochrosite	Calcite
Place	matrix	matrix	matrix	matrix	in MnCal	matrix	matrix	matrix	matrix	Relict
Stage	1	1	1	1	1	1	1	1	1	Limestone
Process	Metasomatic	Metasomatic	Metasomatic	Metasomatic	Metasomatic	Metasomatic	Metasomatic	Metasomatic	Metasomatic	Silurian
FeO	0.36	0.67	1.81	6.07	39.64	1.18	3.32	0.97	0.18	0.14
MnO	14.39	29.59	25.37	16.15	16.73	46.97	47.48	49.89	61.03	0.27
MgO	0.19	0.74	0.98	1.22	2.70	1.06	0.90	0.60	0.07	0.71
CaO	42.31	27.83	30.14	34.46	1.93	10.94	8.51	8.79	0.32	55.52
CO ₂	42.56	41.41	41.57	42.13	39.10	39.61	39.17	39.08	38.32	44.63
Total	99.81	100.23	99.87	100.02	100.10	99.77	99.38	99.33	99.93	101.28
Fe	0.005	0.01	0.027	0.088	0.621	0.018	0.052	0.015	0.003	0.002
Mn	0.21	0.443	0.379	0.238	0.265	0.736	0.752	0.792	0.988	0.004
Mg	0.005	0.019	0.026	0.032	0.075	0.029	0.025	0.017	0.002	0.018
Ca	0.78	0.527	0.569	0.642	0.039	0.217	0.171	0.177	0.007	0.976
CaCO ₃	78.00	52.75	56.84	64.20	3.90	21.70	17.10	17.68	0.70	97.60
MgCO ₃	0.50	1.90	2.60	3.20	7.50	2.90	2.50	1.70	0.20	1.80
FeCO ₃	0.50	1.00	2.70	8.80	62.10	1.80	5.20	1.50	0.30	0.20
MnCO ₃	21.00	44.34	37.86	23.80	26.50	73.60	75.20	79.12	98.80	0.40

which mineralization with the upper crust characteristics originated in the granite exocontact. According to REE normalization this mineralization complies with the source porphyric granite. Variation of elements contents from the group of “upper crust” after normalization to porphyric granite was visualized in isocones (isoconcentrations) and in the logarithmic scale they were evaluated as enrichment or deficiency in the element content. After normalization of element content to granites, the isocone in compared sample is the same in the case of their ratio equal to 1. In good agreement with the reference granite an isocone falls within the range 0.1–10. Values beneath 0.1 represent a deficiency and above 10 the enrichment against granites (Figs. 12–14). The contents of elements have colour division and division to groups, respecting the results of mineralogical investigation and binding of elements in mineral associations, found in type localities by mineralogical and geochemical investigation. Part of the main components of analyses and unclassified element contents occur in the black group. The red and green groups belong to elements prevailing from apophyses, greisens and stockworks. Yellow group is formed by elements from the stockwork mineralization and blue group belongs to elements of vein mineral association (Fig. 13; Radvanec & Gonda, 2019).

The second – younger group of Permian hydrothermal mineralization, having the influence of primitive mantle, was normalized on younger differentiated granite, which correspondingly was displayed as enrichment or deficiency of the element content respectively (Fig. 14).

Minerals in successive formation of skarn

First Mn metasomatic stage and Fe bearing skarn formation

The first Mn metasomatic stage gradually replaced the former Silurian limestones lenses into of Mn-rich calcite, kutnahorite, rhodochrosite, Mn-rich siderite, fluorapatite, tourmaline, phengitic muscovite, Mn-rich chlorite and pyrite. Isolated grains of molybdenite, galena, chalcopryrite, pyrite, sphalerite and Ag-rich tetrahedrite here in the matrix of Mn-rich calcite and kutnahorite were also found (Figs. 2, 3b and 9.). Relics of Mn-rich chlorite, which reach a size of up to 50 μm , have been rarely found together with rhodochrosite (Fig. 7e). However the unreacted relics of former calcite (limestone), Mn chlorite are still frequently present, usually in spessartine and in the grossular/spessartine matrix (Fig. 2). The MnO content in Mn chlorite ranges from 4.45 to 24.71 wt.% and its chemical formula is variable, from the Mn-rich clinocllore to the end member of pennantite (Tab. 2).

The main minerals of this metasomatic stage are Mn calcite, kutnahorite and rhodochrosite (Tab. 1). Between the end members of kutnahorite and rhodochrosite, a group of Mn carbonates was found where the content of

MnCO_3 (6 analyses) ranges from 60.5 to 78.3 mol. % (Fig. 10a). According to the Mn carbonate thermometer in the CaCO_3 – MnCO_3 system, this range of the MnCO_3 content shows the formation of rhodochrosite and kutnahorite at the temperature from 520° to 540 °C (De Capitani & Peters, 1981; Chang et al., 1998).

In the direct contact of former limestone lens at the metapelite, a Fe bearing skarn originated during the metasomatic first stage, and it reaches here a thickness of about 6 cm. The Fe skarn is of black colour having pseudo cast monomineral form of **maghemite** (Fe_2O_3) and therefore the Fe skarn is weakly magnetic. The mass of zonal maghemite with size up to 50 μm , fluorapatite up to 40 μm , rutile, ilmenite where the Mn content reaches up to 7.74 wt.% and aggregates of pyrite up to 150 μm in size are the main assemblage of the Fe skarn. In the pyrite, the inclusions of chalcopryrite and galena are frequently present and the rim of pyrite contains a variable As content up to 5 wt.% (Fig. 3).

Fluorapatite belongs to one of first minerals formed during the replacement of former limestone. It forms inclusions in kutnahorite, relics in spessartine and as well as together with kutnahorite it is enclosed in the mass of maghemite respectively (Fig. 2a, 3c, 7c and 9b–c). The homogeneous grains of fluorapatite do not contain any admixture of other elements and its chemical formula is close to end-member $\text{Ca}_5(\text{PO}_4)_3\text{F}$ (Tab. 2). In different localities of Gemic unit the same pure fluorapatite in assemblage with tourmaline, biotite, phengitic muscovite, margarite, topaz, stilpnomelane, chlorite, quartz, fluorite, calcite, cassiterite, ankerite, dolomite, kutnahorite, rhodochrosite, siderite, magnesite, allanite, goyazite, In-rich sulfides and U-rich minerals occur. In all these localities from greisens in the depth and direct contact with granite to U-SedEx mineralization on the surface, the fluorapatite does not contain any admixture of other elements, however it was formed in different P-T conditions of the Permian hydrothermal mineralization in Gemic unit (Radvanec & Gonda, 2019). The zone, where the fluorapatite occurs with phengitic muscovite and chlorite, was named the chlorite-apatite zone and this zone has a regional enlargement in the Permian hydrothermal mineralization (l. c.). The origin of studied fluorapatite is conditioned by the existence of calcite or limestone, which reacted with residual Fe-bearing fluid phase with H_3PO_4 content forming fluorapatite and maghemite according to reaction (1). Reaction 1 runs simultaneously with Mn metasomatism of limestone to form Mn calcite, kutnahorite and rhodochrosite respectively.

The matrix of Fe skarn is dominantly formed by aggregates of zonal maghemite. In the maghemite core the content of SiO_2 always ranges from 1.12 to 4.77 wt.%, however its rim is almost free of SiO_2 and sometimes contains only 0.08 wt.% of SiO_2 (Fig. 3). According to

Tab. 2
Representative analyses of minerals in Čučma skarns.

Mineral	Fluorapatite	Alleghanyite	Ca spessartine	Ca spessartine	Ca spessartine	Spessartine	Pennantite	Kempite	Grunerite	Cummingtonite	Chlorite	Stilpnomelane	Stilpnomelane	Pyrochroite-1	Pyrochroite-2
Place	in Fe-Mn skarns	in oxides	rim Fe skarn	rim Fe skarn	rim Fe skarn	rim Fe skarn	matrix	rim MnO	matrix	matrix	matrix	in Mn skarn	in Fe skarn	in tephroite	in Mn carbonate
Stage	1	2	2	2	2	2	2	2	2	2	3	3	3	3	3
Process	Metasomatic	Prog.-metam.	Prog.-metam.	Prog.-metam.	Prog.-metam.	Prog.-metam.	Prog.-metam.	Prog.-metam.	Prog.-metam.	Prog.-metam.	Retro.-metam	Retro.-metam	Retro.-metam	Retro.-metam	Retro.-metam
SiO ₂	0.02	23.19	35.81	36.06	37.18	35.52	26.25	0.09	51.46	53.17	46.25	44.93	44.07	5.31	0.09
TiO ₂	0.00	0.01	0.15	0.13	0.09	0.03	0.01	0.00	0.00	0.00	0.00	0.01	0.01	0.00	0.00
Al ₂ O ₃	0.00	0.00	18.71	18.82	20.21	20.21	17.37	0.00	0.01	0.10	5.30	2.86	5.56	0.00	0.00
Cr ₂ O ₃	0.00	0.00	0.00	0.00	0.02	0.02	0.02	0.00	0.00	0.00	0.00	0.00	0.00	0.00	0.00
FeO	1.79	0.16	3.52	0.00	1.41	0.00	9.43	0.22	32.51	24.34	30.89	0.00	0.00	2.10	0.95
Fe ₂ O ₃	0.00	0.00	4.54	5.19	2.40	0.99	0.00	0.00	0.00	0.00	0.00	28.52	35.50	0.00	0.00
MnO	0.2	72.42	31.45	29.12	24.35	41.42	24.71	73.12	6.06	7.74	0.43	15.21	1.02	70.05	70.52
MgO	0.03	0.24	0.07	0.06	0.01	0.03	11.37	0.02	7.57	12.29	4.47	3.06	4.53	0.06	1.28
CaO	54.66	0.06	5.83	10.74	14.38	1.87	0.03	0.12	0.48	1.18	0.52	0.05	0.58	0.25	6.13
Na ₂ O	0.01	0.00	0.00	0.00	0.00	0.00	0.00	0.03	0.00	0.02	0.04	0.07	0.13	0.14	0.00
K ₂ O	0.01	0.00	0.00	0.00	0.00	0.00	0.00	0.02	0.00	0.00	0.84	1.84	2.26	0.02	0.00
P ₂ O ₅	41.26	0.00	0.00	0.00	0.00	0.00	0.00	0.00	0.00	0.00	0.00	0.00	0.00	0.00	0.00
F	4.38	0.00	0.00	0.00	0.00	0.00	0.00	0.16	0.00	0.00	0.00	0.00	0.00	0.00	0.00
Cl	0.00	0.00	0.00	0.00	0.00	0.00	0.01	15.45	0.00	0.01	0.00	0.05	0.01	0.00	0.00
H ₂ O	0.00	3.61	0.00	0.00	0.00	0.00	11.05	14.74	0.00	0.00	11.64	2.22	1.26	21.65	20.74
Total	102.35	99.69	100.07	100.11	100.05	100.08	100.25	103.97	98.09	98.85	100.38	98.82	94.93	99.58	99.70
OFCl	1.84							3.55							
OF	0.00							0.07							
OCl	0.00							3.49							
Total _c	100.51							100.42							
Si	0.002	1.927	2.944	2.930	2.970	2.938	5.695	0.003	8.048	7.990	4.766	10.550	10.432	0.073	0.001
Al ^{IV}	0.000	0.000	0.056	0.070	0.030	0.062	2.305	0.000	0.000	0.010	0.234	0.000	0.000	0.000	0.000
Sum ^T	0.000	1.927	0.000	0.000	0.000	0.000	8.000	0.003	0.000	0.000	5.000	10.550	10.432	0.073	0.001
Al ^{VI}	0.000	0.000	1.757	1.732	1.873	1.908	2.133	0.000	0.002	0.007	0.409	0.791	1.550	0.000	0.000
Ti	0.000	0.001	0.009	0.008	0.006	0.002	0.002	0.000	0.000	0.000	0.000	0.002	0.002	0.000	0.000
Fe ³⁺	0.000	0.000	0.281	0.317	0.144	0.062	0.000	0.000	0.000	0.009	0.000	5.034	6.317	0.000	0.000
Fe ²⁺	0.127	0.011	0.242	0.000	0.094	0.000	1.711	0.006	4.252	3.050	2.662	0.000	0.000	0.024	0.011
Cr	0.000	0.000	0.000	0.000	0.001	0.001	0.003	0.000	0.000	0.000	0.000	0.000	0.000	0.000	0.000
Mn	0.014	5.098	2.190	2.004	1.648	2.902	4.541	1.982	0.803	0.985	0.038	3.025	0.205	0.822	0.863
Mg	0.004	0.030	0.008	0.008	0.002	0.003	3.678	0.001	1.765	2.753	0.687	1.071	1.599	0.001	0.028
Ca	4.958	0.005	0.513	0.935	1.231	0.165	0.007	0.004	0.080	0.190	0.057	0.013	0.147	0.004	0.095
Na	0.002	0.000	0.000	0.000	0.000	0.000	0.000	0.002	0.000	0.006	0.008	0.032	0.060	0.004	0.000
K	0.000	0.000	0.000	0.000	0.000	0.000	0.000	0.001	0.000	0.000	0.110	0.551	0.682	0.000	0.000
P	2.957		0.000	0.000	0.000	0.000	0.000	0.000	0.000	0.000	0.000	0.000	0.000	0.000	0.000
Cations	8.064	7.072	8.000	8.003	8.000	8.044	20.075	1.999	14.950	15.000	8.971	21.069	20.994	0.928	0.998
CF	2.345	0.000	0.000	0.000	0.000	0.000	0.000	0.032	0.000	0.003	0.000	0.000	0.000	0.000	0.000
CCL	0.000	0.000	0.000	0.000	0.000	0.000	0.007	1.677	0.000	0.000	0.000	0.040	0.008	0.000	0.000
OH	1	2.00	0.00	0.00	0.00	0.00	16.00	3.15	0.00	0.00	0.00	3.48	2.00	2.00	2.00
O	13	10	12	12	12	12	36	4	23	23	18	36	36	2	2

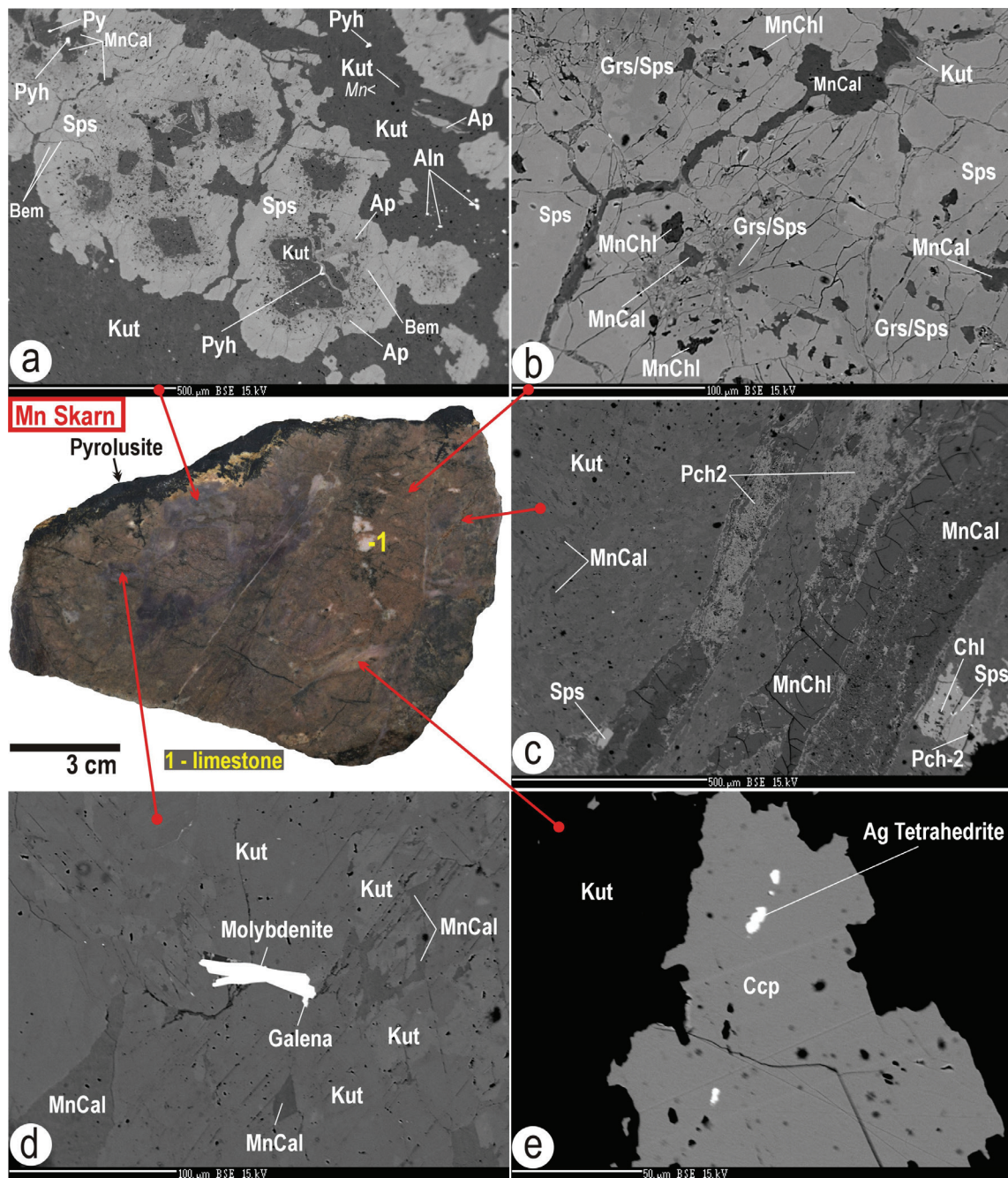


Fig. 2. Metasomatic onset of the Mn skarn formation shows by kutnahorite (Kut) and Mn-rich calcite areas (see cross-section) and other spots in the BSE images. **a** – The spot where kutnahorite and Mn calcite were replaced by spessartine (Sps) of atoll shapes. This garnet formed in second metamorphic stage of Mn skarn formation; pyrite (Py), pyrophanite (Pyh), bementite (Bem), fluorapatite (Ap), allanite (Aln). **b** – Place of spessartine with spots of Ca-rich spessartine (Grs/Sps) and relics of Mn calcite and Mn-rich chlorite (MnChl). **c** – Place of kutnahorite with spessartine, Mn chlorite and veined pyrochroite-2 (Pch-2), chlorite (Chl) in spessartine. **d** – Place with disseminated molybdenite and galena in matrix of kutnahorite and Mn calcite. **e** – This place shows disseminated chalcocopyrite (Ccp) with inclusions of Ag-rich tetrahedrite in kutnahorite matrix.

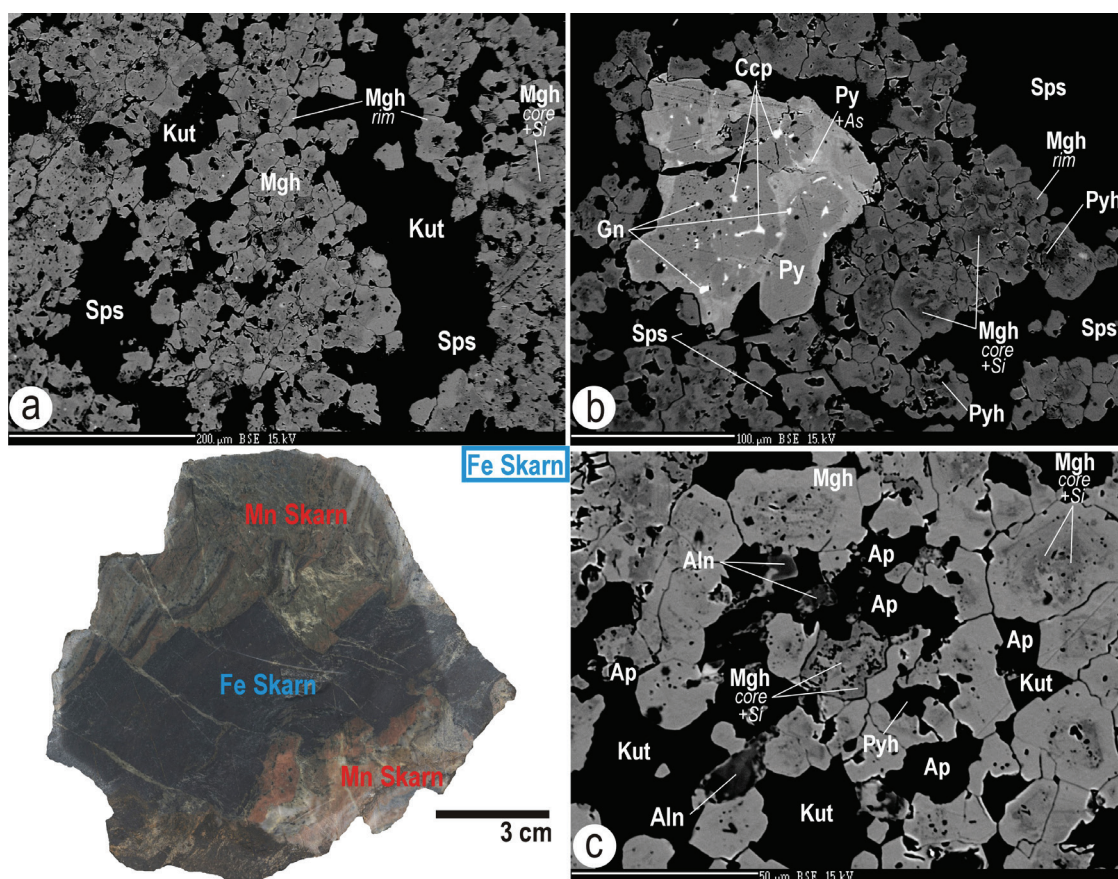
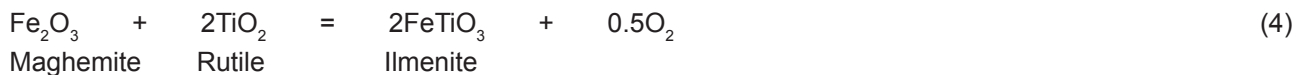
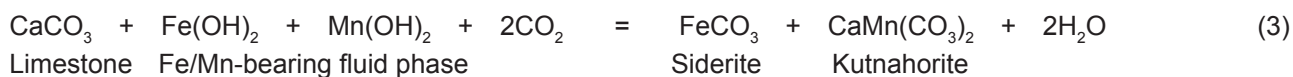
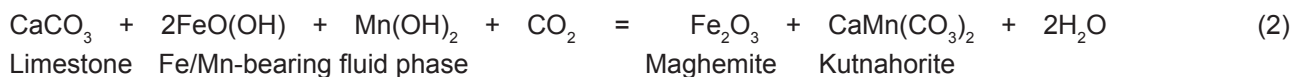
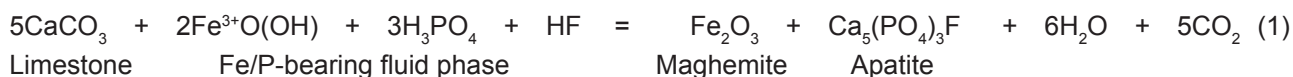


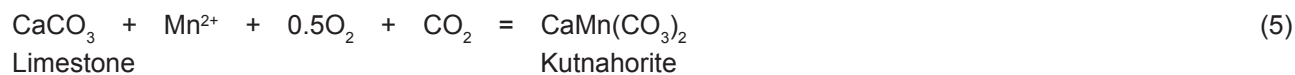
Fig. 3. Successive formation of skarn in the contact of former limestone lens (cross-section) and metapelite. The black Fe bearing part of skarn represents its formation during the first metasomatic stage, than the Fe skarn was rimmed by Mn bearing skarn formed in second metamorphic stage. The BSE images show mineral assemblages in the part of Fe skarn. **a** – In aggregates the cores of individual maghemite (Mgh) contains Si and their rims are of pure maghemite. The space in maghemite aggregates is filled by kutnahorite (Kut) and by spessartine (Sps). **b, c** – Si-rich core and pure rim of maghemite. Disseminated pyrite (Py) with inclusions of galena (Gn), chalcocopyrite (Ccp) and zones rich of As in pyrite. Position of fluorapatite (Ap), allanite (Aln), pyrophanite (Pyh), kutnahorite, and spessartine in maghemite aggregates.

unclear chemical formulas based on EMPA, there is a risk that the SiO₂ content is bound in the submicroscopic form of quartz to the core of maghemite and therefore the determined SiO₂ content does not belong to the real formula of maghemite. In each grain of zonal maghemite,

the F content is always present in the range from 0.28 to 0.37 % wt.% (Tab. 3).

According to identified minerals and their relationships in the metasomatic replaced limestones and minerals in the Fe skarn, following six reactions were inferred.





Tab. 3
Representative analyses of oxides and spinels in Čučma skarns.

Mineral	Maghemite*	Maghemite*	Maghemite	Ilmenite	Rutile	Pyrophanite	Manganosite	Jacobsite	Jacopsite	Hausmannite	Iwakiite	Iwakiite	Iwakiite
Place	core-Fe skarn	core-Fe skarn	rim-Fe skarn	matrix	matrix	in Mn skarn							
Stage	1	1	1	1	1	2	2	2	2	2	2	2	2
Process	Metasomatic	Metasomatic	Metasomatic	Metasomatic	Metasomatic	Prog.-metam.							
SiO ₂	2.96	4.77	0.08	0.47	0.37	0.93	0.00	0.02	0.75	0.00	0.01	0.02	0.01
TiO ₂	0.03	0.08	0.08	51.15	92.56	55.44	0.00	0.28	0.14	0.01	0.00	0.09	0.07
Al ₂ O ₃	0.02	0.13	0	0.18	0.12	0.17	0.00	2.89	0.60	0.13	0.38	2.05	1.93
FeO	0.00	0.00	0	43.62	6.08	6.05	0.27	3.00	19.00	2.57	31.51	30.77	31.72
Fe ₂ O ₃	97.58	94.68	98.72	0.00	0.00	0.00	0.00	64.46	65.32	0.00	13.34	6.67	4.44
Cr ₂ O ₃	0.00	0.00	0.03	0.00	0.03	0.04	0.03	0.01	0.00	0.00	0.00	0.00	0.00
MnO	1.69	2.04	0.36	3.64	0.87	36.00	99.67	28.90	13.92	28.43	0.00	0.00	0.00
Mn ₂ O ₃	0.00	0.00	0.00	0.00	0.00	0.00	0.00	0.00	0.00	68.91	54.12	59.80	61.36
MgO	0.52	0.78	0.04	0.04	0.06	0.00	0.00	0.02	0.02	0.00	0.05	0.02	0.01
CaO	0.13	0.22	0.2	0.59	0.00	1.23	0.00	0.01	0.00	0.00	0.01	0.00	0.00
F	0.33	0.28	0.29	0.00	0.00	0.00	0.00	0.00	0.00	0.00	0.00	0.00	0.00
Total	102.93	102.70	99.51	99.70	100.10	99.86	99.97	99.59	99.75	100.05	99.42	99.42	99.54
Si	0.075	0.119	0.002	0.012	0.005	0.023	0.000	0.001	0.029	0.00	0.000	0.001	0.000
Al	0.001	0.004	0	0.005	0.002	0.005	0.000	0.129	0.027	0.01	0.017	0.092	0.086
Ti	0.001	0.002	0.002	0.974	0.945	1.021	0.000	0.008	0.004	0.00	0.000	0.003	0.002
Fe ²⁺	0.000	0.000	0	0.924	0.069	0.124	0.003	0.095	0.610	0.08	1.014	0.977	1.009
Fe ³⁺	1.857	1.781	1.982	0.000	0.000	0.000	0.000	1.840	1.885	0.00	0.386	0.190	0.127
Cr	0.000	0.000	0.001	0.000	0.000	0.001	0.000	0.000	0.000	0.00	0.000	0.000	0.000
Mn ²⁺	0.036	0.043	0.008	0.078	0.010	0.747	0.997	0.929	0.453	0.92	0.000	0.000	0.000
Mn ³⁺	0.000	0.000	0	0.000	0.000	0.000	0.000	0.000	0.000	1.99	1.583	1.726	1.775
Mg	0.020	0.029	0.002	0.002	0.001	0.000	0.000	0.001	0.001	0.00	0.003	0.001	0.001
Ca	0.004	0.006	0.006	0.016	0.000	0.032	0.000	0.000	0.000	0.00	0.000	0.000	0.000
Cations	1.994	1.984	2.003	2.011	1.032	1.953	1.000	3.003	3.009	3.00	3.003	2.990	3.000

* unstechiometry

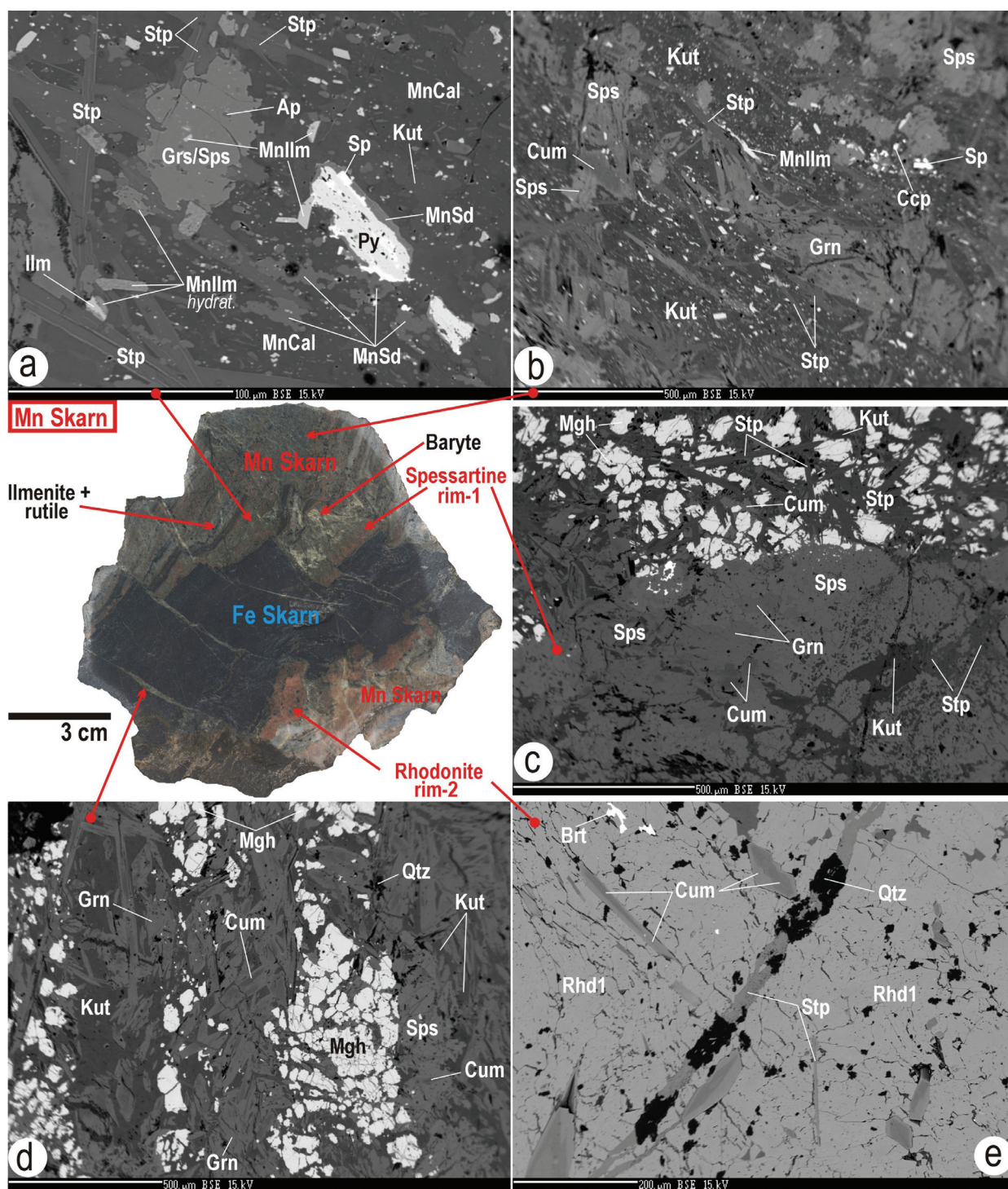


Fig. 4. Successive formation of skarn in the Čučma area. The rose Mn bearing part represents the second prograde and third retrograde metamorphic stages of the skarn evolution. A spessartine margin (rim-1) was formed around the individual segments of Fe skarn, followed by a rhodonite margin (rim-2). The BSE images show places and mineral assemblages in part of Mn skarn. **a, b** – Pyrite (Py) and sphalerite (Sp) are replaced by Mn-rich siderite (MnSd); ilmenite (Ilm) is usually hydrated; cummingtonite (Cum), grunerite (Grn) and chalcopyrite (Ccp) are enclosed in kutnahorite (Kut); prismatic stilpnomelane occurs in kutnahorite, Mn-rich calcite (MnCal) and spessartine (Sps) form the matrix. **c** – rim-1 is formed by the homogeneous spessartine at flanks of maghemite (Mgh) that represents the margin of Fe bearing skarn. The cummingtonite, grunerite and younger stilpnomelane (Stp) independently occur on the contact zone of the Fe skarn. **d** – cracks in the Fe skarn are filled by grunerite, cummingtonite and quartz (Qtz). **e** – rim-2 is composed by the homogeneous rhodonite-1 (Rhd-1) with zonal and prismatic cummingtonite and crack in rhodonite-1 is filled with quartz, stilpnomelane and baryte (Brt).

The reactions above have described first stage with the origin of metasomatic Mn-rich carbonates and Fe bearing skarn. The mineralization of first stage was formed in the process within the chlorite-apatite zone, where the fluorapatite and chlorite represent the indexed minerals. All minerals projections of the chlorite-apatite zone are shown in MgO + FeO – CaO – Fe₂O₃ – MnO tetrahedron (Fig. 10b).

In the chlorite-apatite zone of Gemic unit there were formed greisen in Dlhá dolina, a part of Hnilec greisen, as well as the Sb-sulfidic-tourmaline-Fe carbonate mineralization in Rozabela vein. The U-rich SedEx mineralization related to the Permian volcanism and the apatite-xenotime mineralization from Čučma belong to this zone, too (Radvanec & Gonda, 2019). The stockwork of apatite-xenotime mineralization is located in metapelite, about 400 m from the studied skarn in Čučma area (Fig. 1).

After the formation of the first stage minerals, the Fe skarn was segmented in brittle-ductile deformation conditions. Subsequently the Fe skarn was metamorphosed in the second stage of its formation (Figs. 2 and 3).

The second stage of skarn formation in prograde metamorphism of amphibolite facies

The second stage of skarn formation metamorphically replaced the unstable Mn carbonates mass, which originated in the older metasomatic stage. This second stage produced the Mn bearing group of garnets, humites, oxides, halides, spinels, olivines, pyroxenoids and amphiboles respectively. This assemblage forms younger and a new part of the skarn. Hence the final formation of the skarn is composed of two parts, the older Fe skarn and the younger Mn skarn. The younger Mn bearing part was formed gradually. At first, segments of Fe skarn were coated by the spessartine during the brittle-ductile deformation and then in the process of ductile deformation a rhodonite bearing rim on the spessartine was formed (Fig. 4). The ductile deformation dominantly controlled the formation of minerals during the second metamorphic stage and therefore the final skarn is mostly fine to medium-grained. The following minerals are arranged by their successive formation in the Mn skarn: spessartine, alleghanyite, pyrophanite, manganosite, kempite, jacobsite, iwakiite, hausmannite, tephroite, Ti-rich tephroite, knebelite, rhodonite-1, rhodonite-2, cummingtonite, grunerite and allanite (Figs. 6, 7 and 9).

The brown-pink Mn-rich garnets are composed by spots of **Ca-rich spessartine** Sp_s₅₅₋₇₂Gr_s₉₋₃₄Adr₇₋₁₉Alm₀₋₃ in the **spessartine** Sp_s₆₉₋₉₅Gr_s₀₋₂Adr₃₋₂₅Alm₀₋₅Prp₀₋₁ mass (Figs. 2b and 5, Tab. 2). Formation of Mn-rich garnets on direct segments of the Fe skarn determine the garnets as one of the first mineral of the metamorphic stage (Fig. 4c). In the kutnahorite matrix the spessartine formed an atoll

shapes and in spessartine, relics of Mn-rich chlorite and Mn-rich calcite frequently occur (Figs. 2a, 3 and 4). These relics of Mn-rich chlorite show formation of spessartine according to the reaction 7.

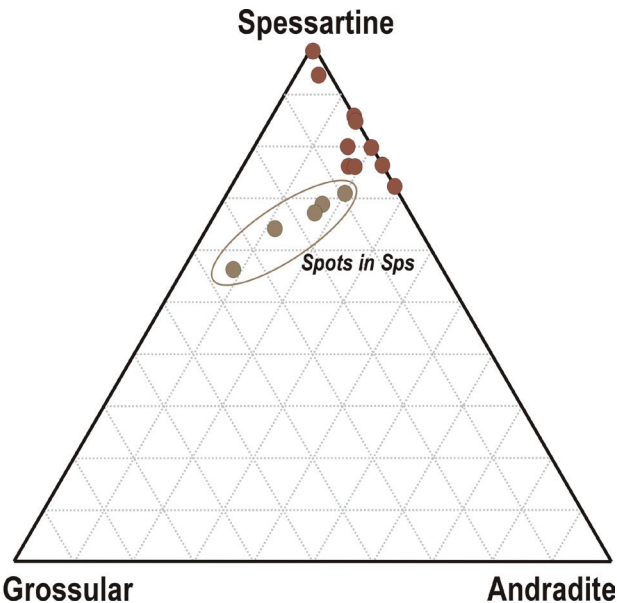
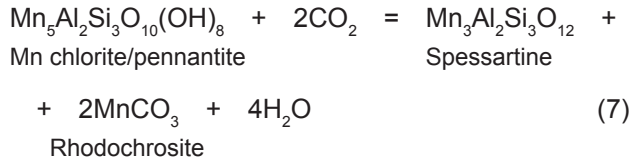
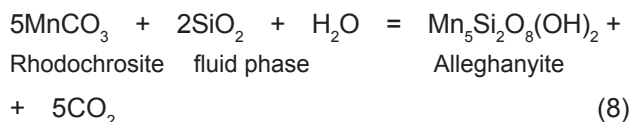


Fig. 5. Chemical composition of Ca rich spessartine and spessartine in triangle diagram grossular-andradite-spessartine end member.



The **alleghanyite** Mn²⁺₅(SiO₄)₂(OH)₂ is homogeneous and does not contain any admixtures of other elements. It originated from the rhodochrosite, in which it often forms atoll shapes up to 200 μm in size and/or the alleghanyite forms the oval inclusions in manganosite respectively (Fig. 6, Tab. 2). The alleghanyite is the first mineral binding the SiO₂ fraction from the fluid phase of metamorphic event according to the empiric reaction 8.



Pyrophanite (Fe_{0.23}Mn_{0.78})TiO₃ contains FeO up to 10.92 wt.% and the Fe/(Fe + Mn) ratio in it ranges from 0.14 to 0.26. The pyrophanite occurs with fluorapatite in the matrix of maghemite and in kutnahorite reaches a size about 20 microns (Figs. 2a and 3b–c). The reaction 9 shows the pyrophanite formation.

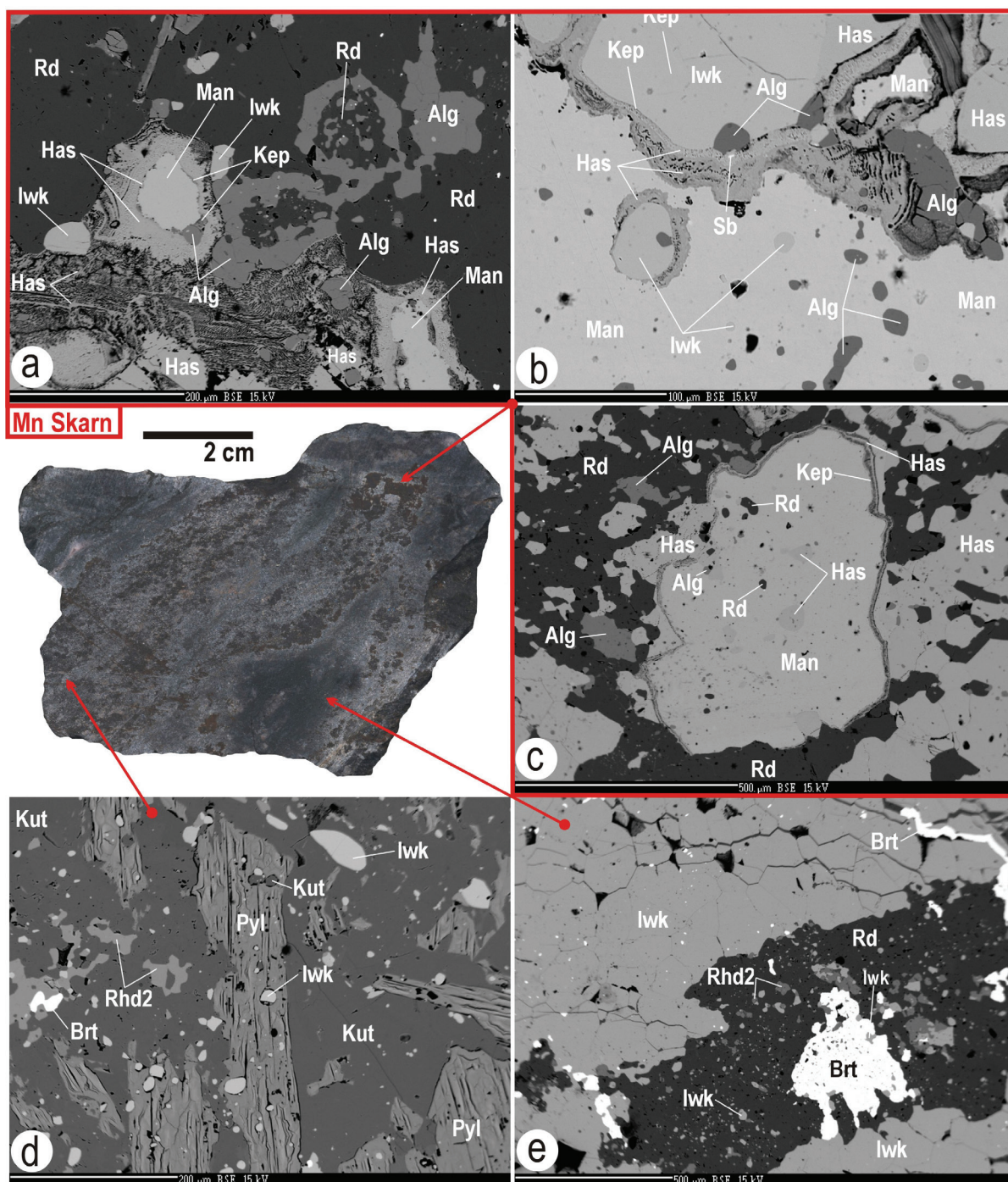


Fig. 6. Broun and black Mn bearing part represents the second prograde metamorphic stages of the skarn evolution. **a** – In rhodochrosite (Rd) spots of alleghanyite (Alg) and iwakite (Iwk) occur and the manganosite (Man) is replaced by kempite (Kep) and by hausmannite (Has) respectively. **b** – In manganosite inclusions of iwakiite and alleghanyite were found. Iwakiite is replaced by hausmannite and rarely native Sb is present in the hausmannite. **c** – In manganosite the relict of rhodochrosite and inclusions of hausmannite were found. **d** – In kutnahorite spots of rhodonite-2 (Rhd-2) the iwakiite occurs and kutnahorite is replaced by pyrolusite (Pyl). **e** – Crack in homogeneous aggregate of iwakiite is filled with baryte (Brt) and in rhodochrosite spots of iwakiite, rhodonite-2 and baryte occur.

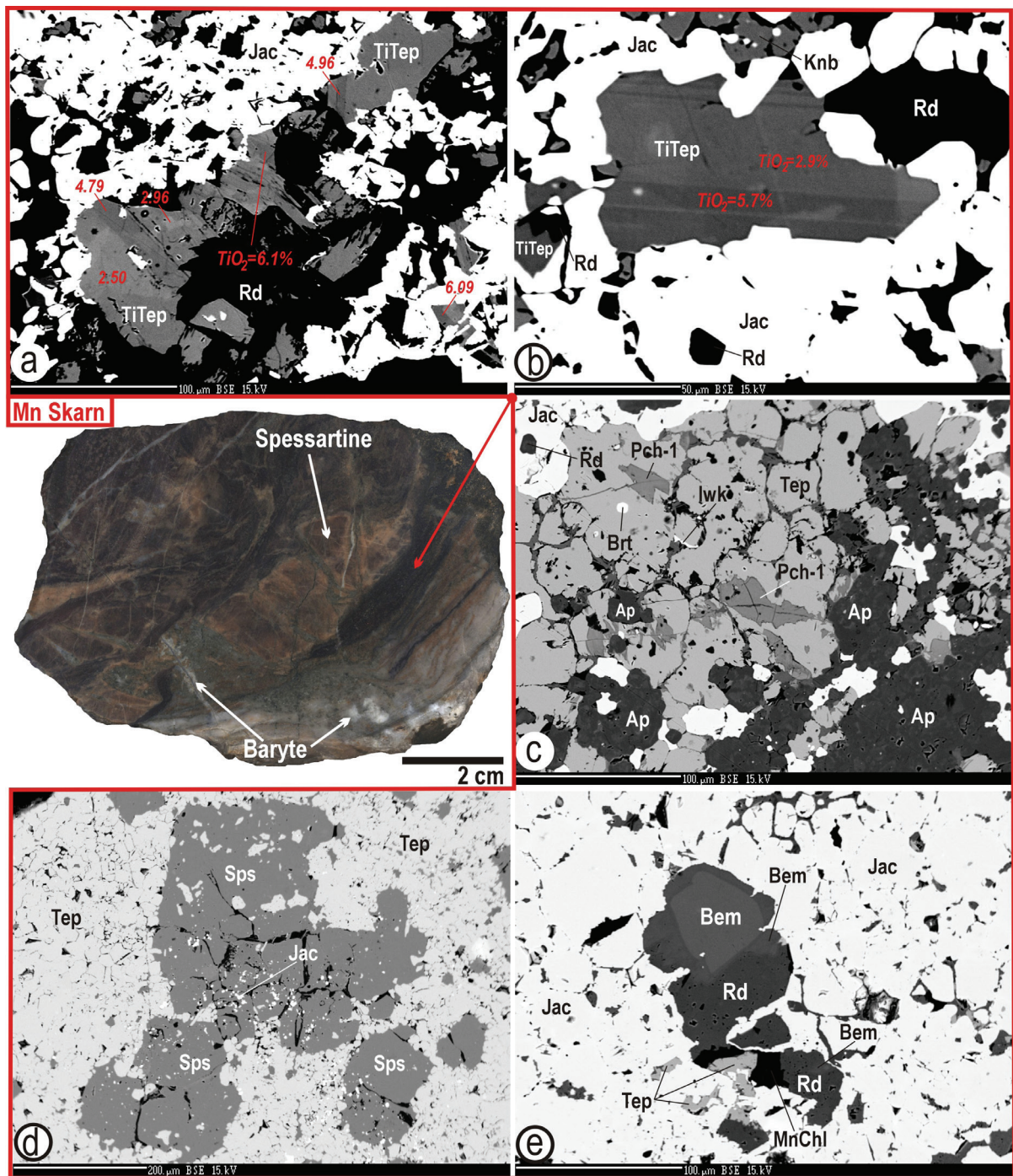
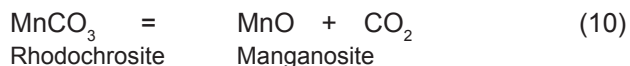


Fig. 7. Mn-rich olivines are located in black part of the skarn and were formed after the spessartine part in prograde metamorphism. Cracks of skarn are filled with baryte. **a, b** – Sectors in Ti-rich tephroite (TiTep) show different TiO_2 content and relics of rhodochrosite (Rd), Ti tephroite and jacobite (Jac) form the aggregates. **c** – In cracks the tephroite (Tep) is replaced by pyrochroite-1 (Pch-1). Aggregates of tephroite are associated with fluorapatite (Ap), iwakiite (Iwk) and jacobite (Jac). Baryte (Brt) shows pseudoinclusion in tephroite. **d** – Spessartine (Sps) is enclosed in tephroite mass. **e** – Rhodochrosite, bementite (Bem), Mn-rich chlorite (MnChl) and tephroite in jacobite matrix.

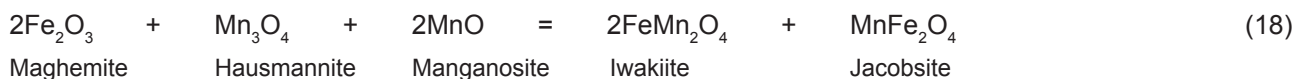
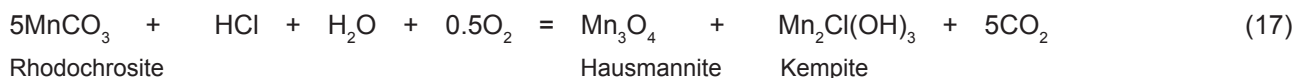
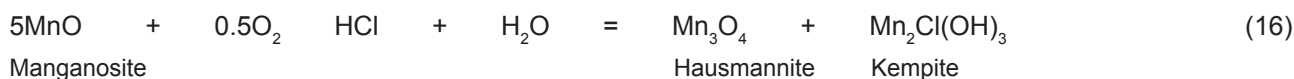
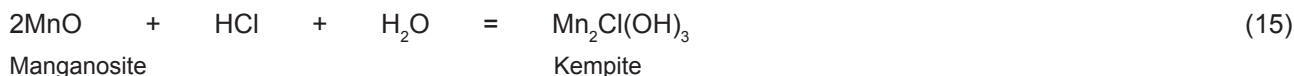
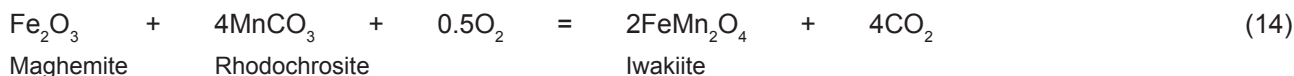
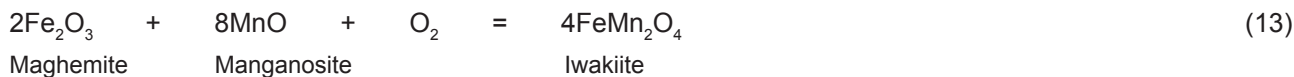


The chemical composition of **manganosite** ($\text{Mn}_{0.997}\text{Fe}_{0.003}$)O is identical to its end member. It forms a maximum of 5 mm large, emerald green, brown-green to black-green, allotriomorphic and isolated grains or their aggregates. Grains of manganosite have the characteristic glass luster. Decomposition of rhodochrosite by the reaction 10 formed manganosite and reaction 11 shows the possible formation of pyrophanite as well.



The manganosite is frequently overgrown in a black fine-grained aggregates of rhodochrosite, alleghanyite and **hausmannite** Mn_3O_4 (Fig. 6). Inclusions of **iwakiite** $\text{Fe}(\text{Al}_{0.09}\text{Fe}_{0.13}\text{Mn}_{1.78})_2\text{O}_4$, alleghanyite, hausmannite are always found in manganosite and relics of former

rhodochrosite are still presented in it. The oval inclusions of iwakiite and hausmannite appear as unmixed phases coexisting with the host manganosite (Figs. 6b–c). The grain of manganosite is usually replaced by **kempite** $\text{Mn}^{2+}_2\text{Cl}(\text{OH})_3$ and then by the hausmannite in that order (Figs. 6a–c). In addition to inclusions in manganosite, the hausmannite and iwakiite replaced kutnahorite and rhodochrosite in the matrix of Mn skarn, where hausmannite and iwakiite often in the form of aggregates occur (Fig. 6c–e). Macroscopically these aggregates are fine- to medium-grained (maximum grain size is 2 mm), have a black to black-brown colour, a semi-metallic lustre and on some grains cleavability is well observable. Microscopically, hausmannite and iwakiite grains have an allotriomorphic to hypidiomorphic shape (Fig. 6c–e). The **jacobsite** was also found in that part of Mn skarn and it has the same size and color as hausmannite and iwakiite (Fig. 7). The jacobsite usually forms a mixture in aggregates with Mn-rich olivines and it has a variable chemical formula $(\text{Mn}_{0.45-0.93}\text{Fe}^{2+}_{0.10-0.61})(\text{Al}_{0.01-0.13}\text{Fe}^{3+}_{1.84-1.94})_2\text{O}_4$ (Tab. 3). The empiric reactions from 12 to 19 explain the formation of jacobsite, iwakiite, kempite and hausmannite.



Jacobsite, hausmannite and iwakiite belong to the group of spinels. Projections of their chemical compositions and relationships in comparison to the position of manganosite, rhodochrosite, Mn siderite and maghemite are shown on the tetrahedron (Fig. 10d). The spinels projections revealed their formation by reactions from the source assemblage of manganosite, rhodochrosite, Mn siderite and maghemite. However, the variable projection of the jacobsite compositions, confirm its formation from the former assemblage of hausmannite, iwakiite, maghemite, manganosite and/or rhodochrosite, respectively (Fig. 10d).

Not only spinels but also a complex of Mn-rich olivines were found. The most common is homogeneous **tephroite** ($\text{Mn}_{1.86-1.91}\text{Fe}_{0.07-0.14}\text{Mg}_{0.02-0.04}\text{SiO}_4$) that always with jacobsite and rarely with iwakiite form the fine-grained black, sometimes dark brown aggregates in the Mn skarn. The tephroite replaced the former association of spessartine, rhodochrosite, fluorapatite and Mn chlorite in aggregates (Fig. 7). In these aggregates **Ti-rich tephroite** with the variable chemical compositions ($\text{Mn}_{1.88-1.95}\text{Fe}_{0.03-0.09}\text{Mg}_{0.03-0.06}(\text{Fe}^{3+}_{0-0.03}\text{Ti}_{0-0.16}\text{Si}_{0.84-0.98})\text{O}_4$) also occurs. It is black and reaches a size of up to 250 μm . The Ti-rich tephroite usually replaced former rhodochrosite and is always enclosed in the matrix of jacobsite. In the Ti-rich tephroite, an oval inclusions of homogeneous tephroite is rarely enclosed and these inclusions are free of TiO_2 . Each grain of Ti-rich tephroite consists of sectors that are visible in BSE images only at high acceleration of 100 nA. Individual sectors were quantified by TiO_2 content. In the sector with the lowest content, TiO_2 ranges from 0.14 to 0.32 wt.%, in the next sector the range is from 1.44 to 2.96 and the sector with a maximum TiO_2 content ranges from 4.83 to 6.22 (Fig. 7a–b). In the chemical formula of the sectors, the Ti content ranges from 0.008 to 0.159

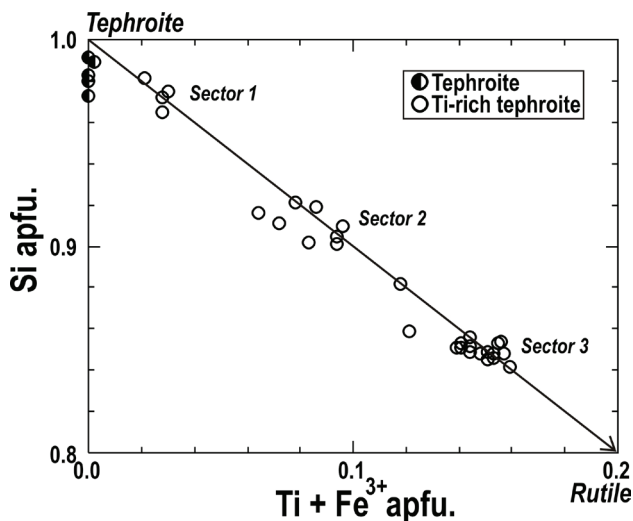


Fig. 8. The content of Si versus Ti + Fe^{3+} between end members of tephroite and rutile shows a new substitution in the olivine group composed of different immiscible sectors in Ti-rich tephroite.

(apfu) and Si from 0.842 to 0.981 respectively. It shows that the Ti content substituted Si and an immiscibility gap between the individual sectors are determined by different contents of Ti and Si in that substitution (Fig. 8). The $\text{Ti}^{4+} = \text{Si}^{4+}$ is a new substitution in the chemical formula of olivine, however according to the olivine stoichiometry this substitution have to be improved by adding a low Fe^{3+} content (apfu) to the Ti component. The Fe^{3+} correction was locally calculated for the first two sectors within the range 0.014–0.057 (apfu) and in the sector with the highest Ti content, there is the substitution of Ti versus Si without an effect of Fe^{3+} (Tab. 4). The $\text{Ti}^{4+} = \text{Si}^{4+}$ substitution was formed between end members of tephroite and rutile by the empiric reactions 22–23.

Homogeneous **knebelite** ($\text{Mn}_{1.66}\text{Fe}_{0.30-0.33}\text{Mg}_{0.06}\text{Si}_{0.99-0.98}\text{O}_4$) is the next from the group of olivines present in the Mn skarn. The $\text{Fe}/(\text{Fe} + \text{Mg})$ ratio in knebelite is 0.84–0.85 and $\text{Fe}/(\text{Fe} + \text{Mg} + \text{Mn})$ ratio is to 0.15–0.16 (Tab. 4). The knebelite of a dark grey to steel color replaces rhodochrosite and fluorapatite. Together with rhodonite, spessartine and bementite form aggregates where knebelite reaches a size of 500 μm . In these aggregates two population of homogeneous rose pink **rhodonite-1** ($\text{Mn}_{0.74}\text{Fe}_{0.09-0.13}\text{Mg}_{0.02-0.030}\text{Ca}_{0.10-0.12}\text{Fe}^{3+}_{0.02-0.04}\text{Si}_{0.98-0.99}\text{O}_3$) and pink **rhodonite-2** ($\text{Mn}_{0.87-0.89}\text{Fe}_{0-0.02}\text{Mg}_{0.02-0.030}\text{Ca}_{0.08-0.10}\text{Fe}^{3+}_{0.03-0.04}\text{Si}_{0.97-0.99}\text{O}_3$) form the matrix, where the knebelite is present respectively (Fig. 9). In the aggregates those two modes of rhodonite unmixed each other and their variation in the molecular components are as follows (in mol.%): rhodonite-1 – 73.72–74.09 MnSiO_3 , 9.97–12.25 CaSiO_3 , 9.10–12.5 FeSiO_3 , 2.11–3.07 MgSiO_3 ; rhodonite-2 – 86.60–88.50 MnSiO_3 , 8.02–9.54 CaSiO_3 , 0–1.80 FeSiO_3 , 2.12–2.51 MgSiO_3 . The wollastonite (CaSiO_3), ferrosilite (FeSiO_3) and enstatite MgSiO_3 components are on average higher in the rhodonite-1, while the MnSiO_3 molecule is higher in rhodonite-2. The wollastonite molecule of both rhodonites ranges from 8.02 to 12.25 (mol.%) and MnSiO_3 ranges from 73.72 to 88.50 (mol.%). If a Mn-rich pyroxenoid has that range of MnSiO_3 molecule, the wollastonite component have to be ranged from 2.7 to 5.5 (mol.%) in the field of pyroxmangite because compositional boundaries between rhodonite and pyroxmangite is determinate by the wollastonite component (Momoi, 1964; Brown et al., 1980). However both studied pyroxenoides are clearly in the field of rhodonite where the wollastonite molecule ranges from 8.02 to 12.25 (mol.%; Tab. 4).

In the rhodonite-1, the $\text{Fe}/(\text{Fe} + \text{Mg})$ ratio ranges from 0.75 to 0.86 and $\text{Fe}/(\text{Fe} + \text{Mg} + \text{Mn})$ from 0.11 to 0.13. The rhodonite-1 and knebelite have values of both ratios approximately the same, indicating the coexistence in their common aggregates (Fig. 9). The rhodonite-2 usually forms irregular grains in rhodochrosite (Fig. 6e). The Fe content in the chemical formula of the rhodonite-2 is

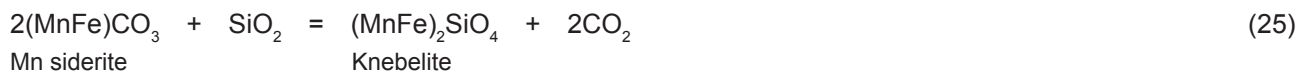
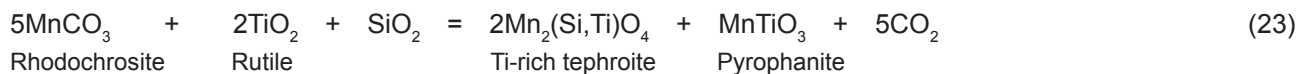
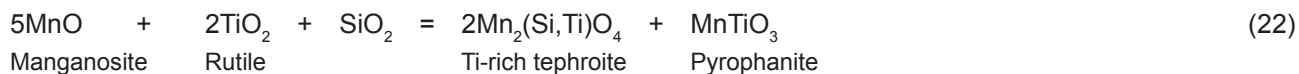
Tab. 4
Representative analyses of olivines and rhodonite in Čučma skarns.

Mineral	Knebelite	Tephroite	Ti tephroite	Ti tephroite	Ti tephroite	Ti tephroite	Ti tephroite	Ti tephroite	Ti tephroite	Ti tephroite	Ti tephroite	Rhodonite 1	Rhodonite 1	Rhodonite 2	Rhodonite 2
Place	Mn skarn	Mn skarn	Sector 1	Sector 1	Sector 2	Sector 2	Sector 2	Sector 3	Sector 3	Sector 3	Sector 3	Mn skarn	Mn skarn	Mn skarn	Mn skarn
Stage	2	2	2	2	2	2	2	2	2	2	2	2	2	2	2
Process	Prog.-metam.														
SiO ₂	29.59	28.54	29.40	29.29	27.12	26.81	25.88	25.19	24.91	24.98	24.68	45.88	45.93	45.15	45.23
TiO ₂	0.00	0.00	0.08	0.31	2.50	2.96	4.61	5.09	5.40	5.78	6.18	0.00	0.00	0.01	0.01
Al ₂ O ₃	0.00	0.00	0.00	0.02	0.00	0.00	0.00	0.00	0.00	0.01	0.00	0.00	0.02	0.00	0.19
Cr ₂ O ₃	0.04	0.03	0.00	0.00	0.00	0.00	0.02	0.00	0.00	0.00	0.03	0.00	0.00	0.00	0.00
FeO	10.85	2.47	4.87	1.83	3.06	3.00	4.83	2.28	2.24	2.75	0.00	8.23	7.11	2.19	1.88
Fe ₂ O ₃	0.00	0.00	0.00	0.54	0.00	0.78	0.00	0.56	0.00	0.00	0.00	0.00	0.00	0.00	0.00
MnO	58.50	68.10	65.33	67.71	67.37	65.94	63.72	65.05	65.19	64.62	64.95	40.72	40.71	48.72	48.08
MgO	1.07	0.72	0.36	0.56	0.48	0.37	0.43	1.36	1.38	1.38	0.56	0.77	0.95	0.70	0.66
CaO	0.03	0.02	0.05	0.03	0.03	0.03	0.04	0.05	0.03	0.04	0.05	4.33	5.35	3.61	4.15
Na ₂ O	0.02	0.00	0.00	0.00	0.03	0.01	0.00	0.00	0.01	0.00	0.02	0.03	0.00	0.01	0.00
K ₂ O	0.00	0.00	0.00	0.01	0.00	0.00	0.00	0.00	0.00	0.00	0.00	0.01	0.01	0.01	0.00
F	0.00	0.00	0.00	0.00	0.00	0.00	0.00	0.00	0.00	0.00	0.00	0.00	0.00	0.00	0.00
Cl	0.00	0.00	0.00	0.00	0.00	0.00	0.00	0.00	0.01	0.00	0.00	0.06	0.01	0.02	0.00
Total	100.11	99.87	100.09	100.30	100.59	99.90	99.53	99.58	99.17	99.56	99.57	100.03	100.11	100.44	100.20
Si	0.991	0.968	0.989	0.981	0.916	0.910	0.882	0.856	0.851	0.848	0.842	0.985	0.982	0.969	0.971
Al	0.000	0.000	0.000	0.001	0.000	0.000	0.000	0.000	0.000	0.000	0.000	0.000	0.001	0.000	0.005
Ti	0.000	0.000	0.002	0.008	0.064	0.076	0.118	0.130	0.139	0.148	0.159	0.000	0.000	0.000	0.000
Fe ³⁺	0.000	0.000	0.000	0.013	0.000	0.020	0.000	0.014	0.000	0.000	0.000	0.031	0.036	0.039	0.034
Fe ²⁺	0.304	0.070	0.137	0.051	0.086	0.085	0.138	0.065	0.064	0.078	0.088	0.117	0.091	0.000	0.000
Cr	0.001	0.001	0.000	0.000	0.000	0.000	0.001	0.000	0.000	0.000	0.001	0.000	0.000	0.000	0.000
Mn	1.658	1.956	1.861	1.921	1.928	1.895	1.839	1.872	1.886	1.858	1.878	0.741	0.737	0.885	0.874
Mg	0.053	0.036	0.018	0.028	0.024	0.019	0.022	0.069	0.070	0.070	0.028	0.025	0.030	0.023	0.021
Ca	0.001	0.001	0.002	0.001	0.001	0.001	0.001	0.002	0.001	0.001	0.002	0.100	0.123	0.083	0.095
Na	0.001	0.000	0.000	0.000	0.002	0.001	0.000	0.000	0.001	0.000	0.001	0.001	0.000	0.001	0.000
K	0.000	0.000	0.000	0.000	0.000	0.000	0.000	0.000	0.000	0.000	0.000	0.000	0.000	0.000	0.000
Cations	3.009	3.032	3.009	3.004	3.021	3.007	3.001	3.008	3.012	3.003	2.999	2.000	2.000	2.000	2.000

calculated as Fe^{3+} hence the $Fe/(Fe + Mg)$ and $Fe/(Fe + Mg + Mn)$ ratios are 0 (Tab. 4). In addition, rhodonite-1 forms the outer rim-2 of spessartine rim-1 and both rims were gradually formed at the Fe skarn (Fig. 4). The knebelite was not found in those rim-2 of rhodonite-1 however the prismatic **cummingtonite** is in the rhodonite-1 frequently occurring and cracks in that rhodonite-1 are filled with quartz, stilpnomelane and baryte (Fig. 4e). Found cummingtonite is zoned and in its core the $Fe/(Fe + Mg)$ ratio ranges from 0.47 to 0.56 and the $Fe/(Fe + Mg + Mn)$ is from 0.35 to 0.39. The rim of cummingtonite shows higher values of $Fe/(Fe + Mg)$, which ranges from 0.69 to 0.71 and the $Fe/(Fe + Mg + Mn)$ is from 0.48 to 0.49. Towards the outer rim-2 and in cracks of Fe skarn the core of cummingtonite was frequently replaced by the grunerite (Fig. 4d). In this position the grunerite has the same value of $Fe/(Fe + Mg) = 0.68-0.72$ as the rim of cummingtonite from those zoned grains, but values of $Fe/(Fe + Mg + Mn) = 0.60-0.64$ are higher in grunerite that had growing on cummingtonite (Tab. 2). Grunerite, frequently occurs with a mix of kutnahorite and spessartine, is prismatic, homogeneous and younger than cummintonite (Fig. 4b-c).

The origin of tephroite, Ti-rich tephroite, knebelite, rhodonite-1, rhodonite-2, cummingtonite and grunerite were successively formed by reactions of 20–32 where the SiO_2 component determined and controled the crystalline system of that assemblage.

The origin of minerals in second metamorphic stage is described by the relationships of minerals and by empiric reactions 7–32. Some reactions were confirmed experimentally and this allowed to determine the P-T conditions of Mn skarn formation in the Čučma area. Using the reaction 21 and experimental study of the stability field between manganosite and tephroite the formation of tephroite was calculated in the range from 640 to 700 °C according to Beardi & Tracy (2002). The pair of rhodonite-1 ($CaSiO_3 = 9.97-12.25$ mol.%) rhodonite-2 ($CaSiO_3 = 8.02-9.54$ mol.%) were formed in $MnSiO_3-CaSiO_3$ system by the reaction 27. Contents of $CaSiO_3$ in rhodonites show their crystallization in the stability field of rhodonite at over 600 °C and pressure lower than 4 kbar (Ito, 1972; Broun et al., 1980; Akimoto & Syono, 1972). According to the experiments with composition of grunerite $Fe_7Si_8O_{22}(OH)_2$ molecule in the Fe-rich amphibole, an thermo-barometer was determined by Fonarev et al. (1977) and Gilbert et al. (1982). In studied grunerite the molecule of $Fe_7Si_8O_{22}(OH)_2$ ranges from 58.84 to 64.06 mol.% and using that thermo-barometer the grunerite formation reached 625–675 °C in the pressure limit from 2 to 4.9 kbar. Evaluating the above data, the P-T formation of Mn skarn around 600–650 °C and pressure from 2 to 5 kbars in the amphibolite facies were deduced.



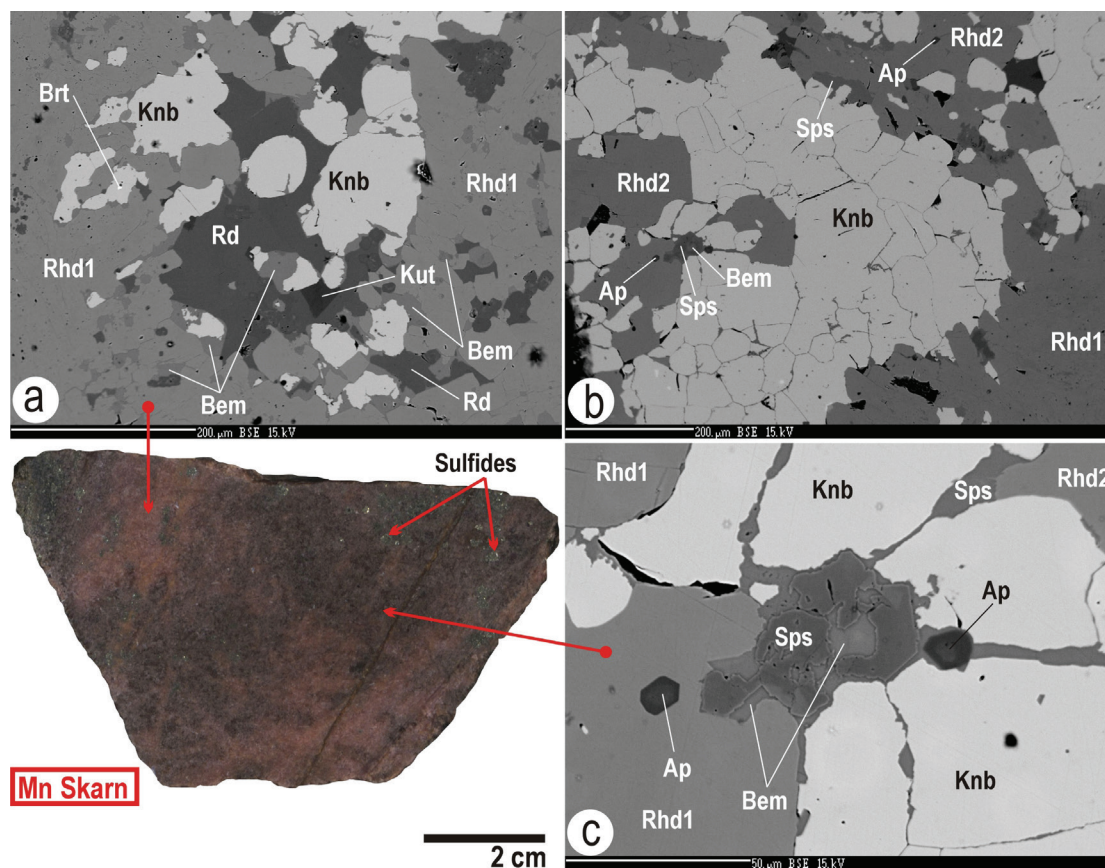
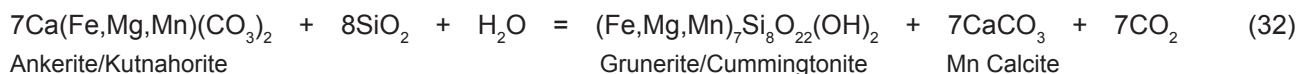
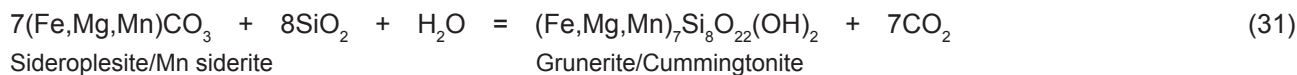
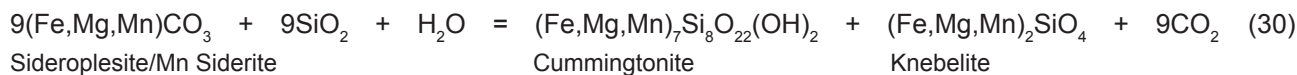


Fig. 9. Rose part of Mn skarn is composed by aggregates of two modes of rhodonite (Rhd-1, Rhd-2), knebelite (Knb), bementite (Bem) and by relicts of rhodochrosite (Rd), kutnahorite (Kut) and fluorapatite (Ap). Amphibolite facies.

Third stage of skarn formation in retrograde metamorphism of stilpnomelane-chlorite zone

Third stage of skarn formation hydrated and replaced the unstable minerals of previous two stages by Si, Ba, H₂S and H₂O bearing fluid phase. Mineral assemblage of the third stage are: Ca-rich spessartine, bementite, pyrochroite, quartz, pyrolusite, baryte, chlorite and stilpnomelane. This

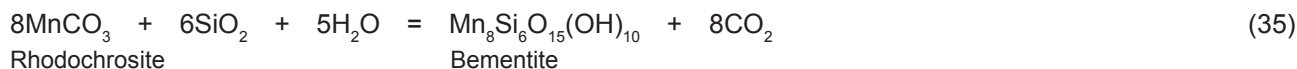
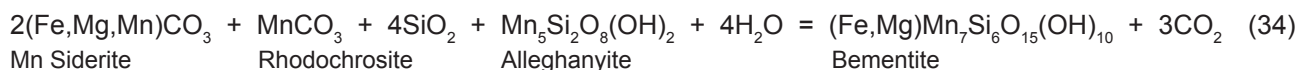
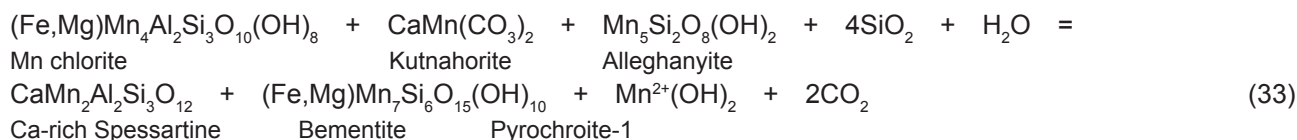
mineral association was formed in descending order with decreasing temperature from amphibolite facies to the stilpnomelane-chlorite zone in retrograde metamorphism. The onset of retrograde phase is indicated by spots of **Ca-rich spessartine** in the matrix of spessartine. Its formation is described by reaction 33 and detailed position of Ca-rich spessartine is given in the previous text (Figs. 2b and 5).

The **bementite** usually replaced rhodochrosite, rhodonite-1 and spessartine (Figs. 2a, 7e and 9a-c). Reactions 33–35 show its formation. The forming of **bementite** has two modes of occurrence and its chemical composition depends on the composition of the former mineral that bementite has replaced. The bementite $(\text{Fe}_{0.32-0.34}\text{Mg}_{0.16-0.22})\text{Mn}_{7.47-7.55}(\text{Al}_{0.05-0.08}\text{Si}_{5.90-5.95})\text{O}_{15}(\text{OH})_{10}$, which replaced the spessartine, has a uniform Fe/(Fe + Mg + Mn) ratio 0.04 (Figs. 2a, 9c). However in the bementite that replaced the rhodochrosite and rhodonite-1 the ratio ranges from 0.09 to 0.18 and that bementite is Fe-rich $(\text{Ca}_{0.01-0.07}\text{Fe}_{0.68-1.47}\text{Mg}_{0.17-0.54})\text{Mn}_{6.26-6.80}(\text{Al}_{0-0.50}\text{Si}_{5.50-6.08})\text{O}_{15}(\text{OH})_{10}$ (Figs. 7a, 9a-b; Tab. 4). In the case of empiric reaction 34, where bementite formation originated from the association of Mn-rich siderite, rhodochrosite and alleghanyite, the increased Fe content in that bementite come from the Mn-rich siderite source. Like bementite, the **pyrochroite** has two modes of occurrence as well, depending on the composition of minerals that the pyrochroite replaced. The pyrochroite-1 $(\text{Si}_{0.07}\text{Fe}_{0.02}\text{Mn}^{2+}_{0.82})(\text{OH})_2$ has the Fe/(Fe + Mg + Mn) ratio of 0.03 like bementite that replaced the spessartine (0.04), indicating coexistence of both minerals and as well as indicating the identical composition of H₂O bearing fluid phase, from which they were formed. The pyrochroite-1 usually replaced the host tephroite along cracks and therefore the pyrochroite-1 contains variable SiO₂ in the range from 5.24 to 5.43 wt.%. The SiO₂ content in pyrochroite-1 comes from the replaced tephroite (Fig. 7a). In the pyrochroite-2 $(\text{Ca}_{0.08-0.09}\text{Mg}_{0.04}\text{Fe}_{0.01-0.07}\text{Mn}^{2+}_{0.79-0.85})(\text{OH})_2$ the Fe/(Fe + Mg + Mn) ratio ranges from 0.01 to 0.08. That pyrochroite-2 frequently replaces the former Mn-rich carbonates and spessartine and this is why pyrochroite-2 is free of SiO₂ (Fig. 2c, Tab. 2). Empirical reactions 33 and 36–38 describe the formation of pyrochroite.

The **pyrolusite** (Mn⁴⁺)O₂ create a homogeneous a black mass, usually amorphous, often with a granular, fibrous

or columnar structure, sometimes is forming a reniform crusts on the individual Mn skarn segments (Fig. 2). The pyrolusite preferably replaces the Mn-rich carbonates in the Mn skarn and was formed according to the reaction 39 (Fig. 6d). Homogeneous **baryte** BaSO₄ frequently occurs in Mn skarn however no baryte was found in the part of Fe skarn (Figs. 4b, 6d–e and 7c). The baryte position to other minerals depends on the cut by which the thin section was made. Therefore, it sometimes takes the form of pseudo inclusion (Figs. 4e, 7c and 9a). Elsewhere, baryte occurs in the form of agglomerates or fills cracks in the Mn skarn (Figs. 6d–e and 7). Other minerals of the third stage of skarn formation are the **chlorite and stilpnomelane**. The stilpnomelane forms prismatic grains namely in cracks and it is rich of Mn with the Mn/(Fe + Mg + Mn) ratio about 0.74 in the matrix of Mn bearing part of skarn. The stilpnomelane occurs also at the rim in Fe bearing part of skarn, where it occurs with maghemite. In stilpnomelane the Mn/(Fe + Mg + Mn) ratio is 0.11 (Fig. 4). The occurrence of stilpnomelane in Fe and Mn skarns shows the different composition of stilpnomelane formulas according to the Mn/(Fe + Mg + Mn) ratio. These ratios are controlled by the place of the stilpnomelane formation however their formulas always show the ferric base in both mode of stilpnomelanes occurrence (Tab. 2). The ferric contents and a different Mn ratio precludes the possibility that stilpnomelane is a coexisting mineral with grunerite or cummingtonite.

Chlorite and stilpnomelane are the indexed minerals of the stilpnomelane-chlorite zone, which ranges within 320–370 °C in the Gemic unit (Radvanec & Gonda, 2019). In skarn formation on Čučma locality the stilpnomelane-chlorite zone is the retrograde metamorphic phase. The third retrograde stage of skarn formation in stilpnomelane-chlorite zone in Čučma area is described by reactions 33–39 and by projection of minerals in tetrahedrons (Fig. 10).





The skarn geochemistry in comparison to reference granites and position of skarn to related metamorphic-magmatic-hydrothermal mineralization

Three representative samples of skarns were analyzed to elements including REE contents. First sample, representing the Fe skarn, is rich of maghemite, second sample, representing metasomatic part has a predominance of rhodochrosite–kutnahorite and third sample representing Mn skarn, includes spinels, Mn/Ti olivines, rhodonite and amphiboles (Tab. 5). According to the procedure of Sun and McDonough (1989), the normalized REE contents distinguish two groups of these skarn samples. First group of Fe bearing part with maghemite and the metasomatic Mn skarn section with a predominance of rhodochrosite and kutnahorite are identically compared with the upper crust. It means that the Mn bearing fluid phase of chlorite-apatite zone that replaced the former limestone to create the Mn-rich carbonates and maghemite was derived from the upper crust source (Fig. 11). Second group represents the metamorphic overprint and formation of Mn skarn in the prograde amphibolite facies and retrograde metamorphic stage in stilpnomelane-chlorite zone. These metamorphic

stages are in good agreement with the formation, influenced by the fluid phase, which has originated from the primitive mantle (Fig. 11). Both groups of the “upper crust” and the “influence of the mantle” were also determined in others mineralizations that were formed during the Permian metamorphic-magmatic-hydrothermal (MMH) cycle in Paleo-Gemeric region. The “upper crust” mineralization is in good accordance of the Lower and Middle Permian events and the “influence of the mantle” was found in mineralizations which were formed in the Middle and Upper Permian (Radvanec & Gonda, 2019).

The Permian metamorphic-magmatic cycle is represented by individual facies of orogenic metamorphism, by S-type granites and by their effusive equivalents (andesite, dacite, rhyolite, basalt) on the surface (Grecula et al., 2009; Radvanec & Grecula, 2016; Vozárová & Vozár, 1988). Permian period is characterized by the low- to medium pressure metamorphism with high temperature gradients in the range of 40–50 °C/km. This extreme overheating of the Paleo-Gemeric region in Permian caused regional metamorphism which culminated with S-type anatectic granite magmatism in amphibolite facies (Radvanec et al., 2007, 2009, 2017; Radvanec & Grecula, 2016; Radvanec

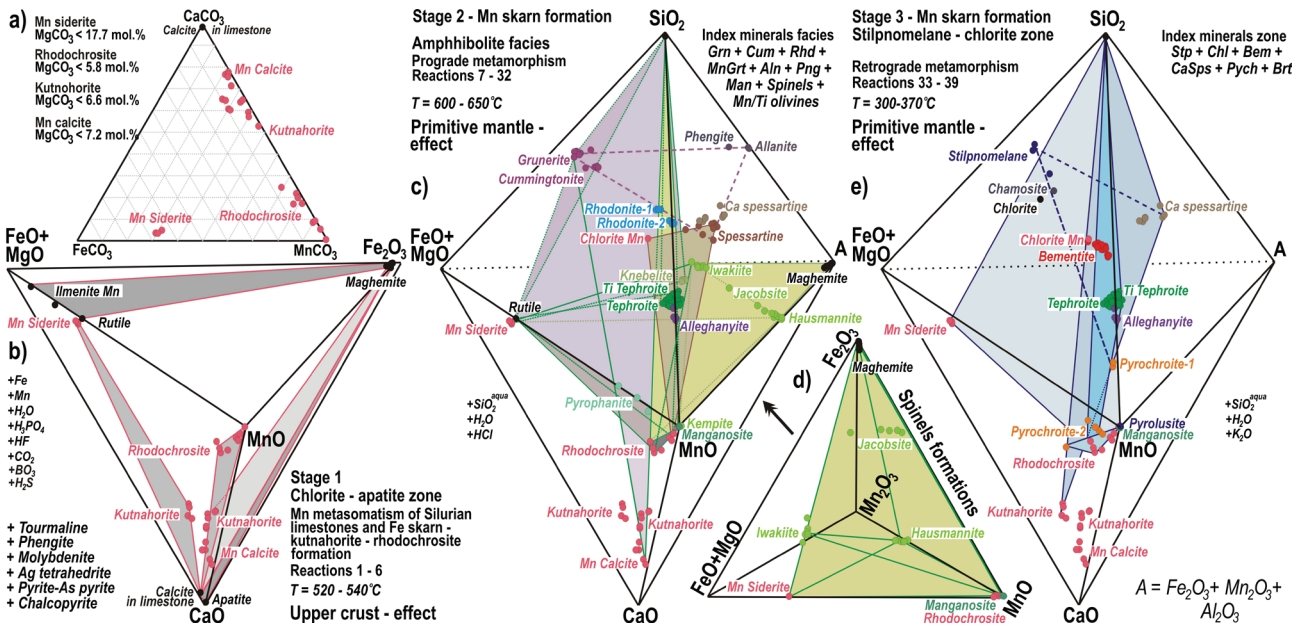


Fig. 10. Projections of minerals according to three successive stages of Fe and Mn skarns formation in triangle diagrams and in individual tetrahedrons that are united by the common base. **a** – Classification of carbonates. **b** – Minerals projection of chlorite-apatite zone in first metasomatic stage and related empiric reactions. **c** – Minerals projection of prograde metamorphism of amphibolite facies in second stage and related empiric reactions of the skarn formation. **d** – Spinel projections in tetrahedron related in the second stage of the skarn formation. **e** – Minerals projection of retrograde metamorphism in third stage of stilpnomelane-chlorite zone and related empiric reactions of the skarn formation.

& Németh, 2018). The Permian MMH cycle was a product of the final (collisional) stage of earlier subduction and related to the volcanic arc magmatism, having mentioned two modes: (1) Older cycle (281–273 Ma) producing porphyric granites of volcanic arc (VAG), cassiterite greisen, apatite-xenotime stockworks, maghemite-cassiterite-ankerite skarn, as well as andesite (K-CAB) and U-rich SedEx mineralization in the North-Gemic zone, having source in the upper crust. (2) Younger cycle (263–251 Ma) had the mantle influence and produced differentiated syn-collisional granites (syn-COLG) with cassiterite-tourmaline-Fe, as well as tourmaline-molybdenite-Fe carbonates greisens, maghemite-cassiterite-Fe carbonate-FeZnCu-BiTeIn sulfides bearing skarn and related Mg-Fe metasomatites, Sb-rich sulfides-tourmaline-Fe carbonates veins, siderite-sulfides veins and rhyolite (K-CAB) with related U Mo-Cu-rich SedEx breccia. According to the Re-Os dating of molybdenite and cassiterite there has been found that mineralization in the Permian cycle formed within an interval of 268–256 Ma and lasted 12 Ma (Kohút & Stein, 2005; Kohút et al., 2013). The igneous cycle lasted 30 Ma

from 281 to 251 Ma (Radvanec et al., 2004, 2007, 2009, 2010; Radvanec & Grecula, 2016; Vozárová & Vozár, 1988; Vozárová et al., 2015; Radvanec & Gonda, 2019). The influence of primitive mantle in younger magmatic cycle in the period of 269–251 Ma indicates that in this period the subducted rocks were melted in deeper part of subduction zone together with the mantle. This deep-located melting in the mantle results in differentiated granitic melt with the mantle influence, found in medium- and fine-grained granites and their effusive equivalent – rhyolite (Radvanec et al., 2007, 2009, 2017; Radvanec & Grecula, 2016; Radvanec & Gonda, 2019; Fig. 11).

Contents of elements in those three parts of skarn in Čučma locality were normalizing by the reference contents of anatectic S-type granites concordantly with the methodology described above. Along with granites the related mineralization were formed in the hotlines above the subduction zone during the Permian development of Paleo-Gemicum according to the MMH cycle of Radvanec et al. (2009) and Radvanec & Gonda (2019). This MMH cycle shows the development of

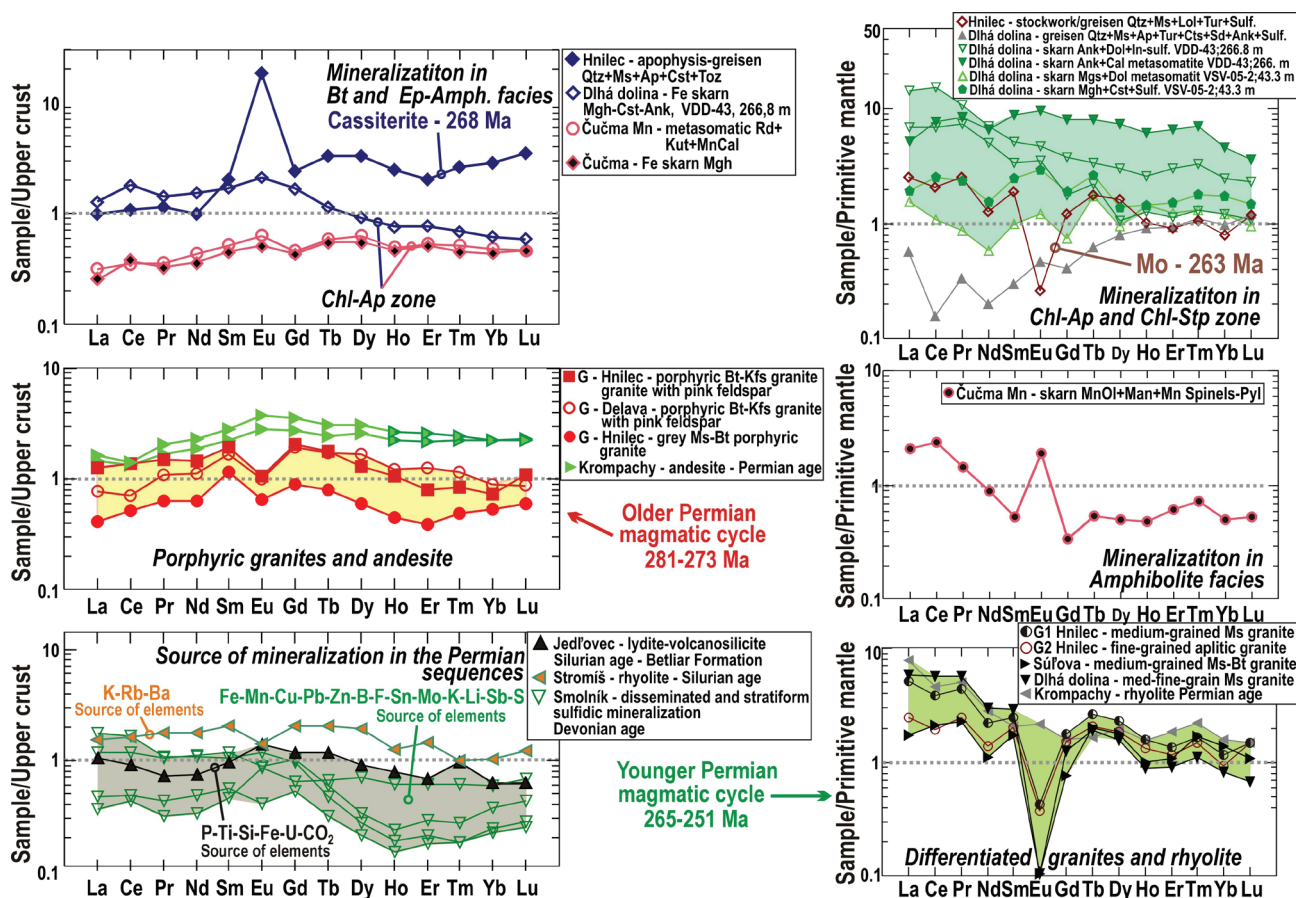


Fig. 11. Classification of Permian metamorphic-magmatic-hydrothermal cycle with the REE contents normalization and related ages. First group is classified by the REE normalization as a group identical with the upper crust and having Lower to Middle Permian age. Second group is according to contents and REE normalization identical with primitive mantle, having Middle to Upper Permian age. Skarns and comparable rocks are reported by Radvanec & Gonda (2019) and in Table 5. Normalization on upper crust and primitive mantle is according to Sun & McDonough (1989).

hydrothermal mineralization from the deep-rooted zone of the amphibolite and epidote-amphibolite facies, including anatectic melting to volcanic-exhalation mineralization of SedEx on the surface. To identify source rocks that have primary anomalous contents of elements, numerous reference Lower Paleozoic rocks were analysed to identify rock from which element was released into the fluid phase on the Permian hotline. Such a pre-Permian rock is the Silurian lydite, with the source association of P-Ti-Si-U-CO₂ and Silurian rhyolite with K-Rb-Ba source association. According to zonality of Devonian stratabound sulfidic mineralization of the Smolník type, from the vent centre on the sea floor, the metabasalt samples with disseminated sulfides were separately normalized in the central and transitional zones. That sulfidic and zoned mineralization was a source of elements Fe-Mn-Cu-Pb-Zn-B-F-Sn-Mo-K-Li-Sb-S. In the metamorphic facies and during the anatectic melting in the amphibolite facies, the elements were released from those source rocks into Permian fluid phase (Figs. 11 and 12, Tab. 5).

The gradual development of skarns formation in the Čučma area is compared to other skarns and greisen that were formed and identified in epidote-amphibolite facies or in the related biotite zone, in the chlorite-apatite and stilpnomelane-chlorite zone in Gemeric unit respectively. Three samples of Čučma skarns were compared using normalization to reference granite and added to the MMH cycle (Fig. 13). The grey muscovite-biotite (Ms/Bt) porphyric anatectic granite G from the Hnilec locality is a reference rock for the Lower and Middle Permian mineralizations – according to normalized REE contents identical with the upper crust. In this case the porphyric anatectic granite G has indistinct negative Eu anomaly, indicating the plagioclase origin from anatectic melt not differentiated in hot line on which the granite was formed (Fig. 11). So the contents of elements in porphyric granite G represent the reference upper crust, which underwent anatectic melting without a magmatic differentiation. The samples of hydrothermal mineralization as well as andesite samples from the Permian MMH cycle were normalized and compared in isocones to this crust (Fig. 13). In the Čučma area the fluid phase from the upper crust source created Fe bearing part and metasomatic part with rhodochrosite – kutnahorite of skarn, where contents of Fe-Mn-Ca-Cu-Zn-Ni-S are anomalous and Na-K-Sn-B-W-As association are depleted in comparison to reference porphyric granite G (Fig. 13; Radvanec & Gonda, 2019).

The reference rock for the second group of samples with the primitive mantle influence is represented by the fine-grained aplitic granite G2 from the Hnilec locality (Fig. 11). Contents of normalized REE in this granite, identical with primitive mantle, show a distinct negative Eu anomaly, related to the origin of plagioclase – albite from

differentiated anatectic magma. The element contents in this fine-grained aplitic granite G2 represent a rock which underwent magmatic differentiation. Analyses of skarns and greisens of amphibolite facies, chlorite-apatite and stilpnomelane-chlorite zones with the primitive mantle nature and Permian rhyolite analyses were compared to this granite G2 in isocones (Fig. 14). The Mn skarn with spinels, Mn/Ti olivines, rhodonite and amphiboles from Čučma locality has positive Eu anomaly and according to primitive mantle influence, the isocone shows Mn-Mo-Cu-Zn-Co-Ba-V anomalies in comparison to reference aplitic granite G2. That Mn skarn of amphibolite facies is depleted of K-Rb-Li-Nb-Sn-W-Sb-Cs elements (Figs. 11 and 14). The source rock for the formation of Fe bearing part and metasomatic Mn bearing part with rhodochrosite-kutnahorite are the mentioned central and transitional Fe and Mn-rich zones of former fluid outflow from the vent centre on the sea floor. The sea floor metabasalt with these disseminated sulfides was recognized in Devonian stratiform sulfide mineralization of Smolník type. The source of Ba, which is bound by baryte is from Silurian rhyolite in the Čučma skarn. Mineral associations and chemical composition of analysed samples of stratiform sulfidic mineralization confirm that the Silurian and Devonian mineralization is a main source of elements to Permian MMH cycle (Figs. 11 and 12).

Studying gradual formation of Fe and Mn skarns in the chlorite-apatite zone, then in the amphibolite facies and finally in the stilpnomelane-chlorite zone on the locality Čučma, closes the type variations of Mn-, Mg- and Fe-metasomatic/metamorphic and skarns mineralization in the former Silurian limestones. In the greenschists facies these limestones were usually replaced to the ankerite and siderite on several localities, like the siderite deposit Manó near Nižná Slaná. On the locality Dlhá dolina that former limestone was replaced to the dolomite, magnesite and to Fe skarn in the stilpnomelane-chlorite zone respectively (Grečula et al., 1995; Radvanec et al., 2010; Radvanec & Gonda, 2019). However most of the Silurian limestone layers were not metasomatically transformed and layers are still presents as marbles or metalimestones bodies in different occurrences from greenschists to amphibolite facies in Gemeric unit (Grečula et al., 2009).

Conclusions

Two lenticular ore bodies of Mn bearing skarn, closing a segment of Fe skarn, are located near the Čučma village, about 6 km north-east of Rožňava town in the Gemeric unit of the Internal (Inner) Western Carpathians. Skarns were formed in three successive stages. The first stage metasomatically replaced the former Silurian limestones lenses into of Mn-rich calcite, kutnahorite, rhodochrosite,

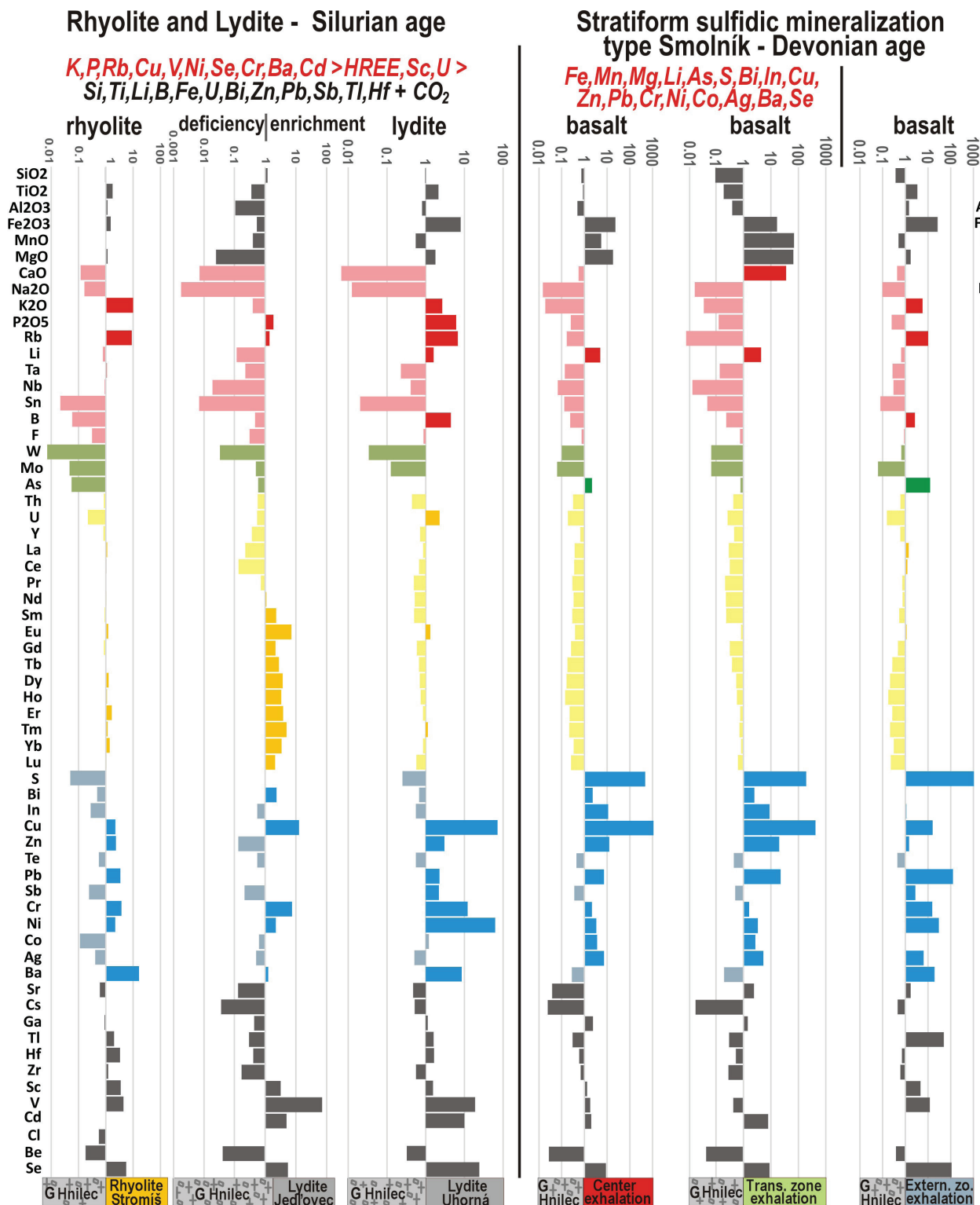


Fig. 12. The enrichment, depletion or isoconcentration – isocon of elements contents after their normalization in rhyolite (Tab. 5), lydites and samples of zonal stratabound sulfidic mineralization of the Smolník type was reported by Radvanec & Gonda (2019). According to sample classification by REE contents normalization to upper crust, the normalization logarithmically visualized the relation with the reference grey Ms/Bt porphyritic granite G from the Hnilec locality. This normalization to granite G shows, which elements from rhyolite, lydites and stratabound mineralization were mobilized to metamorphic-magmatic-hydrothermal cycle in Permian.

Tab. 5
Bulk composition of rocks.

Rock	Fe skarn	Mn skarn	Mn Skarn	Rhyolite	Granite	Granite
Locality	Čučma	Čučma	Čučma	Stromiš	Súľová	Dlhá dolina
Assemblage	Mgh	Mn Carbonates	Ol.Man.Spinel. Pyl	Kfs	Ms-Bt	Ms
Stage/Metamor.	1	1	2 and 3	Greenschist	Amphibolite	Amphibolite
SiO ₂ %	17.50	25.50	1.58	70.80	75.40	74.60
TiO ₂	0.06	0.13	< 0.01	0.37	0.03	0.02
Al ₂ O ₃	1.77	4.48	0.10	15.20	13.40	15.00
Fe ₂ O ₃	55.60	3.18	0.87	1.58	1.17	0.62
MnO	8.98	43.80	85.70	0.02	0.07	0.03
MgO	1.75	0.67	0.08	0.28	0.03	0.27
CaO	6.33	7.90	0.44	0.08	0.19	0.94
Na ₂ O	0.13	0.03	0.04	1.00	3.65	5.16
K ₂ O	0.08	0.02	0.01	10.50	4.13	1.48
P ₂ O ₅	0.32	0.11	< 0.01	0.08	0.20	0.58
S	0.39	0.18	0.08	< 0.02	< 0.02	< 0.02
Cl	< 0.01	< 0.01	< 0.01	< 0.01	< 0.01	< 0.01
F	0.07	0.07	< 0.05	< 0.05	0.26	1.12
LOI	7.41	13.2	9.87	0.65	0.93	0.87
SO ₃ %	0.05	0.35	< 0.02	< 0.02	< 0.02	< 0.02
Rb mg/kg	4.1	1.3	0.3	161	739	488
Li	3.9	6.8	0.4	13.2	387	180
Ta	0.4	0.4	< 0.01	1.2	4.9	14.6
Nb	3.21	4.85	0.03	10.8	15.6	49.9
Sn	10	5	18	3	31	85
B	< 1	< 1	9	1	223	39
W	3	9	< 2	< 2	13	53
Mo	5	6	14	< 3	< 3	< 3
As	4	259	293	6	2	33
Th	2.3	3.1	< 0.5	15.2	8.6	8.7
U	0.8	2.2	< 0.5	2	4.8	21
Y	7.87	8.92	2.78	28.6	5.19	6.89
La	7.6	9.3	1.1	42	3	< 1
Ce	23.7	22.7	4.1	92.8	9.7	3.6
Pr	2.34	2.51	0.3	10.9	1.17	0.47
Nd	9.47	11.1	1.3	40.5	4.25	1.57
Sm	2.03	2.31	0.28	7.84	1.5	0.89
Eu	0.45	0.55	0.36	1.13	0.02	0.02

Tab. 5
Continuation

Rock	Fe skarn	Mn skarn	Mn Skarn	Rhyolite	Granite	Granite	
Locality	Čučma	Čučma	Čučma	Stromiš	Súľová	Dihá dolina	
Assemblage	Mgh	Mn Carbonates	Ol.Man.Spinel. Pyl	Kfs	Ms-Bt	Ms	
Stage/Metamor.	1	1	2 and 3	Greenschist	Amphibolite	Amphibolite	
Gd	1.63	1.74	0.26	6.54	0.93	0.57	
Tb	0.35	0.37	0.07	1.12	0.24	0.25	
Dy	1.94	2.17	0.39	5.81	1.2	1.35	
Ho	0.37	0.39	0.09	0.94	0.16	0.18	
Er	1.17	1.22	0.29	3.04	0.42	0.5	
Tm	0.15	0.17	0.04	0.33	0.06	0.09	
Yb	0.98	1.05	0.25	2.25	0.4	0.68	
Lu	0.15	0.15	0.04	0.37	0.05	0.08	
Bi	< 5	< 5	< 5	< 5	< 5	8	
In	< 0.05	< 0.05	0.07	< 0.05	0.13	0.12	
Cu	147	24	58	9	10	6	
Zn	290	156	479	44	66	38	
Te	< 1	< 1	< 1	< 1	< 1	< 1	
Pb	81	39	< 5	32	22	10	
Sb	7.7	13.1	< 0.5	3.4	1.3	1.1	
Cr	14	15	3	21	8	11	
Ni	58	99	154	< 4	< 4	< 4	
Co	37.9	196	175	1.1	0.5	0.4	
Ag	< 0.4	< 0.4	< 0.4	< 0.4	< 0.4	< 0.4	
Ba	261	44	1586	1013	11	24	
Sr	120	163	53	32	3	33	
Cs	11.5	0.9	< 5	8.2	53.8	22.2	
Ga	13	10.4	10.1	14.2	21.9	32.3	
Tl	0.1	< 0.1	< 0.1	1	3.4	1.3	
Hf	5.8	11.9	16	5.7	3	3	
Zr	30	23	1	164	48	28	
Sc	2.6	2.6	0.2	13.4	3.2	8.4	
V	85	38	24	42	< 1	< 1	
Cd	0.5	0.2	0.5	0.1	0.1	0.1	
Be	2.6	1.7	0.3	1.4	11.7	1.6	
Se	< 1	< 1	< 1	< 1	< 1	< 1	
Ge	mg/kg	10	20	14	2	4	10

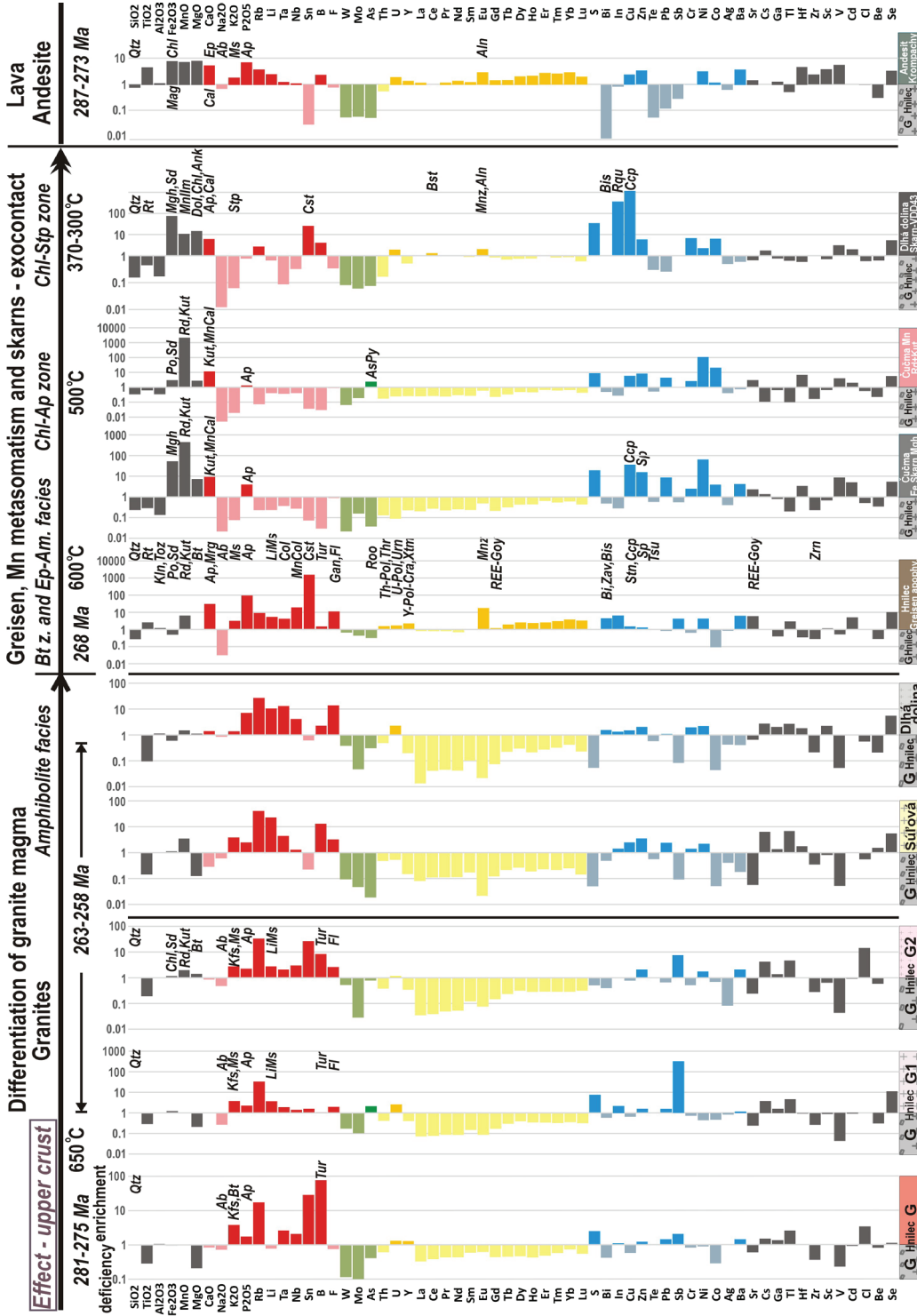


Fig. 13. Enrichment, depletion or isoconcentration – isotope of the elements contents are expressed by the ratio in logarithmic scale after normalization of elements contents of those in grey Ms/Bt porphyritic granite G, representing melting of upper crust in the Hnílec locality. The principle of isotope values is explained in the text. According to samples classification, which are the same after the REE contents normalized to upper crust, the isotope contents were calculated in the greisen from the Hnílec apophysis, Fe-bearing skarn and rhodonite-kutnahorite rich metasomatic part of Cućma locality, in the skarn of borehole V-DD-43 in Dlhá dolina. These type mineralizations are located in epidote-amphibole facies, in biotite zone, in chlorite-apatite zone and in chlorite-stilpnomelane zone, being reported by Radvanec and Gonda (2019) and in Table 5. Isocones were calculated in normalization to grey Ms/Bt porphyritic granite G, to Bt/Kfs porphyritic granite G with pink phenocrysts of feldspar, and also to medium-grained Ms granite G1, fine-grained aplitic granite G2 of Hnílec locality, to medium-grained Ms-Bt granite of Súľová, in medium-fine grained Ms granite of Dlhá dolina and andesite. According this normalization there was found that Permian granites of S-type have increasing contents of K, P, Rb, Li, Ta, Nb, but mainly Sn, B and Sb. Andesite is depleted by association Sn, W, Mo, As, Bi and Te, characterizing greisens. Anomalous ratios in isotope are marked by the abbreviation of mineral – the main bearer of anomalous element. Abbreviations are explained in mineralogical figures.

Mn-rich siderite, fluorapatite, tourmaline, phengitic muscovite, Mn-rich chlorite. The pyrite, molybdenite, galena, chalcopyrite, pyrite, sphalerite and Ag-rich tetrahedrite there occur as well. Near a contact of former limestone with metapelite, the maghemite dominates over assemblage of Mn-rich carbonates to form Fe skarn. The metasomatic first stage formed in the chlorite-apatite zone at a temperature range 520–540 °C where formation of maghemite and Mn-rich carbonates was controlled by the fluid phase, released during anatectic melting of the upper crust during the older Permian metamorphic-magmatic-hydrothermal cycle (MMH of 281–273 Ma).

In the second prograde metamorphic stage, the first-stage minerals were continuously overheated in amphibolite facies at 600–650 °C, forming minerals as follow: spessartine, alleghanyite, pyrophanite, manganosite, kempite, jacobite, iwakiite, hausmannite, tephroite, Ti-rich tephroite, knebelite, rhodonite-1, rhodonite-2, cummingtonite, grunerite and allanite. Grains formation of Ti-rich tephroite are controlled by the sector zoning and the individual sectors were quantified by TiO₂ content. In the sector with the lowest content, TiO₂ ranges from 0.14 to 0.32 wt.%, in the next sector the range is from 1.44 to 2.96 and the sector with a maximum TiO₂ content ranges from 4.83 to 6.22. In the chemical formula of the sectors, the Ti content ranges from 0.008 to 0.159 (apfu) and Si from 0.842 to 0.981 respectively. It shows that the Ti content substituted Si up to 0.159 apfu, having different content of Ti in each sectors and an immiscibility gap between the individual sectors are determined by a new Ti⁴⁺ = Si⁴⁺ substitution in the olivine group.

In the third and final stage of skarns formation, the unstable minerals of previous two stages were replaced by the Si, Ba, H₂S and H₂O bearing fluid phase to form Ca-rich spessartine, bementite, pyrochroite, quartz, pyrolusite, baryte, chlorite and stilpnomelane during the retrograde stilpnomelane-chlorite zone, ranging from 300 to 370 °C. The prograde (second) and retrograde (third) metamorphic stages produced a part of Mn skarn that has the positive Eu anomaly and was formed by the fluid phase influenced by the primitive mantle in younger MMH cycle of the Permian, according by dating in the period of 269–251 Ma.

Three successive formations of skarns describe 39 empiric reactions and the source of Fe, Mn and Ba necessary to skarns formation was released to fluid phase by anatectic melting of the Silurian rhyolite and Devonian stratabound sulfidic mineralization in the Permian amphibolite facies metamorphism.

Acknowledgement

Authors express their thanks to Ministry of Environment of Slovak Republic for funding the metallogenetic re-

search, based on the project *Raw material potential of Slovak Republic – analysis and prognostic re-evaluation of critical raw materials*. The remarks and suggestions of one anonymous reviewer and Z. Németh are greatly appreciated.

References

- AKIMOTO, S. & SYONO, Y., 1972: High pressure transformations in MnSiO₃. *Amer. Mineralogist*, 57, 76–84.
- BARTALSKÝ, J., GREČULA, P., BÁRTA, R., ROZLOŽNÍK, L., SNOPO, L., VARČEK, C., VARGA, J., ILAVSKÝ, J. & ŤAPÁK, M., 1973: Geologicko-ložisková štúdia Spišsko-gemerského rudohoria. *Spišská Nová Ves, Geol. Priesk.*
- BEARDI, J. S. & TRACY, R. J., 2002: Spinels and other oxides in Mn-rich rocks from the Hutter Mine, Pittsylvania County, Virginia, U.S.A.: Implications for miscibility and solvus relations among jacobite, galaxite, and magnetite. *Amer. Mineralogist*, 87, 690–698.
- BROWN, P., ESSENE, E. & PEACOR, D., 1980: Phase relations inferred from field data for Mn pyroxenes and pyroxenoids. *Contr. Mineral. Petrol.*, 74, 417–425.
- DE CAPITANI, C. & PETERS, T., 1981: The solvus in the system CaCO₃–MnCO₃. *Contr. Mineral. Petrology*, 76, 394–400.
- CHANG, L. L. Y., HOWIE R. A. & ZUSSMAN, J., 1998: Non-Silicates: Sulphates, Carbonates, Phosphates, Halides (Rock-Forming Minerals), 2nd Ed., Vol. 5b.
- FARYAD, S. W., 1994: Mineralogy of Mn-rich rocks from greenschist facies sequences of the Gemericum, West Carpathians, Slovakia. *Neu. Jb. Mineral., Mh.*, 10, 464–480.
- FONAREV, V. I., KOROLKOV, G. YA. & DOKINA, T. N., 1977: Experimental study of the assemblage cummingtonite + magnetite + quartz, P_T = P_{H₂O} = 1000kg/cm², NNO buffer. *Contr. Physiochem. Petrol. (Nauka, Mocsow)*, VI, 224–235.
- GILBERT, M. C., HELZ, R. T., POPP, R. K. & SPEAR, F. S., 1982: Experimental studies of amphiboles stability. *Rev. Miner.*, 9b, *Miner. Soc. Amer.*, 229–267.
- GREČULA, P., ABONYI, A., ABONYIOVÁ, M., ANTAŠ, J., BARTALSKÝ, B., BARTALSKÝ, J., DIANIŠKA, I., DUDA, R., GARGULÁK, M., GAZDAČKO, E., HUDÁČEK, J., KOBULSKÝ, J., LÖRINCZ, L., MACKO, J., NÁVESNÁK, D., NÉMETH, Z., NOVOTNÝ, L., RADVANEC, M., ROJKOVIČ, I., ROZLOŽNÍK, L., VARČEK C. & ZLOCHA, J., 1995: Mineral deposits of the Slovak Ore Mountains. Vol. 1. *Bratislava, Geocomplex*, 1–834.
- GREČULA, P. (ed.), KOBULSKÝ, J., GAZDAČKO, E., NÉMETH, Z., HRAŠKO, E., NOVOTNÝ, L. & MAGLAY, J., 2009: Geologická mapa Spišsko-gemerského rudohoria 1 : 50 000. *Bratislava, Ministerstvo život. prostr. Slovenskej republiky – Št. Geol. Úst. D. Štúra*.
- ITO, J., 1972: Rhodonite-pyroxmangite peritectic along the join MnSiO – MgSiO in air. *Amer. Mineralogist*, 57, 865–876.
- KANTOR, J., 1953: Mangánové ložisko pri Čučme. *MS. Bratislava, archive SGIDŠ*, 1–32.
- KANTOR, J., 1954: Origin of manganese ore in Spišsko-gemerské rudohorie Mts. *Geol. Práce, Zpr.*, 1, 70–71 (in Slovak).
- KOHÚT, M. & STEIN, H., 2005: Re-Os molybdenite dating of granite-related Sn-W-Mo mineralization at Hnilec, Gemeric Superunit, Slovakia. *Mineral. Petrol.*, 85, 117–129.

- KOHÚT, M., TRUBAČ, J., NOVOTNÝ, L., ACKERMAN, L., DEMKO, R., BARTALSKÝ, B. & ERBAN, V., 2013: Geology and Re-Os molybdenite geochronology of the Kurišková U-Mo deposit (Western Carpathians, Slovakia). *J. Geosci.*, 58, 271–282.
- PETEREC, D. & ĎUĎA, R., 2003: Zriedkavé minerály Mn-ložiska pri Čučme. *Natura Carpatica*, 44, 229–236.
- PETEREC, D. & ĎUĎA, R., 2009: Mangánová mineralizácia na lokalite Čučma. *Minerál*, 17, 410–414.
- MOMOI, H., 1964. Mineralogical study of rhodonites in Japan, with special reference to contact metamorphism. *Mem. Fac. Sci., Kyushu Univ., ser. D – geol.*, 15, 39–63.
- RADVANEČ, M., GREČULA, P. & ŽÁK, K., 2004: Siderite mineralization of the Gemicum superunit (Western Carpathians, Slovakia): review and revised genetic model. *Ore. Geol. Rev.*, 24, 3–4, 267–298.
- RADVANEČ, M., KONEČNÝ, P., NÉMETH, Z. & GREČULA, P., 2007: P-T-t dráha a lokálne anatektické tavenie metapelitu s prímou psamitického kremeňa vo variskej metamorfóze gemerika. *Miner. Slov.*, 39, 1–44.
- RADVANEČ, M., NÉMETH, Z. & BAIJOŠ, P. (eds.), KODĚRA, P., PROCHASKA, W., RODA, Š., TRÉGER, M., BALÁŽ, P., GREČULA, P., CICMANOVÁ, S., KRÁE, J. & ŽÁK, K., 2010: Magnesite and talc in Slovakia – Genetic and geoenvironmental models. *Bratislava, Št. Geol. Úst. D. Štúra*, 1–189.
- RADVANEČ, M., KONEČNÝ, P., ONDREJKA, M., PUTIŠ, M., UHER, P. & NÉMETH, Z., 2009: Granity gemerika ako indikátor extenzie kôry nad neskorovariskou subdukčnou zónou a pri ranoalpínskej riftogenéze (Západné Karpaty): interpretácia podľa veku monazitu a zirkónu datovaného metódou CHIME a SHRIMP. *Miner. Slov.*, 41, 381–394.
- RADVANEČ, M. & GREČULA, P., 2016: Geotectonic and metallogenetic evolution of Gemicum (Inner Western Carpathians) from Ordovician to Jurassic. *Miner. Slov.*, 48, 104–118.
- RADVANEČ, M., NÉMETH, Z., KRÁE, J. & PRAMUKA, S., 2017: Variscan dismembered metaophiolite suite fragments of Paleo-Tethys in Gemic unit, Western Carpathians. *Miner. Slov.*, 49, 1–48.
- RADVANEČ, M. & NÉMETH, Z., 2018: Variscan epidote-eclogite, blueschists and pumpellyite actinolite facies Cpx/Sr-rich epidote-metagabbro blocks exhumed in Carboniferous, with Permian amphibolite facies overprint (Gemic unit, Western Carpathians). *Miner. Slov.*, 50, 55–99.
- RADVANEČ, M. & GONDA, S., 2019: Genetic model of Permian hydrothermal mineralization in Gemicum unit (W. Carpathians) from the deep-seated zone of anatectic melting to volcanic-exhalative SedEx mineralization on the surface. *Miner. Slov.*, 52, 109–156.
- ROJKOVIČ, I., 1999: Manganese mineralization in the Western Carpathians, Slovakia. *Geol. Carpath.*, 50, 191–192.
- ROJKOVIČ, I., 2001: Early Paleozoic manganese ores in the Gemicum Superunit Western Carpathians, Slovakia. *Geolines*, 13, 34–41.
- RUŽIČKA, P., BAČÍK, P., MYŠĽAN, P. & KURYLO, S., 2020: Grossular and diopside in crystalline limestone from the locality Čučma-Čierna baňa (Slovak Republic). *Bull. Mineral. Petrol.*, 28, 1, 94–104, ISSN 2570-7337.
- SUN, S. S. & McDONOUGH, W. F., 1989: Chemical and isotopic systematics of oceanic basalts; implications for mantle composition and processes. In: Saunders, A. D. & Norry, M. J. (eds.): Magmatism in the ocean basins. *London, Geol. Soc. London*, 42, 313–345.
- ŠTEVKO, M., PLECHÁČEK, J., VENCLÍK, V. & MALÍKOVÁ, R., 2015: Hausmannite and manganosite from the Čučma – Čierna baňa manganese deposit (Slovak Republic). *Bull. mineral.-petrol. Odd. Nár. Muz. (Praha)*, 23, 1.
- VOZÁROVÁ, A. & VOZÁR, J., 1988: Late Paleozoic in West Carpathians. *Bratislava, Geol. Úst. D. Štúra*, 1–314.
- VOZÁROVÁ, A., PRESNYAKOV, S., ŠARINOVÁ, K. & ŠMELKO, M., 2015: First evidence for Permian-Triassic boundary volcanism in the Northern Gemicum: geochemistry and U-Pb zircon geochronology. *Geol. Carpath.*, 66, 5, 375–391.

Postupný vznik Fe a Mn skarnov na lokalite Čučma v gemeriku: od metasomatózy s následnou rekryštalizáciou v amfibolitovej fácií a vznikom Ti tefroitu až po retrográdnú metamorfózu v stilpnomelánovo-chloritovej zóne

Neďaleko obce Čučma asi 6 km severovýchodne od Rožňavy (Vnútorne Západné Karpaty; obr. 1) sa v gemeriku vyskytujú dve šošovkovité telesá Mn skarnu uzatvárajúce segment Fe skarnu. Skarny sa formovali v troch po sebe nasledujúcich etapách. V prvom štádiu sa metasomaticky zmenili šošovky pôvodných silúrskeho vápencov z holeckých vrstiev (Grečula et al., 2009) na Mn kalcit, kutnahorit, rodochroazit, Mn siderit, fluoroapatit, turmalín, fengitický muskovit a Mn chlorit. V tomto Mn metasomatite sa zistil aj pyrit, molybdenit, galenit, chalkopyrit, pyrit, sfalerit a Ag tetradrit. Blízko kontaktu pôvodného vápenca s metapelitom dominuje maghemit nad Mn uhličitanmi (obr. 3). Táto poloha Fe

skarnu má čiernu farbu, je slabob magnetická a je prevažne jemne zrnitá (obr. 2). Metasomatóza pôvodného vápenca vznikla v chloritovo-apatitovej zóne v teplotnom rozsahu 520 – 540 °C (Mn-karbonátový termometer; De Capitani a Peters, 1981; Chang et al., 1998), kde z fluidnej fázy uvoľnenej počas anatektického tavenia vrchnej kôry vznikol maghemit a Mn uhličitan (obr. 11). Táto metasomatóza vznikla v staršom permskom metamorfom magmaticko-hydrotermálnom cykle (MMH) v datovanom období 281 – 273 mil. r. (Radvanec a Gonda, 2019).

V druhom štádiu sa minerály prvého metasomatického štádia kontinuálne metamorfovali v amfibolitovej fácií pri 600 – 650 °C a tlaku nižšom ako 4 kbar (geotermo-

barometre; Ito, 1972; Broun et al., 1980; Akimoto a Syono, 1972; Fonarev et al., 1977; Gilbert et al., 1982). V tomto štádiu vznikla skupina Mn granátov, humity, oxidy, halogenidy, spinely, olivíny, pyroxenoidy a amfiboly. Tieto skupiny minerálov tvoria mladšiu časť Mn skarnu s nasledujúcou asociáciou: spessartín, alleghanyit, pyrofanit, manganozit, kempit, jakobsit, iwakiit, hausmannit, tefroit, Ti tefroit, knebelit, rodonit-1, rodonit-2, kummingtonit, grunerit a allanit (obr. 2 až 7).

Jednotlivé zrná Ti tefroitu sú zložené zo sektorov a jednotlivé sektory sú kvantifikované obsahom TiO_2 v hmot. % (obr. 7, tab. 4). V sektore s najnižším obsahom je obsah TiO_2 od 0,14 do 0,32 hmot. %. V ďalšom sektore je rozpätie od 1,44 do 2,96 a v sektore s maximálnym obsahom TiO_2 je jeho rozsah v rozmedzí 4,83 až 6,22 hmot. %. V chemickom vzorci sektorov je obsah Ti v rozsahu od 0,008 do 0,159 (apfu) a obsah Si od 0,842 do 0,981. V každom sektore je obsah Ti substituovaný obsahom Si postupne až do hodnoty 0,159 apfu a medzi jednotlivými sektormi sa zistila aj medzera nemiesateľnosti. Substitúciu Ti a Si medzi sektormi Ti tefroitu určuje substitúcia $\text{Ti}^{4+} = \text{Si}^{4+}$, ktorá je v skupine olivínu novozistená, rovnako ako aj Ti tefroit (obr. 8).

V tretej, poslednej fáze tvorby skarnov boli nestabilné minerály z predchádzajúcich dvoch štádií zmenené

v retrográdnej metamorfóze stilpnomelánovo-chloritovej zóny v rozmedzí od 300 do 370 °C, pričom retrográdnou metamorfózu kontrolovala fluidná fáza s obsahom Si, Ba, H_2S a H_2O . V tomto treťom štádiu vývoja Mn skarnu vznikol Ca spessartín, bementit, pyrochroit, kremeň, pyroluzit, baryt, chlorit a stilpnomelán (obr. 2 až 7).

Prográdna (druhé štádium) a retrográdna (tretie štádium) metamorfóza postupne vytvorila časť Mn skarnu, ktorý má pozitívnu anomáliu Eu. Vznik tejto časti Mn skarnu bol ovplyvnený primitívnym plášťom a vznikol v mladšom MMH cykle v období permu od 269 do 251 mil. r. (Radvanec a Gonda, 2019, obr. 11).

Tri po sebe nasledujúce štádiá vzniku Fe a Mn skarnov opisuje 39 empirických reakcií. Zdroj Fe, Mn a Ba potrebný na tvorbu hlavných minerálov a barytu v Fe a Mn skarne sa uvoľnil do fluidnej fázy počas anatektického tavenia silúrskeho ryolitu a z devónskej stratiformnej sulfidickej mineralizácie počas permskej metamorfózy v amfibolitovej fácii (obr. 10 až 14).

Doručené / Received: 17. 7. 2020

Prijaté na publikovanie / Accepted: 18. 2. 2021

Nanodegradation of chlorinated hydrocarbons from groundwater in the native geological environment (laboratory batch experiment)

HANA HORVÁTHOVÁ¹, LUBOMÍR JURKOVIČ^{2*}, JURAJ MACEK², ROMAN TÓTH²
and DENYS KRAVCHENKO¹

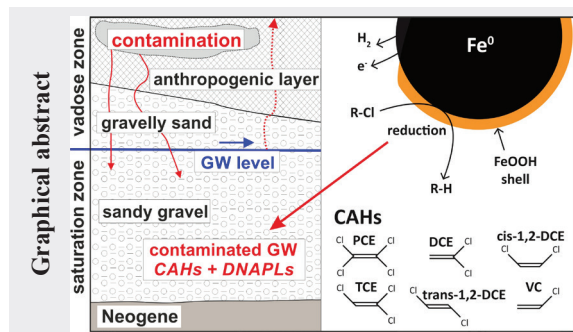
¹The Centre of Environmental Services, Ltd., Kutlikova 17, SK-852 50 Bratislava, Slovakia;
horvathova@cenvis.sk; kravchenko@cenvis.sk

²Comenius University in Bratislava, Faculty of Natural Sciences, Department of Geochemistry, Ilkovičova 6,
SK-842 15 Bratislava, Slovakia;

*lubomir.jurkovic@uniba.sk (corresp. author); juraj.macek@uniba.sk; roman.toth@uniba.sk

Abstract: Degradation of chlorinated aliphatic hydrocarbons (CAHs) by application of nanoscale zerovalent iron (nZVI) to the geological environment represents an innovative remediation procedure. For a successful process of removing hazardous pollutants from the geological environment there is necessary to carry out experiments simulating a real geological environment in a longer series of observations. This experimental study represents the nanodegradation of chlorinated ethenes using four concentrations of synthetic nZVI from the contaminated groundwater in the simulated geological conditions of model environmental burden (non-contaminated gravel). The concentration of CAHs in the closed environment decreased even without nZVI addition, but nZVI accelerated the removal of CAHs. The complete degradation of CAHs was achieved already at the lowest concentration of nZVI – 1 g.l⁻¹. No vinyl chloride has been determined after the nanodegradation, therefore it is assumed that the degradation pathway led to the formation of non-toxic products. The gravel attenuates the alkalization of the groundwater after the nZVI addition, giving a perspective to further *in situ* application. The concentrations of selected CAHs (*cis*-1,2-DCE, PCE, TCE and the sum of five CAHs) after degradation by nZVI were below the hygienic limits for groundwater according to Directive by the Ministry of Environment of the Slovak Republic No. 1/2015-7.

Key words: nZVI, nanodegradation, reduction, chlorinated aliphatic hydrocarbons, CAHs



Highlights

- Nanodegradation of chlorinated aliphatic hydrocarbons (CAHs) from the native contaminated groundwater is proposed.
- Nanoiron particles readily degrade CAHs by the mechanism of reduction
- The impact of the native geological environment on the CAHs nanodegradation is explored
- Results show the great potential for *in situ* application of nanoremediation technique

Introduction

The group of chlorinated aliphatic hydrocarbons (CAHs) belongs to the most significant environmental contaminants. They are widespread and pose a health risk already at low concentrations (Barbee, 1994). CAHs are less soluble in the water, but soluble enough to migrate through the flow of groundwater over long distances with ability to contaminate the ecosystems, which haven't been contaminated primarily (Yu & Chou, 2000). The contamination of the environment with the chlorinated hydrocarbons is the result of release into the soils and waters during their production and application, originating during the years, when its potential toxicity was no

priority. Chlorinated hydrocarbons are considered toxic even at the concentration of 5 µg.l⁻¹ due to their potential carcinogenicity (Schiefler et al., 2018).

The fate of CAHs in the environment

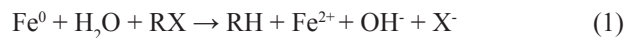
This study deals with chlorinated ethenes: vinyl chloride (VC), 1,1-dichloroethylene (DCE), *cis*-1,2-dichloroethylene (*cis*-1,2-DCE), *trans*-1,2-dichloroethylene (*trans*-1,2-DCE), trichloroethylene (TCE), perchloroethylene (tetrachloroethylene, PCE) and their removal from the groundwater with nanoscale zerovalent iron particles (nZVI) in microcosm. CAH solvents are important industrial agents used for degreasing of metals, cleaning electronic components, dissolution of rubber, removing of

oil and wax from fibers, and dry cleaning of fabrics (Bhatt et al., 2007). CAHs are used as extracting agents for fish meal, leather, oil-containing seeds, soy, coffee beans, and are important intermediates in manufacturing, especially for polyvinyl chloride (PVC) production (Barbee, 1994). Generally, the most common exposition way of CAHs is the inhalation of the contaminated air and the dermal contact with the polluted material. After ingestion, VC is transformed to the high-reactive epoxide chloroethylene-dioxide, which converts to chloroacetaldehyde and binds to DNA, therefore it is considered mutagenic. Acute poisoning with VC occurs up to a concentration of 20–50 mg.l⁻¹ with irritation of the respiratory tract and eyes. Chronic poisoning lead to “vinyl chloride disease” – summary name for the headache, liver damage, and pulmonary fibrosis, not excluding carcinoma of liver, lungs, digestive tract and brain (Frankovská et al., 2010). Breating of high concentrations of 1,2-DCE may cause nausea, vertigo, drowsiness, weakness, tremor and fatigue. Chronic exposure to TCE may cause kidney and liver cancer, the non-Hodking lymphoma, and also poses a potential hazard for noncancer toxicity to the central nervous system, immune system, male reproductive system, and the developing embryo/fetus (Chiu et al., 2013). PCE inhaled at the high concentration may be toxic to the central nervous system, liver and kidneys, the carcinogenity was proved on many animal studies, but in relation with human body, it is still a probable carcinogen (Mundt et al., 2003). Among chlorinated ethenes, only VC and TCE are classified as carcinogenic to humans by all routes of exposure (Group A) by US EPA (Rusyn et al., 2014; Walter et al., 2011).

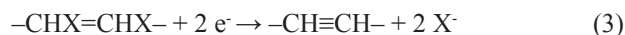
Nanoiron as the tool for CAHs degradation

Based on the chemical structure of CAHs, they are predestinated for reductive degradation, therefore one of the best options for their removal is the nanoiron. Iron is well-known due to its reduction abilities. When transferred into the nano-dimensions, iron acquires new features and properties: greater specific surface, higher concentration of reactive sites, stronger reduction capability, higher reactivity through the whole range of contaminants, including CAHs, and better mobility in the matrix. One of the most critical limitations of the use of nZVI is their tendency of agglomeration into the clusters, therefore it is recommended to provide the surface modification of nZVI, or addition of substances increasing their mobility (Stefaniuk et al., 2016; Tian et al., 2000). The options for preventing the unwanted agglomeration, passivation, and sedimentation of nZVI is covering of the nZVI particles with a layer of stabilizing compound that may cause the changes in surface charge and decrease their aggregation. The most used compounds are (bio)polymers, anionic surfactants, starch, carboxymetyl cellulose (CMC), guar gum, and polyacrylic acid. Another type of stabilization is

the emulsification of nZVI, where nanoiron particles pass to the hydrophobic medium. Encapsulation into the matrix and immobilization on the surface of matrix solves the problem of difficult separation from the remediation zone (Stefaniuk et al., 2016). CAHs are nanodegraded mainly by the mechanism of adsorption and reduction (Eq. 1),



where R is the hydrocarbon chain and X halogen. In the aquatic environment, zerovalent iron oxidizes from Fe⁰ to Fe²⁺, while releasing electrons, which is crucial for contaminant reduction. Depending on the type of hydrocarbon, the reaction can run by the mechanism of sequential hydrogenolysis (Eq. 2), taking place in the strong reductive conditions, or by reductive β-elimination (Eq. 3), which occurs when two vicious carbons in the chain are substituted by chlorine, resulting in the release of halogen as halide.



When there is a high concentration of dissolved oxygen in the water, another mechanism of action is proposed (Eq. 4). With a decreasing concentration of O₂, the redox potential drops into the anoxic values. In this case, groundwater reacts with iron by the process of corrosion with hydrogen depolarization (Eq. 5), with the formation of hydrogen, which stimulates the growth of anaerobic microorganisms with the ability of dehalogenation of contaminants. Regardless of aerobic or anaerobic dehalogenation, in the result, there is an increasement in the OH⁻ concentration, accompanied with the pH increase. In this case, it is possible to buffer the environment with solubilized CO₂ or by the addition of bicarbonates (Černík, 2010).



From the above-mentioned mechanisms, the most common pathway of CAH degradation via nZVI is a reduction, mainly α- or β-elimination. The observed products of PCE and TCE reduction include *cis*-1,2-DCE and VC (Wacławek et al., 2015). CAHs may be degraded in the natural biological environment, as well. The degradation kinetics of all biological reactions are complex and might depend on several biochemical and environmental factors. Generally, it is a first-order decay, when the biodegradation rate is primarily a function of the CAH concentration.

A conceptual anaerobic-aerobic model for biological reactions of CAHs is proposed PCE is assumed to degrade

only via the anaerobic pathway, the less-chlorinated CAHs can be degraded by both—anaerobic and aerobic mechanisms even to ethene (Clement et al., 2000). Nanodegradation of various hazardous substances is still a subject of current interest, but recently the research is focused on improving of remediation efficiency by a combination of nZVI with another physico-chemical or biological technique. PCE from artificially contaminated medium was completely removed after 6 days of simultaneous application of anaerobic microbial consortium and nZVI modified by layered double hydroxide (Wang et al., 2020). Bimetallic FePd nanoparticles incorporated in the pores of granular activated carbon was synthesized by Zhang et al. (2017) and integrate the mechanisms of reduction and absorption with 100 % removal efficacy in microcosm. The combination of nZVI stabilized with polyvinylpyrrolidone and surfactants (CTAB, SDS) enhanced the PCE degradation resulting in complete removal of TCE from the soil-water system within 3 hours (Tian et al., 2020). Application of nZVI (Nanofer 25S) and bacterial strain *Ochrobactrum anthropi* isolated from the contaminated sediment has been shown to be effective in removing of polychlorinated biphenyls (PCBs) with 99 % degradation of Delor 103 – industrial mixture of PCBs (Horváthová et al., 2019).

Taking into the account the further *in situ* application of nZVI, the toxicity of nZVI towards various trophic levels should be considered. When introduced into the environment, bacteria are the “first line” of contact with nZVI. The impact of nZVI exposure cannot be generalized, because it is strongly influenced by the bacterial strain. One of the most negative effect of nZVI exposure is the formation of reactive oxygen species (ROS), that may cause the peroxidation of membrane lipids and DNA damage (Auffan et al., 2008). For example, the reaction of *Bacillus cereus* to nZVI exposure was the accelerated entry into the sporulation phase (Fajardo et al., 2013). Several cycles of the exposure of *Pseudomonas putida* F1 to low concentration of nZVI (0.1 g.l⁻¹) led to the rise of persistent phenotype with a higher tolerance to nZVI, and complete inhibition of cell growth was observed at 5 g.l⁻¹ of nZVI (Kotchaplaí et al., 2017). The concentration of bacterial strain *Stenotrophomonas maltophilia* decreased 4 times after 140 h exposure to nZVI Nanofer 25S in the concentration of 2 g.l⁻¹ (Horváthová et al., 2019). Several studies indicate the positive effect of nZVI – effective degradation of nitrates (Shin & Cha, 2008); the formation of H⁺, that can act as a biostimulant for methanogene and sulphate-reducing bacteria (Cecchin et al., 2017); or the stimulation of growth of the Gram(+) bacteria (Němeček et al., 2014). Among water and soil organisms, a negative effect on reproduction, body mass and mortality were noted at earthworms *Eisenia fetida* and *Lumbricillus rubellus* already at concentrations above 100 mg soil kg⁻¹ (El-Temsah & Joner, 2012). The same research team

examined a collembola *Folsomia candida* and ostracods *Heterocrypsis incongruens* incubated with 1 or 10 g nZVI kg⁻¹ and observed severe toxic effects short time (7 days) after addition of nZVI, with a high mortality of adults. After 30 days, adults could survive in treated soils, while no juveniles were produced. The adverse effects of nZVI on test organisms seem temporary and reduces after oxidation of nZVI particles (El-Temsah & Joner, 2013). Yang et al. (2016) shows no significant mortality after 24 h exposure of the nematode *Caenorhabditis elegans* to environmentally significant concentration of nZVI coated with CMC, but the reproductive toxicity assays revealed that CMC-nZVI decreased offsprings in parental generation and increased the concentration of ROS. The reproductive toxicity was transferable from the F0 (parental) to F1 and F2 generations, but recovered in the F3 and F4 generations after parental exposure. The mammalian cells are the least examined group. The nZVI particles are able to overcome biological barriers and migrate through the body by absorption by the alveolus, small intestine or skin up to tissues and provoke the oxidative stress (Keane et al., 2009). Recently, the application of nZVI has been one of the commonly used environmental technologies. It is necessary to find a balance between the beneficiary effect of nanoremediation and potential toxicity of nZVI introduced into the environment.

This paper is focused on the nanodegradation of chlorinated ethenes using the synthetic nZVI dispersion Nanofer 25S (NANO IRON, s.r.o., CZ) from the native groundwater samples with CAH contamination from model locality: a) nanodegradation of CAH from the contaminated groundwater; b) nanodegradation of CAHs in the contaminated groundwater in the simulated geological environment representing real conditions of model locality. The main goal of the experiments was to define the effective concentrations of nZVI in the removal of CAH from saturation geological zone to the given hygienic limits (Indication (ID) and intervention (IT) criteria according to Directive of Ministry of Environment of the Slovak Republic No. 1-2015/7). Obtained experimental data will be used for the purposes of designing a real application of nanoremediation at the model locality of environmental burden.

Characterization of investigated problem

The contaminated groundwater has been sampled from model locality in the central part of Bratislava. The area of interest is situated in the wide center of Bratislava and is a part of a large environmental load classified as confirmed environmental burden (registered as “B1 (002) / Bratislava – Old Town – Apollo – wider area of the former refinery” in the Register of environmental burdens). In the past, the

area of interest belonged to the industrial zone of the city with industrial production facilities, which significantly affected the current environmental condition of the area. The area has been used industrially since 1896, when the former Apollo oil refinery was opened. The recent pollution represented by the free phase of petroleum hydrocarbons on the groundwater surface most likely comes from a historical accident after the bombing of the Apollo refinery during the Second World War (in 1944). Pollution of groundwater and geological environment was also increased by production facilities such as Kablo, Gumon, Heating plant ZSE and Chemika. Significant extensive pollution of the rock environment and groundwater has been confirmed by several geological surveys (e.g. Janták and Polák, 2001; Auxt et al., 2002; Maloveský et al., 2006; Jantáková et al., 2018). Important contaminants such as non-polar extractable substances, C_{10} – C_{40} , BTEX, PAHs and CAHs exceeded the ID and IT criteria several times (Directive of Ministry of environment of SR No. 1/2015-7) in the rock environment and groundwater. Nowadays, the industrial objects are mostly demolished and there is an intensive development of polyfunctional buildings and several remediation projects in the area of interest.

In the depths relevant from the point of view of potential remediation works, the geological environment is formed by rocks of Quaternary cover formations (Pleistocene to Holocene facies of Quaternary fluvial and anthropogenic sediments). Neogene sediments are found in their subsoil. The area of floodplain valley is mostly flat with altitude differences lower than 2 m and minimal slope of natural relief, which is formed by the Danube river – the dominant natural factor of area. The surface of area is formed by Neogene and Quaternary sediments and artificially settled with the anthropogenic layer (up to 5.1 m). The Quaternary formation is formed by 0.7–1.8 m thick positions of various anthropogenic sediments, and positions up to 4.0 m are present in some part of the model area (Janták & Polák, 2001). Below this layer are located original and compact sandy soils of the Quaternary alluvial complex. These are the youngest and most widespread fluvial sediments, rising in form of bottom lands of creeks and rivers (Pristaš et al., 1992). The thickness of this layer varies widely and in some areas is completely missing. Then the anthropogenic layer is in direct contact with the gravel layer. It is up to 12 m thick, with pebbles of \varnothing 1–5 cm, in the lower parts \varnothing 15–30 cm. Neogene is formed by 10.6–15.9 m thick clayey – sandy complex with pitches of gravels (Vlasko et al., 2015).

Methodology

Contaminated water sampling

Contaminated groundwater has been pumped from the hydrogeological well in central part of studied area

according to appropriate standards and technical norms into the storage container (50 l), avoiding its contact with air. Groundwater sample to determine the concentration of contaminants has been withdrawn and pH, E_c (conductivity), E_h (redox potential) values have been determined *in situ* immediately after pumping. To simulate the geological profile of the locality of environmental load, native geological substrates from drilling cores were collected. A fine gravel (fraction 4–8 mm) from the saturated zone without contamination served as the native solid samples for filling the experimental containers.

Characterization of the nZVI dispersion Nanofer 25S

The degradation of CAHs was performed by aqueous dispersion Nanofer 25S (NANO IRON, Ltd., CZ) stabilized with biodegradable organic and inorganic modifiers. The iron content: 14–18 % w/w, with the particle size > 50 nm and the specific surface > 25 m²g⁻¹. More information available at www.nanoiron.cz.

Decontamination of the groundwater with Nanofer 25S nanoparticles

Static experiment of CAHs nanodegradation processed in 2 l glass containers closed with a joint cap with 2 l of contaminated water from the storage container. Dispersion of nZVI Nanofer 25S in the concentration 0, 1, 2, and 4 g.l⁻¹ has been added. Water samples for determining of CAHs degradation have been withdrawn after 1, 3, 7, 14, 28, and 62 days.

Decontamination of the groundwater in the simulated geological environment using Nanofer 25S nanoparticles

The 5 l glass containers have been filled with inert, non-contaminated gravel with fraction 4–8 mm, representing the gravel collector of groundwater (Fig. 1). The gravel was drenched with approx. 2.5 l of contaminated water and the Nanofer 25S dispersion has been added in the same concentrations as above: 0, 1, 2 and 4 g.l⁻¹. Each container had two drain valves for H₂ release and water sampling. Water samples to determine of CAHs degradation have been withdrawn after 1, 3, 7, 14, and 28 days.

While sampling, the pH, E_c , E_h and temperature were measured in the same time intervals. pH was measured by METTLER TOLEDO Seven Compact (USA); E_c and E_h by AQUAREAD Water Monitoring Instruments (UK). Containers were mixed regularly and stored in the dark place. Water samples were immediately delivered to the laboratories. A chemical analyses of water samples were conducted in the accredited laboratories ALS Czech Republic (Praha, Czech Republic) by the gas chromatography with FID and ECD detector (method

W-VOCFID01 – CZ_SOP_D06_03_156 except chap. 9.3 (US EPA 601, US EPA 8260, US EPA 8015, RBCA Petroleum Hydrocarbon Methods) and were tested to the following CAHs: VC, *trans*-1,2-DCE, 1,1-DCE, *cis*-1,2-DCE, TCE, PCE and the sum of five chlorinated hydrocarbons.

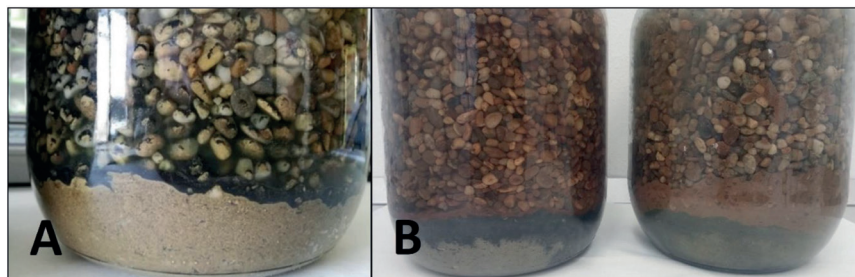


Fig. 1. Experimental setup: Container with contaminated groundwater in simulated geological environment with nZVI. A – closeup of non-contaminated gravel applied as a geological environment after nZVI application. B – closeup of model geological environment after 62 days of nZVI application.

Obtained new data and discussion

Degradation of CAHs using nZVI Nanofer 25S was carried out in the real contaminated groundwater, pumped out from the area of environmental burden and in the same contaminated water with the simulated geological environment – gravel in fraction 4–8 mm. Analysis of the CAHs concentration showed that VC, *trans*-1,2-DCE and 1,1-DCE were measured at insignificant concentrations already at the input (immediately after pumping from the well) (Tab. 1), therefore their degradation was not evaluated.

Decontamination of the groundwater with Nanofer 25S nanoparticles

Fig. 2 summarizes the nanodegradation of CAHs in the contaminated groundwater with Nanofer 25S dispersion at various concentrations (1, 2 and 4 g.l⁻¹). A bottle without the addition of nZVI served as the control of nZVI effectivity and the figure shows that the degradation of selected hydrocarbons (*cis*-1,2-DCE, TCE and PCE) runs even without the nZVI addition (Fig. 2 A). In a closed environment, PCE was degraded spontaneously in the same extent as with the nZVI particles. Various concentrations of nZVI had no effect on the degradation of CAHs, only minimal differences were observed. After 62 days of degradation, almost 100 % of 1,2-DCE, TCE, PCE and a sum of 5 CAHs was removed from the contaminated groundwater.

Decontamination of the groundwater in the simulated geological environment using Nanofer 25S nanoparticles

To approach the real conditions of the contaminated area, nanodegradation of CAHs was provided in the simulated geological environment represented with inert non-contaminated gravel. Results are summarized in Fig. 3. Obviously, degradation of all determined CAHs runs faster in the comparison of CAHs nanodegradation without gravel. Rock environment has a natural capability to

Tab. 1

Concentrations of CAHs at the input – immediately after pumping from the well and concentrations after application of nZVI in amount 1 g.l⁻¹ to the contaminated water (A) and contaminated water in simulated geological environment (B) after 1 and 62/28 days of nanodegradation.

Contaminant	Limit of determination [µg.l ⁻¹]	Concentration at the input [µg.l ⁻¹]	Hygienic limits for water* [µg.l ⁻¹]		A. Concentration in the contaminated water [µg.l ⁻¹]	B. Concentration in the contaminated water in the simulated geological environment [µg.l ⁻¹]
			ID	IT	62 days of nanodegradation	28 days of nanodegradation
Σ 5 CAHs	5.0	854	n/a	n/a	22	8.5
PCE	1.0	156	10	20	7.3	4.8
TCE	1.0	396	25	50	1.2	1.3
<i>cis</i> -1,2-DCE	1.0	299	25	50	13.5	2.4
1,1-DCE	1.0	1.1	10	20	< 1.0	< 1.0
<i>trans</i> -1,2-DCE	1.0	1.0	25	50	< 1.0	< 1.0
VC	4.0	< 4.0	10	20	< 4.0	< 4.0

ID – indication criteria, IT – intervention criteria according to Directive of Ministry of Environment of the Slovak Republic No. 1/2015 – 7 for the elaboration of risk assessment analysis of contaminated sites.

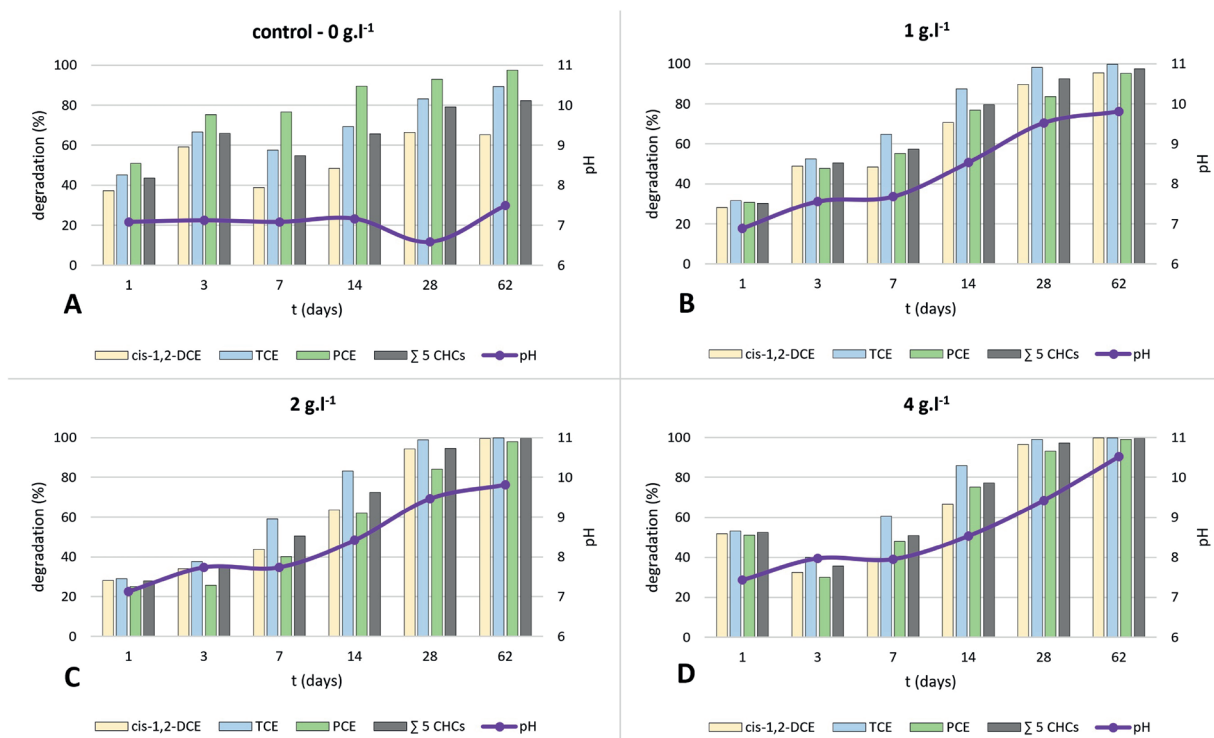


Fig. 2. Degradation of *cis*-1,2-DCE, TCE, PCE, sum of 5 CHCs from the contaminated groundwater by nanoparticles Nanofer 25S in concentration 0 – control (A), 1 (B), 2 (C), 4 g.l⁻¹ (D), and the pH course. Sampling of water for pH, E_c, and E_h after 1, 3, 7, 14, 28, and 62 days of static degradation.

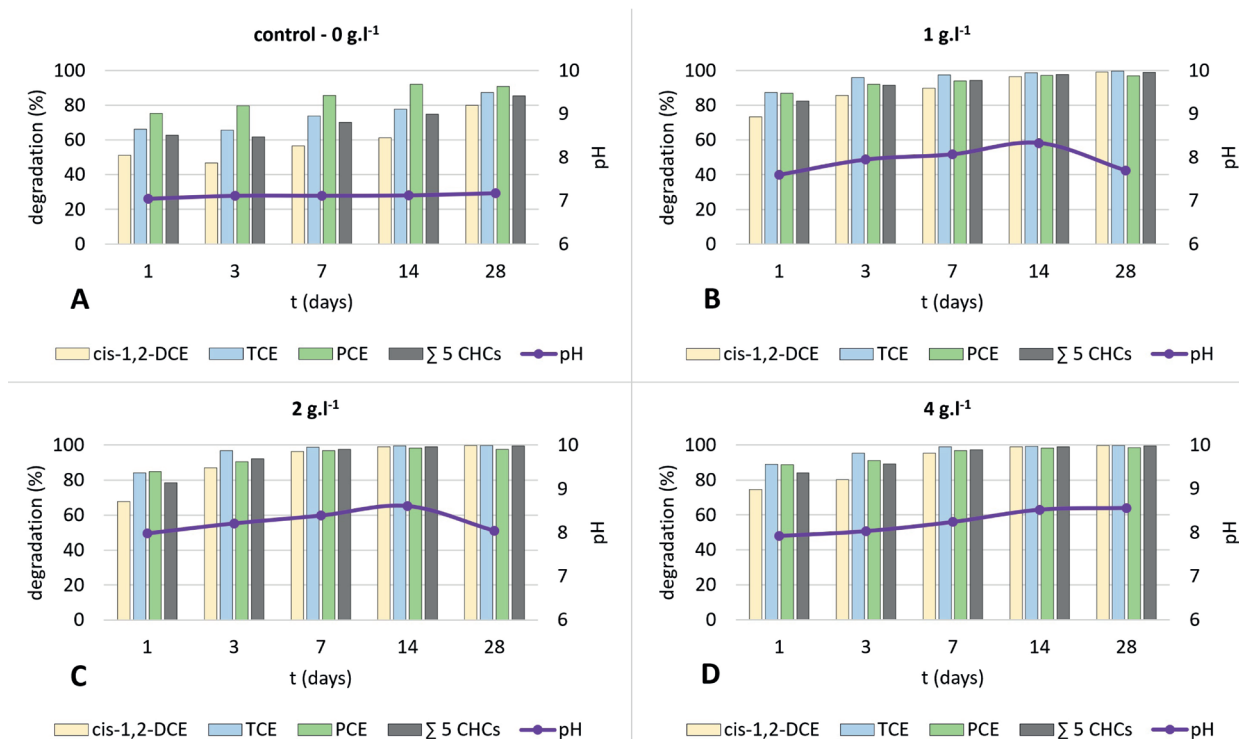


Fig. 3. Degradation of *cis*-1,2-DCE, TCE, PCE, and sum of 5 CHCs from the contaminated groundwater in the simulated geological environment (non-contaminated gravel, fraction 4–8 mm) by nanoparticles Nanofer 25S in concentration 0 – control (A), 1 (B), 2 (C), and 4 g.l⁻¹ (D), and the pH course. Sampling of water for pH, E_c, and E_h after 1, 3, 7, 14, and 28 days of static degradation.

degrade and eliminate chlorinated compounds, especially due to the iron content.

Furthermore, carbonates of the gravel buffer the pH fluctuations caused by the addition of nZVI and release of OH⁻ anions. In the bottles without gravel, pH value was slightly rising up from neutral to basic values after the nZVI addition (Fig. 2, Tab. 2), while in the presence of gravel, pH value remained slightly basic (7.6–8.3) throughout the nanodegradation. That could indicate the potential success of future *in situ* groundwater nanoremediation in the real geological environment. The “buffering” capacity of geological environment may attenuate the change of pH that can be responsible for undesired changes in the environmental balance (e.g. metal leaching). The temperature was increasing slightly from 20 °C to 26 °C, which designate this environment as favorable for the autochthonous bacteria with the biodegradation capabilities. Redox potential (E_h) has a significant impact to the natural attenuation; bioavailability and toxicity of chemical substances correlate with oxidative and reductive reactions in the matrix. The groundwater without nZVI had positive E_h values, but the addition of nZVI caused the decrease to negative values, indicating the creation of reductive conditions. As mentioned above, reductive conditions are favorable for the degradation of highly chlorinated CAHs – PCE, TCE, which has been confirmed by the degradation results.

The addition of nZVI brought about the decreasing of conductivity (E_c) values in both environments after addition of nZVI. The conductivity of the non-treated groundwater remained almost at the same level; the nZVI in the concentration of 1 g.l⁻¹ did not cause a change in conductivity immediately after addition, but during the experiment, the values were slightly decreasing. The conductivity change may be related with the pH change; alkaline environment can cause a precipitation of electrolytes in the experimental container (Waclawek et al., 2015). The crucial finding is, both approaches decreased the concentration of *cis*-1,2-DCE, TCE and PCE below the hygienic limits – ID and IT criteria (Tab. 1) for water according to the above-mentioned Directive of Ministry of Environment.

Conclusion

It was confirmed that degradation of the groundwater CAHs in the isolated environment occurs even without the application of remediation techniques. However, spontaneous degradation in the real contaminated water is determined with the inflow of the native water. Injection of nZVI accelerated the CAH degradation, especially in the contaminated groundwater in the simulated geological environment. Almost complete degradation of *cis*-1,2-DCE, TCE, PCE and the sum of 5 CAHs were achieved, independent of the dose of nZVI (1 vs 4 g.l⁻¹). Taking into

Tab. 2

Physical parameters (t , E_h , pH and E_c) measured during the nanodegradation of CAHs in the contaminated water (A) and in the contaminated water with simulated geological environment (B).

A. Contaminated water									
without nZVI, $c_{nZVI} = 0 \text{ g.l}^{-1}$					$c_{nZVI} = 1 \text{ g.l}^{-1}$				
Day	t [°C]	E_h [mV]	pH	E_c [$\mu\text{S.cm}^{-1}$]	day	t [°C]	E_h [mV]	pH	E_c [$\mu\text{S.cm}^{-1}$]
1	20.8	230.1	7.08	1 066	1	20.8	-147.1	6.89	1 046
3	22.5	140.0	7.12	930	3	23.3	-76.2	7.56	973
7	21.3	78.4	7.08	927	7	20.9	-155.8	7.68	876
14	23.5	78.8	7.16	975	14	23.5	-18.1	8.53	782
28	22.8	101.6	6.58	1 062	18	21.5	-201.7	9.52	725
62	26.3	272.6	7.49	1 017	62	25.8	-337.0	9.81	618
B. Contaminated water in the simulated geological environment									
without nZVI, $c_{nZVI} = 0 \text{ g.l}^{-1}$					$c_{nZVI} = 1 \text{ g.l}^{-1}$				
Day	t [°C]	E_h [mV]	pH	E_c [$\mu\text{S.cm}^{-1}$]	day	t [°C]	E_h [mV]	pH	E_c [$\mu\text{S.cm}^{-1}$]
1	20.7	83.1	7.04	1 022	1	21.1	-365.1	7.60	950
3	22.3	132	7.11	1 023	3	22.4	-387.0	7.95	843
7	24.6	54.2	7.11	935	7	22.1	-316.2	8.07	769
14	25.6	56.8	7.12	890	14	24.1	-253.2	8.33	692
28	22.7	106.2	7.17	1 024	28	21.8	-217.9	7.70	674

account the economic aspect, the concentration of nZVI 1 g.l⁻¹ is considered as sufficient for nanodegradation. In addition, no VC was determined, therefore it is assumed that the degradation pathway led to the formation of non-toxic products. The gravel, representing the geological environment, attenuated the alkalization of the groundwater after the nZVI addition, creating the suitable conditions for microbes with degradation abilities. Results show a potential for successful *in situ* application of nZVI, possibly in combination with other remediation approaches, which may be the definitive solution for the cleanup of polluted sites.

Acknowledgement

We are grateful to the Centre of Environmental Services, Ltd. (Bratislava) for financing this research and NANO IRON, s.r.o. (Czech Republic) for providing samples of synthetic nZVI. We express our thanks to reviewer Jozef Kordík and one anonymous reviewer for corrections in the primary manuscript.

References

- AUFFAN, M., ACHOUAK, W., ROSE, J., RONCATO, M. A., CHANÉAC, C., WAITE, D. T., MASON, A., WOICIK, J. C., WIESNER, M. R. & BOTTERO, J. Y., 2008: Relation between the redox state of iron-based nanoparticles and their cytotoxicity toward *Escherichia coli*. *Environ. Sci. Technol.*, 42, 6730–6735. <https://doi.org/10.1021/es800086f>.
- AUXT, A., ŠUCHOVÁ, M., MURIN, M., DRASTICHOVÁ, I. & MURINOVÁ, M., 2002: Partial final report – ecological solution of the Košická–Landererova Area in Bratislava. Remediation of the ecological burden in the wider area of the industrial zone of the former Apollo refinery. Partial task: Risk analysis (risk assessment). *Final Report, archive St. Geol. Inst. D. Štúr, Bratislava, 149 p.* (In Slovak).
- BARBEE, C. G., 1994: Fate of chlorinated aliphatic hydrocarbons in the vadose zone and ground water. *Ground Water Monit. R., winter 1994, 129–140*. <https://doi.org/10.1111/j.1745-6592.1994.tb00098.x>.
- BHATT, P., KUMAR, M. S., MUDLIAR, S. & CHAKRABARTI, T., 2007: Biodegradation of chlorinated compounds – a review. *Crit. Rev. Env. Sci. Tec.*, 37, 165–198. <https://doi.org/10.1080/10643380600776130>.
- CECCHIN, I., REDDY, K. R., THOMÉ, A., TESSARO, E. F. & SCHNAID, F., 2017: Nanobioremediation: Integration of nanoparticles and bioremediation for sustainable remediation of chlorinated organic contaminants in soils. *Int. Biodeter. Biodegr.*, 119, 419–428. <https://doi.org/10.1016/j.ibiod.2016.09.027>.
- CLEMENT, T. P., JOHNSON, CH. D., SUN, Y., KLECKA, G. M. & BARTLETT, C., 2000: Natural attenuation of chlorinated ethene compounds: model development and field-scale application at the Dover site. *J. Contam. Hydrol.*, 42, 113–140. [https://doi.org/10.1016/S0169-7722\(99\)00098-4](https://doi.org/10.1016/S0169-7722(99)00098-4).
- ČERNÍK, M., 2010: Chemically supported *in situ* remediation technologies. 1. Ed, *Praha, Vyd. VŠCHT, 348 p.* ISBN 978-80-7080-767-5 (In Czech).
- Directive of Ministry of Environment of the Slovak Republic No. 1/2015-7 for the elaboration of risk assessment analysis of contaminated sites. http://www.minzp.sk/files/sekcia-geologie-prirodných-zdrojov/ar_smernica_final.pdf. Accessed 27 June 2018 (In Slovak).
- EL-TEMSAH, Y. S. & JONER, E. J., 2012: Ecotoxicological effects on earthworms of fresh and aged nano-sized zero-valent iron (nZVI) in soil. *Chemosphere*, 89, 76–82. <https://doi.org/10.1016/j.chemosphere.2012.04.020>.
- EL-TEMSAH, Y. S. & JONER, E. J., 2013: Effects of nano-sized zero-valent iron (nZVI) on DDT degradation in soil and its toxicity to collembola and ostracods. *Chemosphere*, 92, 131–137. <https://doi.org/10.1016/j.chemosphere.2013.02.039>.
- FAJARDO, C., SACCÀ, M. L., MARTINEZ-GOMARIZ, M., COSTA, G., NANDE, M. & MARTIN, M., 2013: Transcriptional and proteomic stress responses of a soil bacterium *Bacillus cereus* to nanosized zero-valent iron (nZVI) particles. *Chemosphere*, 93, 1077–1083. <https://doi.org/10.1016/j.chemosphere.2013.05.082>.
- FRANKOVSKÁ, J., KORDÍK, J., SLANINKA, I., JURKOVIČ, E., GREIF, V., ŠOTTNÍK, P., DANAJAJ, I., MIKITA, S., DERCOVÁ, K. & JÁNOVÁ, V., 2010: Atlas of remediation methods of environmental loads. *Bratislava, St. Geol. Inst. D. Štúr, 360 p.* ISBN 978-80-89343-39-3 (In Slovak).
- HORVÁTHOVÁ, H., LÁSZLOVÁ, K. & DERCOVÁ, K., 2019: Bioremediation vs. nanoremediation: degradation of polychlorinated biphenyls (PCBs) using integrated remediation approaches. *Water Air Soil Pollut.*, 230, 204. <https://doi.org/10.1007/s11270-019-4259-x>.
- CHIU, W. A., JINOT, J., SCOTT, CH. S., MARKIS, S. L., COOPER, G. S., DZUBOW, R. C., BALE, A. S., EVANS, M. V., GUYTON, K. Z., KESHAVA, N., LIPSCOMB, J. C., BARONE JR., S., FOX, J. F., GWINN, M. R., SCHAUM, J. & CALDWELL, J. C., 2013: Human health effects of trichloroethylene: key findings and scientific issues. *Environ. Health Perspect.*, 121, 303–311. <https://doi.org/10.1289/ehp.1205879>.
- JANTÁK, V. & POLÁK, R., 2001: The Košická Bridge – Delimitation of the area with the possibility of contamination of soils and groundwater. *Final Report. Bratislava, archive St. Geol. Inst. D. Štúr, 17 p.* (In Slovak).
- JANTÁKOVÁ, N., ŽENIŠOVÁ, Z., KORDÍK, J. & BENKOVÁ, K., 2018: Monitoring the impact of environmental burdens from the former Apollo Refinery, the Chemika and Gumon plants in Bratislava. *Acta Geol. Slov.*, 10, 2, 73–87.
- KEANE, E., 2009: Fate, transport, and toxicity of nanoscale zero-valent iron (nZVI) used during superfund remediation. National network for environmental management studies fellow Duke University, for: U.S. Environmental Protection Agency, Office of solid waste and emergency response. *Office of superfund remediation and technology innovation, Washington, DC, 18–23*.
- KOTCHAPLAI, P., KHAN, E. & VANGNAI, A. S., 2017: Membrane alterations in *Pseudomonas putida* F1 exposed to nanoscale zerovalent iron: Effects of short-term and repetitive nZVI exposure. *Envi. Sci. Tec.*, 51, 7804–7813. <https://doi.org/10.1021/acs.est.7b00736>.

- MALOVESKÝ, M., SOČUVKA, M. & BRUTENIČ, P., 2006: Remediation of old ecological burdens in the wider area of the industrial zone of the former Apollo Bratislava refinery. *Final Report. Bratislava, archive St. Geol. Inst. D. Štúr, 18 p.* (In Slovak).
- MUNDT, K. A., BIRK, T. & BURCH, M. T., 2003: Critical review of the epidemiological literature on occupational exposure to perchloroethylene and cancer. *Int. Arch. Occup. Environ. Health, 76, 473–491.* <https://doi.org/10.1007/s00420-003-0457-2>.
- NĚMEČEK, J., LHOTSKÝ, O. & CAJTHAML, T., 2014: Nanoscale zero valent iron application for *in situ* reduction of hexavalent chromium and its effects on indigenous microorganism populations. *Sci. Total Environ., 485–486, 739–747.* <https://doi.org/10.1016/j.scitotenv.2013.11.105>.
- PRISTAŠ, J., HORNÍŠ, J., HALOUZKA, R., MAGLAY, J., KONEČNÝ, V., LEXA, J., NAGY, A., VASS, D. & VOZÁR, J., 1992: Surface geological map of the Danube region, 1 : 50 000. *Manuscript. Bratislava, archive St. Geol. Inst. D. Štúr.*
- RUSYN, I., CHIU, W. A., LASH, L. H., KROMHOUT, H., HANSEN, J. & GUYTON, K. Z., 2014: Trichloroethylene: mechanistic, epidemiologic and other supporting evidence of carcinogenic hazard. *Pharmacol. Ther., 141, 55–68.* <https://doi.org/10.1016/j.pharmthera.2013.08.004>.
- SCHIEFLER, A. A., TOBLER, D. J., OVERHEU, N. D. & TUXEM, N., 2018: Extent of natural attenuation of chlorinated ethenes at a contaminated site in Denmark. *Energy Procedia, 146, 188–193.* <https://doi.org/10.1016/j.egypro.2018.07.024>.
- SHIN, K. H. & CHA, D. K., 2008: Microbial reduction of nitrate in the presence of nanoscale zero-valent iron. *Chemosphere, 72, 257–262.* <https://doi.org/10.1016/j.chemosphere.2008.01.043>.
- STEFANIUK, M., OLESZCZUK, P. & OK, Y. S., 2016: Review on nano zerovalent iron (nZVI): From synthesis to environmental applications. *Chem. Eng. J., 287, 618–632.* <https://doi.org/10.1016/j.cej.2015.11.046>.
- TIAN, H., LIANG, Y., YANG, D. & SUN, Y., 2020: Characteristics of PVP – stabilized NZVI and application to dechlorination of soil-sorbed TCE with ionic surfactant. *Chemosphere, 239, 124807.* <https://doi.org/10.1016/j.chemosphere.2019.124807>.
- VLASKO, I., VLASKO ML., I., VÝBOCH, M. & ZATLAKOVIČ, M., 2015: Bratislava, TWIN CITY north. Detailed geological survey of the environment. Final report. V&V GEO, s.r.o. *Manuscript. Bratislava, archive St. Geol. Inst. D. Štúr* (In Slovak).
- WACLAWEK, S., NOSEK, J., CÁDROVÁ, L., ANTOŠ, V. & ČERNÍK, M., 2015: Use of various zero valent irons for degradation of chlorinated ethenes and ethanes. *Ecol. Chem. Eng., 22, 577–587.* <https://doi.org/10.1515/eces-2015-0034>.
- WALTER, R. K., LIN, P-H., EDWARDS, M. & RICHARDSON, R. E., 2011: Investigation of factors affecting the accumulation of vinyl chloride in polyvinyl chloride piping used in drinking water distribution systems. *Water Res., 48, 2607–2615.* <https://doi.org/10.1016/j.watres.2011.02.016>.
- WANG, Q., SONG, X., TANG, S. & YU, L., 2020: Enhanced removal of tetrachloroethylene from aqueous solutions by biodegradation coupled with nZVI modified by layered double hydroxide. *Chemosphere, 243, 125–260.* <https://doi.org/10.1016/j.chemosphere.2019.125260>.
- YANG, Y. F., CHEN, P. J. & LIAO V. H. CH., 2016: Nanoscale zerovalent iron (nZVI) at environmentally relevant concentrations induces multigenerational reproductive toxicity in *Caenorhabditis elegans*. *Chemosphere, 150, 615–623.* <https://doi.org/10.1016/j.chemosphere.2016.01.068>.
- Yu, J. J. & Chou, S. Y., 2000: Contaminated site remedial investigation and feasibility removal of chlorinated volatile organic compounds from groundwater by activated carbon fiber adsorption. *Chemosphere, 41, 371–378.* [https://doi.org/10.1016/S0045-6535\(99\)00437-3](https://doi.org/10.1016/S0045-6535(99)00437-3).
- Zhang, W., Xiao, T., Liu, N. & Ying, W., 2017: The removal of chlorinated aliphatic hydrocarbons from water using reactive activated carbon: the influence of synthesis factors and reaction environments. *Environ. Technol., 39, 1328–1339.* <https://doi.org/10.1080/09593330.2017.1329350>.

Nanodegradácia chlórovaných uhl'ovodíkov z podzemnej vody v natívnom geologickom prostredí (laboratórny vsádzkový experiment)

Degradácia chlórovaných uhl'ovodíkov (CIU) aplikáciou nanočastíc železa s nulovým mocenstvom (nZVI) do geologického prostredia predstavuje inovatívnu remediáciu metódu. Úspech takejto remediácie CIU *in situ* je podmienený realizáciou experimentov v podmienkach, ktoré čo naj dôvernejšie simulujú reálne geologické prostredie. Jednými z najnebezpečnejších a zároveň najčastejšie sa vyskytujúcich chlórovaných uhl'ovodíkov sú chlórované etény – vinylchlorid (VCM), 1,1-dichlórétén (1,1-DCE), *cis*-1,2-dichlórétén (*cis*-1,2-DCE), *trans*-1,2-dichlórétén (*trans*-1,2-DCE), trichlórétén (TCE) a tetrachlórétén (perchlórétén, PCE). V minulosti sa potenciálnej toxicite CIU nevenovala pozornosť, no v súčasnosti je známe,

že izoméry DCE a PCE sú organizáciou US EPA klasifikované ako pravdepodobné karcinogény a VCM a TCE ako potvrdené karcinogény. Cieľom tohto výskumu bola degradácia chlórovaných uhl'ovodíkov z natívnej vzorky kontaminovanej podzemnej vody v simulovanom geologickom prostredí aplikáciou disperzie nZVI Nanofer 25S. Nanočastice ako silné redukčné činidlo CIU sa degradujú mechanizmom sekvenčnej hydrogenolýzy alebo za určitých podmienok v prípade CIU s vicinálnymi chlórými substitúciami redukčnou β -elimináciou. CIU podliehajú nasledujúcemu rozkladu: PCE \rightarrow TCE \rightarrow DCE \rightarrow VCM \rightarrow etén. Výsledkom redukcie je teda zníženie stupňa chlórácie.

Natívna kontaminovaná voda pochádza z lokality Klingerka, nachádzajúcej sa v širšom centre Bratislavy. Podzemná voda je kontaminovaná ropnými uhl'ovodíkmi z čias bombardovania rafinérie Apollo. Voda bola odobraná jednorazovo z vrtu CS-21 čerpadlom podľa príslušných noriem a technických noriem STN.

Stacionárny experiment degradácie CIU v natívnej vode (A) prebiehal v sklenených nádobách (2 l) s natívnou kontaminovanou vodou zo zásobnej nádrže (2 l). Do fliaš bola pridaná disperzia nZVI Nanofer 25S v koncentracii 1, 2 a 4 g · l⁻¹. Jedna nádoba ostala bez prídavku nZVI (kontrola). Stacionárny experiment degradácie CIU vo vode v simulovanom geologickom prostredí (B) sa realizoval s použitím inertného nekontaminovaného štrku s frakciou 4 – 8 mm. Takýto systém reprezentoval štrkový kolektor podzemnej vody. Test prebiehal v sklenených nádobách (5 l) naplnených štrkom a doplnených natívnou vodou zo zásobnej nádrže (ca 1,5 l). Do nádob bola pridaná disperzia nZVI Nanofer 25S v koncentracii 1, 2 a 4 g · l⁻¹. Jedna nádoba ostala bez prídavku nZVI (kontrola). Experimenty prebiehali pri teplote 20 – 25 °C. Z nádob sa po 1, 3, 7, 14 a 28 dňoch [z nádob s natívnou vodou (experiment A) aj po 62 dňoch] odoberali vzorky a zmerali sa základné fyzikálne veličiny (t, pH, E_h, E_c). Koncentrácia 5 CIU (VCM, 1,1-DCE, *trans*-1,2-DCE a *cis*-1,2-DCE, TCE, PCE) a jej sumy v odobraných vzorkách sa stanovila v akreditovaných laboratóriách ALS Česká republika.

V kontaminovanej natívnej vode (experiment A) aj vo vode v simulovanom horninovom prostredí (experiment B) sa bez prídavku nZVI v priebehu trvania experimentu (62/28 dní) degradovalo vyše 80 % sumy 5 CIU. Degradácia CIU v uzavretom priestore (sklenená nádoba) prebieha do značnej miery aj samovoľne. Za túto degradáciu okrem bežných fyzikálno-chemických javov môžu byť zodpovedné aj mikroorganizmy prítomné v natívnej vode (Schiefler et al., 2018). Tie sa pri vyššej teplote (20 – 25 °C) mohli podieľať na úbytku CIU ich biodegradáciou. Realizovanými experimentmi sa

potvrdila aj účinnosť aplikácie nZVI, prídavkom disperzie Nanofer 25S sa v oboch systémoch za rovnaký čas (62/28 dní) dosiahla kompletná, 100 % degradácia sumy 5 CIU. Sledovali sa len minimálne rozdiely v degradácii pri rôznej koncentrácii nZVI, takže na degradáciu CIU v uzavretom prostredí postačuje disperzia nZVI v koncentrácii 1 g · l⁻¹.

V simulovanom horninovom prostredí vytvorenom prídavkom inertného štrku prebiehala degradácia rýchlejšie – v nádobách s nZVI aj v kontrole. Už po 7 dňoch pôsobenia nZVI sa degradácia približovala k 100 %, no v nádobách bez štrku sa za rovnaký čas sledovala degradácia nižšia takmer o 40 %. Horninové prostredie má prirodzenú schopnosť odbúravať a eliminovať chl'ované uhl'ovodíky najmä vďaka prítomnosti železa. Prítomnosť karbonátov horninového prostredia zároveň tlmí výkyvy pH spôsobené prídavkom nZVI. V nádobách bez štrku sa pH po prídavku nZVI zvyšovalo, v prítomnosti štrku sa hodnota pH držala v neutrálnej, resp. jemne bázičkej oblasti. Takéto prostredie je potenciálne vhodné aj pre autochtónne mikroorganizmy s biodegradáčnymi schopnosťami.

Sanácia vodného, resp. horninového prostredia nanoželezom patrí medzi inovatívne sanačné technológie a je možné ju efektívne kombinovať s rôznymi biologickými prístupmi či fyzikálno-chemickými postupmi, napr. podporou elektrickým prúdom a pod. Potvrdilo sa, že proces degradácie CIU prebieha aj bez aplikácie akýchkoľvek sanačných techník, no v reálnom prostredí by bola samovoľná degradácia determinovaná prítokom čerstvej natívnej vody. Injektáž nZVI vo vhodne zvolenej koncentrácii do podzemnej kontaminovanej vody by v takomto prípade mohla proces degradácie urýchliť a zefektívniť. V uzavretom prostredí sa v natívnej vode aj vo vode v simulovanom geologickom prostredí dosiahla kompletná degradácia sumy 5 chl'ovaných uhl'ovodíkov.

Doručené / Received: 14. 10. 2020
Prijaté na publikovanie / Accepted: 18. 2. 2021

Inštrukcie autorom

Etika publikovania, záväzná pri publikovaní v časopise Mineralia Slovaca:

www.geology.sk/mineralia položka **Publikačná etika**

1. Geovedný časopis Mineralia Slovaca publikuje scientometricky hodnotné recenzované pôvodné vedecké články s vysokým citačným potenciálom. V úvode príspevku musí autor jasne deklarovať, čím konkrétnym je jeho príspevok prínosný pre rozvoj geovied. Rešeršné štúdie sa publikujú len ojedinele.

2. Články na publikovanie (manuskripty) sa do redakcie zasielajú poštou (dva vytačené exempláre a CD so všetkými súbormi v editovateľnej podobe) alebo e-mailom (editovateľné súbory a kompletná verzia vo formáte PDF).

3. Súčasne s článkom je potrebné redakcii poslať autorské vyhlásenie o originalite textu a obrázkov. Kópie obrázkov z iných publikácií musia byť legalizované získaním práva na publikovanie. Vyhlásenie musí obsahovať meno autora (autorov), akademický titul a trvalé bydlisko.

4. Rozsah manuskriptu na publikovanie je najviac 25 rukopisných strán (MS Word, Times New Roman, veľkosť písmen 12 bodov, riadkovanie 1,5) vrátane literatúry, obrázkov a vysvetliviek. V prípade veľkého odborného prínosu sú v ojedinelých prípadoch povolené aj dlhšie články.

5. Články sú publikované v angličtine alebo v slovenčine. Články v slovenčine musia obsahovať anglický preklad názvu, abstraktu, kľúčových slov, resumé a popisov k obrázkom a tabuľkám. Články písané v angličtine musia obsahovať slovenské resumé.

Text

1. Abstrakt stručne sumarizuje článok. Môže mať najviac 200 slov a nemá obsahovať citácie. Počet kľúčových slov je maximálne 6. Text má mať úvod, charakteristiku (stav) skúmaného problému, použitú metodiku, nové zistenia, ich interpretáciu, diskusiu, záver a zoznam literatúry. Východiskové údaje musia byť zreteľne odlišené od interpretácií. V texte musia byť odvolávky na všetky použité obrázky a tabuľky.

2. Hierarchiu nadpisov v texte je potrebné vyznačiť ceruzkou na ľavom okraji strany manuskriptu: 1 – najvyššia, 2 – nižšia, 3 – najnižšia.

3. V texte sa uprednostňuje citácia v zátvorke, napr. (Dubčák, 1987; Hrubý et al., 1988), pred formou ... podľa Dubčáka (1987).

4. Pozícia obrázkov a tabuľiek v texte sa označí. Nie je vhodné, aby text v editore MS Word obsahoval vložené obrázky, ale náhľadová verzia v pdf ich má obsahovať.

5. Grécke písmená treba identifikovať na ľavom okraji slovom (napr. sigma). Potrebné je odlišovať pomlčku od spojovníka. Symboly, matematické značky, názvy skamenelín a pod., ktoré sa majú vysádzať kurzívou, autor v rukopise podčiarkne vlnkou.

Obrázky a tabuľky

1. Ilustrácie a tabuľky vysokej kvality bývajú publikované buď na šírku stĺpca (81 mm), alebo strany (170 mm). Optimálna veľkosť písma a čísiel v publikovaných obrázkoch je 2 mm. Články v slovenčine musia mať popisy v obrázkoch a tabuľkách v slovenčine, záhlavie tabuľiek a texty pod obrázkami a tabuľkami sú v slovenčine a angličtine. Články v angličtine majú všetky texty v angličtine. **Maximálny rozmer ilustrácie a tabuľky vytačený v časopise je 170 x 230 mm.** Väčšie (skladané) ilustrácie sú publikované len v ojedinelých prípadoch.

2. Pri počítačovej tvorbe obrázkov odporúčame používať programy s vektorovým zobrazením (Corel Draw, Adobe Illustrator a pod.). Čiary tzv. vlasovej hrúbky, softvérová alebo rastová výplň plôch (napr. v Corel Draw) nie sú prípustné. Výplne v obrázkoch musia pozostávať zo samostatne vyzádaných objektov.

3. Ilustrácie vrátane fotografií musia obsahovať grafickú mierku v centimetrovej či metrovej škále, prípadne sa rozmer zobrazených objektov vyjadri v popise obrázka. Mapy a profily musia mať aj **azimutálnu orientáciu** a jednotné vysvetlivky, ktoré sa uvedú pri prvom obrázku. Zoskupené obrázky, napr. fotografie a diagramy, sa uvádzajú ako jeden obrázok s jednotlivými časťami označenými písmenami (a, b, c atď.).

4. Pri zasielaní fotografií vo forme počítačových súborov (formáty JPG alebo TIF) sa požaduje rozlíšenie minimálne 600 DPI. Publikovanie farebných ilustrácií môže byť spoľahlivé.

Literatúra

1. Minimálne 50 % citácií musí reprezentovať publikácie od roku 2000. V zozname literatúry sa v abecednom poradí uvádza len literatúra citovaná v danom článku.

2. Spôsob uvádzania literatúry v zozname literatúry

Knižná publikácia: GAZDA, L. & ČECH, M., 1988: Paleozoikum medzevského príkrovu. Bratislava, Alfa, 155 s.

Časopis: VRBA, P., 1989: Strižné zóny v metapelitoch. *Miner. Slov.*, 21, 135 – 142.

Zborník: NÁVESNÝ, D., 1987: Vysokodraselné rhyolity. In: *Romanov, V. (ed.): Stratiformné ložiská gemerika. Spec. publ. Košice, Slov. geol. spol.*, 203 – 215.

Manuskript: RADVANSKÝ, F., SLIVKA, B., VIKTOR, J. & SRNKA, T., 1985: Žilné ložiská jedloveckého príkrovu gemerika. Záverečná správa z úlohy SGR-geofyzika. *Manuskript. Spišská Nová Ves, archív Št. Geol. Úst. D. Štúra*, 28 s.

3. Pri článku viac ako dvoch autorov sa v texte cituje iba prvý autor s dodatkom et al., ale v zozname literatúry sa uvádzajú všetci.

Instructions to authors

Publication ethics, being obligatory for publishing in the journal Mineralia Slovaca:

www.geology.sk/mineralia item **Publication ethics**

1. Geoscientific journal Mineralia Slovaca publishes scientometrically valuable original peer-reviewed scientific articles with a high citation potential. In the introduction of each article the author(s) must clearly declare, which innovative data the paper brings for the development of geosciences. The retrieval studies are published only exceptionally.

2. The articles for publishing (manuscripts) must be sent to Editorial Office by post (two printed copies and CD with editable files), or by e-mail (editable files plus complete preview version in PDF format).

3. Simultaneously with the article the Editorial Office must receive the author's proclamation that no part of the manuscript was already published and figures and tables are original as well. Copied illustrations from other publications must contain a copyright.

4. The extent of the manuscript for publishing is limited to 25 manuscript pages (MS Word, 12 points Times New Roman, line spacing 1.5) including figures, tables, explanations and references. In the case of contribution with a high scientific value, the longer manuscripts for publishing are exceptionally permitted.

5. Articles can be published in Slovak or English languages. The title, abstract, key words, shortened text (resumé), as well as description to figures and tables in Slovak articles are published also in English. Articles published in English contain Slovak resumé.

Text

1. Abstract briefly summarizing the article is limited to 200 words, no references are allowed. The maximum number of key words is 6. Text of the article has to contain the introduction, characterization (state) of investigated problem, applied methodology, obtained new data, discussion, conclusion and references. The obtained data must be distinctly separated from interpretations. All applied figures and tables must be referred in the text.

2. The hierarchy of headings in the manuscript must be indicated by a pencil note: 1 – highest level, 2 – lower, 3 – lowermost level.

3. The references in the text prefer parentheses, e.g. (Dubčák, 1987; Hrubý et al., 1988). The form "according to Dubčák (1987)" should be used only exceptionally.

4. Position of figures and tables must be indicated in the manuscript. Editable text of manuscript sent to editorial office must be without figures and tables, though the preview PDF has to contain them in a correct position.

5. Greek letter in the text must be identified at the left margin of the text (e.g. sigma). The text should strictly distinguish the dash from hyphen. Symbols, mathematic signs, names of fossils, etc., which should be printed in italics, must be underlined by the wavy line in the manuscript.

Figures and tables

1. The high quality figures and tables can be published either in **maximum width of column (81 mm) or page (170 mm)**. The optimum size of letters and numbers in the camera-ready figure is 2 mm. Articles published in Slovak contain the Slovak descriptions in figures and tables, the tables headings and descriptions beneath figures and tables are in Slovak and English. English articles contain all texts in English. **Maximum dimension of figures and tables in the journal is 170 x 230 mm. Larger (folded) illustrations are published only exceptionally.**

2. For figures drawing the editorial office recommends the vector graphics editors (Corel Draw, Adobe Illustrator, etc.). The very thin lines (hair lines), the pre-defined software or raster fillings of polygons (e.g. in Corel Draw) are not allowed. The filling must consist from separately set objects.

3. Each illustration including photographs must contain graphic (metric) scale, eventually the dimensions of visualized objects have to be stated in the describing text to figure. Maps and profiles must contain also the azimuth orientation, their detail explanations are stated at the first figure. Grouped figures, e.g. photographs and diagrams, are compiled as one figure with separate parts designated by letters (a, b, c, etc.).

4. The photographs sent as JPG or TIF files are required for having minimum 600 DPI resolution. Publishing of colour illustrations can be charged by a fee.

References

1. Minimum 50 % of referred works must represent contemporary publications after 2000. The references in alphanumeric order encompass only literature cited in the article.

2. Examples of referring:

Book: GAZDA, L. & ČECH, M., 1988: Paleozoic of the Medzev nappe. Bratislava, Alfa, 155 p.

Journal: VRBA, P., 1989: Shear zones in the metapelite complexes. *Miner. Slov.*, 21, 135–142.

Anniversary volume: NÁVESNÝ, D., 1987: High-potassium rhyolites. In: *Romanov, V. (ed.): Stratiform deposits of Gemericum. Spec. publ. Košice, Slov. geol. soc.*, 203–215.

Manuscript: RADVANSKÝ, F., SLIVKA, B., VIKTOR, J. & SRNKA, T., 1985: Vein deposits of the Jedľovec nappe of Gemericum. Final report from the project SGR-geophysics. *Manuscript. Spišská Nová Ves, Archive Št. Geol. Úst. D. Štúra*, 28 p.

3. The article with more than two authors is referred by the name of the first author with the amendment et al., but the list of references contains names of all authors.

OBSAH – CONTENT

PŮVODNÉ ČLÁNKY – ORIGINAL PAPERS

Marko, F., Sigdel, A., Bielik, M., Bezák, V., Mojzeš, A., Madarás, J., Papčo, J., Siman, P., Acharya, S. & Fekete, K.
A comparison of Cenozoic Neo-Alpine tectonic evolution of the Western Carpathian and Himalayan orogenic belts (Slovakia – Nepal)
Porovnanie kenozoickej neoalpínskej tektonickej evolúcie Západných Karpát a Himalájí (Slovensko – Nepál)

Potočný, T., Méres, Š. & Plašienka, D.

Geological structure and tectonometamorphic evolution of the Veporic–Gemic contact zone constrained by the monazite age data (Slavošovce–Štítnik area, Western Carpathians, Slovakia)
Geologická stavba a tektonometamorfný vývoj kontaktnej zóny veporika a gemerika dokumentovaný rádiometrickými vekmi monazitu (oblasť Slavošovce – Štítnik, stredné Slovensko)

Radvanec, M. & Gonda, S.

Successive formation of Fe and Mn skarns in the Čučma locality (Gemic unit, W. Carpathians): from metasomatic stage through the amphibolite facies overprint with Ti-rich tephroite to retrograde stilpnomelane-chlorite zone
Postupný vznik Fe a Mn skarnov na lokalite Čučma v gemeriku: od metasomatózy s následnou rekryštalizáciou v amfibolitovej fácii a vznikom Ti tefroitu až po retrográdnú metamorfózu v stilpnomelánovo-chloritovej zóne

Horváthová, H., Jurkovič, L., Macek, J., Tóth, R. & Kravchenko, D.

Nanodegradation of chlorinated hydrocarbons from groundwater in the native geological environment (laboratory batch experiment)
Nanodegradácia chlórovaných uhľovodíkov z podzemnej vody v natívnom geologickom prostredí (laboratórny vsádzkový experiment)

Indexed / Abstracted / Accessed by SCOPUS and EBSCO

Indexované / abstraktované / sprístupňované databázami SCOPUS a EBSCO

